Université du Québec
Institut national de la recherche scientifique
Centre Énergie Matériaux Télécommunications

THE EFFECTS OF INTERPARTICLE POTENTIALS ON NANOPARTICLE COAGULATION IN LOW-TEMPERATURE PLASMAS

Par

M.Sc. Benjamin Santos

Thèse présentée pour l'obtention du grade de
Doctorat en Sciences, Ph.D.
en sciences de l'énergie et des matériaux

Jury d'évaluation

Président et examinateur interne	Jean-Pierre Matte INRS-ÉMT
Examinateur externe	Steven L. Girshick University of Minnesota
Examinateur externe	Gerjan Hagelaar Université Paul-Sabatier
Directeur de recherche	François Vidal INRS-ÉMT

ACKNOWLEDGMENTS

I would like to thank immensely all the people who helped me, supported me and dedicated their time in the shaping of this work. Especially, in this brief note, my thanks go to the following people.

François Vidal for his help and patience when I was stuck and also for pushing me and motivating me to improve. I do not doubt that his great intuition as a physicist and researcher is reflected in this thesis.

Claude Boucher for starting the project and accepting me as a student even if I came from another domain of physics. Claude gave me what I think is the best start a student can have when starting their studies. Thank you for the trust you gave me and all your kindness.

To the evaluation committee for agreeing to evaluate the thesis during these difficult times due to the Coronavirus pandemic (COVID-19).

Jean-Pierre Matte, director of the evaluation committee, who also taught me a lot as a teacher. Your detailed report was very valuable.

Steven L. Girshick, for his excellent evaluation report and his feedback that makes me think about the importance of the results of this research.

Gerjan Hagelaar, for his pleasant and motivating comments on the thesis.

Alexander López, my mentor and great friend, for his invaluable help in all this process that started with my bachelor degree. Thanks for bringing me back to physics.

Laura Cacot, for the discussions and for your feedback.

Compute Canada and Calcul Québec for the maintenance and support of the clusters in which half of this work was carried out.

American Physical Society, Canadian Association of Physicists, International Plasma Chemistry Society, International HPC Summer School, Colloque Plasma-Québec, and GDRI Nanomateriaux Multifonctionnels Contrôlés for their support in all the events in which I participated.

Tsuneyuki Ozaki, director of the EMT center, for his support and follow-up work.

Hélène Sabourin and Sandra Poirier, for all the help with the paperwork and the support they gave me.

To all INRS staff, teachers, administration and technicians.

To the open source community, for their hard altruistic work that made this work possible.

Vanessa, my beloved wife, who was always by my side suffering and encouraging me in this fight. For carrying the load with me, for your patience, for your intelligence and your unconditional support.

VAMOS. Thank you for my children, Lucas and Thomas, who were born during this project and have given me so much happiness.

Ana, my mother, who has always believed in me. Ricardo, my father, whose good sense of humor and empathy I will always remember. To my brothers, Pío, who with his hard work allowed me to continue my studies; Anita, who will continue to inspire me with her strength; Israel, who helped me at a crucial moment and who always makes me happy. Layla and Ibrah, my dear niece and nephew. To my crazy uncles.

Gloria and Pepe, who supported me in every way. To my brothers-in-law Polo and Eduardo for so many moments of happiness.

To the Martinez family, Celestino, Eduardo, I could not have redirected my career without their support. To the Vásquez and Felce family for the pleasant moments.

To all my friends and colleagues.

Thank you.

RÉSUMÉ

Les plasmas poussiéreux sont composés d'électrons, de particules neutres et ionisées d'un gaz et des grains de matière condensée, que nous dénommerons nanoparticules. Les plasmas poussiéreux sont omniprésents dans la nature, en particulier dans l'espace, et peuvent également être générés en laboratoire dans différentes conditions de mélange du gaz, de température, de pression, et de type de décharge. Nous limiterons notre étude à la croissance de nanoparticules de silicium dans un plasma capacitif radiofréquence à basse température, dans un mélange argon-silane.

La croissance des nanoparticules démarre avec la nucléation, où des amas sont formés à partir de la polymerization des molécules de silane et ses derivés. Après, suit la phase de coagulation, qui démarre lorsqu'une densité critique de nanoparticules est atteinte. Dans cette phase, les nanoparticules s'agglomèrent pour former des particules plus grandes, qui peuvent atteindre des dizaines de nanomètres. Cette phase est caractérisée par une augmentation de la taille des particules et une diminution de la densité de particules. Ensuite, vient la phase de collage, dans laquelle de petites molécules collent à la surface des nanoparticules, qui devient le mécanisme de croissance plus important.

Il est bien établi que les nanoparticules dans les plasmas froids d'argon-silane sont principalement chargées négativement en raison du bombardement à haute fréquence des électrons. Par conséquent, la distribution en taille et en charge des nanoparticules dépendra de leurs interactions électrostatiques mutuelles. Pour calculer le potentiel électrostatique entre les nanoparticules, nous avons utilisé une formulation rigoureuse, basée sur des coefficients de moment multipolaires. Le potentiel d'interaction résultant n'est pas singulier au point de contact, ce qui permet d'utiliser la théorie "Orbital Motion Limited" (OML) pour calculer le facteur d'augmentation de la coagulation, ce dernier étant défini comme un facteur multiplicatif du taux de coagulation, qui dépend des forces entre les nanoparticules. Nous montrons qu'en raison de la polarisation induite dans les particules dielectriques la coagulation peut être augmentée de plusieurs ordres de grandeur entre les particules chargées et neutres. De plus, la force à courte portée entre des nanoparticules chargées ayant la même polarité peut devenir attractive. Ce potentiel multipolaire est comparé à une forme analytique approximative qui peut être utilisée directement pour simplifier les calculs.

Dans la dernière partie de ce travail, nous proposons un cadre numérique pour étudier la croissance des nanoparticules dans les plasmas froids. Ce système représente un défi en raison de sa complexité: les nanoparticules accumulent des charges, coalescent et croissent tout en étant fortement couplées au plasma. En utilisant une approche similaire à celle employée en physique des aérosols, nous décrivons l'évolution dans le temps de la distribution en taille et en charge des nanoparticules à l'aide d'une équation dite de dynamique générale qui tient compte des mécarnismes de chargement et de croissance. Une distribution en taille comportant deux populations, comme observée dans les expériences, résulte naturellement de ce modèle. On trouve que la force multipolaire électrostatique améliore la coagulation par rapport à la force coulombienne élémentaire. De plus, nous avons considéré les forces de van der

Waals. Nos résultats montrent que le modèle électrostatique considéré et l'interaction de van der Waals peuvent jouer un rôle significatif dans le processus de croissance des nanoparticules.

ABSTRACT

Nanodusty plasmas are composed of electrons, neutral and ionized particles of a gas, and nanometric sized grains of condensed matter that we call nanoparticles. Dusty plasmas are ubiquitous in nature, in particular in space, and they can also be generated over different laboratory conditions of the gas mixture, temperature, pressure, and type of discharge. We limit our study to the growth of silicon nanoparticles in low-temperature radiofrequency capacitively coupled argon-silane (Ar-SiH_4) plasmas.

The evolution of nanoparticle in size starts with the nucleation phase, where primary dust is formed from the polymeric assembly of silane molecules. Then follows the coagulation phase, which starts when a critical nanoparticle density is reached. In that phase, nanoparticles coalesce to form bigger particles, which can grow to tens of nanometers. This phase is identified by an increase in the nanoparticle size and a decrease in the nanoparticle number density. Then follows the surface growth phase, in which small molecules stick on the surface of the nanoparticles, which becomes the most important growth mechanism.

It is well established that nanoparticles in low-temperature Ar-SiH_4 plasmas are mostly charged negatively due to the high-frequency electron bombardment. Hence the nanoparticles size-charge distribution depends on their mutual electrostatic interactions. To compute the complete interparticle electrostatic potential between dielectric particles, we used a rigorous formulation, based on multipole moment coefficients. The resulting interaction potential is non-singular at the contact point, which allows using the orbital-motion limited (OML) theory to calculate the enhancement factor, which is defined as a multiplying factor of the coagulation rate which depends on the forces between the nanoparticles. We show that, due to induced polarization, coagulation can be enhanced in neutral-charged particles encounters up to several orders of magnitude. Moreover, the short-range force between like-charged nanoparticles can become attractive as a direct consequence of the dielectric nature of the nanoparticles. The multipolar coefficient potential is compared to an approximate analytic form, which can be readily used to simplify the calculations.

In the last part of this work, we propose a framework to study nanoparticle growth in low-temperature plasmas. This system is quite challenging because of its complexity: nanoparticles can accumulate charge, coagulate, and grow while being strongly coupled with the plasma. By using an approach similar to that used in the physics of aerosols, we describe the evolution of the size and charge distribution of the nanoparticle using a General Dynamics Equation, which takes into account the charging and growth mechanisms. A two-population size distribution, as observed in experiments, results naturally from this model. The electrostatic multipolar force is found to enhance the coagulation as compared to the elementary Coulomb force. Additionally, we considered the van der Waals forces. Our results point out that the electrostatic model and the van der Waals interaction may both play a significant role in the nanoparticle growth process.

TABLE OF CONTENTS

LIST OF FIGURES

LIST OF TABLES

NOMENCLATURE

Acronyms

CVD	Chemical vapor deposition
EEDF	Electron energy distribution function
FPT	Fixed Pivot Technique
GDE	General Dynamics Equation
PECVD	Plasma enhanced chemical vapor deposition

Symbols

Γ	Electron coupling parameter
Γ_α	Flux of particle α
Γ_ε	Electron energy flux
k_B	Boltzmann constant
λ	Neutral mean free path
$\lambda_{\mathrm{D}e}$	Electron Debye length
$\lambda_{\mathrm{D}i}$	Ion Debye length
μ_α	Mobility of particle α
$\omega_{\mathrm{p}e}$	Electron plasma frequency
ρ	Charge density
ε	Electron mean energy
ε_0	Vacuum electric permittivity
D_α	Diffusion coefficient for particle α
e	Elementary charge
f_w	Electron energy distribution function
g	Plasma parameter

m_e	Electron mass
n_α	Density of particle α
N_D	Debye number
n_ε	Electron energy density
n_e	Electron density
n_i	Ion density
q_α	Charge of particle α
T_e	Electron temperature
T_i	Ion temperature
T_i	Ion temperature
v_α	Speed of particle α

1 General Introduction

The goal of this chapter is to give the reader the basic concepts that are needed to understand the methods and results discussed in the research articles of chapters 2, 3, and 4.

First, we introduce plasmas in a general fashion and then we explain in some detail low-temperature plasmas along with the numerical models used to describe them. Second, we discuss dusty plasmas and the physical processes involved. Third, we introduce the numerical model implemented to generate the results of chapter 4. Finally, we expose our motivations behind this work.

1.1 Basic concepts of plasma physics

Plasma is composed of a gas mixture which contains neutral and ionized atoms or molecules, and many interacting electrons. Macroscopically, plasma as a substance is neutral, and the charged species exhibit collective behavior [5]. The long-ranged Coulomb interaction influences this collective behavior, which is non-local because the motion of the particle species depends on the local and remote state of the plasma.

Plasma is considered to be the fourth state of matter [5], along with the other states solid, liquid, and gaseous. The binding forces between its constituents characterize a state of matter. These range from strong coupling (solid) to practically zero coupling (gas). If one applies sufficient energy to a gas, the atoms and molecules break into ions and electrons by the ionization process and can become a plasma. A high degree of ionization, the ratio between charged particles and total particles, is needed to transform the gas into a plasma.

Plasmas exist naturally in the universe: on the Earth as flames and lightning bolts, in space, as the ionosphere and solar wind, and outside our solar system, as nebulae, and in the surroundings of black holes and supernovae. In this regard, we can safely state that most of the matter in the universe is in the plasma state [10] or interacts with it.

Besides naturally occurring plasmas on Earth and in interplanetary and interstellar space, plasmas that can also be produced in the laboratory. For instance, intense research is conducted to promote the nuclear fusion between deuterium and tritium to release useful power. Several concepts aiming to achieve this goal have been experimented, like magnetic mirrors, tokamaks, theta pinch devices,

and laser-pellet fusion [5]. The confinement is necessary to produce a plasma at sufficiently high temperatures and density to allow the nuclear fusion reaction.

Probably the most common human-engineered plasmas are the glow discharges, which can be found in neon signs, fluorescent lamps, and plasma television screens. Often, the plasma in a glow discharge is generated by imposing a current through a low-pressure gas by applying a voltage between electrodes.

Plasmas can be classified in a chart of the electron density versus plasma temperature, as shown in figure 1.1. For a better interpretation of this figure, one must define the plasma temperature.

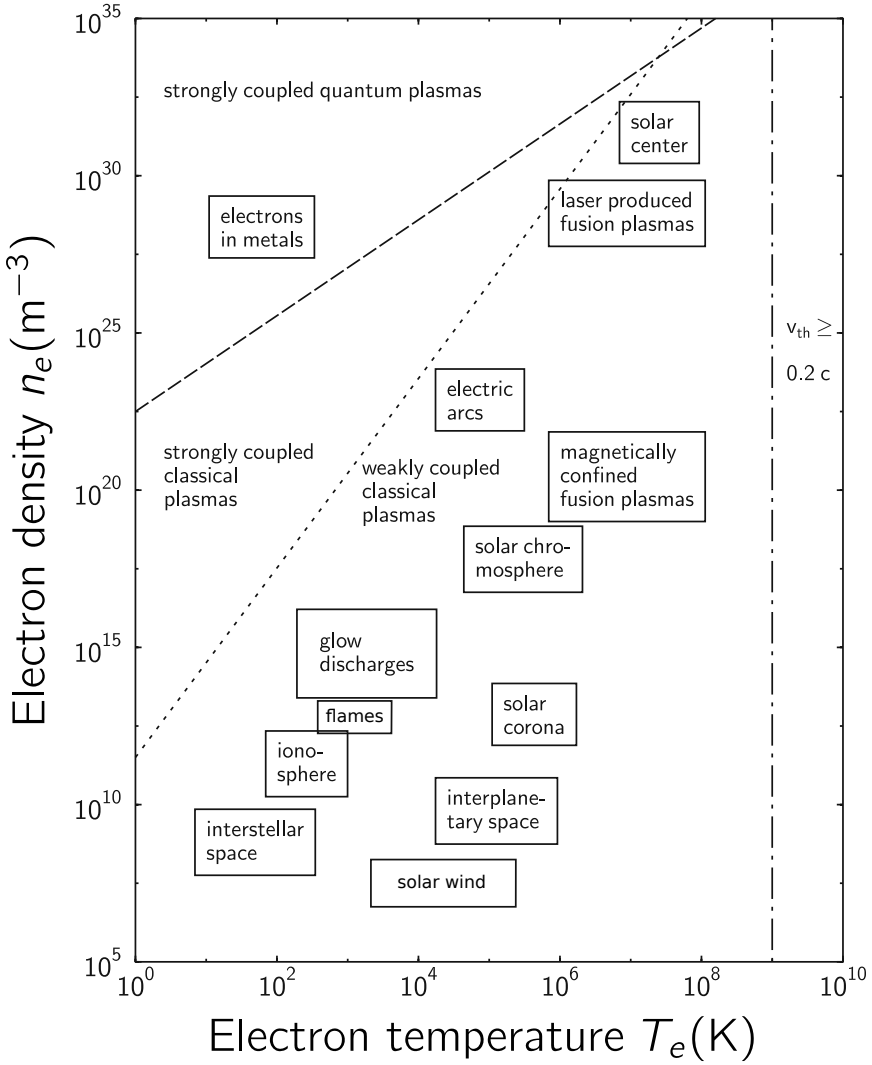

Figure 1.1: Chart of the plasma types. Adapted from [31].

The most probable distribution for the velocities of the particles in a gas, at thermal equilibrium, is a Maxwellian distribution [10],

$$f_\alpha(v_\alpha) = n_\alpha \left(\frac{m_\alpha}{2\pi k_\mathrm{B} T_\alpha}\right)^{3/2} \exp\left(-\frac{m_\alpha v_\alpha^2}{2k_\mathrm{B} T_\alpha}\right), \tag{1.1}$$

where $k_\mathrm{B} = 1.38 \times 10^{-23}\,\mathrm{JK}^{-1}$ is the Boltzmann constant, $v_\alpha = |\boldsymbol{v}|$ and m_α are the speed and the mass of particle α, and n_α is the total number of particles α per m^3, or density, which is defined as

$$n_\alpha = \int_0^\infty f(v_\alpha)\,\mathrm{d}v_\alpha\,. \tag{1.2}$$

The constant T_α, the temperature, is related to the average kinetic mean energy for the particle α, which is defined as

$$\varepsilon_\alpha = \frac{\int_0^\infty \frac{1}{2} m v^2 f(v_\alpha)\,\mathrm{d}v_\alpha}{\int_0^\infty f(v_\alpha)\,\mathrm{d}v_\alpha} = \frac{3}{2} k_\mathrm{B} T_\alpha. \tag{1.3}$$

Because of this relation, plasma physicists often give the electron temperature in the unit of energy of electronvolt. However, in figure 1.1, for instance, the electron temperature is given in Kelvin. In the following, to avoid ambiguity, we will use ε_e for the electron mean energy in eV, T_e for the electron temperature in K, and n_e for the electron density in m^{-3}, as we will see these quantities play an important role in the description of plasmas.

Quasi-neutrality or macroscopic neutrality means that in a significant volume of plasma with no external forces exerted, the net charge is nearly zero. This occurs because, at the microscopic level, the space charge fields cancel each other with the consequence of no net electric charge at the macroscopic level. A consequence of the collective behavior in plasmas is that the particles will organize themselves to screen the electrostatic fields both at atomic and macroscopic levels. The Debye length for electrons (ions), is defined as

$$\lambda_{\mathrm{D}e,i} \equiv \left(\frac{\varepsilon_0 k_\mathrm{B} T_{e,i}}{n_{e,i} e^2}\right)^{1/2}. \tag{1.4}$$

It provides a measure of the distance at which this shielding is effective, and inside it, the quasi-neutrality is not guaranteed.

Another essential concept of plasma physics is the coupling parameter. It relates the electric potential energy of the particles to the thermal energy. For electrons, the coupling parameter is

$$\Gamma \equiv \frac{e^2}{4\pi\varepsilon_0 r_\mathrm{WS}^2 k_\mathrm{B} T_e}, \tag{1.5}$$

where $r_\mathrm{WS} \equiv (3/4\pi n_e)^{1/3}$ is the Wigner-Seitz radius, a measure of interparticle distance. A weakly coupled plasma is defined as $\Gamma < 1$ and characterizes the gaseous phase. The liquid and solid phases are characterized by $1 < \Gamma < 200$ and $\Gamma > 200$, respectively [31]. A related criterion also used is the plasma parameter g

$$g \equiv \frac{4\pi}{3N_\mathrm{D}^3} \approx \Gamma_e^{3/2}, \tag{1.6}$$

where,

$$N_{\mathrm{D}} \equiv \frac{4}{3}\pi \left(\frac{\varepsilon_0 k_{\mathrm{B}} T_e}{n_e^{1/3} e^2} \right)^{3/2} . \tag{1.7}$$

is the number of electrons in the Debye sphere whose radius is the Debye length. The dashed line in figure 1.1 separates weakly from strongly coupled plasmas and is defined by $N_D = 1$.

When perturbing a plasma, the collective behavior of the particles will tend to restore the charge neutrality. The plasma frequency

$$\omega_{\mathrm{p}e} \equiv \left(\frac{n_e e^2}{m_e \varepsilon_0} \right)^{1/2} , \tag{1.8}$$

characterizes the natural oscillation frequency of the perturbed electron gas. Because ions are more massive than electrons, they move slowly while electrons oscillate at high frequency (ultraviolet) around the ions to recover neutrality. The electron response time is approximately $\tau = 2\pi\omega_{\mathrm{p}e}^{-1}$.

Finally, we can list all the criteria which define the plasma state [10, 31, 5],

- Plasmas are quasi-neutral.
- $\lambda_{\mathrm{D}e} \ll L$, with L the characteristic dimension of the system. This condition allows having sufficient space to obtain the collective shielding effect.
- $N_{\mathrm{D}} \ggg 1$. It is necessary to have a significant number of electrons inside the Debye sphere to produce a collective behavior. Conversely, the average distance between electrons must be smaller than the Debye length, and this implies $g \ll 1$.
- The frequency response to a perturbation in the plasma is given by $\omega_{\mathrm{p}e}$. To be meaningful, this frequency has to be higher than the frequency associated with the collision of electrons with neutral atoms.

For instance, if the Debye length is greater than the dimensions of the system, quasi-neutrality cannot be guaranteed and collective effects will not be observed. The prevailing quantities used to define these criteria are the electron density and the electron temperature. As we show in figure 1.1, plasmas have a wide range of variation for these quantities. This allows us to observe distinct behavior in plasmas as a function of n_e and T_e, and opens the possibility of a vast number of applications, from plasma thrusters to power generation. In this work, we are interested in the description of low-temperature plasmas used frequently in materials and thin layers processing.

1.2 Low-temperature radio-frequency capacitive plasmas

In low-temperature plasmas, the temperature of electrons $T_e \approx 1 \times 10^4 - 1 \times 10^5\,\mathrm{K}$ is much higher than the temperature of the ions, usually in the range of room temperature $T_i \approx 300\,\mathrm{K}$. The electron density is around $n_e \approx 1 \times 10^{14} - 1 \times 10^{19}\,\mathrm{m}^{-3}$, and the pressure is low $p \approx 1 - 1000\,\mathrm{mTorr}$ [24].

These parameters allow to trigger ionization and dissociation of molecules, even though the electron temperature is lower than the threshold energies for these processes. This is possible because of the high-energy tail of the electron energy distribution function which contains highly energetic particles. Later, we will see that the distribution function often deviates from the Maxwell distribution.

The difference of temperature between electrons and heavy species, is exploited by two techniques used in materials processing: plasma enhanced chemical vapor deposition (PECVD) and chemical vapor deposition (CVD) [20]. In the first technique, dissociation of molecules of a precursor gas is produced in a low-temperature plasma by electron impact. Then the byproducts condensate on a substrate at room temperature. In the second technique, the substrate is heated to allow thermal dissociation of the gas thus promoting condensation on the surface.

In plasma etching, plasmas are used to etch metals or silicon materials. IIn this method, the surface is modified by taking advantage of ion bombardment on the surface in addition to that of neutrals and radicals. Usually these plasmas are generated in a capacitive RF plasma configuration. Fig. 1.2 shows a parallel plate configuration powered by an RF source, customarily at 13.56 MHz. The substrate lies on one electrode, and gas flows through the chamber. A vacuum pump sustains the pressure in the reactor.

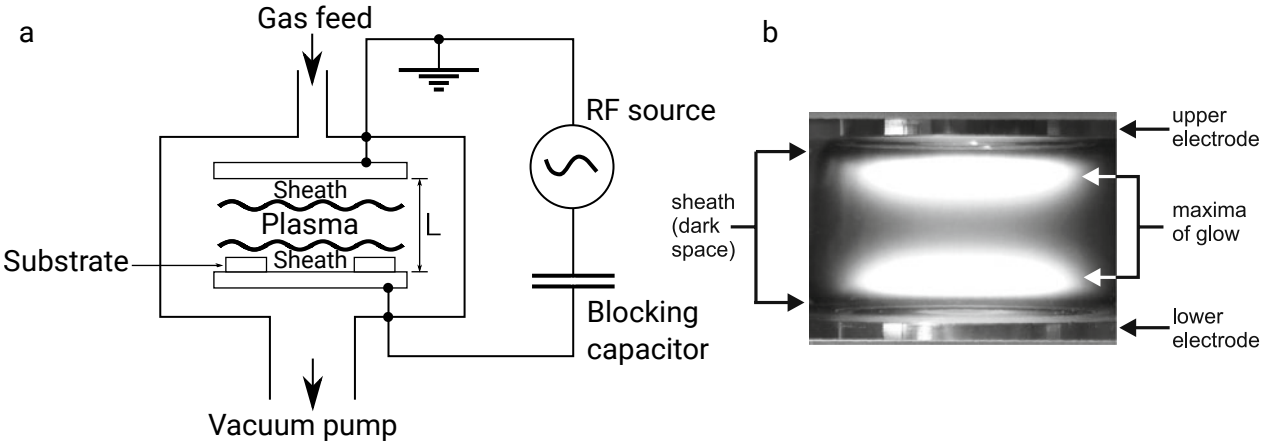

Figure 1.2: a) Schematics of a parallel plate RF plasma chamber. b) Plasma luminosity for this type of discharge. Adapted from [24, 31].

We can simplify the elements of the reactor of figure 1.2 in the way shown in figure 1.3. The electrons respond to the RF source by oscillating at the frequency of the electric field. The ions feel a time averaged electric field and can be considered in a stationary state with respect to the electrons. Near the boundaries, an excess of positive charge creates an electric field from the plasma to the wall. Ions are accelerated and electrons are repulsed by this plasma sheath. The ion flux Γ_i towards the boundary can be large enough to trigger desired reactions on the substrate. The quasi-neutrality takes place in the center of the reactor where the potential is uniform.

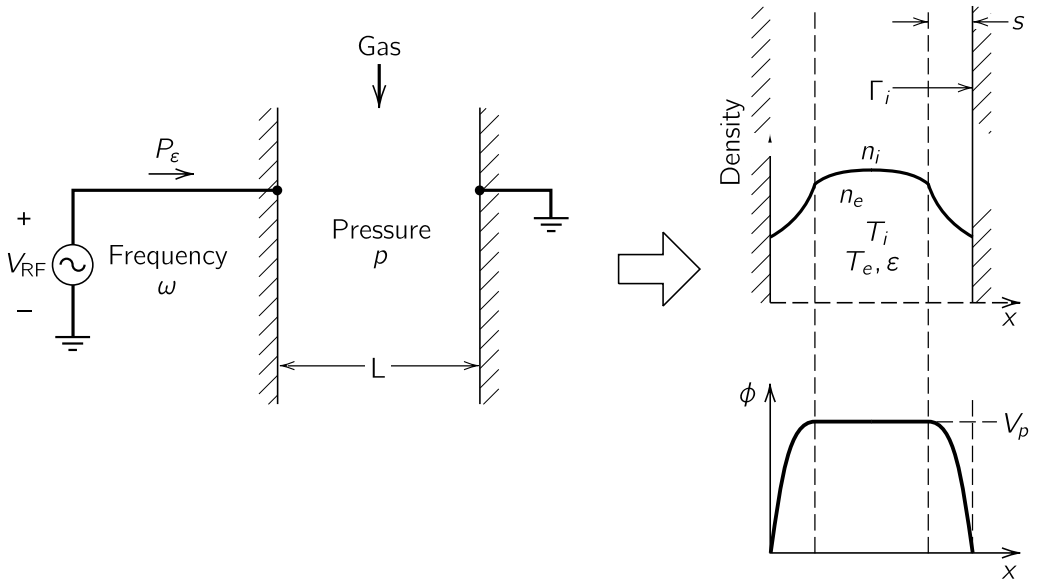

Figure 1.3: The parameters that describe a capacitive RF plasma. Profile densities illustrating the sheath and potential profile. Adapted from [24].

In this work we are interested in an argon plasma, in the following configuration: $L = 3\,\text{cm}$, $V_{\text{peak}} = 100\,\text{V}$, $T_i \approx T = 300\,\text{K}$, and $p = 100\,\text{mTorr}$. In the next section, we see that these conditions give an electronic density around $n_e \approx 1 \times 10^{16}\,\text{m}^{-3}$ and average energy $\varepsilon_e \approx 3\,\text{eV}$.

1.2.1 Modelling

Several numerical approaches exist to understand and predict plasma behavior. In the case of low-temperature plasmas, these approaches include particle-in-cell, fluid, and global models. The particle-in-cell approach deals with computing the classical motion of an arbitrary number of plasma particles. By calculating the force on each particle, one obtains their position and velocity that allow computing the particle distribution function and thus the plasma density and other quantities of interest. The major drawback of this technique is that a large number of particles is needed to obtain accurate results, which requires extensive computational resources. In the next sections, we develop the fluid and global models that we consider suitable for our goals.

1.2.1.1 Plasma fluid models

In this approach the electron and ion densities, flux, energy, etc. are calculated as a function of time and space from the first few moments of the Boltzmann equation [17]. The first set of equations are the continuity equations for the density of each species α,

$$\frac{\partial n_\alpha}{\partial t} + \nabla \cdot \Gamma_\alpha = S_\alpha, \tag{1.9}$$

where S_α is the source term describing the appearance or disapearance of the particle S_α. The flux Γ_α can be approximated by the drift-diffusion equation for the particle α of charge q_α,

$$\Gamma_\alpha = \mathrm{sgn}(q_\alpha)\mu_\alpha \boldsymbol{E} - D_\alpha \nabla n_\alpha, \tag{1.10}$$

which is a simplification of the momentum-transfer equations resulting from the second moment of the Boltzmann equation. This approximation allows describing the flux in terms of the mobility μ_α, and the diffusion coefficient D_α, where it is assumed that these quantities depend on space and time only through the local value of the electric field $\boldsymbol{E}$ [6]. The drift-diffusion approximation remains valid at radio-frequencies provided the momentum-transfer collision time is shorter than the RF period, and the mean free path for these collisions is much smaller than the distance between the electrodes [30]. The electron energy density, $n_\varepsilon = n_e \varepsilon_e$, is given by,

$$\frac{\partial n_\varepsilon}{\partial t} + \nabla \cdot \Gamma_\varepsilon = S_\varepsilon, \tag{1.11}$$

where Γ_ε is the electron energy flux,

$$\Gamma_\varepsilon = -\frac{5}{3}\mu_e e \boldsymbol{E} n_\varepsilon - \frac{5}{3} D_e \nabla n_\varepsilon, \tag{1.12}$$

and the source term S_ε takes into account losses by ohmic heating and the power transferred by electron collisions. The electric field is found by solving the Poisson equation,

$$\nabla \cdot (\varepsilon_0 \boldsymbol{E}) = \rho. \tag{1.13}$$

where ρ is the charge density,

$$\rho = \sum_\alpha q_\alpha n_\alpha. \tag{1.14}$$

Argon plasma. To apply the fluid model to a capacitive RF argon plasma, first, we must identify the species involved and write out the source term S_α that modifies the population of these species. For simplicity, let us consider the process of ionization for argon,

$$\mathrm{Ar} + \mathrm{e} \longrightarrow \mathrm{Ar}^+ + 2\,\mathrm{e}. \tag{1.15}$$

This process produces argon ions, Ar^+ and free electrons due to electron impacts on argon atoms. An estimation for the probability of such collisions can be obtained from the cross section. For example, if the colliding bodies, 1 and 2, are perfect hard spheres then the cross section is a geometrical quantity given by $\sigma = \pi(r_1 + r_2)^2$ (see figure 1.4). From the cross section, one obtains the mean free path, which is the distance that a particle can travel without making a collision. The mean free path associated with electron collisions on the neutral particles is

$$\lambda = (n_g \sigma)^{-1}, \tag{1.16}$$

where n_g is the density of the feedstock gas, argon in this example, and is calculated from the ideal gas law,

$$n_g = \frac{p}{k_\mathrm{B} T_g}, \tag{1.17}$$

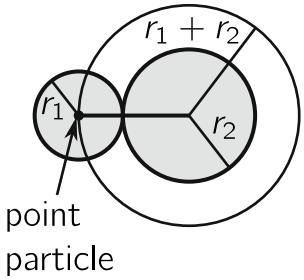

Figure 1.4: Collision between two spheres of radius r_1 and r_2. The collision can be described by a point particle colliding an effective cross section $\sigma = \pi(r_1 + r_2)^2$.

with the simplifying assumption that the gas does not flow and remains at a constant temperature T_g. For electron-atom collisions, the cross-section cannot be obtained from a hard-sphere collision model, but it can generally be obtained from experimental data as a function of the energy of the incoming electron. Given the cross section σ_{ion} for process 1.15 as a function of the energy or velocity, one can calculate an ionization rate coefficient averaged over all the electron velocities as

$$k_{\text{ion}} \equiv \langle \sigma_{\text{ion}} v \rangle \sim \int_0^\infty \sigma_{\text{ion}} v f_e(v)\, \mathrm{d}v\,, \tag{1.18}$$

The collision frequency is given by $n_g \langle \sigma_{\text{ion}} v \rangle$, and the total number of ionization processes per unit volume and time is [31] is

$$R_{\text{ion}} = n_e n_g \langle \sigma_{\text{ion}} v \rangle = n_e n_g k_{\text{ion}}. \tag{1.19}$$

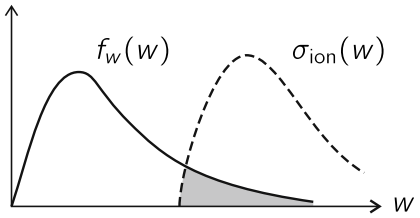

Figure 1.5: The high energy electrons in the tail of the distribution function (shaded) are responsible for triggering ionization. Adapted from [31].

In figure 1.5 we sketch the overlap of the distribution function with the cross section 1.18. Here the distribution function f_w is given in terms of energy $w = \frac{1}{2}mv^2$, and it is called the electron energy distribution function (EEDF). This overlap explains the fact that argon, which has an ionization energy of 15.8 eV, is ionized in a plasma of 3 eV. Often, the rate coefficients, $k_r = \langle \sigma_r v \rangle$, for the process r, are computed according to or fitted to the Arrhenius expression, which in the case of ionization reads,

$$k_{\text{ion}} = A_{\text{ion}} \left(\frac{\varepsilon_{\text{ion}}}{\varepsilon} \right)^{\beta} \exp\left(-\frac{\varepsilon_{\text{ion}}}{\varepsilon} \right),$$

In this expression, ε_{ion} is the threshold energy for ionization to occur, A_{ion} is a constant in $\mathrm{m^3 s^{-1}}$, and β is a dimensionless constant.

Table 1.1: Fluid plasma models characteristics

	Simple model	Detailed model
Reactions	ionization from Arrhenius equation	ionization, excitation from BOLSIG+ and metastables
Transport	constant coefficients	coefficients from BOLSIG+ and constant coefficients for metastables
Boundary conditions	Dirichlet and Neumann	conditions imposed on the flux [16] and Dirichlet for metastables.

In this example, the source term appearing in the argon ion density continuity equation is simply $S_i = R_{\text{ion}} = n_e n_g k_{\text{ion}}$. In general, the source term contains all the positive and negative contributions to the species population. The source term for the energy density reads in the case of ionization

$$S_\varepsilon = -e\Gamma_e \cdot \boldsymbol{E} - n_e n_i \varepsilon_{\text{ion}} k_{\text{ion}}. \tag{1.20}$$

where the first term is due to the heating of electrons by the electric field and the second term is the electron energy loss by electron impact in the plasma reactions. As for the rate coefficients, the transport coefficients, namely mobility and diffusion, can be also calculated from the EEDF. To compute the rate coefficients and the transport coefficients from cross sections, a Maxwell EEDF can be used as a first approximation but it is more advisable to use the EEDF from a Boltzmann equation solver such a BOLSIG+ [18]. In either cases, the coefficients depend on the mean electron energy ε_e,

$$k = k(\varepsilon_e), \qquad \mu_e = \mu_e(\varepsilon_e), \qquad D_e = D_e(\varepsilon_e), \tag{1.21}$$

These functions obtained from the EEDF can be readily used in the fluid equations. The deviations of the EEDF from a Maxwellian distribution are reflected in the transport and rate coefficients.

Another topic of importance is the choice of the boundary conditions for the fluid model [16]. To illustrate the differences resulting from the choice of reaction sets, the boundary conditions, and the transport coefficients, we used two fluid approaches to resolve the densities, the electric field and the average electronic energy of an RF argon capacitive plasma. The results are shown in figure 1.6. Table 1.1 shows the characteristics for these models, which are developed in detail in the appendix. In the detailed model we included the excited states or metastables n_m.

Figure 1.6 provides some valuable information which can be summarized as follows,

- Both models give very similar values for the density and electric field.
- As expected, quasi-neutrality occurs at the center of the reactor (see figure 1.3), where $n_e = n_i$, as the excited states are neutral. The flat region of the densities is more extended in the detailed model.
- The electron Debye length is $\lambda_{De} \sim 0.1\text{mm} \ll L$, with $L = 3\,\text{cm}$ the electrode gap.

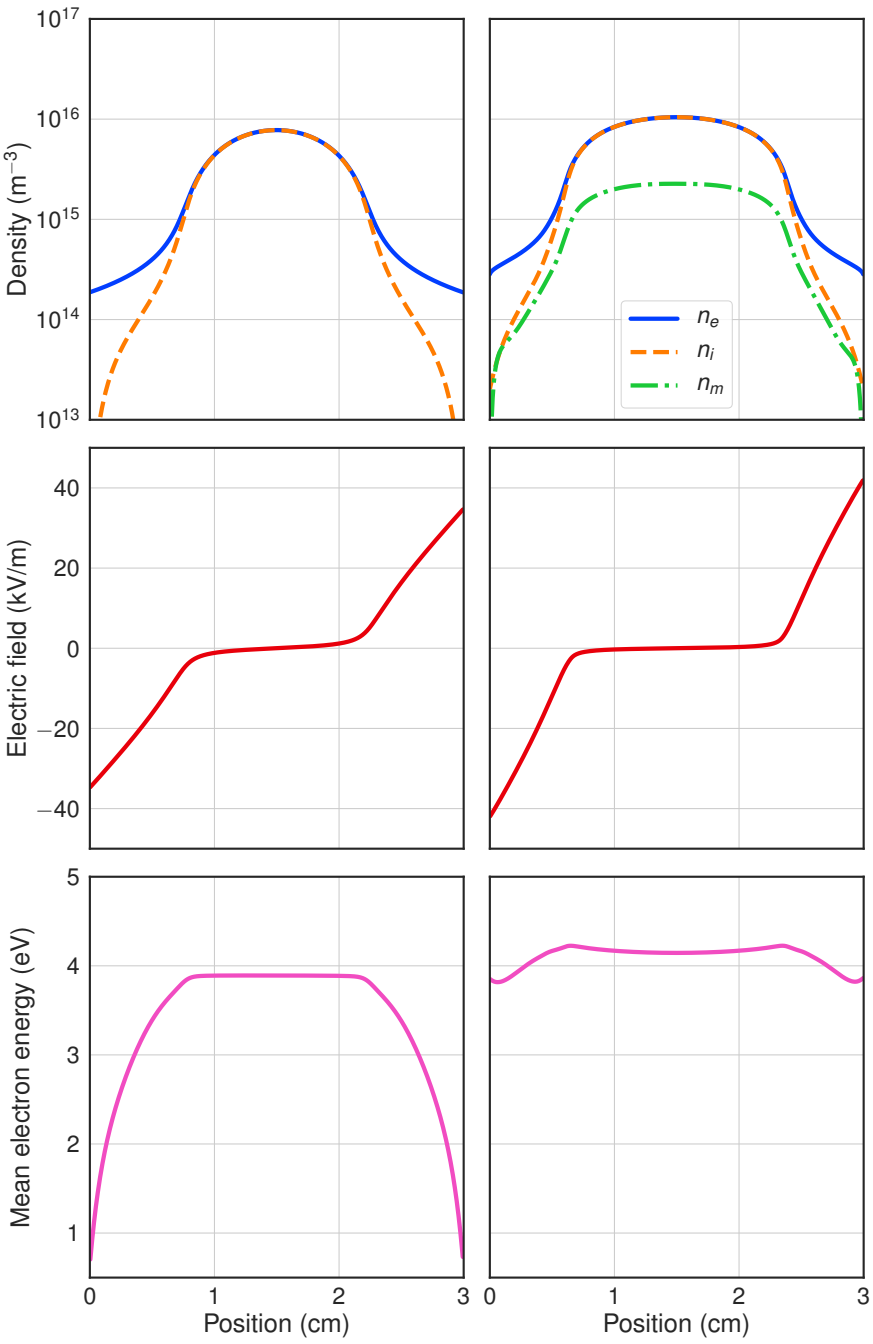

Figure 1.6: Plasma profiles comparison for simple (left) and detailed model (right) of a capacitive RF argon plasma.

- The difference between the two models, particularly the boundary conditions, produces significant difference in the electron energy at the walls, as expected.

To close this section, we can conclude that fluid models give us an insight into the properties of RF capacitive plasmas. In the next section, we explain a more straightforward approach aimed to solving the plasma densities and mean electron energy.

1.2.1.2 Global plasma models

A simplified description of the plasma bulk is given by the ambipolar diffusion and the ambipolar electric field. As we see in figure 1.6, in the center of the reactor, the density profiles are nearly flat and the electric field is zero. This supports the criterion of quasi-neutrality. The ion and electron fluxes must be equal because otherwise, a macroscopic space charge would appear. The electron and ion fluxes are given by,

$$\Gamma_e = -\mu_e E_x n_e - D_e \frac{\mathrm{d}n_e}{\mathrm{d}x}, \tag{1.22}$$

$$\Gamma_i = \mu_i E_x n_i - D_i \frac{\mathrm{d}n_i}{\mathrm{d}x}. \tag{1.23}$$

$$\tag{1.24}$$

In the bulk, we can assume $n_e = n_i = n$ and $\Gamma_e = \Gamma_i = \Gamma_a$. Then we can solve for the electric field,

$$E_x = -\frac{D_e - D_i}{\mu_e + \mu_i} \frac{1}{n} \frac{\mathrm{d}n}{\mathrm{d}x}. \tag{1.25}$$

The ambipolar field is the response of a collisional plasma to the charge imbalance since the electron flux exceeds the ion flux [31]. Using this result, one obtains the common flux for electrons and ions Γ_a,

$$\Gamma_a = -D_a \frac{\mathrm{d}n}{\mathrm{d}x}, \tag{1.26}$$

where D_a is expressed as,

$$D_a \equiv \frac{D_i \mu_e + D_e \mu_i}{\mu_e + \mu_i}. \tag{1.27}$$

D_a is the ambipolar diffusion coefficient. Ambipolar diffusion implies that electrons and ions are lost by diffusion at the same rate, thus preserving the quasi-neutrality. Another simplified approach that can be used to describe plasma is the global plasma model.

Global models resemble the fluid model equations with the difference that the balance equations do not have spatial dependence. They are used to investigating plasma chemical kinetics over different scenarios because numerical calculations are simpler and faster. The two important assumptions underlying global models are: (i) the EEDF does not change significantly over the quasi-neutral bulk plasma volume, (ii) all the reaction rates are spatially uniform over the bulk plasma volume [28]. To derive, the equations of the global model, let us start from the continuity equation for species α,

$$\frac{\partial n_\alpha}{\partial t} + \nabla \cdot \Gamma_\alpha = a_i n_i n_j k_{i,j}, \tag{1.28}$$

where particles i and j are involved in the generation of a_i particles α. Now, let's integrate over the entire plasma volume V as follows,

$$\frac{\partial}{\partial t} \int_V n_\alpha \, \mathrm{d}v + A\Gamma_\alpha = a_i k_{i,j} \int_V n_i n_j \, \mathrm{d}v \, . \tag{1.29}$$

where A is the area of the reactor.Defining the average density at the center of the reactor as,

$$\bar{n}_\alpha \equiv \frac{1}{V}\int_V n_\alpha \,\mathrm{d}v = \frac{n_\alpha^0}{V}\int_V g_\alpha \,\mathrm{d}v\,, \tag{1.30}$$

the volume-averaged continuity equation can be expressed as,

$$\frac{\mathrm{d}\bar{n}_\alpha}{\mathrm{d}t} = a_i\theta_i k_{i,j}\bar{n}_i\bar{n}_j - \frac{A}{V}\Gamma_\alpha, \tag{1.31}$$

where,

$$\theta_{ij} = \frac{V\int_V n_i n_j \,\mathrm{d}v}{\int_V n_i \,\mathrm{d}v \int_V n_j \,\mathrm{d}v}. \tag{1.32}$$

We can assume $\theta_{ij} \simeq 1$ for neutral-neutral and charged-neutral $(i-j)$ collisions. In the case of charged-charged θ_i can deviate from 1 [28]. The ion flux is given by,

$$\Gamma_i = h_i n_i u_\mathrm{B}, \tag{1.33}$$

where u_B is the Bohm velocity, v_T is the thermal velocity, and the geometrical factor h_i is,

$$h_i = (\sqrt{3 + L/2\lambda_i})^{-1}. \tag{1.34}$$

For neutral particles one has,

$$\Gamma_\alpha = h_n v_T/4, \qquad h_n = (1 + (L/2)v_T/(4D_n))^{-1}. \tag{1.35}$$

Finally, an energy balance equation is needed to close the system, as discussed in section 4.2.3.

Argon-silane plasma. We are now able to solve the densities of the simplified argon-silane chemistry model considered in Chapter 4. This model includes the species e, Ar^+, Ar^*, $SiH_3{}^+$, SiH_3, SiH_2 with the 15 reactions specified in table 4.1. Details of the balance equations for this model are given in section 7.2. The evolution of the densities is shown in figure 1.7.

One can see that the electron density of figure 1.7 at late times is in agreement with that of figure 1.6 at the center of the reactor. The main advantages of global models are their simplicity and their ability to provide an overview of complex plasma processes at a relatively low computational cost.

1.3 Nanodusty plasmas

In general, we call dust the collection of small particles of condensed matter usually produced by disintegration processes [13]. Dust is omnipresent on the Earth, from fine particles of debris, soot, pollen to dead skin cells. In the atmosphere, the suspended dust particles in the air constitute an aerosol, and they are the source of numerous health problems. Particulates are inhalable dust particles in the air with a size of less than 10 μm. The Canada government monitors the number of particulates to estimate the Air Quality Health Index [9], which is used to inform the population of the health risks posed by air contamination.

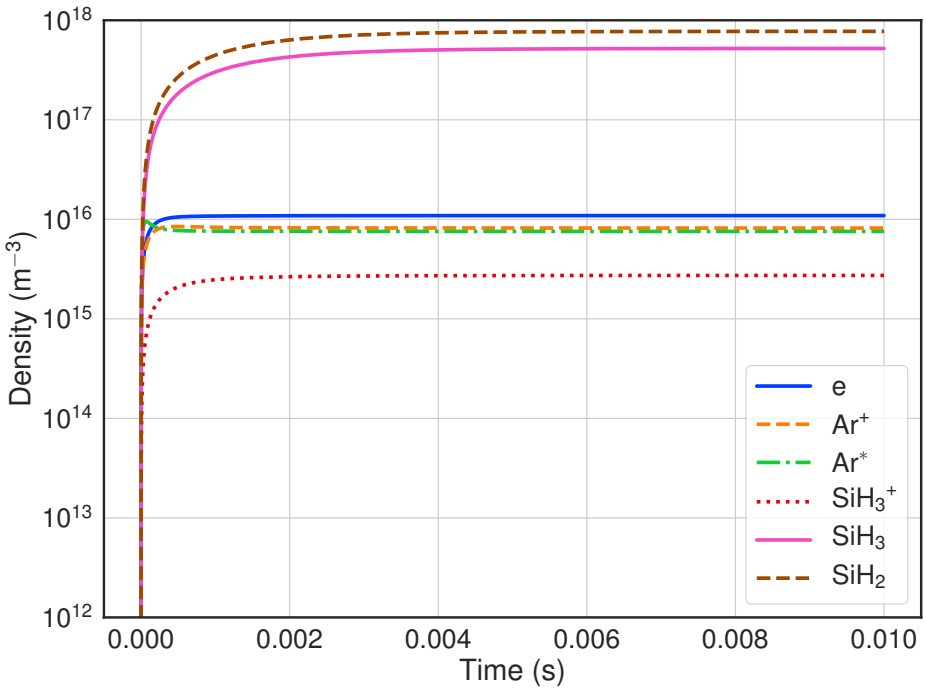

Figure 1.7: Global argon-silane plasma model. The ratio of the gas mixture is Ar:SiH_4 = 30:1

Another example of dust impact on the environment was the eruption of the Krakatoa that ejected soot up to 50 km to the atmosphere, and clouds of dust traveled around the world. Wharton collected dust to prove that it originated from the Krakatoa eruption. Dust in the atmosphere produces changes in colors due to scattering [38]. Moreover, the shadow produced by the dust produced climate changes, lowering the northern hemisphere temperature in the summer.

A more striking example, perhaps, is the influence of atmospheric dust on the fertilization of the Amazon and its biodiversity [8]. The dust, rich in iron and phosphorous, travels around 10 days from the Bodélé Depression in the Sahara to reach the Amazon basin. One of the sources of eroded sediments is diatoms. They are responsible for around one-fifth of all the photosynthesis on Earth, equivalent to all terrestrial rainforests combined and are also a vital component in the cycle of silicon [2].

The indirect evidence of dust outside our planet, in space, came as a source of obscuration that prevented astronomers from obtaining a clear view of the stars and galaxies. In figure 1.8, we show the dust clouds in the Carina nebula. We now know that dust participates in the formation of planets, stars, and galaxies. During star formation, dust grains accumulate in disks in orbit around the star, and eventually planets will form from accretion of dust grains from these disks, where grain charge could be of importance in this formation process [40]. All these examples make obvious that if plasma and dust are ubiquitous in nature, then they can co-exist in some natural systems like nebulae.

An important application of plasma physics occurs in microchip manufacturing, where several plasma processing techniques are used, from etching, cleaning to thin film deposition. In these pro-

Figure 1.8: The Carina Nebula. The left image shows central glowing filaments of interstellar gas and obscuring cosmic dust clouds. Image Credit & Copyright: Maicon Germiniani. The right images, show how these dust clouds shadow the images of the Carina Nebula. In comparison, however, these clouds are typically much less dense than Earth's atmosphere. Image Credit & Copyright: NASA, ESA, N. Smith (U. California, Berkeley) *et al.*, & Hubble Heritage Team (STScI/AURA).

cesses, grown particles were found to be trapped in the plasma near the wafers (see figure 1.9). The charge in nanoparticles forces them to these localized traps. These traps are determined by different forces acting on nanoparticles such as electric, ion drag, gravity, neutral drag and thermophoresis. Furthermore, material and topographic discontinuities on electrodes relate to the location of the traps [33]. These dust particles falling on the etched structures lead to damages and malfunctions of the chips and are thus considered as contaminants. Thus, the removal of dust particles is necessary. Likewise, particles can also appear in nuclear fusion reactors and their implication on operational performances of the reactor is currently discussed. [26]. Currently the incorporation of dust particles into thin films

Figure 1.9: Dust clouds trapped above silicon wafers in a plasma processing discharge. Adapted from [26, 33]

can be exploited to create new materials with interesting properties. Fig. 1.10 shows a nanoparticle

synthesis reactor that achieves high-speed impact of nanoparticles to a moving substrate. The rectangular nozzle accelerates nanoparticles to hypersonic velocities which then impact a target. This system enables the deposition of a high density of nanoparticles from the gas phase by moving the substrate at a uniform speed. For instance, for the deposition of germanium nanocrystals, the authors demonstrated film densities of up to 60% of the solid state density, which approaches the theoretical limit for randomly packed spheres [22].

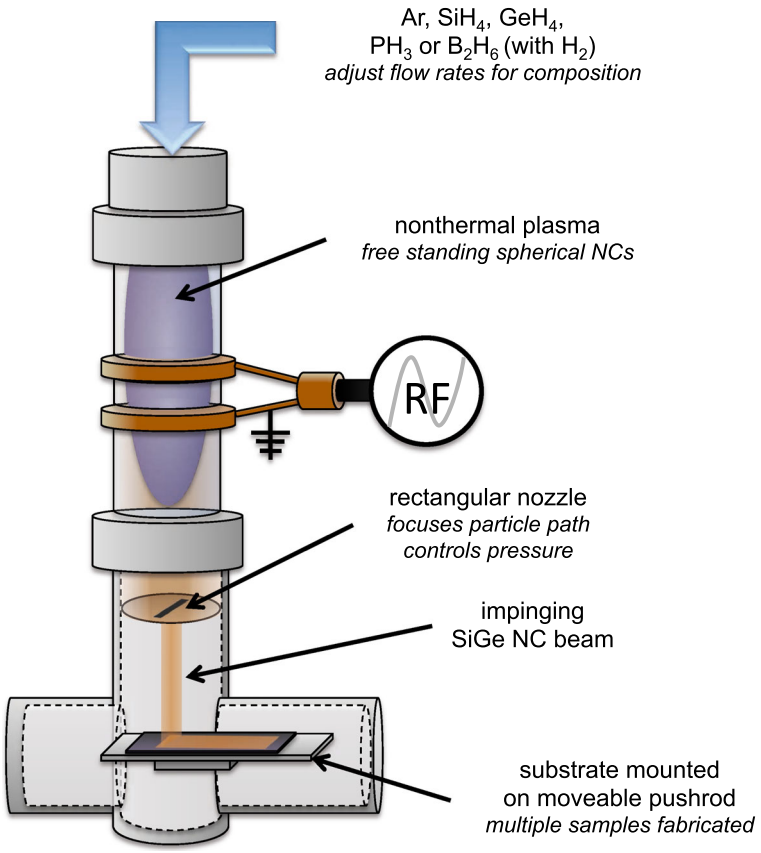

Figure 1.10: Plasma nanocrystal synthesis reactor[22].

Dusty plasmas are defined as those that are composed of electrons, neutral and ionized particles of a gas and particulates of condensed matter. Dust particles acquire charges from the charged plasma species, and the electrostatic energy of the mutual interaction of microparticles can be high. Hence, a strong electrostatic coupling in the dust subsystem can be achieved much more easily than in the electron–ion subsystem [12]. A measure of the coupling between the dust particles in a plasma can be defined as for electrons in the previous section.

Another phenomenon of interest in dusty plasmas is crystallization. Crystallization occurs for high values of the coupling parameter for dusty plasmas. Dust crystals consist of ordered arrangements of dust grains at low-temperature. They can have varied crystal structures, with a lattice constant of the order of a fraction of a millimetre, which makes it possible to observe it under light illumination with

the naked eye [34]. Dusty plasma crystals are studied as highly non-ideal plasmas and as a macro-sized analogy of condensed matter physics.

In this work, we are interested in the description of the interaction between silicon nanoparticles and in their growth process in low-temperature RF capacitive argon-silane (Ar-SiH_4) plasmas. Fig. 1.11 illustrates the growth of nanoparticles in this system. It starts with the nucleation phase, where protoparticles are created from plasma chemistry. Then the coagulation phase follows, which is a physical process that occurs when two nanoparticles encounter and form a new particle. This phase is identified by an increase in the size of the particles and a decrease in the nanoparticle number density. Later, the surface growth process, in which small molecules stick on the surface of the nanoparticles, becomes the most important growth mechanism.

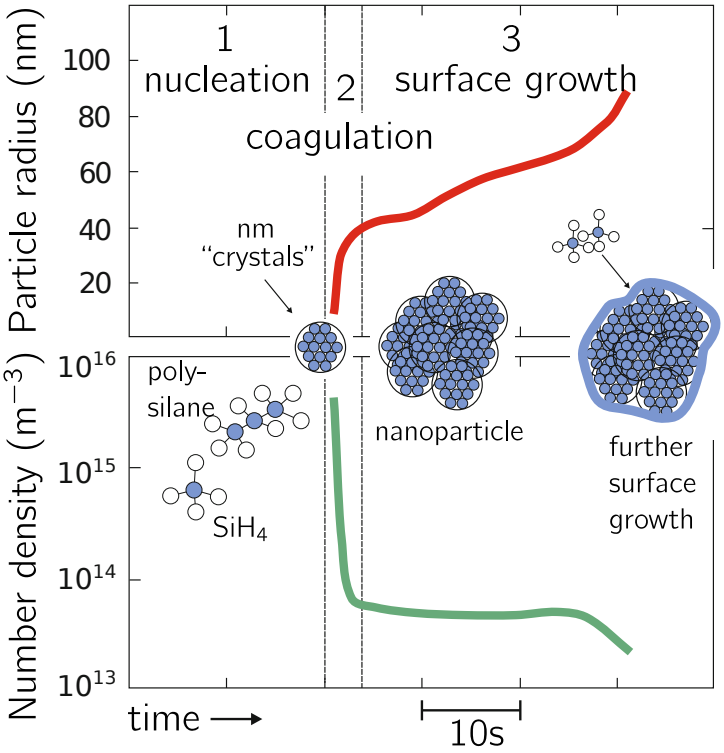

Figure 1.11: Evolution of particle size and number density. Adapted from [26]. It shows the three main phases of growth: nucleation, coagulation, and surface growth.

1.3.1 Coagulation

Coagulation occurs when particles collide and coalesce to form a new particle (see figure 1.13). Strictly speaking, we only consider coagulation between two spherical particles, and when they collide, the new particle has the volume of its constituent particles. Some of the experimental evidences of coagulation in nanodusty plasmas are: (i) morphology of nanoparticles as shown in figure 1.12, (ii) fast decrease of the nanoparticle density as shown in figure 1.11, and (iii) increase of size during this phase.

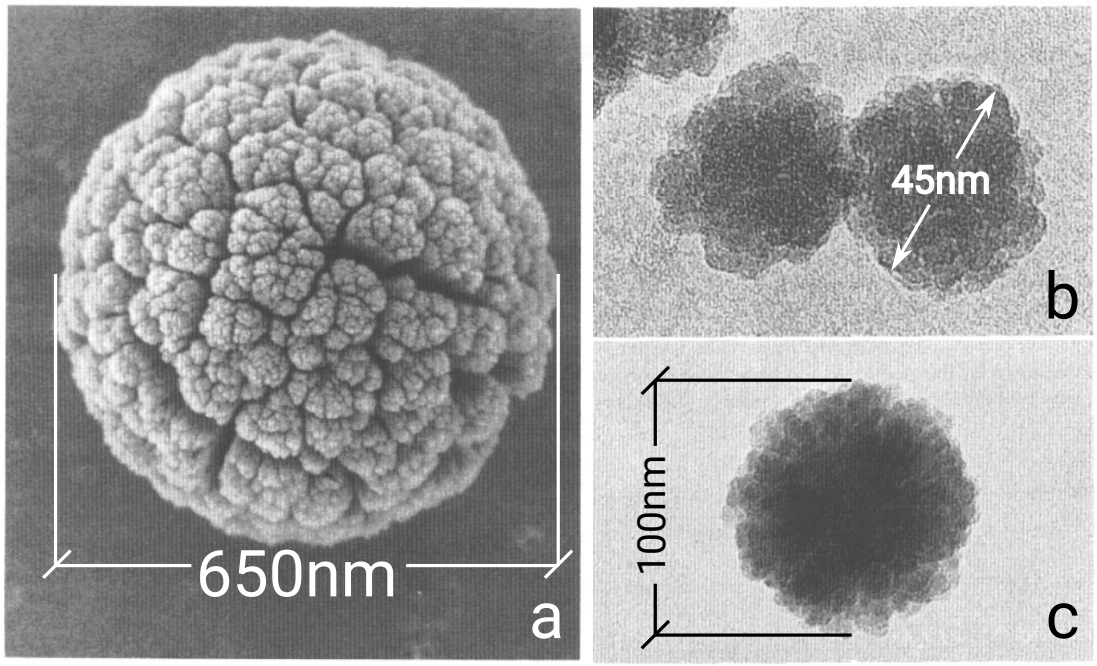

Figure 1.12: Micrographs of nanoparticles. a) Dust generated in a Helium plasma with graphite (adapted from [14]). b) and c) (adapted from [7])

Let B_{ij} be the number of collisions per unit time per unit volume between two classes of particles with densities n_i and n_j and volumes v_i and v_j. In terms of these quantities, B_{ij} is given by[13],

$$B_{ij} = K(v_i, v_j) n_i n_j, \tag{1.36}$$

where $K(v_i, v_j)$ is the collision frequency function in $\mathrm{m^3 s^{-1}}$ and the densities are in $\mathrm{m^{-3}}$. The rate of formation of particles of size m resulting from the collision between those of size i and j is,

$$\frac{1}{2} \sum_{v_i + v_j = v_m} B_{ij}, \quad \text{or equivalently,} \quad \frac{1}{2} \sum_{j=1}^{m-1} K(v_j, v_m - v_j) n_{m-j} n_j. \tag{1.37}$$

Expressing the loss rate of particles with size m due to collisions with all other particles as $\sum_{i=1}^{\infty} D_{im}$, the net generation of particles of size m is,

$$\begin{aligned} \frac{\mathrm{d}n_m}{\mathrm{d}t} &= \frac{1}{2} \sum_{v_i + v_j = v_m} B_{ij} - \sum_{i=1}^{\infty} D_{im} \\ &= \frac{1}{2} \sum_{v_i + v_j = v_m} K(v_i, v_j) n_i n_j - n_m \sum_{i=1}^{\infty} K(v_i, v_m) n_i \qquad (1.38) \\ &= \frac{1}{2} \sum_{j=1}^{m-1} K(v_j, v_m - v_j) n_{m-j} n_j - n_m \sum_{i=1}^{\infty} K(v_i, v_m) n_i. \qquad (1.39) \end{aligned}$$

which is the discretized form of the Smoluchowski equation. Several techniques have been proposed to solve the Smoluchowski equation numerically such as: sectional, Monte Carlo, moment, modal

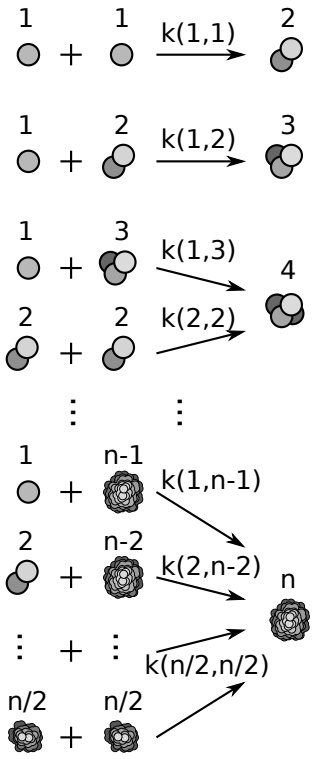

Figure 1.13: Coagulation schematics for particles of discrete sizes. Adapted from `https://en.wikipedia.org/wiki/Smoluchowski_coagulation_equation`.

methods [39]. One of particular interest is the fixed pivot technique (FPT) [23](see appendix I), since it ensures the exact preservation of number, and volume density [23]. For these reasons, we selected the FPT to compute the coagulation.

Another advantage of the FPT is that the charge can be treated separately and exactly, without partitioning its domain, contrary to the two-component, volume and charge, FPT [35]. In appendix 1, we develop this idea which contrasts with Kim's approach which consisted in using FPT by treating volume and charge as continuous variables. Alternatively, Warthesen & Girshick [36] applied a different sectional method [15], which requires to solve a set of double integrals and can preserve only one moment [23].

In sections 1.3.4 and 3.2.2 we give details on the coagulation rate and the derivation of the enhancement factor due to the interaction energy between coalescing nanoparticles.

What further enhances the interest in coagulation in dusty plasmas is the fact that the dust particles are charged. Therefore the charge must be preserved in the coagulation process. In the next section, we discuss the processes by which particles capture charges.

1.3.2 Charging

The nanoparticles in a plasma undergo collisions by charged species present in the plasma. This allows nanoparticles to collect charges. In low-temperature plasmas, the electrons being the more energetic species, one can predict that electron capture determines the nanoparticle charging.

Dust particle charging can influence deeply the properties of the plasma.The depletion of electrons due to nanoparticle charging causes an increase of the mean electron energy. Moreover, if the nanoparticle density is comparable to the electron density, the total charge of the nanoparticles is involved in the balance of charges in the plasma.

In figure 1.14 we show a possible trajectory for a plasma species near a nanoparticle. This corresponds to a plasma particle of same charge polarity as the nanoparticle.

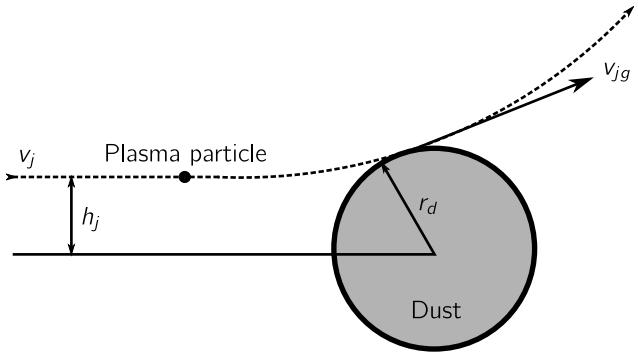

Figure 1.14: Impact of a plasma particle onto a nanoparticle with the same charge polarity.

To estimate the charges gained by a nanoparticle, one needs to derive the collision cross section from the conservation of momentum and energy. The conservation of momentum reads

$$m_j v_j h_j = m_j v_{jg} r_d, \tag{1.40}$$

where v_j, and m_j are the velocity and mass of the plasma particle j which starts at a distance h_j from the centerline of the nanoparticle, commonly called the impact parameter. v_{jg} is the velocity of the particle when it attains the surface of the nanoparticle. The conservation of energy reads

$$\frac{1}{2} m_j v_j^2 = \frac{1}{2} m_j v_{gj}^2 + q_j \phi_d, \tag{1.41}$$

where q_j is the charge of the plasma particle, and ϕ_d is the potential of the nanoparticle,

$$\phi_d = \frac{q_d}{r_d}, \tag{1.42}$$

These equations can be used to solve for the impact parameter. The cross section for the plasma particle-nanoparticle interaction is,

$$\sigma_j^d = \pi h_j^2 = \pi r_d^2 \left(1 - \frac{2 q_j \phi_d}{m_j v_j^2} \right). \tag{1.43}$$

The charging current is given by the following integral over velocities

$$I_j = q_j \int_{0,v_j^{\min}}^{\infty} v_j \sigma_j^d f_j(v_j) d\mathbf{v}_j, \tag{1.44}$$

where the minimum velocity (defined by $\sigma_j^d = 0$) is $v_j^{\min} = -2q_j\phi_d/m_j$ if $q_j\phi_d \geq 0$, and $v_j^{\min} = 0$ otherwise.

Assuming a Maxwellian distribution for velocities,

$$f_j(v_j) = n_j \left(\frac{m_j}{2\pi k_B T_j}\right)^{3/2} \exp\left(-\frac{m_j v_j^2}{2k_B T_j}\right), \tag{1.45}$$

the integral can be computed analytically to give the currents for $q_j\phi_d < 0$,

$$I_j = \pi r_d^2 n_j q_j \sqrt{\frac{8k_B T_j}{\pi m_j}} \left(1 - \frac{q_j\phi_d}{k_B T_j}\right), \tag{1.46}$$

and for $q_j\phi_d > 0$,

$$I_j = \pi r_d^2 n_j q_j \sqrt{\frac{8k_B T_j}{\pi m_j}} \exp\left(-\frac{q_j\phi_d}{k_B T_j}\right). \tag{1.47}$$

One can see that the electron current is diminished around a negative nanoparticle,

$$I_e = \pi r_d^2 e n_j \sqrt{\frac{8k_B T_e}{\pi m_e}} \exp\left(\frac{e\phi_d}{k_B T_e}\right), \tag{1.48}$$

A resistor-capacitor model can be solved to estimate the charging time for a nanoparticle of radius r_d,

$$Q_d(t) = Q_0 e^{-t/\tau_i} + 4\pi\varepsilon_0 r_d \frac{k_B T_i}{e}, \tag{1.49}$$

with charging time given by,

$$\tau_i = 4\pi\varepsilon_0 r_d \frac{k_B T_i}{e} \frac{1}{\pi r_d^2 e n_i v_i}, \tag{1.50}$$

this is around $10^{-5}\,\mathrm{s} \sim 10^{-6}\,\mathrm{s}$ which is very small compared to the time for nanoparticle growth [26], and higher than the electron response time for the RF discharge.

In section 3.2.3, we discuss in detail the charge at equilibrium and deviations from the OML theory. Other fundamental mechanisms [34, 12, 26] that affect charging such as, photoemission, ion trapping, and secondary electron emission, were not considered in this work and are left to future investigation along with nanoparticle heating.

1.3.3 Plasma chemistry, nucleation, and surface growth

Nucleation deals with the growth of small protoparticles or clusters from gas species, that will continue to grow by other processes, such as coagulation and condensation. The generation of these

protoparticles starts by a series of chemical reactions in the ionized gas phase, also called gas phase polymerization. Several pathways were proposed to explain the generation of protoparticles in silane plasmas. Primarily, negative ions react and group in the plasmas as they become trapped in the plasma due to the sheath potential repulsion, as consequence they have a longer residence time in the plasma. For instance, a possibility is the reaction of negative silylene ions with excited silane [3], given by the following reaction,

$$Si_nH^-_{2m-1} + SiH_4 \rightleftharpoons Si_{n+1}H^-_{2m+1} + H_2, \tag{1.51}$$

and silylene,

$$Si_nH_{2m}B^- + SiH_4 \rightleftharpoons Si_{n+1}H_{2m+2}B^- + H_2, \tag{1.52}$$

Another possibility for polymerization is shown in figure 1.15. In this situation, gas polymerization starts with the formation of cyclic and polycyclic structures, which grow from silane to small clusters ($n < 4$) that will form silyls or silylenes. Larger clusters $n > 4$ can form rings or more complicated structures [26].

Nanoparticles became microparticles due to surface growth. In this phase the particles behave like small substrates on which additional layers of silicon-hydrogen films are deposited, and the growth rate is often found to be close to the rate of thin-film deposition on large surfaces [26].

In section 4.2.1, for sake of simplicity, we approximate the generation of protoparticles and the surface growth to a constant rates, following Agarwal [1] as the main process we are interested is the coagulation and the enhancement by the electrostatic and van der Waals interaction.

A less probable pathway was proposed by Watanabe *et al.* [37, 4]. They inferred from their experiments that short lifetime radicals like SiH_2 play an important role in particle nucleation. From their observations the authors concluded that clustering proceeds by SiH_2 insertion reactions. However, Hollenstein *et al.* [11, 4] observed particle formation as long as the anions remained trapped in the plasma, and no correlation was found between particle generation and neutral clusters. On the contrary, anionic clusters were found in greater sizes and concentration than neutral clusters. Furthermore, they found that positive ions play a negligible role in the nucleation [4].

1.3.4 Interparticle interactions

The collision kernel for hard spheres i and j that move ballistically until a collision occurs, i.e., free molecular regime, is given by the product of the cross-section (see figure 1.4) and the thermal velocity,

$$\beta^0_{ij} \equiv \sigma v_{\text{th}} = \left(\frac{8\pi k_B T}{m_{ij}}\right)^{1/2} (r_i + r_j)^2, \tag{1.53}$$

where $m_{ij} = {}^{m_i m_j}/_{m_i + m_j}$ is the reduced mass. Equation 1.53 can be rewritten in terms of the mass density $\rho = {}^{m}/_{v}$ and the volume of the particles, v_i and v_j,

$$\beta^0_{ij} = \left(\frac{3}{4\pi}\right)^{1/6} \left[\frac{6k_B T}{\rho_p}\left(\frac{1}{v_i} + \frac{1}{v_j}\right)\right]^{1/2} \left(v_i^{1/3} + v_j^{1/3}\right)^2. \tag{1.54}$$

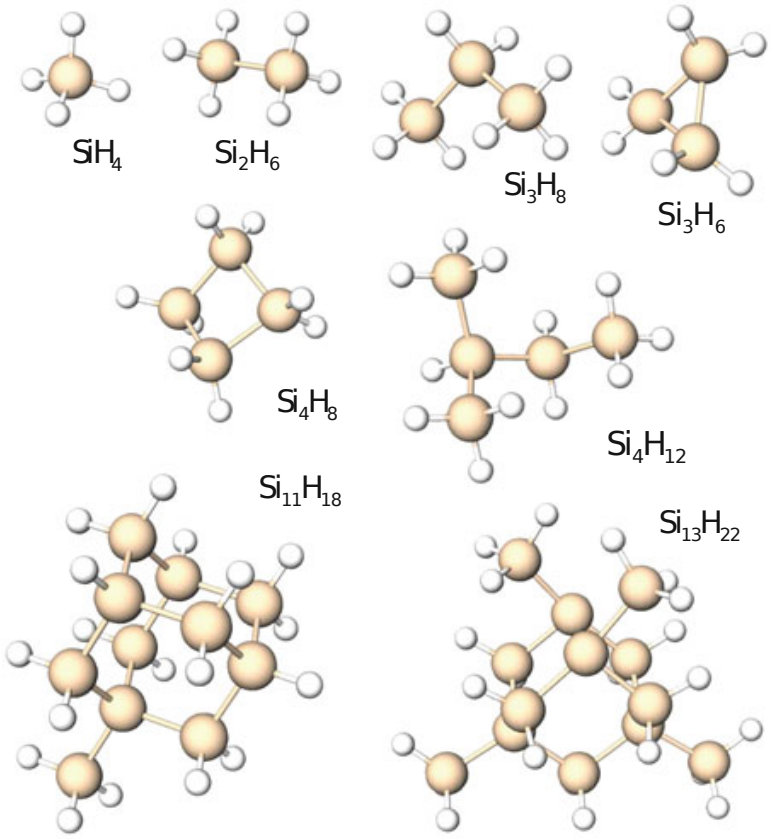

Figure 1.15: A possible pathway for silicon clustering. Adapted from [26].

This is equivalent to the Brownian coagulation coefficient in the free molecular regime. If the particles interact between them modifying their collision frequency, we can define the enhancement factor η as the ratio of the modified collision kernel β and the collision kernel β^0 where such interaction is not present,

$$\eta \equiv \frac{\beta}{\beta^0}. \tag{1.55}$$

Ouyang *et al.* [29] reviewed different approaches to compute the enhancement factor, here we write them to give the reader a better introduction to the methods employed in chapter 2. The interaction between particles is always assumed to be described by a central force. Mainly, Ouyang focused in the case of singular contact potentials, as is the case of ionic charging, where the ion is considered to be a point particle that impacts a finite-sized body.

1.3.4.1 Marlow enhancement factor

Marlow [25, 29, 1] introduced the following approach to compute the enhancement factor for singular contact potentials,

$$\eta^{\mathrm{M}} = \frac{1}{2}\int_0^1 \frac{1}{x^2}\frac{\mathrm{d}}{\mathrm{d}x}\left(x\frac{\mathrm{d}\phi(x)}{\mathrm{d}x}\right) \times \exp\left(\frac{x}{2}\frac{\mathrm{d}\phi(x)}{\mathrm{d}x} - \phi(x)\right)\mathrm{d}x \tag{1.56}$$

$$+ \exp\left(\frac{1}{2}\left.\frac{\mathrm{d}\phi(x)}{\mathrm{d}x}\right|_{x=1} - \phi(1)\right), \tag{1.57}$$

$$x = \frac{r_1 + r_2}{r}, \tag{1.58}$$

where r and ϕ are the distance and dimensionless potential between the nanoparticles (2.2), respectively.

1.3.4.2 Sceats enhancement factor

In this method we need to solve the distance of approach, where the interacting potential overcomes the thermal energy. This distance Λ is the root of [29],

$$\left.\frac{\Lambda}{2}\frac{\mathrm{d}\phi(r^*)}{\mathrm{d}r^*}\right|_{r^*=\Lambda} = k_{\mathrm{B}}T_g, \tag{1.59}$$

and the enhancement factor is defined by,

$$\eta^{\mathrm{S}} = \Lambda^2 \exp\left[-\frac{\phi(\Lambda)}{k_{\mathrm{B}}T_g}\right]. \tag{1.60}$$

1.3.4.3 Fuchs and Sutugin enhancement factor

The free molecular enhancement factor from Fuchs and Sutugin is expressed as [29],

$$\eta^{\mathrm{FS}} = b_{\mathrm{crit}}^2\left(\sqrt{\frac{3}{2}}\right), \tag{1.61}$$

where b_{crit} is found from the relation,

$$b = r_{\mathrm{min}}\sqrt{1 + \frac{|\phi(r_{\mathrm{rmin}})|}{k_{\mathrm{B}}T_g\tilde{v}}}, \tag{1.62}$$

b_{crit} is taken to be the smallest value of b at and above which r_{min} is found to be a real number > 1, and below which r_{min} is a complex number or is a real number < 1, where $\tilde{v}$ is the dimensionless speed and r_{min} is the (dimensionless) distance of closest approach for the two particles.

With these definitions for the enhancement factor and the numerical values given by Ouyang *et al.* [29], we reproduced the enhancement factor for the dimensionless ionic potential eq. 2.3 in figure 1.16.

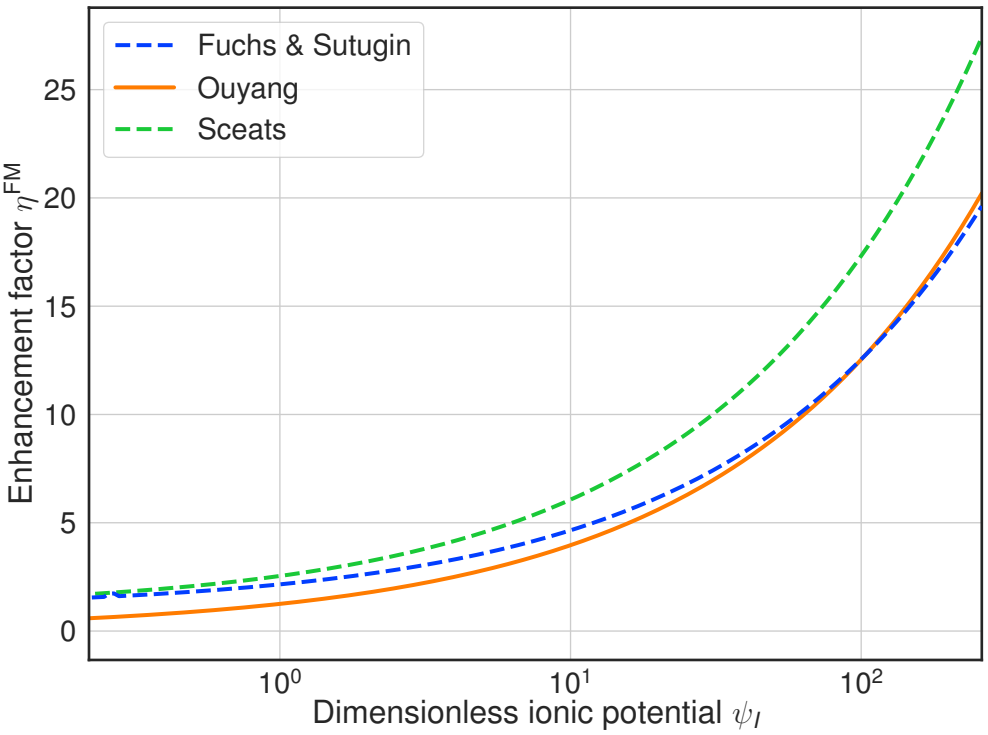

Figure 1.16: Enhancement factor for the ionic potential eq. 2.3.

1.3.4.4 Electrostatic interaction

In this section we show the enhancement factor and the electrostatic image potential from the work of Ravi *et al.* [32, 1].

The rate of coagulation between two particles of charge size 1 and 2 is given by,

$$R_{\text{coag},1,2} = f\left(z_1, z_2, r_1, r_2\right)\beta_{1,2}n_1n_2, \tag{1.63}$$

where $\beta_{1,2}$ is the kernel of coagulation for spherical particles $i = 1$, $j = 2$. With the enhancement factor $f\left(z_1, z_2, r_1, r_2\right)$ that depends on the charge and size of particles, it is defined by,

$$f\left(z_1, z_2, r_1, r_2\right) = \begin{cases} 1 & \text{if } z_1 = 0 \text{ and } z_2 = 0, \\ 1 - \frac{z_1 z_2 e^2}{4\pi\varepsilon_0(r_1+r_2)k_B T} & \text{if } z_1 z_2 < 0, \\ 0 & \text{if } z_1 z_2 > 0, \\ \eta^{M} & \text{if } z_1 \neq 0 \text{ and } z_2 = 0, \end{cases} \tag{1.64}$$

$$\phi(x) = \frac{aMx^2}{2(1-bx^2)}, \tag{1.65}$$

with the following definitions,

$$M = \frac{e^2}{4\pi\varepsilon_0 k_B T(r_1 + r_2)}, \tag{1.66}$$

$$a = \frac{\varepsilon - 1}{\varepsilon + 1} z_1^2 \left(1 - \frac{r_1}{r_1 + r_2}\right), \tag{1.67}$$

$$b = \left(\frac{\varepsilon - 1}{\varepsilon + 1}\right)^2 \left(\frac{r_1}{r_1 + r_2}\right)\left(1 - \frac{r_1}{r_1 + r_2}\right). \tag{1.68}$$

This interacting potential $\phi(x)$ is derived from Huang's approach [19], that we developed extensively in section 7.4.2. Furthermore, we found that the Sceats' approach gives the same results as the complicated expression of Marlow, as is shown in 2.1.

In section 3.2.2 we introduce a different way to compute the enhancement factor, along with a more rigorous description for the interaction energy between coalescing nanoparticles 3.2.4.

1.3.5 Nanoparticle growth model

The General Dynamics Equation (GDE) for Dusty Plasmas expresses the rate of change for the dust particle density represented by the size i and charge k in terms of the transport, nucleation, coagulation, growth and charging processes [1],

$$\frac{\mathrm{d}N_{i,k}}{\mathrm{d}t} + \nabla\Gamma_{i,k} = \left[\frac{\mathrm{d}N_{i,k}}{\mathrm{d}t}\right]_{\text{coag}} + \left[\frac{\mathrm{d}N_{i,k}}{\mathrm{d}t}\right]_{\text{charging}} + \left[\frac{\mathrm{d}N_{i,k}}{\mathrm{d}t}\right]_{\text{nuc}} + \left[\frac{\mathrm{d}N_{i,k}}{\mathrm{d}t}\right]_{\text{growth}}, \tag{1.69}$$

where $N_{i,k}$ is the particle density, expressed in number of particles per unit volume (m^{-3}) and $\Gamma_{i,k}$ is the local spatial flux. The four terms on the right-hand side represent coagulation, charging, nucleation, and surface growth, respectively. For simplicity, we neglect losses of nanoparticles to the boundaries of the reactor, and we consider an isotropic dusty plasma. Thus, we assume $\nabla\Gamma_{i,k} = 0$. With this simplification, we can develop a global plasma model and solve the population balance equation for the nanoparticles.

We used a time-splitting scheme to separate the computation of the plasma densities and nanoparticle charging from the processes of nanoparticle growth. The scheme is depicted in figure 1.17. We start with an initial density for the smallest size and neutral charge. Then, we compute the plasma and the charges on nanoparticles. Next, the nanoparticles are allowed to grow within an adaptive time step. A new plasma and charging step completes the evolution of nanoparticles and plasma densities. In this sense, the plasma and nanoparticles are computed self-consistently.

Obviously, a more accurate description of the dusty plasma would take into account space coordinates as done in [36, 32, 1]. Still, these computations are time-consuming, and we believe that this extra effort was not necessary to draw the main conclusions of this thesis. Nevertheless, some perspectives towards a 1D model are detailed in the appendix.

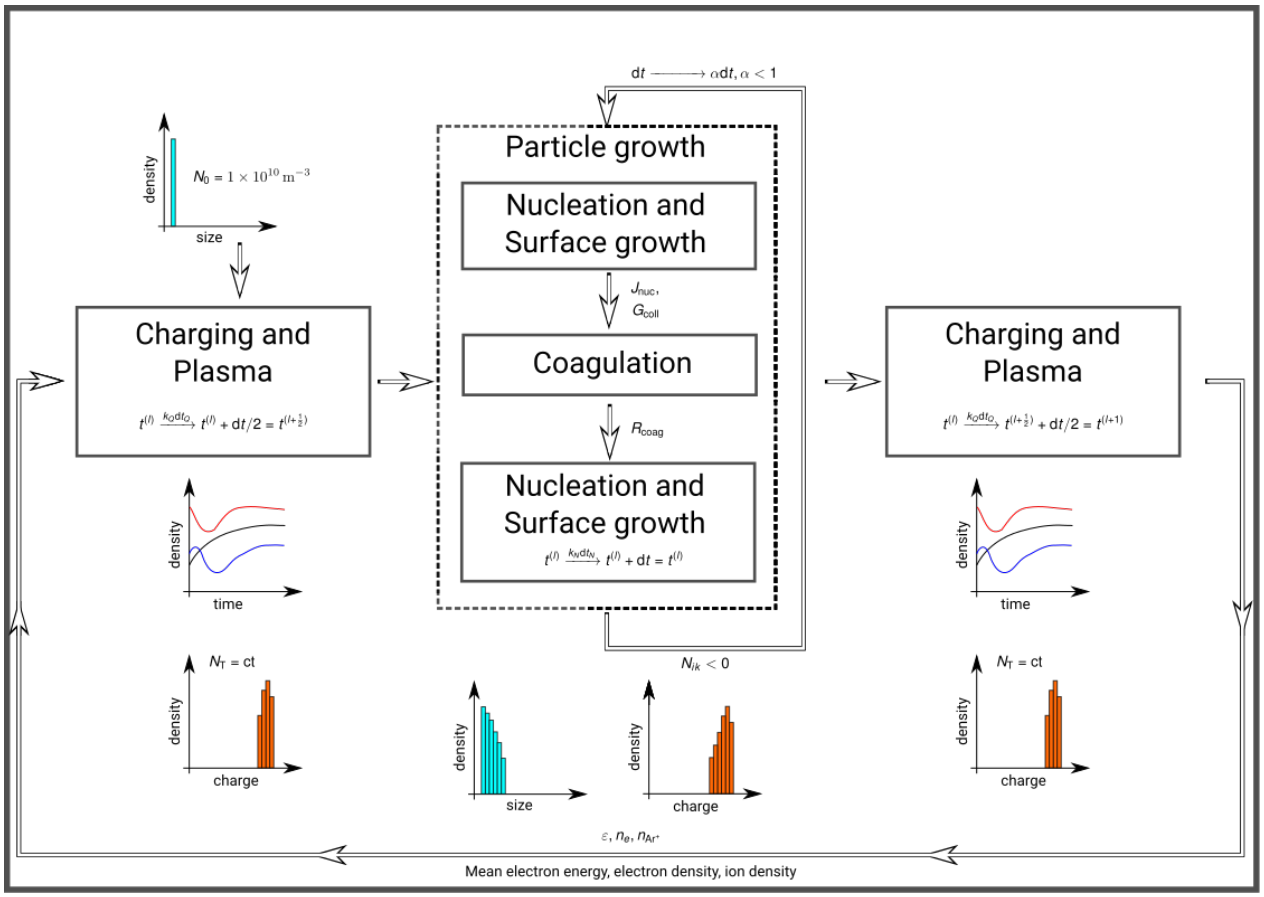

Figure 1.17: Numerical model

1.4 Motivation

Numerical modeling is a fascinating approach for understanding the evolution over time of the charge and the size of nanoparticles, given the difficulty of observing nanometric-sized dust. The experiments carried out in [21] were able to perform spatio-temporal monitoring of the dust in the plasma, but only in the case of dust of micrometric size.

Some important results in the modeling of nanoparticle plasma are reported in [36, 32, 27, 1]. However, the interaction forces assumed in this work imply non-physical singularities at the point of contact of the particles, which poses significant difficulties in obtaining the enhancement factor. This thesis intends to conduct a more rigorous analysis of the interactions between nanoparticles and to distinguish the influence of interaction forces on their growth in plasma. We are convinced that future work on this topic should take into account the conclusions drawn in this research.

1.5 Thesis structure

This thesis is presented as follows, in this chapter 1 we intended to deliver the essential concepts to understand the research articles presented in the following chapters. In chapter 2, we pose the problem of the accuracy in the description of the electrostatic enhancement factor in the coagulation. Then, in chapter 3, we derive rigorously this electrostatic enhancement factor. In chapter 4, we present the results that uses the results of chapter 2, in nanodusty growth simulations. Finally, we present a summary, conclusions and related future work.

1.6 References

[1] P. Agarwal and S.L. Girshick. Sectional modeling of nanoparticle size and charge distributions in dusty plasmas. *Plasma Sources Sci. Technol.*, 21(5):055023, October 2012.

[2] A.-S. Benoiston, F. M. Ibarbalz, L. Bittner, L. Guidi, O. Jahn, S. Dutkiewicz, and C. Bowler. The evolution of diatoms and their biogeochemical functions. *Philosophical Transactions of the Royal Society B: Biological Sciences*, 372(1728):20160397, September 2017.

[3] U. Bhandarkar, U. Kortshagen, and S. L. Girshick. Numerical study of the effect of gas temperature on the time for onset of particle nucleation in argon–silane low-pressure plasmas. *J. Phys. D: Appl. Phys.*, 36(12):1399, 2003.

[4] U. Bhandarkar, M. T. Swihart, S. L. Girshick, and U. R. Kortshagen. Modelling of silicon hydride clustering in a low-pressure silane plasma. *J. Phys. D: Appl. Phys.*, 33(21):2731, November 2000.

[5] J. A. Bittencourt. *Fundamentals of Plasma Physics*. Springer New York, 2004.

[6] J.-P. Boeuf. Numerical model of rf glow discharges. *Phys. Rev. A*, 36(6):2782–2792, September 1987.

[7] A. Bouchoule and L. Boufendi. Particulate formation and dusty plasma behaviour in argon–silane RF discharge. *Plasma Sources Sci. Technol.*, 2(3):204, August 1993.

[8] C. S. Bristow, K. A. Hudson-Edwards, and A. Chappell. Fertilizing the Amazon and equatorial Atlantic with West African dust. *Geophysical Research Letters*, 37(14), 2010.

[9] Environment and Climate Change Canada. Air Quality Health Index. `https://www.canada.ca/en/environment-climate-change/services/air-quality-health-index.html`, January 2008. Accessed: 2019-10-16.

[10] F. F. Chen. *Introduction to Plasma Physics and Controlled Fusion: Volume 1: Plasma Physics*. Springer US, 2013.

[11] C. Courteille, J.-L. Dorier, Ch Hollenstein, L. Sansonnens, and A. A. Howling. Partial-depth modulation study of anions and neutrals in low-pressure silane plasmas. *Plasma Sources Sci. Technol.*, 5(2):210, May 1996.

[12] V. E. Fortov, A. V. Ivlev, S. A. Khrapak, A. G. Khrapak, and G. E. Morfill. Complex (dusty) plasmas: Current status, open issues, perspectives. *Physics Reports*, 421(1–2):1–103, December 2005.

[13] S. K. Friedlander. *Smoke, Dust, and Haze: Fundamentals of Aerosol Dynamics*. Oxford University Press, 2000.

[14] A. Garscadden, B. N. Ganguly, P. D. Haaland, and J. Williams. Overview of growth and behaviour of clusters and particles in plasmas. *Plasma Sources Sci. Technol.*, 3(3):239–245, August 1994.

[15] F. Gelbard, Y. Tambour, and J. H. Seinfeld. Sectional representations for simulating aerosol dynamics. *Journal of Colloid and Interface Science*, 76(2):541–556, August 1980.

[16] G. J. M. Hagelaar, F. J. de Hoog, and G. M. W. Kroesen. Boundary conditions in fluid models of gas discharges. *Phys. Rev. E*, 62(1):1452–1454, July 2000.

[17] G. J. M. Hagelaar and G. M. W. Kroesen. Speeding up fluid models for gas discharges by implicit treatment of the electron energy source term. *Journal of Computational Physics*, 159(1):1–12, March 2000.

[18] G. J. M. Hagelaar and L. C. Pitchford. Solving the Boltzmann equation to obtain electron transport coefficients and rate coefficients for fluid models. *Plasma Sources Sci. Technol.*, 14(4):722, November 2005.

[19] D. D. Huang, J. H. Seinfeld, and K. Okuyama. Image potential between a charged particle and an uncharged particle in aerosol coagulation—enhancement in all size regimes and interplay with van der waals forces. *Journal of colloid and interface science*, 141(1):191–198, 1991.

[20] A. von Keudell and V. Schulz-von der Gathen. Foundations of low-temperature plasma physics—an introduction. *Plasma Sources Sci. Technol.*, 26(11):113001, October 2017.

[21] C. Killer, M. Mulsow, and A. Melzer. Spatio-temporal evolution of the dust particle size distribution in dusty argon rf plasmas. *Plasma Sources Sci. Technol.*, 24(2):025029, April 2015.

[22] U. Kortshagen. Nonthermal Plasma Synthesis of Nanocrystals: Fundamentals, Applications, and Future Research Needs. *Plasma Chem Plasma Process*, 36(1):73–84, January 2016.

[23] S. Kumar and D. Ramkrishna. On the solution of population balance equations by discretization—I. A fixed pivot technique. *Chemical Engineering Science*, 51(8):1311–1332, April 1996.

[24] M. A. Lieberman and A. J. Lichtenberg. *Principles of Plasma Discharges and Materials Processing*. John Wiley & Sons, April 2005.

[25] H.W. Marlow. Derivation of aerosol collision rates for singular attractive contact potentials. *The Journal of Chemical Physics*, 73(12):6284–6287, December 1980.

[26] A. Melzer. *Physics of Dusty Plasmas: An Introduction*. Number 962 in Lecture Notes in Physics. Springer International Publishing, 1st edition, 2019.

[27] A. Michau, G. Lombardi, C. Arnas, L. Colina Delacqua, M. Redolfi, X. Bonnin, and K. Hassouni. Modelling of dust grain formation in a low-temperature plasma reactor used for simulating parasitic discharges expected under tokamak divertor domes. *Plasma Sources Sci. Technol.*, 19(3):034023, June 2010.

[28] D. D. Monahan and M. M. Turner. On the global model approximation. *Plasma Sources Sci. Technol.*, 18(4):045024, September 2009.

[29] H. Ouyang, R. Gopalakrishnan, and C. J. Hogan Jr. Nanoparticle collisions in the gas phase in the presence of singular contact potentials. *The Journal of Chemical Physics*, 137(6):064316, August 2012.

[30] J. D. P. Passchier and W. J. Goedheer. A two-dimensional fluid model for an argon rf discharge. *Journal of Applied Physics*, 74(6):3744–3751, September 1993.

[31] A. Piel. *Plasma Physics - An Introduction to Laboratory, Space, and Fusion Plasmas*. Springer Berlin Heidelberg, January 2010.

[32] L. Ravi and S. L. Girshick. Coagulation of nanoparticles in a plasma. *Phys. Rev. E*, 79(2):026408, February 2009.

[33] G. S. Selwyn. Optical characterization of particle traps. *Plasma Sources Sci. Technol.*, 3(3):340, August 1994.

[34] P. K. Shukla and A. A. Mamun. *Introduction to Dusty Plasma Physics*. CRC Press, December 2010.

[35] H. M. Vale and T. F. McKenna. Solution of the Population Balance Equation for Two-Component Aggregation by an Extended Fixed Pivot Technique. *Ind. Eng. Chem. Res.*, 44(20):7885–7891, September 2005.

[36] S. J. Warthesen and S. L. Girshick. Numerical simulation of the spatiotemporal evolution of a nanoparticle–plasma system. *Plasma Chem Plasma Process*, 27(3):292–310, June 2007.

[37] Y. Watanabe, M. Shiratani, H. Kawasaki, S. Singh, T. Fukuzawa, Y. Ueda, and H. Ohkura. Growth processes of particles in high frequency silane plasmas. *Journal of Vacuum Science & Technology A*, 14(2):540–545, March 1996.

[38] J. Wharton. Dust from the Krakatoa Eruption of 1883. *Proceedings of the American Philosophical Society*, 32(143):343–345, 1894.

[39] E. R. Whitby and P. H. McMurry. Modal Aerosol Dynamics Modeling. *Aerosol Science and Technology*, 27(6):673–688, January 1997.

[40] D.A. Williams and C. Cecchi-Pestellini. *The Chemistry of Cosmic Dust*. Royal Society of Chemistry, 2015.

2 Analysis on the effect of the electrostatic interaction in the coagulation of silicon nanoparticles in argon-silane plasma simulations

Ravi & Girshick [9] introduced the nanoparticle coagulation enhancement by the action of the image potential in argon-silane plasma simulations. The image potential used, which is based on the work of Huang *et al.* [4], involves a non-physical singularity at the contact point of the particles. This feature necessitates the use of particular approaches to calculate the enhancement factor. In this paper, we use a more rigorous approach, which includes polarization induction and which is free of unphysical singularity at the contact point, for calculating the electrostatic force between dielectric particles. However, to compare with existing literature, we use the approach of Ouyang *et al.* [7, 3], designed for singular potentials, to calculate the enhancement factor. We show that the coagulation is enhanced in neutral-charged particles encounters. This analysis will be extended to study the enhancement in like-charged cases.

Analyse sur l'effet de l'interaction électrostatique dans la coagulation de nanoparticules de silicium dans des simulations de plasma argon-silane

Auteurs
Benjamin Santos[1], François Vidal[1], Laura Cacot[1,2] et Claude Boucher[1]
[1] INRS - Énergie Matériaux Télécomunications, Varennes, QC J3X 1P7, Canada
[2] Université Toulouse III - Paul Sabatier, 31062 Toulouse, France

23rd International Symposium on Plasma Chemistry (ISPC 23)
Proceedings
Juillet, 2018

Résumé traduit
Ravi & Girshick [9] ont introduit l'augmentation de la coagulation des nanoparticules par l'action du potentiel d'image dans les simulations de plasma argon-silane. Le potentiel d'image utilisé, basé sur les travaux de Huang *et al.* [4], implique une singularité non physique au point de contact des particules. Cette caractéristique nécessite l'utilisation d'approches spéciales pour calculer le facteur d'augmentation. Dans cet article, nous utilisons une approche plus rigoureuse, qui inclut l'induction

de la polarisation et qui est exempte de la singularité non physique au point de contact, pour calculer la force électrostatique entre les particules diélectriques. Cependant, pour comparer contre la littérature existante, nous utilisons l'approche d'Ouyang *et al.* [7, 3], conçue pour des potentiels singuliers, pour calculer le facteur de rehaussement. Nous montrons que la coagulation est améliorée lors de l'interaction entre des particules chargées et neutres. Cette analyse sera étendue pour étudier l'augmentation de la coagulation pour des particules ayant la même polarité de charge.

2.1 Introduction

It is known that nanoparticles in low-temperature plasmas are mostly charged negatively. Recently Mamunuru *et al.* [6], studied the existence of positively charged and neutral nanoparticles. This possibility promotes the coagulation because of the Coulomb interaction enhancement between particles of opposite charge. Ravi & Girshick[9], studied the coagulation enhancement between neutral and charged particles, which is due to the image potential. The image potential used in their work [8] is a rough approximation of the work of Huang [4], which is already an approximation. We propose a numerical study of the effects of the electrostatic interaction between nanometric sized particles of silicon on particle growth in an argon-silane plasma. Our simulations are based on the general dust-plasma self-consistent model proposed by S. L. Girshick's group [8, 11, 1].

2.2 Methodology

2.2.1 Plasma

For the sake of simplicity, we considered fixed plasma parameters [9], as listed in table 2.1. It is worth to mention that for this fixed electron - positive ion ratio, the present approach is not realistic because the remaining negative charge must reside in the nanoparticles, and charging evolves in time along with the plasma. Neverthelss we are interested in showing that a rigorous calculation of the interparticle potential leads to a different behavior compared to the simple Coulomb potential.

Table 2.1: Plasma parameters

Pressure	1 Torr
Ion density	$1 \times 10^{15}\,\mathrm{m}^{-3}$
Electron density	$1 \times 10^{14}\,\mathrm{m}^{-3}$
Mean electron energy	2 eV
Ion temperature	300 K

To simulate particle growth, we used the fixed-pivot technique [5] to solve the General Dynamics Equation, which accounts for nucleation, coagulation, and surface growth [8, 11, 1]. In the free molecular regime, the coagulation rate for particles of volume v_i and v_j is given by [9],

$$\beta(v_i, v_j) = \left(\frac{3}{4\pi}\right)^{1/6} \left[\frac{6kT}{\rho_p}\left(\frac{1}{v_i} + \frac{1}{v_j}\right)\right] \left(v_i^{1/3} + v_j^{1/3}\right)^2, \tag{2.1}$$

where k is the Boltzmann constant, T is absolute temperature, and ρ_p is the mass density of silicon. The total coagulation rate is $\eta\beta$, with η the enhancement factor.

The image potential between a charged and a neutral sphere can be approximated by [7, 3],

$$\frac{\phi(r^*)}{kT} = -\frac{\psi_{\mathrm{I}}}{2r^{*^2}\left(r^{*^2}-1\right)}. \tag{2.2}$$

The dimensionless image potential Ψ is defined by,

$$\psi_{\mathrm{I}} = \left(\frac{\varepsilon_p - 1}{\varepsilon_p - 2}\right)\frac{ze^2}{4\pi\varepsilon_0 kT a_i}, \tag{2.3}$$

where ε_p is the dielectric constant of bulk silicon, ε_0 the vacuum permittivity, e the elementary charge, z the charge number, and a_i the radii of the neutral particle. This is an approximation because we neglected the radius of the second sphere. Bichoutskaia *et al.* [2] derived a more general approach to describe the potential, which includes the polarization effects of dielectric particles.

Ouyang *et al.* [7] in the supplementary document gives the following regression formula for the image enhancement factor for eq. 2.4,

$$\eta_{\mathrm{I}} = 1.2534\sqrt{\psi_{\mathrm{I}}} \tag{2.4}$$

To compute the enhancement factor, we also used the Sceats' approach [10] to compare our results with those of Ravi & Girshick [9].

2.3 Discussion and results

Using the same parameters as Ravi & Girshick [9], we show in Fig 2.1. the enhancement factor and our results for the Sceats enhancement factor for the potential eq. 2.2. This figure shows that Ravi & Girshick's results overestimate the enhancement by a factor 10. It can be easily seen that using a more accurate description of the potential decreases the total number density as expected because we obtain lower coagulation rates.

In the following, we use eq. 2.4 to compute the enhancement factor for neutral-charged particles. In Fig. 2.2, we show the total particle number with and without image potential enhancement, in Fig. 2.3 total volume density of particles and in Fig. 2.4 the total charge density. We can see that the image potential continues to have a considerable effect on the coagulation and must be taken into account in self-consistent plasma calculations because it affects the total charge density.

2.4 Concluding remarks

We have shown that coagulation is overestimated in the work of Ravi & Girshick [9, 8] The main reason is that he used a rough approximation for the image potential.

Figure 2.1: Coagulation coefficients between particle 1 of 1 nm and particle 2 of the diameter shown in the x-axis. In the red dot-dashed line, the case of neutral coagulation eq. 2.1, coagulation between the neutral particle 1 and a negatively charged particle 2, in green using the potential eq. 2.2, in blue in the case of the potential of Ravi & Girshick, and black dashed line coagulation of the particle 1 with an elementary positive charge and particle 2. The charge for particle 2 is the most probable.

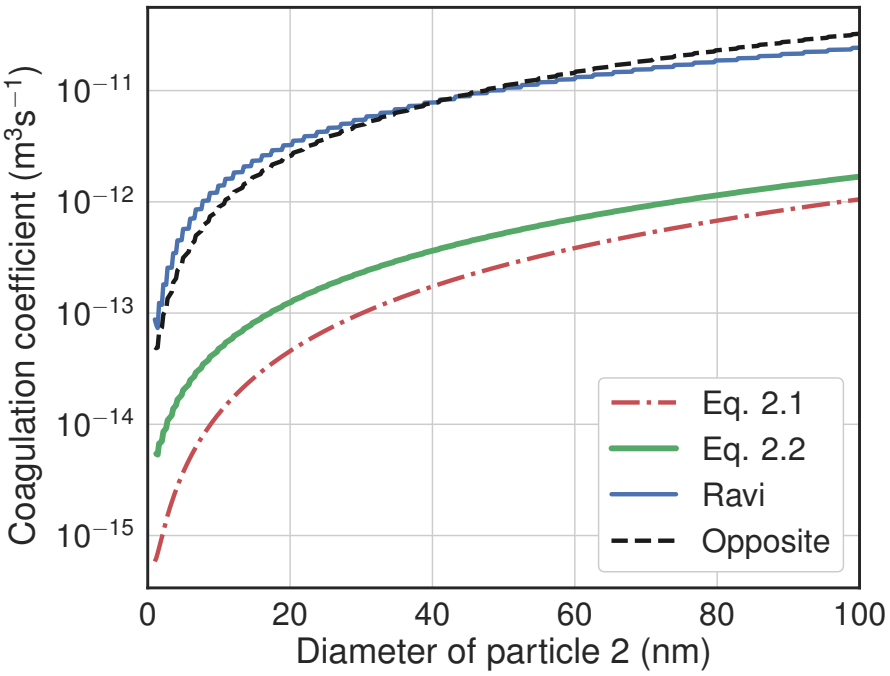

The image potential must be considered in self-consistent plasma calculations, because it modifies the total nanoparticle charge which affects the plasma.

We found that the approximated potential eq. 2.2 agrees with the more accurate description of Bichoutskaia [2] in the neutral-charged case. However, we found that using this approach, we could have an attractive potential even for particles of same polarity. This will be discussed in future works.

Figure 2.2: Total number density in black dashed line accounting for the image potential and red without image potential. Higher coagulation rates reduce the particle number.

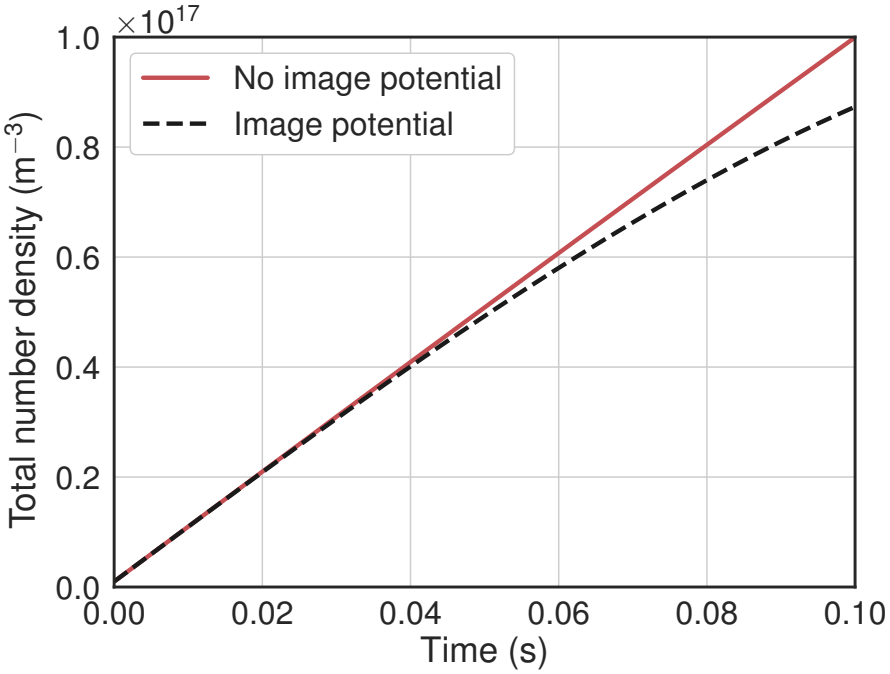

Figure 2.3: Total volume density in black dashed line with image potential enhancement factor and red without enhancement. The total volume decreases when the image potential is considered.

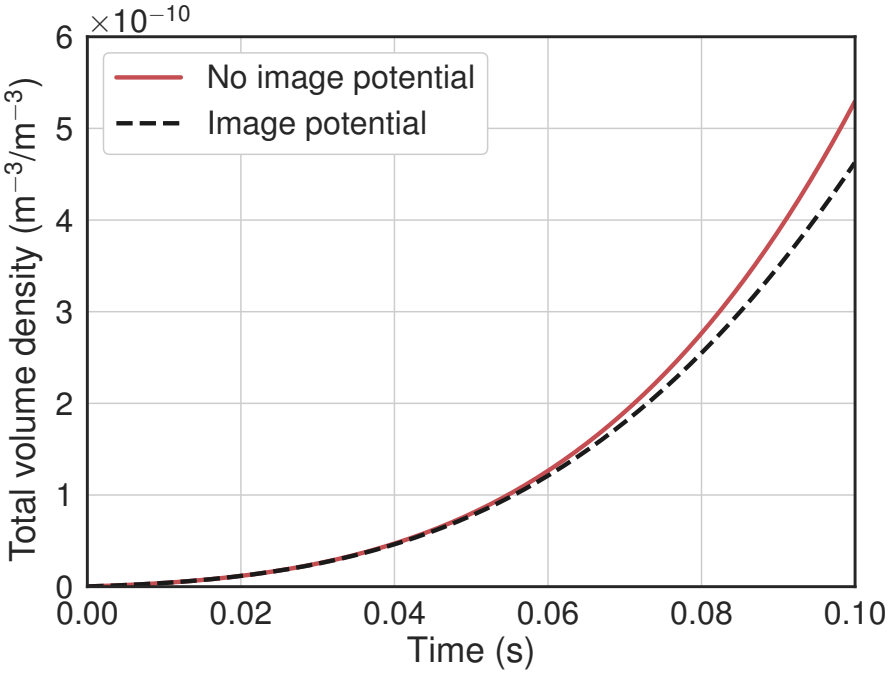

Figure 2.4: Total charge density in black dashed line with image potential enhancement factor and red without enhancement. The total charge decreases for higher coagulation rates.

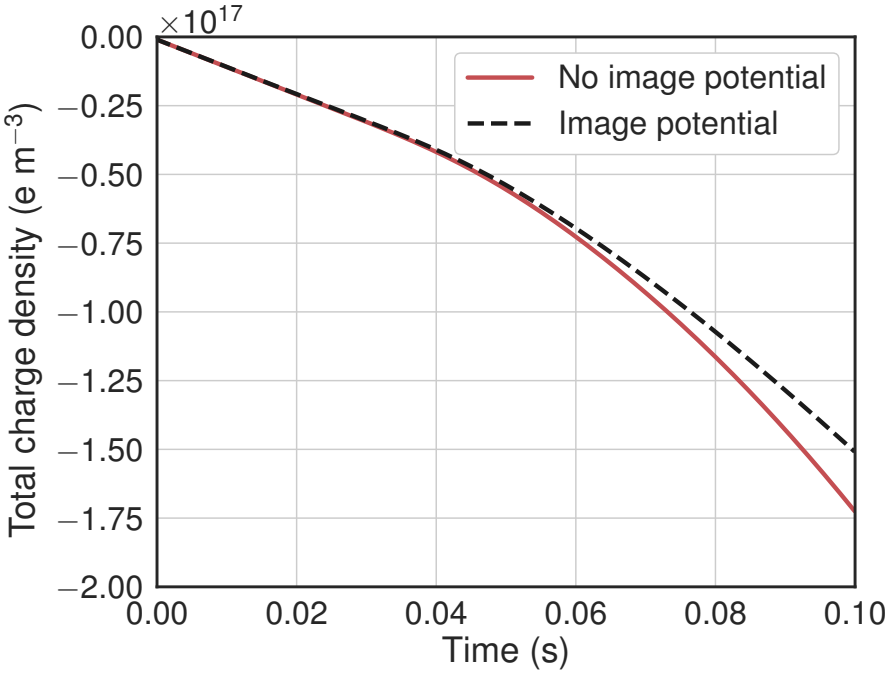

2.5 References

[1] P. Agarwal and S.L. Girshick. Sectional modeling of nanoparticle size and charge distributions in dusty plasmas. *Plasma Sources Sci. Technol.*, 21(5):055023, October 2012.

[2] E. Bichoutskaia, A. L. Boatwright, A. Khachatourian, and A. J. Stace. Electrostatic analysis of the interactions between charged particles of dielectric materials. *The Journal of Chemical Physics*, 133(2):024105, July 2010.

[3] B. T. Draine and Brian Sutin. Collisional charging of interstellar grains. *The Astrophysical Journal*, 320:803, September 1987.

[4] D. D. Huang, J. H. Seinfeld, and K. Okuyama. Image potential between a charged particle and an uncharged particle in aerosol coagulation—enhancement in all size regimes and interplay with van der waals forces. *Journal of colloid and interface science*, 141(1):191–198, 1991.

[5] S. Kumar and Ramkrishna D. On the solution of population balance equations by discretization—I. A fixed pivot technique. *Chemical Engineering Science*, 51(8):1311–1332, April 1996.

[6] M. Mamunuru, R. Le Picard, Y. Sakiyama, and S. L. Girshick. The Existence of Non-negatively Charged Dust Particles in Nonthermal Plasmas. *Plasma Chem Plasma Process*, 37(3):701–715, May 2017.

[7] H. Ouyang, R. Gopalakrishnan, and C. J. Hogan Jr. Nanoparticle collisions in the gas phase in the presence of singular contact potentials. *The Journal of Chemical Physics*, 137(6):064316, August 2012.

[8] L. Ravi. *Numerical Study of Nanodusty Plasmas*. PhD thesis, University of Minnesota, 2008.

[9] L. Ravi and S. L. Girshick. Coagulation of nanoparticles in a plasma. *Phys. Rev. E*, 79(2):026408, February 2009.

[10] M. G. Sceats. Brownian coagulation in aerosols—the role of long range forces. *Journal of Colloid and Interface Science*, 129(1):105–112, April 1989.

[11] S. J. Warthesen and S. L. Girshick. Numerical simulation of the spatiotemporal evolution of a nanoparticle–plasma system. *Plasma Chem Plasma Process*, 27(3):292–310, June 2007.

3 Electrostatic enhancement factor for the coagulation of silicon nanoparticles in low-temperature plasmas

The coagulation enhancement factor due to electrostatic (Coulomb and polarization-induced) interaction between silicon nanoparticles was numerically computed for different nanoparticle sizes and charges in typical low-temperature argon-silane plasma conditions. We used a rigorous formulation, based on multipole moment coefficients, to describe the complete electrostatic interaction between dielectric particles. The resulting interaction potential is non-singular at the contact point, which allows to adapt the orbital-motion limited theory to calculate the enhancement factor. It is shown that, due to induced polarization, coagulation is enhanced in neutral-charged particles encounters up to several orders of magnitude. Moreover, the short-range force between like-charged nanoparticles can become attractive as a direct consequence of the dielectric nature of the nanoparticles. The multipolar coefficient potential is compared to an approximate analytic form, which can be readily used to simplify the calculations. The results presented here provide a better understanding of the electrostatic interaction in coagulation and can be used in dust growth simulations in low-temperature plasmas, where coagulation is a significant process.

Keywords: coagulation, agglomeration, nanoparticles, low-temperature plasmas

Facteur d'augmentation électrostatique pour la coagulation de nanoparticules de silicium dans des simulations de plasma argon-silane

Auteurs

Benjamin Santos[1], Laura Cacot[1,2], Claude Boucher[1] et François Vidal[1]

[1] INRS - Énergie Matériaux Télécomunications, Varennes, QC J3X 1P7, Canada

[2] Université Toulouse III - Paul Sabatier, 31062 Toulouse, France

Plasma Sources Science and Technology

Article journal

`https://doi.org/10.1088%2F1361-6595%2Fab0a2b`

Janvier, 2019

Résumé traduit

Le facteur d'augmentation de la coagulation dû à l'interaction électrostatique entre les nanoparticules

de silicium a été calculé numériquement pour différentes tailles et charges de nanoparticules dans des conditions typiques de plasma froids d'argon-silane. Nous avons utilisé une formulation rigoureuse, basée sur des coefficients de moment multipolaires, pour décrire l'interaction électrostatique complète entre les particules diélectriques. Le potentiel d'interaction résultant n'est pas singulier au point de contact, ce qui permet d'adapter la théorie OML pour calculer le facteur de d'augmentation. Il est démontré qu'en raison de la polarisation induite, la coagulation est augmentée dans l'interaction entre particules chargées et neutres jusqu'à plusieurs ordres de grandeur. De plus, la force à courte portée entre des nanoparticules ayant des charges de même polarité peut devenir attractive en conséquence directe de la nature diélectrique des nanoparticules. Le potentiel de coefficient multipolaire est comparé à une forme analytique approximative qui peut être facilement utilisée pour simplifier les calculs. Les résultats présentés ici fournissent une meilleure compréhension de l'interaction électrostatique dans la coagulation et peuvent être utilisés dans des simulations de croissance de poussières dans des plasmas froids où la coagulation est un processus important.

Mots-clés: coagulation, agglomération, nanoparticules, plasmas froids

3.1 Introduction

Nanodusty plasmas are composed of electrons, neutral and ionized particles of a gas and nanometric sized grains of condensed matter, that we will call nanoparticles. The growth of silicon nanoparticles in low-temperature radio frequency capacitively coupled plasmas (RF-CCP) in an argon-silane (Ar-SiH_4) mixture has been the subject of many experimental investigations [5, 17, 6, 35, 23, 36]. In this paper, we limit the study to this configuration. Dusty plasmas are, however, ubiquitous in nature, in particular in space, and can also be generated over different laboratory conditions of gas mixture, temperature, pressure, and type of discharge [8].

The evolution of nanoparticle size starts with the nucleation phase [5, 17, 6], where primary dust is formed from the polymeric assembly of small molecules. Then follows the coagulation or agglomeration phase, which starts when a critical nanoparticle density is reached. In that phase, nanoparticles coalesce to form bigger particles, which can grow to tens of nanometers. This phase is identified by an increase in the size of the particles and a decrease in the nanoparticle number density. Then the surface growth, in which small molecules stick on the surface of the nanoparticles, becomes the more important mechanism of growth.

It is known that nanoparticles in low-temperature Ar-SiH_4 plasmas are mostly charged negatively due to the high-frequency electron bombardment. Recently, Mamunuru *et al.* [27] have pointed out the existence of positively charged and neutral nanoparticles, along with the expected negatively charged particles. Such a charge distribution promotes the coagulation because of the Coulomb attraction between particles of opposite charge polarity and the polarization-induced attraction taking place between all particles, but mostly between a neutral and a charged dielectric particle.

This polarization-induced attraction force results from the polarization of the bound charges residing in one particle induced by the electric field due to the presence of a net charge in the second particle. Several mathematical approaches have been used to calculate this force between two dielectric spherical particles (see for instance [25] and references therein). The ratio between the coagulation rate due to the electrostatic forces and the coagulation rate of two neutral particles is called the electrostatic enhancement factor.

Ravi & Girshick [31] have studied theoretically the coagulation enhancement between neutral and charged silicon nanoparticles by using the approximate image potential proposed by Huang *et al.* [18] and the Amadon and Marlow's expression [3] to calculate the enhancement factor. Both, van der Waals and electrostatic charge-like interaction have not been taken into consideration in their treatment. They concluded that the coagulation enhancement due to induced polarization can be very significant. For instance, they found that the neutral-charged enhancement factor can be higher than the oppositely charged under certain conditions (see figure 1 in [31]). Using this model, they performed extensive self-consistent nanodusty plasma simulations to investigate nanoparticle growth.

The use of point charges in the approach of Huang *et al.* to approximate the potential is, however, clearly inadequate when the sizes of the nanoparticles are comparable. Moreover, the divergence of this potential at the contact point between coalescing particles does not seem to have any physical ground. In addition, the complex Amadon and Marlow's expression for the enhancement factor, which was designed to handle such singular potentials, was found to provide higher coagulation enhancements as compared to some alternative forms [28].

These considerations motivated a revision of the calculation of the enhancement factor due to the electrostatic interaction between dielectric particles. In this work, we compute this enhancement factor between two dielectric spheres by using the multipolar coefficient potential (MCP) of Bichoutskaia et al. [4], which we consider more rigorous and appropriate to tackle this problem than the potential of Huang *et al.* Since the MCP of Bichoutskaia *et al.* is not singular at the contact point, a simple adapted orbital motion limited (OML) theory [2] can be used to calculate the enhancement factor.

Besides the electrostatic interaction, the van der Waals interaction is also known to play a significant role in the coalescence of particles [14]. The consistent treatment of the latter in our particular context is, however, outside the scope of this paper, which focuses essentially on the electrostatic interaction (see [30] for an overview of the general problem of the van der Waals interaction).

This article is organized as follows. First, in section 3.2.1 we present the parameters and assumptions of the following calculations. Next, in section 3.2.2 we express the coagulation rate along with the enhancement factor. Their derivations are developed in the appendix. Then, in section 3.2.3, we show the most probable equilibrium charge for a given nanoparticle size under the conditions of interest. In section 3.2.4 we describe the MCP used to compute the interaction between the particles. Computational and numerical details are given in section 3.2.5. Numerical results and their discussion are reported in section 3.3. Finally, we present the conclusions in section 3.4.

Table 3.1: Nanodusty plasma parameters

Parameter	value
Pressure (p)	100 mTorr
Mean electron energy (ε)	3 eV
Gas/ion/nanoparticle temperature (T)	300 K
Ion density (n_i)	$10^{15}\,\mathrm{m}^{-3}$
Electron density (n_e)	$10^{15}\,\mathrm{m}^{-3}$
Total nanoparticle density (N_p)	$10^{13}\,\mathrm{m}^{-3}$
Nanoparticle charge (q)	-238 to 5 e
Nanoparticle diameter (d_p)	1 to 100 nm
Nanoparticle mean free path (λ_p)	$\gg$1 mm
Neutral mean free path (λ)	0.44 mm
Ion mean free path (l_i)	0.30 mm
Dusty Debye length (λ_D)	0.04 mm
Ion Debye length (λ_i)	0.04 mm
Interparticle distance $\left(d = (3/4\pi N_p)^{1/3}\right)$	0.03 mm
Structure parameter ($\kappa_\mathrm{d} = d/\lambda_\mathrm{D}$)	0.77
Knudsen number ($\mathrm{K_n} = \lambda/d_p$)	$\gg 1$
Coupling parameter (Γ_d)	0 to 48

3.2 Methods

3.2.1 Plasma parameters and simplifying assumptions

Typical parameters in low-temperature low-pressure RF-CCP are shown in table 3.1. The choices for p, ε, n_i, and T, are motivated by experiments and numerical studies reported in [10, 27]. For illustrative purposes, we assume a low nanoparticle density so that we can consider the ion and electron densities to be nearly equal. The densities and temperatures are only indicative since these quantities evolve with dust growth. From table 3.1, it is possible to deduce the following conditions,

- **Free molecular regime prevails.** At low pressure and low gas density, neutral nanoparticles move ballistically and behave like hard spheres ($\lambda_p \gg d_\mathrm{p}, K_\mathrm{n} \gg 1$). As a consequence, only binary collisions are relevant.

- **Screening by ions is negligible.** The dusty Debye length is of the order of the ion Debye length, $\lambda_\mathrm{D} \sim \lambda_i$ [32]. For the selected parameters, λ_D is much greater than the nanoparticle sizes and greater than the interparticle distance d. This is a prerequisite for using the classical OML theory for nanoparticle charging and interaction. Effects of ion collisions on particle charging within the Gatti and Kortshagen's approach [12] are discussed at the end of section 3.2.3.

- **Nanoparticle collective effects are negligible.** These effects are characterized by the coupling parameter $\Gamma_\mathrm{d} = \frac{1}{4\pi\varepsilon_0}\frac{q^2}{k_\mathrm{B}Td}\exp(-\kappa_\mathrm{d})$, which is defined as the ratio between the Coulomb interaction energy and the nanoparticle thermal energy [32]. This coupling is relatively low for this

system. As a consequence, we assume that the nanoparticles are not strongly interacting to form a crystal ($\Gamma_d < 170$) and that classical electrostatics can be used to describe the interaction between two particles inside the Debye sphere [9].

In addition, we make the following simplifying assumptions,

- **The average nanoparticle charge is provided by the argon ion and electron currents.** While many ion species can coexist in Ar-SiH_4 plasmas, in the absence of a plasma chemistry model, we assume that the average nanoparticle charge is mainly given by the argon ion and electron currents, as given by the OML theory and electron tunneling.
- **Nanoparticles are spherical and have bulk silicon properties**. As required by the MCP potential [4], the charging models and the coagulation rate model used in this work, nanoparticles are treated as spheres [5]. We also assume that they have a relative permittivity $\varepsilon = 11.68$, electron affinity $A_\infty = 4.05\,\mathrm{eV}$ [24], and a mass density $\rho_p = 2330\,\mathrm{kg\,m^{-3}}$[15] as in bulk silicon at 300 K. These are the only parameters considered related to the nanoparticle composition. We should point out that a different composition of nanoparticles could lead to different results, as in the case of the paper of Mamunuru *et al.* [27]. They show that SiO_2 nanoparticles have more non-negative charge fraction than Si nanoparticles in their numerical calculations, which could lead to a large enhancement factor, as a consequence of the difference in the electron affinity constant.
- **The charge is uniformly distributed at the surface of the nanoparticles**. As in our system, dielectric nanoparticles are being bombarded by the electrons and ions of the plasma at a rapid rate from all directions, we assume, consistently with the tunnel effect and OML theory for charging, that the charges are uniformly distributed at the surface of the nanoparticles.

3.2.2 Coagulation rate and enhancement factor

The coagulation rate ($\mathrm{m^{-3}\,s^{-1}}$) for two colliding spherical particles i and j, with densities n_i and n_j ($\mathrm{m^{-3}}$), is expressed as,

$$R = \beta_{ij} n_i n_j, \tag{3.1}$$

where β_{ij} ($\mathrm{m^3\,s^{-1}}$) is the total coagulation kernel. Thus, when two particles of volume v_i and v_j coalesce, they form a new particle with volume v_k which is equal to the sum of the two constituent particles, i.e. $v_k = v_i + v_j$. In the case of discrete particle sizes, the dynamics of coagulation is governed by the Smoluchowski equation [11]:

$$\frac{\mathrm{d}n_k}{\mathrm{d}t} = \frac{1}{2}\sum_{i+j=k} \beta_{ij} n_i n_j - n_k \sum_{i=1}^{\infty} \beta_{ik} n_i, \tag{3.2}$$

where the first term of the right side represents the creation rate of the particle k from the collision between the particles i and j, and the second term is the annihilation of k when it collides with any particle i.

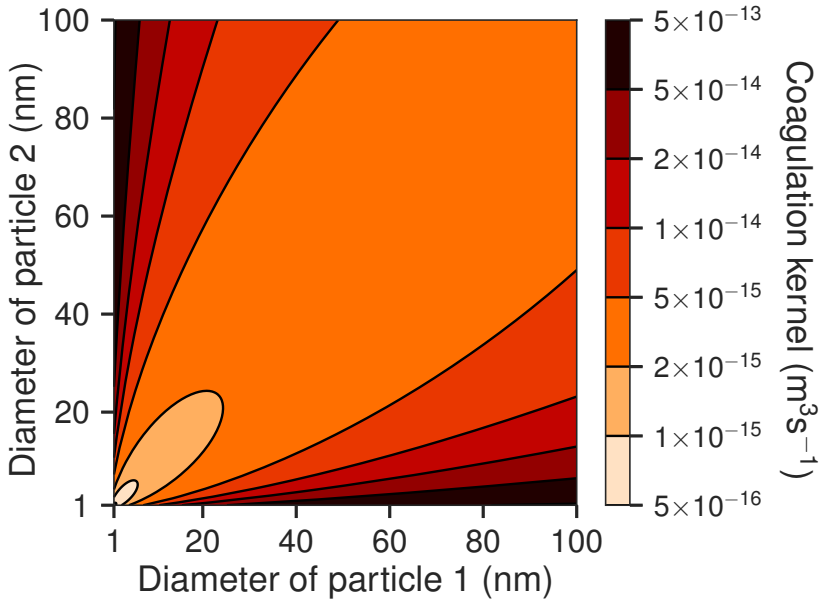

Figure 3.1: Coagulation kernel eq. 3.4 in the free molecular regime as a function of coalescing particle sizes for T =300 K and ρ_p=2330 kg/m^3.

The total coagulation kernel can be separated into two factors,

$$\beta_{ij} = \eta_{ij}\beta^0_{ij}. \tag{3.3}$$

where η_{ij} is the enhancement factor, which accounts for the electrostatic interaction between nanoparticles. β^0_{ij} is the coagulation kernel (or rate coefficient) for neutral particles in the free molecular regime, which can be expressed as [11, 31],

$$\beta^0_{ij} = \left(\frac{3}{4\pi}\right)^{1/6} \left[\frac{6k_\mathrm{B}T}{\rho_p}\left(\frac{1}{v_i}+\frac{1}{v_j}\right)\right]^{1/2} \left(v_i^{1/3}+v_j^{1/3}\right)^2, \tag{3.4}$$

where k_B is the Boltzmann constant, T is the kinetic temperature of the nanoparticles, and ρ_p is their mass density. Fig. 3.1 shows the coagulation rate for spherical particles in the range of sizes of interest. One observes that coagulation between small and big particles is more efficient than between particles of the same size. This situation typically occurs in nanodusty plasmas where there are small nucleated particles with $d \sim 1$ nm and particles grown by coagulation and surface growth with $d \sim 20$ to 100 nm [31].

Within the framework of the OML theory [2], the enhancement factor can be written explicitly (see 3.A),

$$\eta_{ij} = \exp\left(-\frac{\Phi_{ij,\max}}{k_\mathrm{B}T}\right)\left[1+\frac{\Phi_{ij,\max}-\Phi_{ij}(r_{\min})}{k_\mathrm{B}T}\right]. \tag{3.5}$$

In this expression, $r_{\min} = r_i + r_j$ is the distance between the centers of the spherical particles i and j, of radius r_i and r_j, respectively, when they are in contact, and $\Phi_{ij,\max}$ is the maximum value of the interparticle potential (see section 3.2.4). Obviously, $\eta_{ij} = \eta_{ji}$ since $\Phi_{ij} = \Phi_{ji}$.

Two important particular cases can be distinguished,

- monotonically increasing (attractive) potential ($\Phi_{ij}(r_{\min}) < 0, \Phi_{ij,\max} = 0$):

$$\eta_{ij} = 1 - \frac{\Phi_{ij}(r_{\min})}{k_B T}, \qquad \Phi_{ij}(r) \leq 0 \,\forall\, r \geq r_{\min}, \tag{3.6}$$

- monotonically decreasing (repulsive) potential ($\Phi_{ij,\max} = \Phi_{ij}(r_{\min}) > 0$):

$$\eta_{ij} = \exp\left(-\frac{\Phi_{ij}(r_{\min})}{k_B T}\right), \qquad \Phi_{ij}(r) \geq 0 \,\forall\, r \geq r_{\min}. \tag{3.7}$$

Naturally, these last two cases arise for instance when Φ_{ij} is the Coulomb potential for point charges [32, 2]. In the present situation, where induced polarization exerts an attractive force between particles, case eq. 3.6 is met for neutral-charge and oppositely charged particles, while either case eq. 3.7 or $\Phi_{ij,\max} > 0$ and $\Phi_{ij}(r_{\min}) < \Phi_{ij,\max}$ can be met for like-charged particles.

3.2.3 Equilibrium charge and charge distribution width

Two regimes of nanoparticle charging can be identified. In the first, the negative charge is limited by the tunnel effect, making the occurrence of small positively charged particles possible [16, 27]. In the second regime, the mean charge and the charge distribution width are inferred from the balance between the electronic and ionic currents towards the particle, as given by the OML theory [2]. The OML collision frequencies for the plasma species $j = e$, Ar^+ charging the nanoparticle of radius r_i and charge q_i, is [2],

$$\nu_{ji} = 4\pi r_i^2 n_j \left(\frac{E_j}{2\pi m_j}\right)^{1/2} \alpha_{ji}, \tag{3.8}$$

where n_j and m_j are the number density and mass, respectively. E_j is the average kinetic energy, specifically $E_e = \varepsilon$ and $E_{Ar^+} = {}^{3k_B T}/_{2}$, according to table 3.1. The coefficient α_{ji} and the surface nanoparticle potential ϕ_i are given by,

$$\alpha_{ji} = \begin{cases} \exp\left(-\frac{q_j \phi_i}{k_B T_j}\right) & \text{for } q_j q_i \geq 0, \\ 1 - \frac{q_j \phi_i}{k_B T_j} & \text{for } q_j q_i < 0, \end{cases} \tag{3.9}$$

$$\phi_i \equiv \phi(r_i, q_i) = \frac{q_i}{4\pi\varepsilon_0 r_i}. \tag{3.10}$$

The charging current associated with the species j is simply the product of the OML frequency and the charge, i.e. $I_{j,\mathrm{OML}} = q_j \nu_{ji}$.

The electron tunneling current is expressed as [16, 27, 13],

$$I_{e,\text{tunnel}} = \frac{2|q_i|}{\hbar}\left[k_\text{B}T e\phi(r_a, q_i)\right]^{\frac{1}{2}}\left[\beta\cos^{-1}\left(\beta^{-\frac{1}{2}}\right) - (\beta-1)^{\frac{1}{2}}\right], \tag{3.11}$$

where it is assumed that $q_i \leq 0$. In this expression, $\hbar$ is the reduced Planck constant,

$$\beta = \frac{r_a}{r_i} = \frac{q_i}{q_i + 5e/8 - 4\pi\varepsilon_0 r_i A_\infty/e}, \tag{3.12}$$

where $A_\infty = 4.05\,\text{eV}$ is the electron affinity of the uncharged flat bulk silicon, and $r_a \geq r_i$ is the location where electrons must tunnel to leave the nanoparticle [27]. This result uses the fact that, on a negatively charged nanoparticle, electrons lie in a potential well, characterized by the electron affinity A_∞, while outside the well electrons undergo the repulsive Coulomb force. The current eq. 3.11 expresses the probability for these electrons to pass through the barrier.

By balancing the currents, $I_{e,\text{OML}} + I_{e,\text{tunnel}} + I_{\text{Ar}^+,\text{OML}} = 0$, the equilibrium charge can be estimated as a function of the particle size. Comparing the positive currents, it is possible to distinguish two regimes: the tunnel regime, where $I_{e,\text{tunnel}} \gg I_{\text{Ar}^+,\text{OML}}$, for $d < 4$ nm, and the OML regime, where $I_{e,\text{tunnel}} \ll I_{\text{Ar}^+,\text{OML}}$, for $d > 4$ nm. This is shown in figure 3.2 for the plasma conditions given in table 3.1. Since the tunnel current acts very fast, the equilibrium tunnel charge can be approximated as the maximum negative charge the particle can bear [24, 27, 16]. For a mean charge number z, the width of the charge distribution can be expressed as $z \pm 3\sigma$, where σ^2 is the variance of the charge distribution as given by the OML theory [24],

$$\sigma^2 = \frac{4\pi\varepsilon_0 r_i k_\text{B} T_e}{e^2}\left(1 - \frac{T_e}{T_e + T - \frac{e^2}{4\pi\varepsilon_0 r k_\text{B}} z}\right). \tag{3.13}$$

For completeness, we also show in figure 3.2 the equilibrium charge resulting from the improved OML theory of Gatti and Kortshagen [12], which includes collisional effects in the ion current. Two types of corrections are considered in that model: the collision-enhanced (CE) current, which is due to the collection of ions which remain in the vicinity of a nanoparticle or are slowed down by collisions with neutrals [22], and the hydrodynamic (HY) current which appears in the highly collisional regime, when the ion mean free path is comparable or smaller than the dusty Debye length. Within this framework, the equilibrium charge equation reads,

$$I_{e,\text{OML}} + I_{e,\text{tunnel}} + P_0 I_{\text{Ar}^+,\text{OML}} + P_1 I_{\text{Ar}^+,\text{CE}} + P_{>1} I_{\text{Ar}^+,\text{HY}} = 0, \tag{3.14}$$

where P_n represents the probability for a positive ion coming from the unperturbed plasma to experience n collisions within a capture radius R_0, which depends on the mean charge and size of the nanoparticle [12].

Figure 3.2 shows that ion collisional effects tend to reduce, here by a factor between 1 and 2, the negative charge of the particles with sizes >3 nm as compared to the classical OML theory. It

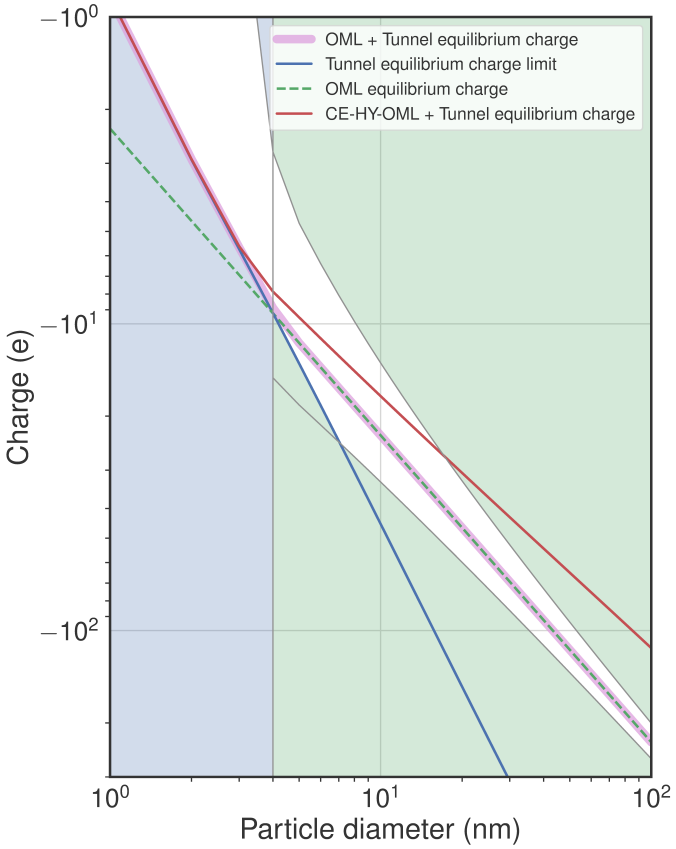

Figure 3.2: Equilibrium charge and charge distribution width as a function of particle diameter using the parameters of table 3.1. The equilibrium charge in the tunnel regime is represented by the blue solid line and is considered as the maximum negative charge that a particle can bear when it is greater than the charge in the OML regime. The equilibrium charge in the OML regime is given by the green dashed line enclosed by two lines which delineate the width of the charge distribution. The blue and green zones outside the white area denote less likely combinations of size and charge for nanoparticles close to equilibrium with the plasma. The equilibrium charge resulting from the three currents, $I_{e,\mathrm{OML}} + I_{e,\mathrm{tunnel}} + I_{\mathrm{Ar}^+,\mathrm{OML}} = 0$, is represented by the plum curve. The red curve represents the mean charge from Gatti & Kortshagen's model [12], denoted CE-HY-OML.

should be stressed that, besides collisional effects, lower plasma electronegativity n_e/n_i will also tend to decrease the charge of the nanoparticles. On the other hand, a decrease of pressure or an increase of electron temperature will have the opposite effect. Therefore, in the following, we consider the equilibrium charge given by the classical OML theory as a reference.

3.2.4 Interparticle potential

Considering the uniform surface charge distribution implied by the tunnel effect and the OML theory for charging, the multipolar coefficients potential (MCP), developed by Bichoutskaia *et al.* [4, 33], appears to be well suited for the problem of interest since their MCP deals with the electrostatic interaction of two dielectric particles with charges distributed on their surface. The MCP was found

to provide a well-behaved solution that agrees with the more general but more complicated solution of Khachatourian *et al.* [21] expressed in terms of bispherical coordinates. Furthermore, the MCP solution converges rapidly using fewer terms in the expansion than the bispherical solution [25].

The MCP reads [4, 33],

$$\Phi_{\mathrm{MCP}}(r, r_i, q_i, r_j, q_j) \equiv \Phi_{\mathrm{MCP,ij}}(r) \tag{3.15}$$

$$= K\frac{q_i q_j}{r} - \frac{q_i}{2}\sum_{m=1}^{\infty}\sum_{l=0}^{\infty} A_l \frac{(\varepsilon-1)\,m}{(\varepsilon+1)\,m+1}\frac{(l+m)!}{l!m!}\frac{r_j^{2m+1}}{r^{2m+l+2}} - \frac{1}{2K}\sum_{l=1}^{\infty} A_l^2 \frac{(\varepsilon+1)\,l+1}{(\varepsilon-1)\,l r_i^{2l+1}}, \tag{3.16}$$

where r is the distance between the centers of the particles, q_i and q_j are the charges of particles i and j, respectively, and $K = 1/4\pi\varepsilon_0$. The multipolar coefficients A_l, which takes into account the mutual polarization of the particles, are the solutions of the following linear system of equations,

$$A_{j_1} = Kq_1\delta_{j_1,0} - \frac{(\varepsilon-1)\,j_1}{(\varepsilon+1)\,j_1+1}\frac{r_1^{2j_1+1}}{r^{j_1+1}}Kq_j + \frac{(\varepsilon-1)\,j_1}{(\varepsilon+1)\,j_1+1}\sum_{j_2=0}^{\infty}\sum_{j_3=0}^{\infty}\frac{(\varepsilon-1)\,j_2}{(\varepsilon+1)\,j_2+1}\frac{(j_1+j_2)!}{j_1!j_2!}\frac{(j_2+j_3)!}{j_2!j_3!}\frac{r_i^{2j_1+1}r_j^{2j_2+1}}{r^{j_1+2j_2+j_3+2}}A_{j_3}. \tag{3.17}$$

In practice, the sums in equations eq. 3.16 and eq. 3.17 are truncated with maximum indices determined as explained below.

3.2.5 Outline of the numerical calculations

In order to find the enhancement factor eq. 3.5 using the MCP, it is necessary to solve the linear system of equations eq. 3.17 and calculate the potential eq. 3.16 at various relative distances r. This procedure can be quite time-consuming depending on the size of the linear system of multipolar coefficients. We determined the number of terms retained in the summations in equations eq. 3.16 and eq. 3.17 from the convergence rate of the series as a function of the number of terms considered, knowing that the series converges uniformly. If few consecutive values of the potentials with decreasing number of terms were in agreement within 1% or less, we considered that the number of terms was sufficient. Otherwise, we raised the number of terms until the required convergence rate is achieved. The number of terms satisfying this condition is between 25 and 500, depending on the MCP arguments.

Calculations were done using C++ codes complemented by the Boost library for solving linear systems of equations and finding roots [26]. Additional calculations were performed in Python with the scipy package [20] (results in 3.B and 3.C). The results were plotted using matplotlib [19].

More details can be found in the supplementary material from FigShare (https://doi.org/10.6084/m9.figshare.c.420

The calculation procedure can be summarized as follows,

1. Set the nanoparticle kinetic temperature, relative permittivity, sizes and charges pairs (r_i, q_i).
2. For each combination of pairs (r_i, q_i) and (r_j, q_j), compute the potential eq. 3.16 at the contact point $r_{\min} = r_i + r_j$.
3. In the case of like-charged particles, find the zero of the electrostatic force $-d\Phi_{ij}/dr$ for $r > r_{\min}$. If a zero force exists at a finite value of r, it corresponds to the potential barrier. Its height $\Phi_{ij,\max}$ can thus be computed, and then the enhancement factor (3.5). If such a root cannot be found, then the interaction is either purely repulsive or purely attractive and only $\Phi_{ij}(r_{\min})$ is needed (cases (3.7) and (3.6), respectively).

The MCP can be expressed in terms of diameter and charge ratios d_i/d_j and q_i/q_j, but the enhancement factor cannot be factorized that way. Thus, it is necessary to calculate the MCP for all distinct combinations of (d_i, q_j) and (d_i, q_j) of interest. To accelerate the calculations, the MCP was calculated for specific ratios and then extracted for all combinations of (d_i, q_j) and (d_i, q_j) to obtain the enhancement factor. For this work, we have considered $L = 100$ diameters and $Q = 302$ charges for each particle, which gives a total of $LQ(LQ+1)/2 \approx 4.56 \times 10^8$ distinct combinations of pairs of coagulating particles. Only a subset of these combinations are, however, discussed in section 3.3.

Furthermore, we have found that significant speedup can be achieved to calculate $\Phi_{ij,\max}$ by using an approximate formulation of the MCP, the Image Potential Approximation (IPA), which is discussed in 3.B. The IPA provides an useful approximation of the MCP for all interparticle distances r when the size of the particles are very different and at large distance for any particle size ratios (see figure 3.37 for instance). The IPA proves to be convenient to localize the position of $\Phi_{ij,\max}$. With this hybrid approach, the MCP needs to be computed no more than two times: at contact and at the barrier, for each combination of (r_i, q_i) and (r_j, q_j) where $q_i q_j > 0$. The full MCP was used, however, in this paper to calculate $\Phi_{ij,\max}$.

3.3 Results and discussion

3.3.1 Coulomb enhancement factor

For the sake of comparison with the MCP, we first present in figure 3.3 the enhancement factor η_{ij} for the Coulomb interaction, as given by equations eq. 3.6 and eq. 3.7. Each panel shows contour levels of the enhancement factor as a function of the size and charge of particle 1, whereas the size and charge of particle 2 are specified in columns and rows, respectively. The panels along the diagonal from upper left to lower right correspond to equilibrium combinations of size and charge of particle 2 in the stated plasma conditions (see figure 3.2). The size and charge of particles 1 and 2 outside the equilibrium values are also included to represent possible, but less likely, states that could occur in dynamic out of equilibrium systems.

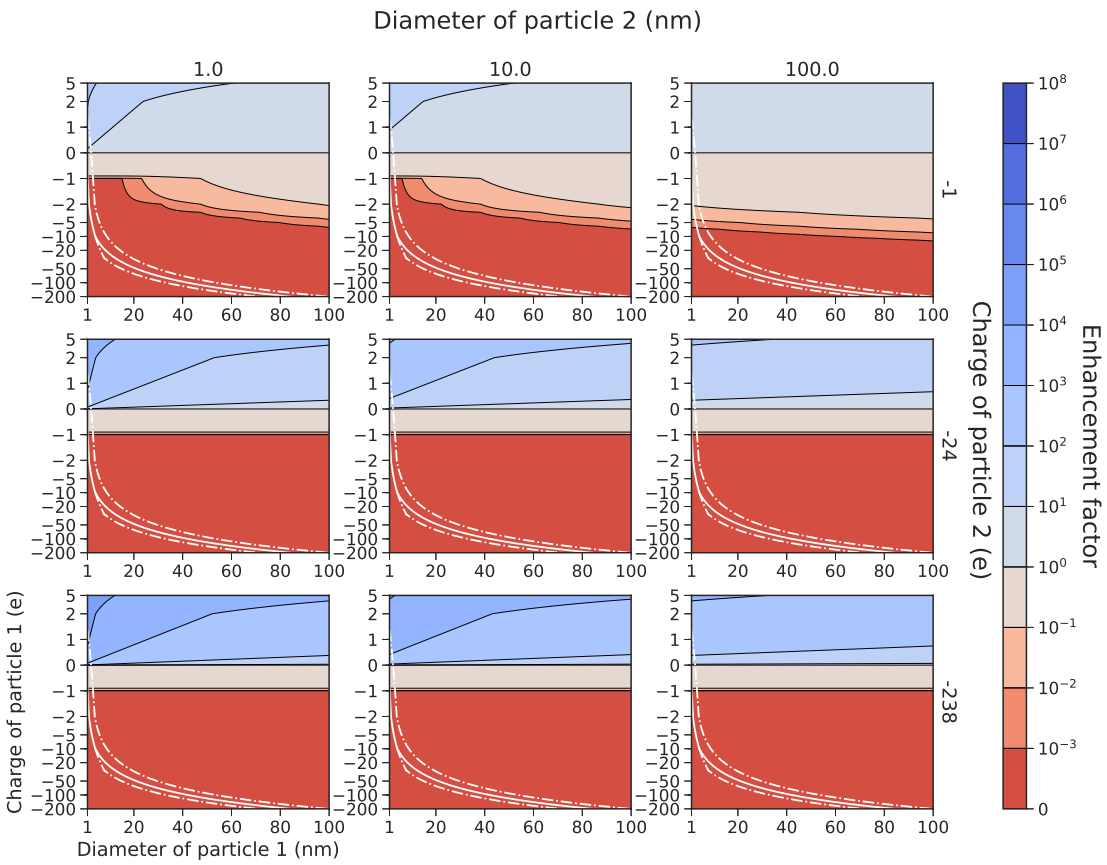

Figure 3.3: Contour levels of the Coulomb enhancement factor as a function of the size and charge of particle 1. Each row corresponds to a charge and each column to a diameter of particle 2. The continuous white curve represents the most probable charge at equilibrium while the dot-dashed curves delimit the width of the charge distribution (see figure 3.2). Note that the particle charges are discrete and the contours are being interpolated between the different discrete levels.

As expected, enhancement $\eta_{12} > 1$ (blue zones) occurs for opposite charge particles and suppression $\eta_{12} < 1$ (red zones) for like-charged particles. For the neutral-charged particles interaction, the enhancement factor is identically equal to 1 and is thus not represented. The enhancement factor shown in figure 3.3 reflects the fact that the Coulomb interaction decreases as r_{min} increases for a given charge q_1, and that attraction increases as $-q_1 q_2$ increases. Since the white curve in figure 3.3 represents the most likely charge at equilibrium (the same as in figure 3.2), one can see that suppression occurs along this curve for all the selected pairs of size and charge of particle 2.

For use in the following sections, figure 3.4 shows a chart of the enhancement factor as a function of the size and charge of small particles 1, for a particle 2 of size 1 nm and charge $+e$.

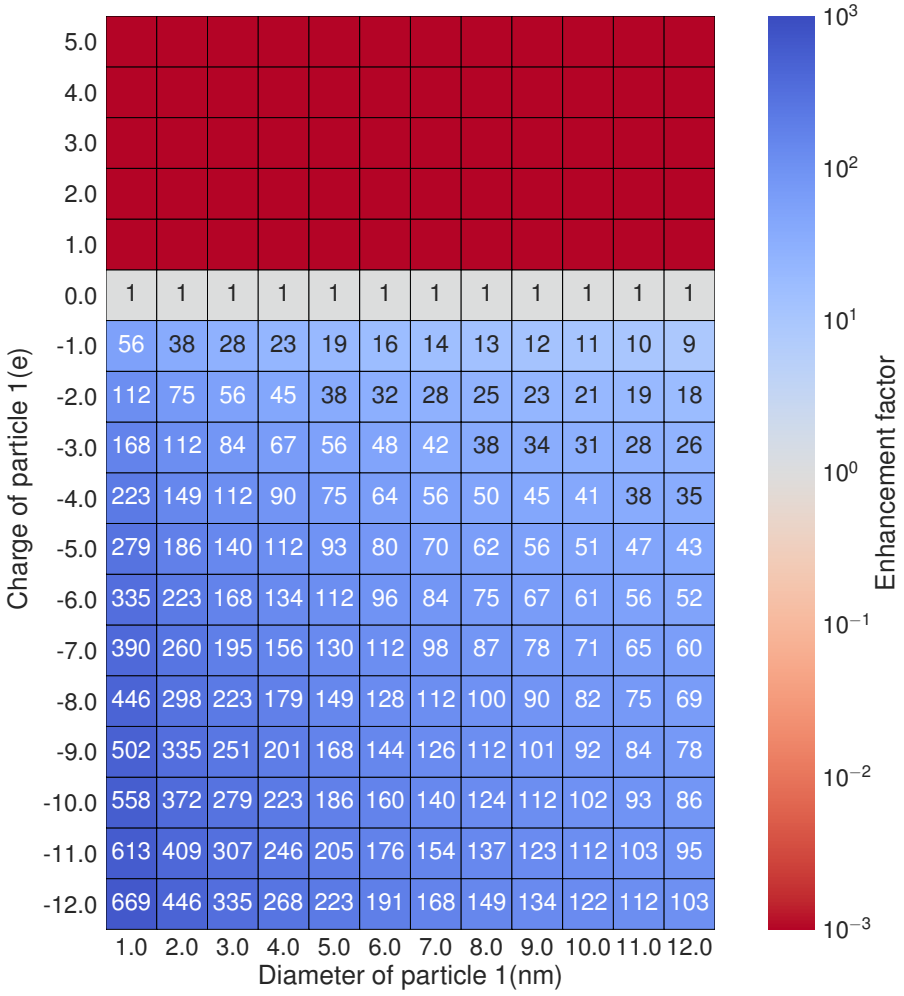

Figure 3.4: Chart of the Coulomb enhancement factor for small particles. The particle 2 has $d_1 = 1$ nm and $q_1 = +e$. Strong suppression occurs when charges have the same sign and the enhancement factor is exactly 1 when the particle 1 is neutral.

3.3.2 MCP charged-charged enhancement factor

The MCP enhancement factor is shown in figure 3.5 for the same sizes and charges of particles 1 and 2 as those of figure 3.3. Significant differences can be observed between the two cases. Red zones have recessed while blue zones have expanded in all panels, indicating a larger enhancement factor, which is a consequence of the polarization-induced attraction. These changes are evident when the particle 1 has a few charges. It is important to recall that particle charges are discrete, and the contours are interpolated between the different discrete charges.

3.3.2.1 Opposite charge interaction.

Contrary to the Coulomb interaction, the enhancement factor does not always decrease as d_1 increases for opposite charge interaction, as can be seen in some panels for $q_2 = -24e$ and $-238e$ (horizontal sections for $q_1 > 0$). This effect is due to stronger induced polarization in larger particles. It is not observed for $q_2 = -e$ because the charge is too small to induce a significant polarization in particle 1. These trends can be understood by using the IPA, equation (3.37), which provides a useful approximation to the MCP at the contact point $r_{\min} = {}^{(d_1+d_2)}/_2$ when the particle sizes d_1 and d_2 are very different, as this case is close to the one considered by Draine and Sutin [7] on which the IPA is based. The IPA at the contact point reads, to the first order in $d_2/d_1 \ll 1$,

$$\Phi_{\mathrm{IPA},12}(r_{min}) \approx 2K\frac{q_1 q_2}{d_1}\left(1-\frac{d_2}{d_1}\right) - \frac{K\kappa}{2}\frac{q_2^2}{d_2}\left(1-\frac{5}{2}\frac{d_2}{d_1}\right), \tag{3.18}$$

where the first term is the Coulomb interaction and the second term is the induced polarization. From this expression, one finds that, for a given charge ratio $q_1/q_2 < 0$ and for size ratios such that $d_2/d_1 \ll 1$, the enhancement factor η_{12}, here given by equation (3.6), increases as d_1 increases if

$$-\frac{q_1}{q_2} < \frac{5}{8}\kappa. \tag{3.19}$$

When this inequality is satisfied, the increase of the attractive force of the induced polarization is able to counterbalance the decrease of the Coulomb attraction as the size of the particle 1 increases. This condition works in all panels for $d_2 = 1$ nm and 10 nm, where $d_2/d_1 \ll 1$.

For size ratios such that $d_1/d_2 \ll 1$, as is the case in the panels where $d_2 = 100$ nm, the condition for η_{12} to increase as d_1 increases is,

$$-\frac{q_1}{q_2} < \kappa\left[\frac{3}{2}\left(\frac{d_1}{d_2}\right)^2 - \left(\frac{q_1}{q_2}\frac{d_2}{d_1}\right)^2\right]. \tag{3.20}$$

This condition can be satisfied only if the right-hand side is positive, namely

$$\left|\frac{q_1}{q_2}\right| < \sqrt{\frac{3}{2}}\left(\frac{d_1}{d_2}\right)^2. \tag{3.21}$$

Therefore the ratio $|q_1/q_2|$ must be very small and this is the case for $q_2 = -238e$.

In conclusion, in both limiting cases $d_2/d_1 \ll 1$ and $d_1/d_2 \ll 1$, the enhancement factor will increase as d_1 increases provided the charge ratio $-q_1/q_2$ is sufficiently small. Otherwise, the Coulomb attraction dominates the trend.

3.3.2.2 Like-charged interaction.

For like-charge particles, one observes that the enhancement factor generally increases as d_1 increases, as in the Coulomb case, and this effect is enhanced due to the attraction induced by polarization. One exception is the $d_2 = 100$ nm, $q_2 = -e$ panel where the opposite trend is observed. In this

particular case, the induced polarization is large for small values of d_1 and decreases as d_1 increases for a sufficiently high charge ratio $q_1/q_2 > 0$ (as also observed in [25]). This can be readily seen from the IPA in the limit $d_1/d_2 \ll 1$,

$$\Phi_{\mathrm{IPA},12}(r_{min}) \approx 2K\frac{q_1 q_2}{d_2}\left(1-\frac{d_1}{d_2}\right) - \frac{K\kappa}{2}\frac{q_2^2}{d_2}\left[\left(\frac{q_1}{q_2}\right)^2\frac{d_2}{d_1} + 2\left(\frac{d_1}{d_2}\right)^3\right], \tag{3.22}$$

where the first term is the Coulomb interaction and the second term is the induced polarization.

Moreover, contrary to the Coulomb interaction, the enhancement factor does not always increase monotonically as $-q_1 q_2$ increases for a given d_1. For instance, in the $d_2 = 100\,\mathrm{nm}$, $q_2 = -e$ panel, one can see that the enhancement factor at $d_1 = 40\,\mathrm{nm}$ has a maximum near $q_1 = -10e$, where $\eta_{12} > 1$, although the repulsive Coulomb force is weaker near $q_1 = -e$, where $\eta_{12} < 1$. This effect is the result of peculiar combinations of $\Phi_{12,\mathrm{max}}$, and $\Phi_{12}(r_{\mathrm{min}})$ entering in the expression of the enhancement factor, equation (3.5). In such cases, the IPA is of little use to understand the trends since the mathematical expressions are quite complicated.

The most striking features of figure 3.5 is certainly that enhancement occurs for like-charged particles, as can be observed in panels for $q_2 = -e$, and $-24e$. For $q_2 = -238e$, the Coulomb repulsion is too strong for this effect to happen. The enhancement for like-charged particle interaction takes place, however, outside the equilibrium diameter-charge curve shown in figure 3.2. For instance, large particles with a low charge (e.g. $d > 20\,\mathrm{nm}$ and $q \approx -e$), where enhancement is observed, are unlikely at equilibrium.

Fig. 3.6 shows a chart of the enhancement factor for the same size and charge pairs as those in figure 3.4. It appears clear that most values are increased in comparison with figure 3.4. In particular, η_{12} for like-charged particles is higher for the largest particles, and the neutral-charged interaction for the smallest particles is significantly increased.

3.3.3 MCP neutral-charged enhancement factor

Fig. 3.7 shows the enhancement factor for the interaction between neutral particles 2 of different diameters with particles 1 of different charges and sizes. It can be seen that $\eta_{12} \geq 1$ for all combinations of (d_1, q_1) and d_2. Some features of figure 3.7 can be understood by looking at the IPA for $d_2/d_1 \ll 1$,

$$\Phi_{\mathrm{IPA},12}(r_{min}) \approx -K\kappa q_1^2\frac{d_2^3}{d_1^4}\left(1-4\frac{d_2}{d_1}\right). \tag{3.23}$$

In particular, one can see that $\eta_{12} - 1 \propto q_1^2 d_2^3/d_1^4$. The charts of figures 3.8 and 3.9 show the behavior of η_{12} when $d_1/d_2 \sim 1$. One can see that the enhancement factor is larger when the particles have comparable sizes. It is interesting to note that this trend is opposite to the behavior of the kernel β_{ij}^0 shown in figure 3.1 where collisions between dissimilar particles are more likely.

Most interestingly, the equilibrium charge of particle 1 lies in the region where enhanced coagulation occurs, as can be seen clearly in figure 3.7. Thus, from the coagulation perspective, the most important

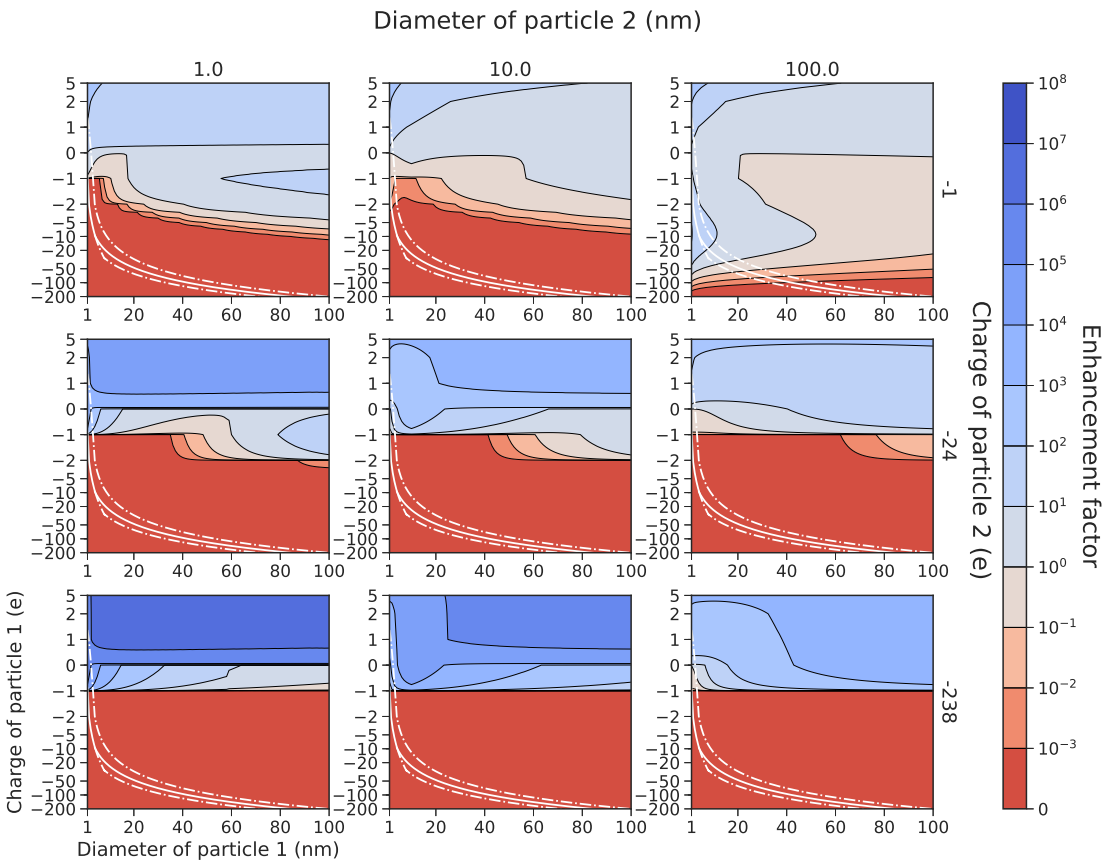

Figure 3.5: Contour levels of the MCP enhancement factor for particle sizes and charges as in figure 3.3.

consequence of induced polarization appears to be the increase of the coagulation rate of small particles (which have more chances to be neutral than bigger ones) and charged particles. Small particles are likely to be neutral, and the coagulation between them and larger ($> 10\,\text{nm}$) charged particles is enhanced, as can be noted by following the mean charge represented by the white line. This possibility contrasts with the case of no image potential, which has no enhancement. We expect this phenomenon could be of importance because, in silane nanodusty plasmas, a bimodal size distribution was found in experiments and simulations [1, 34].

By comparing the charts of figures 3.6 and 3.8, it appears that the neutral-charged enhancement is always lower than the opposite charge enhancement for the same d_1 and q_1. The enhancement factors for high-charge states of $d_1 = 1$ nm can, however, be larger than in the pure Coulomb case of figure 3.4. Such high-charge states are however unlikely for $d_1 = 1$ nm particles.

Fig. 3.10 shows the coagulation enhancement factor between particles 1 with their equilibrium charge (figure 3.2) and neutral particles 2 of different sizes, as a function of d_1. Since in Coulomb interaction the enhancement factor for a neutral and a charged particle is 1, one sees that induced polarization can increase coagulation by one or two orders of magnitude. This result suggests that induced polarization could play an essential role in the growth of nanoparticles in dusty plasmas.

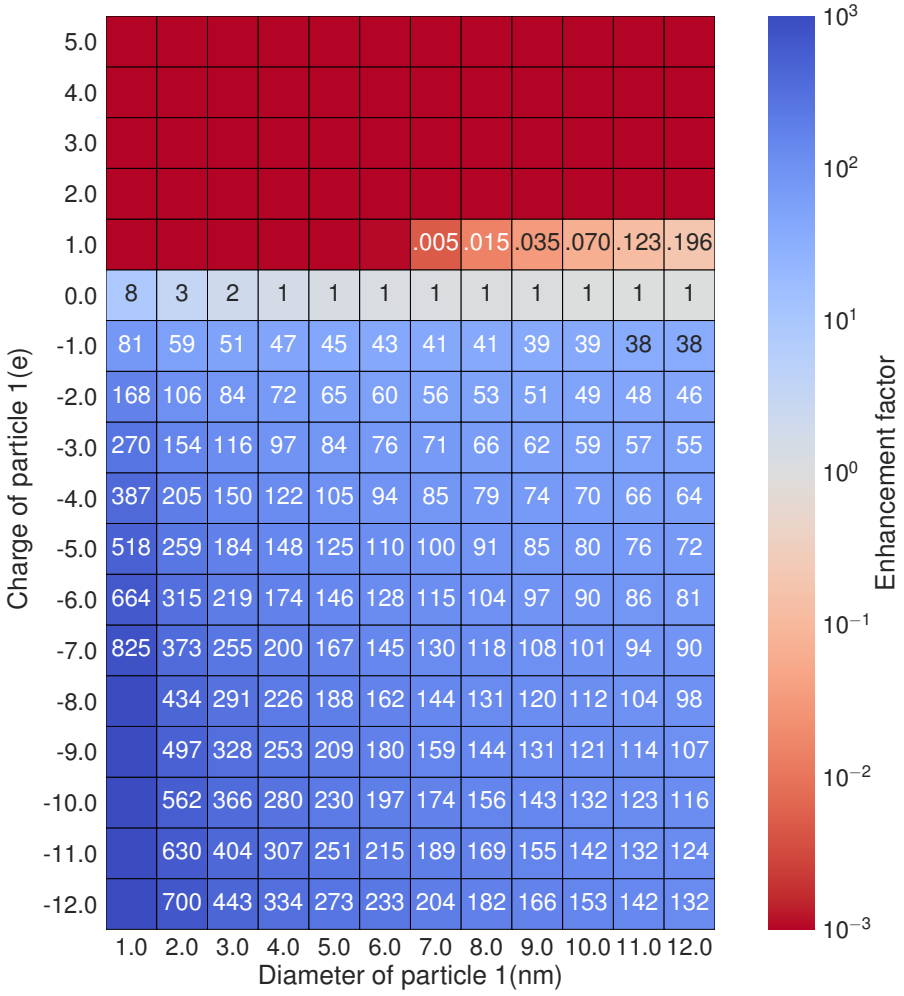

Figure 3.6: Chart of the MCP enhancement factor for small particles. The particle 2 has $d_1 = 1$ nm and $q_1 = +e$. The range of parameters for particle 1 is the same as in figure 3.4 for the Coulomb case.

3.4 Conclusion

This paper revisits the calculation of the coagulation enhancement factor resulting from the electrostatic interaction of silicon nanoparticles in typical laboratory conditions of low-temperature argon-silane plasmas. The approach used is based on the rigorous multipolar coefficient potential (MCP) of Bichoutskaia *et al.* [4]. In contrast to previous investigations using simpler potentials forms [31, 18, 3, 28], the MCP is not singular at the contact. This property allows using the straightforward orbital-motion limited (OML) theory to calculate the enhancement factor.

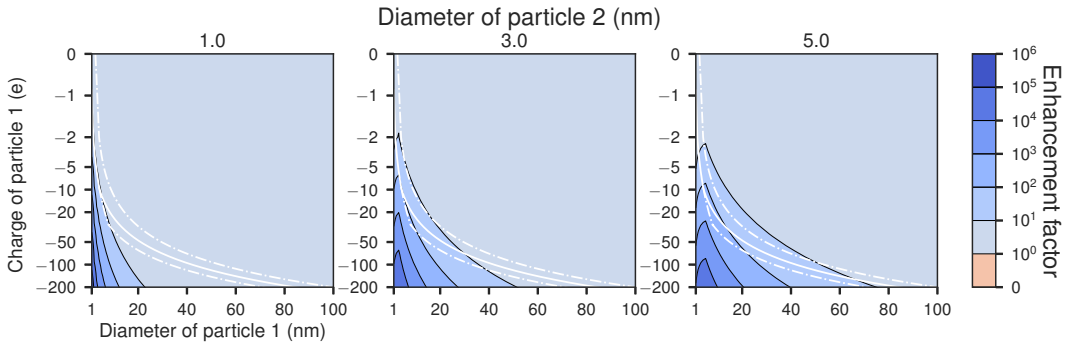

Figure 3.7: Contour levels of the MCP enhancement factor for a negatively charged particle 1 and a neutral particle 2 with sizes $d_2 = 1, 3,$ and 5 nm.

The induced polarization as calculated by the MCP produces an attractive force component when one of the two interacting particles is charged. Several significant differences have been observed as compared to the pure Coulomb interaction. In particular, enhancement ($\eta_{ij} > 1$), i.e. overall attraction, can be found in like-charged interaction. Such cases involve, however, particles far from charge equilibrium in the plasma, as calculated using the tunnel electron current and the OML plasma currents. In addition, the enhancement in neutral-charged particles interaction provided by the MCP can be several orders of magnitude and takes place for particles near charge equilibrium in the plasma. This enhancement is, however, always lower than for the Coulomb attraction for particles close to charge equilibrium, but it can be higher for unlikely highly charged particles. Other significant differences with respect to the pure Coulomb interaction have been observed, such as the opposite variation of the enhancement factor with the particle sizes for given charges, and the non-monotonous variation of the enhancement factor as a function of the charges for given particle sizes.

Several of the trends observed in our numerical calculation using the MCP have been understood using a simple approximate analytical potential, called the image potential approximation (IPA), which provides an useful approximation of the MCP at large interparticle distance and when the particle sizes are very different. On the computational side, the IPA provides a convenient means to calculate the potential barrier $\Phi_{ij,\mathrm{max}}$ involved in the enhancement factor, which is a time-consuming operation when using only the MCP.

The findings of this work could be readily extended to different materials as well as to different laboratory conditions, granted that the Debye length is larger than the average distance between nanoparticles and the system remains in the free molecular regime. The enhancement factor presented here can be implemented in a dynamic coagulation model, involving coupled sectional, charging, and plasma chemistry models [1], to describe the nanoparticle charge and size distributions as a function of time. Besides, a proper description of the van der Waals interaction would be required. These topics are currently under investigation.

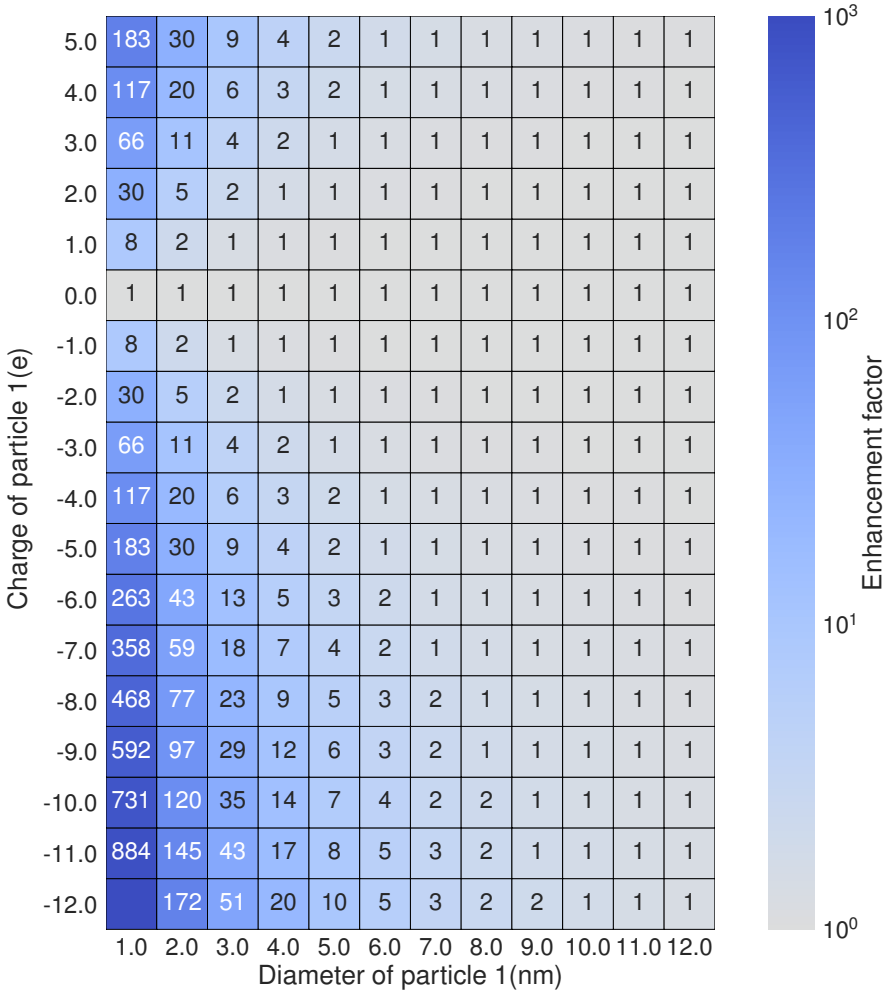

Figure 3.8: Chart of the MCP enhancement factor for small particles 1 and a neutral particle of size $d_2 = 1$ nm.

3.A Derivation of the coagulation kernel

The coagulation rate for two hard spheres is [11]:

$$R = \beta_{ij} n_i n_j, \tag{3.24}$$

where the coagulation kernel β_{ij} is the collision frequency defined as the product of the collection cross-section and the relative velocity of the two spheres,

$$\beta_{ij} = \sigma_{ij} v_{ij}, \tag{3.25}$$

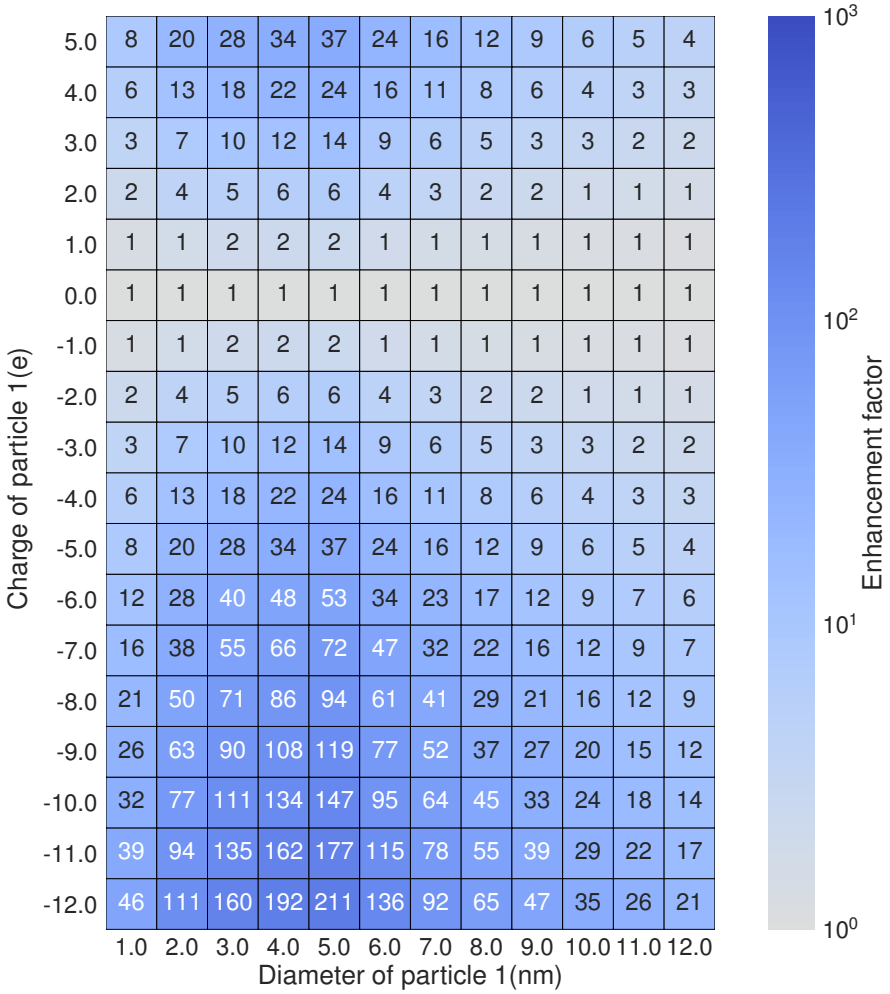

Figure 3.9: Chart of the MCP enhancement factor for small particles 1 and a neutral particle of size $d_2 = 5$ nm.

In this expression, $m_{ij} = m_i m_j/(m_i + m_j)$ is the reduced mass for particles i and j. Suppose that the particle velocity distribution is Maxwellian,

$$f_{ij}(v) = 4\pi v^2 \left(\frac{m_{ij}}{2\pi k_B T}\right)^{3/2} \exp\left(-\frac{m_{ij} v^2}{2k_B T}\right). \tag{3.26}$$

Hence, it is necessary to integrate over all possible velocities,

$$\beta_{ij} = \int_0^\infty v\sigma_{ij}(v) f_{ij}(v) \mathrm{d}v. \tag{3.27}$$

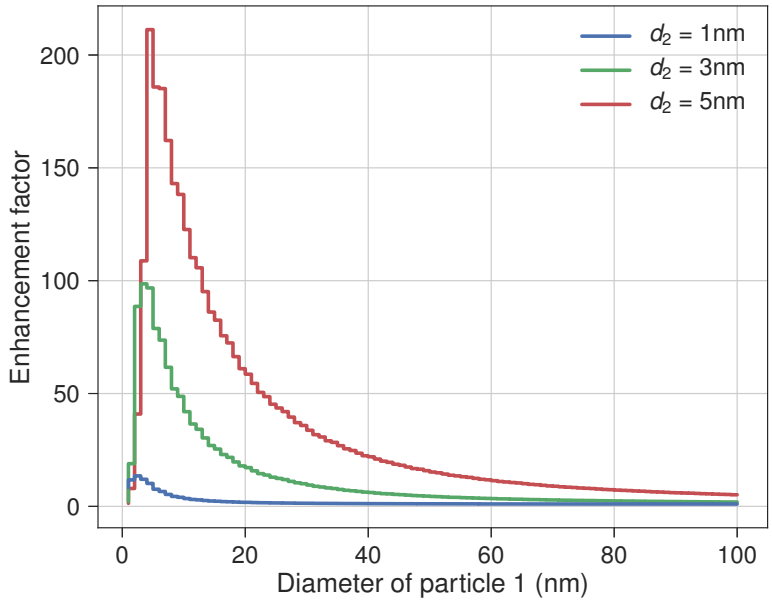

Figure 3.10: MCP enhancement factor as a function of the size of particle 1, with the corresponding equilibrium charge (figure 3.2), interacting with neutral particles 2 of 1, 3 and 5 nm. The steps arise because of the discreteness of the charge and the discretization of the size of particle 1

Furthermore, the collection cross section is obtained in terms of the impact parameter [29] as,

$$\sigma_{ij} = \pi b_{ij}^2, \tag{3.28}$$

In case of a central force, the impact parameter can be derived from laws of conservation of energy and angular momentum [2],

$$b_{ij} = r_{\text{min}} \left(1 - \frac{2\Phi_{ij}(r_{\text{min}})}{m_{ij} v^2}\right)^{1/2}. \tag{3.29}$$

Then, from eq. 3.27 it follows,

$$\beta_{ij} = 4\pi^2 r_{\text{min}}^2 \left(\frac{m_{ij}}{2\pi k_{\text{B}} T}\right)^{3/2} \int_{v_{\text{min}}}^{\infty} \left(1 - \frac{2\Phi_{ij}(r_{\text{min}})}{m_{ij} v^2}\right) \exp\left(-\frac{m_{ij} v^2}{2k_{\text{B}} T}\right) v^3 \text{d}v, \tag{3.30}$$

where v_{min} is given by,

$$v_{\text{min}}^2 = \frac{2\Phi_{ij,\text{max}}}{m_{ij}}, \qquad v_{\text{min}} = \text{Re}\left[\left(\frac{2\Phi_{ij,\text{max}}}{m_{ij}}\right)^{1/2}\right]. \tag{3.31}$$

is the minimum relative velocity required to breach the potential barrier (if such a barrier exists). Rearranging the integral eq. 3.30 gives,

$$\beta_{ij} = \left(\frac{8\pi k_{\text{B}} T}{m_{ij}}\right)^{1/2} (r_i + r_j)^2 \, 2 \int_{\tilde{v}_{\text{min}}}^{\infty} \left(1 - \frac{\Phi_{ij}(r_{\text{min}})}{k_{\text{B}} T v^2}\right) \exp\left(-v^2\right) v^3 \text{d}v, \tag{3.32}$$

with $\tilde{v}_{\min} = \mathrm{Re}\left[\left(\frac{\Phi_{ij,\max}}{k_B T}\right)^{1/2}\right]$. Now it is possible to identify the coagulation kernel for hard spheres as [11],

$$\beta_{ij}^{0} = \left(\frac{8\pi k_B T}{m_{ij}}\right)^{1/2} \left(r_i + r_j\right)^2, \tag{3.33}$$

This result is equivalent to eq. 3.4 but expressed in terms of the radii of the colliding particles. Thus, the enhancement factor is [28]:

$$\eta_{ij} = 2\int_{\tilde{v}_{\min}}^{\infty} \left(1 - \frac{\Phi_{ij}(r_{\min})}{k_B T v^2}\right) \exp\left(-v^2\right) v^3 \mathrm{d}v, \tag{3.34}$$

Finally, after integration, one obtains,

$$\eta_{ij} = \exp\left(-\frac{\Phi_{ij,\max}}{k_B T}\right)\left[1 + \frac{\Phi_{ij,\max} - \Phi_{ij}(r_{\min})}{k_B T}\right]. \tag{3.35}$$

3.B Image Potential Approximation (IPA)

As mentioned in section 3.2.5, using the MCP to compute the enhancement factor is generally time-consuming. Moreover, it is difficult to draw general conclusions from this formulation. Thus, it would be desirable to find an alternative description for the electrostatic interaction which retains most features of the MCP. Draine & Sutin [7] derived the following simple expression for the image potential of a point charge q_j and a sphere of radius r_i and charge q_i,

$$\Phi_{\mathrm{DS}}(r, r_i, q_i, q_j) = K\frac{q_i q_j}{r} - \frac{K\kappa q_j^2 r_i^3}{2r^2\left(r^2 - r_i^2\right)}. \tag{3.36}$$

where $\kappa = (\varepsilon - 1)/(\varepsilon + 2)$. This potential corresponds to the classical Coulomb interaction potential energy plus a correction corresponding to the image potential due to the dielectric nature of the spherical particle.

For the problem of interest here, it is not possible to assume a point charge particle. Therefore, a more suitable expression would include the image potential energy of the nanoparticle i in the nanoparticle j,

$$\Phi_{\mathrm{IPA}}(r, r_i, r_j, q_i, q_j) \equiv \Phi_{\mathrm{IPA,ij}} = K\frac{q_i q_j}{r} - \frac{K\kappa q_i^2 r_j^3}{2r^2\left(r^2 - r_j^2\right)} - \frac{K\kappa q_j^2 r_i^3}{2r^2\left(r^2 - r_i^2\right)}. \tag{3.37}$$

We call this formulation the Image Potential Approximation (IPA). From equation (3.37), it is easy to find an analytical expression for the force $F_{\mathrm{IPA,ij}} = -d\Phi_{\mathrm{IPA,ij}}/dr$ which can be used to find $\Phi_{ij,\max}$, as required to calculate the enhancement factor.

One can see readily that, in the case of spheres of same charge polarity, the IPA eq. 3.37 is composed of a repulsive Coulomb term plus two attractive contributions. As a result, a competition between the long-range Coulomb repulsion and the short-range image potential attraction creates the potential barrier $\Phi_{ij,\max}$, which can be breached only if the nanoparticles have sufficient kinetic energy.

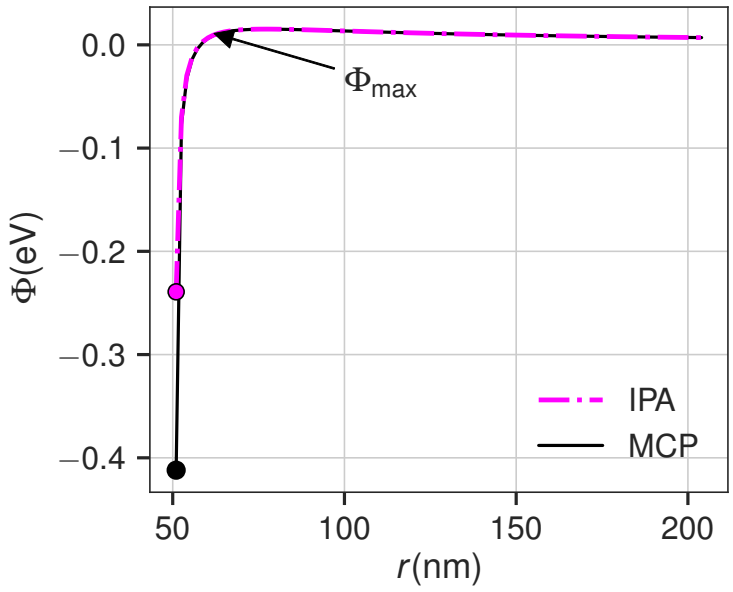

Figure 3.11: Potential energies as a function of the interparticle distance when $r_1 = 1\,\text{nm}$, $r_2 = 50\,\text{nm}$, and $q_1 = q_2 = -e$, where Φ_{max} is the height of the potential barrier.

For the neutral-charged interaction there is no Coulomb contribution; hence enhanced coagulation always takes place.

Fig. 3.11 shows a comparison between the IPA and the MCP in a case where there is a potential barrier whose maximum occurs at $r = r_{\text{max}}$. The IPA nicely reproduces the long-range behavior of the MCP. This is computationally advantageous because the potential barrier can be located using the simple IPA, and then the MCP can be computed at that location, r_{max}. This procedure proves to be 15 to 20 times faster than finding r_{max} directly from the MCP. Figure 3.12 shows the enhancement factor using this hybrid approach: the location of the barrier was determined using the IPA force, and then the height of the barrier and the potential at contact were computed using the MCP formulation. One can hardly see any difference between figures 3.12 and 3.5.

3.C Image Potential Approximation (IPA) Barrier

The purposes of this Appendix are to (i) write out the equation used to calculate r_{max}, i.e., the location of the maximum of the potential, from the IPA prescription, (ii) show graphical solutions in particular cases, and (iii) show that r_{max} is on the order of magnitude of the particles size, and thus much smaller than the Debye length in the conditions stated in table 3.1.

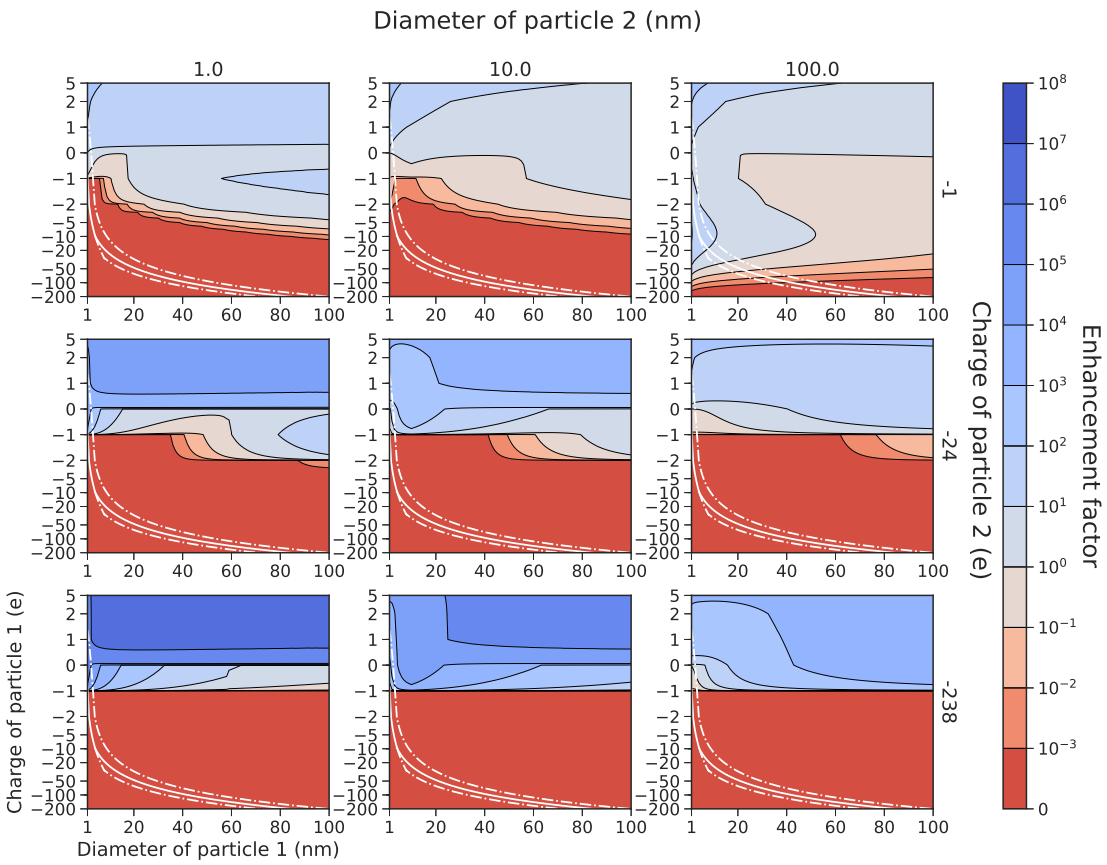

Figure 3.12: Contour levels of the enhancement factor for the hybrid approach for the same values as in figures 3.3 and 3.5. These results are in qualitative agreement with 3.5.

Equation (3.37) can be expressed in the dimensionless form,

$$\hat{\Phi}_{\mathrm{IPA},12} = \frac{q_{21}}{\tilde{r}} - \frac{\kappa r_{21}^3}{2\tilde{r}^2\left(\tilde{r}^2 - r_{21}^2\right)} - \frac{\kappa q_{21}^2}{2\tilde{r}^2\left(\tilde{r}^2 - 1\right)}, \tag{3.38}$$

where $\tilde{r} = r/r_1$, $r_{21} = r_2/r_1$, and $q_{21} = q_2/q_1$. For particles of same polarity $q_{21} > 0$ the associated dimensionless force is,

$$\hat{F}_{\mathrm{IPA},12} = -\frac{\mathrm{d}\hat{\Phi}_{\mathrm{IPA},12}}{\mathrm{d}\tilde{r}}, \tag{3.39}$$

which is equal to zero at the potential barrier located at $\tilde{r} = \tilde{r}_{\max}$,

$$\tilde{r}_{\max} = \kappa \frac{r_{21}^3\left(2\tilde{r}^2 - r_{21}^2\right)}{q_{21}\left(\tilde{r}^2 - r_{21}^2\right)^2}\bigg|_{\tilde{r}=\tilde{r}_{\max}} + \kappa \frac{q_{21}\left(2\tilde{r}^2 - 1\right)}{\left(\tilde{r}^2 - 1\right)^2}\bigg|_{\tilde{r}=\tilde{r}_{\max}}. \tag{3.40}$$

A simple case arises for particles of the same size, i.e., $r_{21} = 1$,

$$\tilde{r}_{\max} = \kappa \frac{\left(1 + q_{21}^2\right)}{q_{21}} \frac{\left(2\tilde{r}_{\max}^2 - 1\right)}{\left(\tilde{r}_{\max}^2 - 1\right)^2}. \tag{3.41}$$

As shown in figure 3.13, the solution of equation (3.41) is the value of $\tilde{r}$ at the intersection between the dotted line (left-hand side of (3.41)) and the full lines (right-hand side of (3.41)) corresponding to

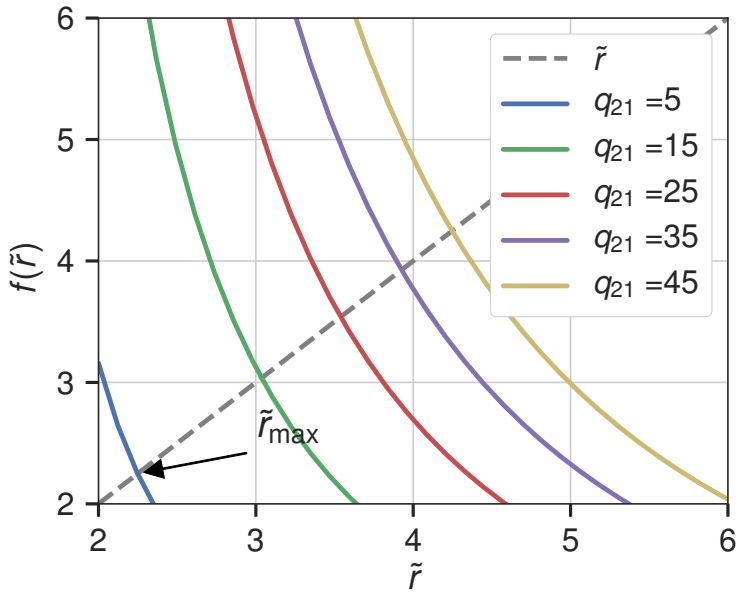

Figure 3.13: Graphical solution of equation eq. 3.41. The intersection of the dashed line and the full lines gives $\tilde{r}_{\max}$ which is near the contact radius $\tilde{r} = 2$.

various values of q_{21}. It can be seen that a solution is found for each value of q_{21} beyond the contact radius $\tilde{r} > 1 + r_{21} = 2$. Figure 3.13 also shows that $\tilde{r}_{\max}$ is on the order of magnitude of the size of the particles and thus close to the contact radius.

The analysis can be repeated for the other simple cases of equally charged spheres $q_{21} = 1$ and different size ratios r_{21}. The graphical solution of equation (3.40) in such cases is shown in figure 3.14. Same as in the previous case where $r_{21} = 1$, the solutions $r_{\max}$ are on the same order of magnitude as the particles size. The same conclusion can be drawn in the case of high charge and size ratios $r_{21} = q_{21} = 50$ as shown in figure 3.15.

The fact that $r_{\max}$ is similar to the particles size is due to the fast decrease in r^{-5} as $(r/r_k)^2 \gg 1$ of the induced polarization force, which must produce a zero of the force at short separation distance, if such a zero is to exist.

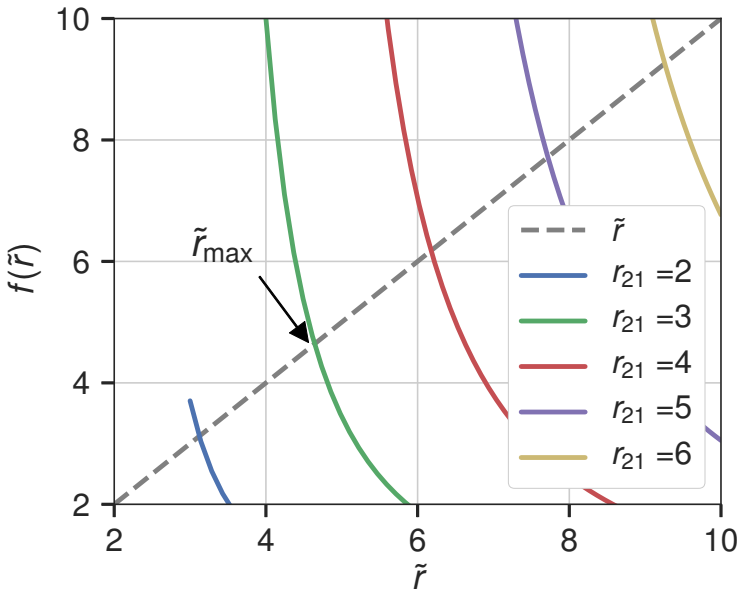

Figure 3.14: Graphical solution of equation eq. 3.40 for equally charged nanoparticles. For the selected charge ratios q_{21}, the solutions $\tilde{r}_{max}$ is near the contact radius $\tilde{r} = 1 + r_{21}$.

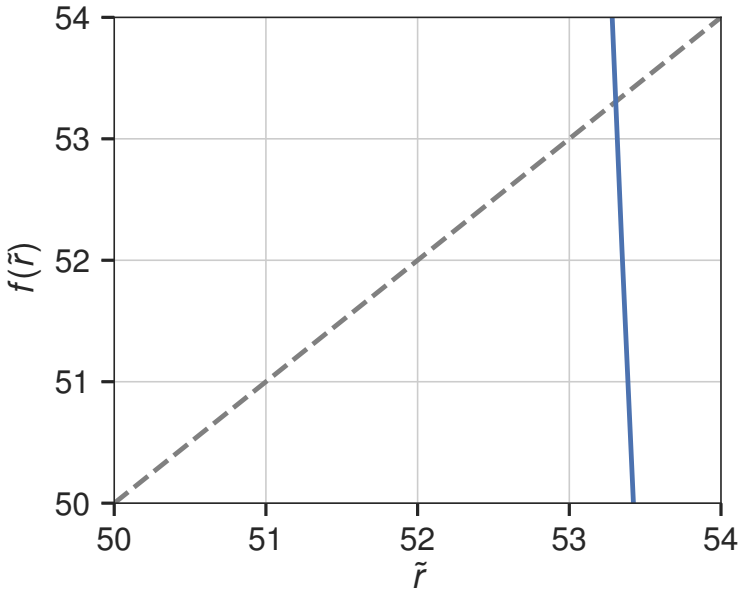

Figure 3.15: Graphical solution of equation eq. 3.40 for high charge and size ratios $r_{21} = q_{21} = 50$.

3.4 References

[1] P. Agarwal and S.L. Girshick. Sectional modeling of nanoparticle size and charge distributions in dusty plasmas. *Plasma Sources Sci. Technol.*, 21(5):055023, October 2012.

[2] J. E. Allen. Probe theory - the orbital motion approach. *Phys. Scr.*, 45(5):497, May 1992.

[3] A. S. Amadon and W. H. Marlow. Cluster-collision frequency. II. Estimation of the collision rate. *Physical Review A*, 43(10):5493–5499, May 1991.

[4] E. Bichoutskaia, A. L. Boatwright, A. Khachatourian, and A. J. Stace. Electrostatic analysis of the interactions between charged particles of dielectric materials. *The Journal of Chemical Physics*, 133(2):024105, July 2010.

[5] L. Boufendi and A. Bouchoule. Particle nucleation and growth in a low–pressure argon–silane discharge. *Plasma Sources Sci. Technol.*, 3(3):262, August 1994.

[6] L. Boufendi, M. Ch Jouanny, E. Kovacevic, J. Berndt, and M. Mikikian. Dusty plasma for nanotechnology. *J. Phys. D: Appl. Phys.*, 44(17):174035, May 2011.

[7] B. T. Draine and Brian Sutin. Collisional charging of interstellar grains. *The Astrophysical Journal*, 320:803, September 1987.

[8] V. E. Fortov, A. V. Ivlev, S. A. Khrapak, A. G. Khrapak, and G. E. Morfill. Complex (dusty) plasmas: Current status, open issues, perspectives. *Physics Reports*, 421(1–2):1–103, December 2005.

[9] V. E. Fortov, A. G. Khrapak, S. A. Khrapak, V. I. Molotkov, and Petrov Petrov. Dusty plasmas. *Physics - Uspekhi*, 47:447–492, 2004.

[10] A. A. Fridman, L. Boufendi, T. Hbid, B. V. Potapkin, and A. Bouchoule. Dusty plasma formation: Physics and critical phenomena. Theoretical approach. *Journal of Applied Physics*, 79(3), February 1996.

[11] S. K. Friedlander. *Smoke, Dust, and Haze: Fundamentals of Aerosol Dynamics*. Oxford University Press, 2000.

[12] M. Gatti and U. Kortshagen. Analytical model of particle charging in plasmas over a wide range of collisionality. *Physical Review E*, 78(4):046402, October 2008.

[13] D. J. Griffiths. *Introduction to Quantum Mechanics*, chapter The WKB Approximation, pages 315–339. Pearson Prentice Hall, Upper Saddle River, NJ, 2nd edition, 2005.

[14] H. C. Hamaker. The London-van der Waals attraction between spherical particles. *Physica IV*, 10:1058, November 1937.

[15] W.M. Haynes. *CRC Handbook of Chemistry and Physics, 97th Edition*. CRC Press, 2016.

[16] L. C. J. Heijmans, F. M. J. H. van de Wetering, and S. Nijdam. Comment on 'The effect of single-particle charge limits on charge distributions in dusty plasmas'. *Journal of Physics D: Applied Physics*, 49(38):388001, 2016.

[17] Ch Hollenstein. The physics and chemistry of dusty plasmas. *Plasma Phys. Control. Fusion*, 42(10):R93, October 2000.

[18] D. D. Huang, J. H. Seinfeld, and K. Okuyama. Image potential between a charged particle and an uncharged particle in aerosol coagulation—enhancement in all size regimes and interplay with van der waals forces. *Journal of colloid and interface science*, 141(1):191–198, 1991.

[19] J. D. Hunter. Matplotlib: A 2d graphics environment. *Computing In Science & Engineering*, 9(3):90–95, 2007.

[20] E. Jones, T. Oliphant, P. Peterson, et al. SciPy: Open source scientific tools for Python, 2001–.

[21] A. Khachatourian, H.-K. Chan, A. J. Stace, and E. Bichoutskaia. Electrostatic force between a charged sphere and a planar surface: A general solution for dielectric materials. *The Journal of Chemical Physics*, 140(7):074107, February 2014.

[22] S. A. Khrapak, S. V. Ratynskaia, A. V. Zobnin, A. D. Usachev, V. V. Yaroshenko, M. H. Thoma, M. Kretschmer, H. Höfner, G. E. Morfill, O. F. Petrov, and V. E. Fortov. Particle charge in the bulk of gas discharges. *Physical Review E*, 72(1):016406, July 2005.

[23] K. Koga, Y. Matsuoka, K. Tanaka, M. Shiratani, and Y. Watanabe. In situ observation of nucleation and subsequent growth of clusters in silane radio frequency discharges. *Applied Physics Letters*, 77(2):196–198, July 2000.

[24] R. Le Picard and S. L. Girshick. The effect of single-particle charge limits on charge distributions in dusty plasmas. *Journal of Physics D: Applied Physics*, 49(9):095201, 2016.

[25] E. B. Lindgren, H.-K. Chan, A. J. Stace, and E. Besley. Progress in the theory of electrostatic interactions between charged particles. *Physical Chemistry Chemical Physics*, 18(8):5883–5895, February 2016.

[26] J. Maddock, P. Bristow, H. Holin, X. Zhang, B. Lalande, J. Rade, G. Sewani, and T. Van Den Berg. *Boost C++ Math Toolkit*. hetp, 2009.

[27] M. Mamunuru, R. Le Picard, Y. Sakiyama, and S. L. Girshick. The Existence of Non-negatively Charged Dust Particles in Nonthermal Plasmas. *Plasma Chem Plasma Process*, 37(3):701–715, May 2017.

[28] H. Ouyang, R. Gopalakrishnan, and C. J. Hogan Jr. Nanoparticle collisions in the gas phase in the presence of singular contact potentials. *The Journal of Chemical Physics*, 137(6):064316, August 2012.

[29] A. Piel. *Plasma Physics - An Introduction to Laboratory, Space, and Fusion Plasmas*. Springer Berlin Heidelberg, January 2010.

[30] A. Priye and W. H. Marlow. Computations of Lifshitz–van der Waals interaction energies between irregular particles and surfaces at all separations for resuspension modelling. *J. Phys. D: Appl. Phys.*, 46:425306, 2013.

[31] L. Ravi and S. L. Girshick. Coagulation of nanoparticles in a plasma. *Phys. Rev. E*, 79(2):026408, February 2009.

[32] P. Shukla. Colloquium: Fundamentals of dust-plasma interactions. *Rev. Mod. Phys.*, 81(1):25–44, 2009.

[33] A. J. Stace and E. Bichoutskaia. Reply to the 'Comment on "Treating highly charged carbon and fullerene clusters as dielectric particles"' by H. Zettergren and H. Cederquist, Phys. Chem. Chem. Phys., 2012, 14, DOI: 10.1039/c2cp42883k. *Physical Chemistry Chemical Physics*, 14(48):16771–16772, November 2012.

[34] Y. Watanabe. Formation and behaviour of nano/micro-particles in low pressure plasmas. *J. Phys. D: Appl. Phys.*, 39(19):R329–R361, September 2006.

[35] Y. Watanabe, M. Shiratani, H. Kawasaki, S. Singh, T. Fukuzawa, Y. Ueda, and H. Ohkura. Growth processes of particles in high frequency silane plasmas. *Journal of Vacuum Science & Technology A*, 14(2):540–545, March 1996.

[36] Y. Watanabe, M. Shiratani, and K. Koga. Nucleation and subsequent growth of clusters in reactive plasmas. *Plasma Sources Sci. Technol.*, 11(3A):A229, August 2002.

4 Influence of multipolar electrostatic and van der Waals forces on the coagulation of silicon nanoparticles in low-temperature argon-silane plasmas.

Numerical calculations have been performed to investigate the effects of electrostatic and van der Waals interactions on coalescing silicon nanoparticles in isotropic low-temperature argon-silane plasmas. The electrostatic interaction between nanoparticles is modeled using three approaches, including the elementary Coulomb interaction, a rigorous electrostatic multipolar expansion, and an approximate form of the latter. The van der Waals interaction is described using the Hamaker expression regularized at short separation distance to manage the singularity at the contact surface. The evolution of the size and charge distributions are calculated by solving the general dynamic equation numerically for the coagulation of charged particles and using simplified approaches for nucleation, surface growth, and self-consistent plasma dynamics. A two-population size distribution, as observed in experiments, results naturally from this model. The electrostatic multipolar force is found to enhance the coagulation as compared to the elementary Coulomb force. The details of the growth process depend, however, significantly on the adopted regularization of the Hamaker expression at a short distance.

Keywords: coagulation, agglomeration, nanoparticles, low-temperature plasmas, multipolar electrostatics, van der Waals

Influence de la force multipolaire electrostatique et la force de van der Waals dans la coagulation de nanoparticules de silicium en plasmas froids d'argon silane

Auteurs

Benjamin Santos[1] et François Vidal[1]

[1] INRS - Énergie Matériaux Télécomunications, Varennes, QC J3X 1P7, Canada

Plasma Sources Science and Technology

Article journal

`https://doi.org/10.1088/1361-6595/ab85b5`

April, 2020

Résumé traduit

Des calculs numériques ont été effectués pour étudier les effets des interactions électrostatiques et de

van der Waals sur la coagulation des nanoparticules de silicium dans les plasmas froids d'argon-silane. L'interaction électrostatique entre les nanoparticules est approximée à l'aide de trois approches, dont l'interaction coulombienne élémentaire, une expansion multipolaire électrostatique et une forme approximative de cette dernière. L'interaction de van der Waals est décrite en utilisant l'expression de Hamaker à courte distance de séparation pour gérer la singularité à la surface de contact. L'évolution des distributions de taille et de charge est calculée en résolvant numériquement l'équation dynamique générale et les densités d'espèces du plasma de façon auto-cohérente. On trouve que la force multipolaire électrostatique augmente la coagulation par rapport à la force coulombienne élémentaire. Cependant, les détails du processus de croissance dépendent fortement de la régularisation adoptée pour l'expression de Hamaker à courte distance.

Keywords: coagulation, agglomeration, nanoparticules, plasmas froids, électrostatique multipolaire, force de van der Waals

4.1 Introduction

Coagulation of particles in plasmas is a topic of fundamental interest in dusty plasma physics [36, 19, 18, 34, 10]. The growth of silicon nanoparticles in low-temperature radio-frequency capacitively coupled plasmas (RF-CCP) in an argon-silane (Ar-SiH_4) mixture begins with nucleated protoparticles [6, 15, 7]. Then, when a critical density is reached, it starts the coagulation phase. As nanoparticles coagulate, they increase in size, and their number density decreases. In the final stage, the surface growth, where molecules stick on the surface of the nanoparticles, becomes the primary growth process. At this stage, particles can grow up to several micrometers in size.

Nucleation, coagulation, charging, and surface growth are the processes which determine the size evolution of nanoparticles in plasmas. These can be simulated altogether by solving the general dynamic equation (GDE), also called the population balance equation (PBE). This approach was used in several theoretical works related to the growth of nanoparticles in plasmas. For instance, Kortshagen *et al.* developed an isotropic (0-D) model including a detailed argon-silane plasma chemistry model coupled with the GDE [19, 4, 3]. De Bleecker *et al.* worked out a 1-D acetylene plasma model with transport and considered the drag and electric forces exerted on the nanoparticles [8]. Girshick *et al.* developed 1-D and 2-D models coupling the argon-silane plasma to the nanoparticle growth processes [43, 34, 1, 23].

The coagulation rate, R_{jpmq}, between a particle of size j and charge p, and a particle of size m and charge q can be expressed as the coagulation rate for neutral random-walking spheres sticking at contact, R^0_{jpmq}, times the enhancement factor, η_{jpmq}, which depends on the forces acting between particles [1],

$$R_{jpmq} = \eta_{jpmq} R^0_{jpmq}. \tag{4.1}$$

These forces are essentially the van der Waals (vdW) and electrostatic forces. The latter result from charges acquired by the nanoparticles through electron and ion collisions in the plasma. Their overall charge is negative due to the greater mobility of electrons as compared to ions. For small

particles, electrons can escape from the surface due to the tunnel current [13], reducing the electron collection rate and increasing the probability of forming neutral and positively charged particles. Since nanoparticles are finite size objects, polarization-induced effects can take place in addition to the elementary Coulomb interaction. In the context of aerosol physics, Huang *et al.* introduced the electrostatic material-dependent interaction through the image potential method to take into account the polarization effects. They then combined this electrostatic potential with the vdW interaction through the Hamaker expression to calculate the enhancement factor [16]. Thereafter, a series of works from Girshick *et al.* [34, 1, 23] adopted the approach of Huang *et al.* to simulate the growth of silicon nanoparticles in argon-silane plasmas but neglecting the vdW interaction.

Recently, we derived the enhancement factor for an electrostatic multipolar coefficient potential (MCP) [5] which provides a more rigorous description of the electrostatic interaction between dielectric particles than that of Huang *et al.* [35]. In particular, in contrast to the latter approach, the MCP does not suffer from an unphysical singularity at the contact point. This property allowed us to use the well-established orbital motion limited (OML) theory [2] to calculate the enhancement factor. Besides the MCP, we investigated an approximate and simplified form of it, named the image potential approximation (IPA), which proves more convenient than the MCP for numerical calculations. We showed that the MCP and IPA enhance the attraction between nanoparticles through induced polarization as compared to the elementary Coulomb interaction. Polarization effects in the coagulation of dust particles have also been investigated in the context of astrophysical dusty plasmas by Matthews *et al.* [30, 28, 29]. They performed self-consistent N-body simulations of the coagulation of fractal aggregates of micrometric size bearing a few electrical charges and they found that oppositely charged dust particles significantly enhance coagulation rates when compared to like charged or neutral particles as a consequence of dipole-dipole interaction. Interesting consequences have been drawn on the mechanisms of planet formation.

In this work, we solved the GDE for an isotropic dusty plasma to investigate the time evolution of the nanoparticle size and charge by using the electrostatic MCP, IPA, and Coulomb potential as well as the vdW interaction as given by the Hamaker potential [12]. The latter arises from the fluctuating dipolar moments of the molecules in spherical particles. The local dipole-dipole interaction underlying Hamaker's result produces a singularity of the form $\sim r^{-1}$ at the contact point, where r is the shortest distance between the surfaces of spherical particles. However, it has been shown that a proper derivation of the vdW interaction that includes nonlocal effects leads to a finite value of the vdW potential at the contact point [25]. Despite the valuable efforts made to go beyond Hamaker's result, in this work, we adopt the more straightforward approach of regularizing the Hamaker potential by assuming that the latter is constant for $r \leq r_c$, leaving r_c as a parameter to investigate. In addition to the complexity of including nonlocal (and retardation effects [31]) in the vdW interaction, we justify this simpler approach by considering that the actual nanoparticles have an undetermined surface roughness [37] which softens the vdW potential near the contact point [33]. Such an investigation focusing on the

influence of the fundamental forces on particle growth in plasmas has, to the best of our knowledge, never been done so far.

This article is organized as follows. First, in section 4.2.1, we present the GDE and discuss the models adopted for the various terms. Numerical results are discussed in section 4.3. Finally, the conclusions are presented in section 4.4. Computational and numerical details are given in 4.A. Details about the MCP and IPA are given in 4.B. A discussion of the effects of the tunnel current on the charge distribution is given in 4.C. Finally, in 4.D, a study of the influence of nucleation and surface growth rates is reported.

4.2 Methods

4.2.1 Nanoparticle growth and charging

The modeling of particle growth starts with the GDE for a dusty plasma, which expresses the rate of change of the dust particle density of size i and charge k [1]:

$$\frac{\partial N_{i,k}}{\partial t} + \nabla \cdot \Gamma_{i,k} = \left[\frac{\mathrm{d}N_{i,k}}{\mathrm{d}t}\right]_{\text{coag}} + \left[\frac{\mathrm{d}N_{i,k}}{\mathrm{d}t}\right]_{\text{charging}} + \left[\frac{\mathrm{d}N_{i,k}}{\mathrm{d}t}\right]_{\text{nuc}} + \left[\frac{\mathrm{d}N_{i,k}}{\mathrm{d}t}\right]_{\text{growth}}. \tag{4.2}$$

In this expression, $N_{i,k}$ is the particle number density, expressed as the number of particles per unit volume (m^{-3}) and $\Gamma_{i,k}$ is the local spatial flux. The four terms on the right-hand side represent coagulation, charging, nucleation, and surface growth, respectively. In what follows, we set $\nabla \cdot \Gamma_{i,k} = 0$ since we neglect losses of nanoparticles at the reactor boundaries to focus on the four terms on the right side of (4.2). This approximation mainly concerns neutral and positively charged particles since the negatively charged particles are confined by the plasma sheaths.

Coagulation occurs when two nanoparticles collide and adhere to form a new particle with a volume equal to the sum of those of the two primary particles. The Smoluchowski equation describes the coagulation rate. To solve this equation numerically, we used the fixed-pivot technique [21] for the volume along with an exact computation for the charges. This hybrid approach is more accurate than a two-component fixed-pivot [42] as it avoids sectionalizing the charge, which is an integer value in units of the elementary charge. Partitioning the volume v in M sections, and considering upper bounds for negative and positive charges, $q_{\min}$ and $q_{\max}$, respectively, the discretized form of the Smoluchowski equation reads,

$$\left[\frac{\mathrm{d}N_{i,k}}{\mathrm{d}t}\right]_{\text{coag}} = \frac{1}{2} \sum_{\substack{\tilde{v}_{i-1} \le v < \tilde{v}_{i+1} \\ p+q=k}} \xi_i K_{jpmq} N_{jp} N_{mq} - N_{ik} \sum_{p=-q_{\min}}^{q_{\max}} \sum_{m=1}^{M} K_{ikmp} N_{mp}. \tag{4.3}$$

where the indices j, m, p, and q run over their whole range of values in the first sum. In these equations, K is the coagulation kernel in $\mathrm{m}^3\mathrm{s}^{-1}$, $v = \tilde{v}_j + \tilde{v}_m$ is the coalesced volume, $\tilde{v}_i$ is the representative

volume included in section i, which is defined by the interval $\left[\frac{1}{2}(\tilde{v}_{i-1}+\tilde{v}_i), \frac{1}{2}(\tilde{v}_i+\tilde{v}_{i+1})\right]$, and the weighting factor,

$$\xi_i = \begin{cases} \frac{\tilde{v}_{i+1}-v}{\tilde{v}_{i+1}-\tilde{v}_i}, & \tilde{v}_i \leq v \leq \tilde{v}_{i+1} \\ \frac{v-\tilde{v}_{i-1}}{\tilde{v}_i-\tilde{v}_{i-1}}, & \tilde{v}_{i-1} \leq v \leq \tilde{v}_i \end{cases}, \tag{4.4}$$

is used to conserve the total volume fraction by distributing the new particles among adjacent sections [21].

Nanoparticle charging is linked to the plasma via the collision frequencies of electrons, ν_e, and positive ions, ν_+, with nanoparticles as given by the OML theory [35]. Furthermore, the tunnel frequency ν_T is necessary to describe electrons that escape the affinity potential well [13, 35]. The rate of charging can be expressed as,

$$\begin{aligned}\left[\frac{\mathrm{d}N_{i,k}}{\mathrm{d}t}\right]_{\text{charging}} &= \left(\nu_{+(i,k-1)} + \nu_{T(i,k-1)}\right) N_{i,k-1} + \nu_{e(i,k+1)} N_{i,k+1} \\ &\quad - \left(\nu_{+(i,k)} + \nu_{T(i,k)} + \nu_{e(i,k)}\right) N_{ik},\end{aligned} \tag{4.5}$$

where the frequencies ν_e, ν_+, and ν_T are given in [35]. This model relates to the master equation of a one-step Markov process, where the charging currents depend on the instantaneous charge but not on the prior history [27, 38].

Nucleation is the formation of the smallest nanoparticles by silane-plasma chemistry. Therefore nucleation feeds only the first (smallest) volume section. In this study, which focuses on the coagulation process, we follow [1] and assume that the nucleation rate takes the constant value $J_{00} = 10^{18}$ m^{-3} s^{-1}. Thus, the nucleation rate is expressed as,

$$\left[\frac{\mathrm{d}N_{i,k}}{\mathrm{d}t}\right]_{\text{nuc}} = \delta_{i,0}\delta_{k,0}J_{00}, \tag{4.6}$$

where δ is the Kronecker delta function.

Finally, the surface growth process is calculated consistently with the sectional model, represented by (4.3-4.4), by the two-point formulae,

$$\left[\frac{\mathrm{d}N_i}{\mathrm{d}t}\right]_{\text{growth}} = \frac{I_{i-1}N_{i-1}}{v_i - v_{i-1}} - \frac{I_i N_i}{v_{i+1} - v_i}. \tag{4.7}$$

In this expression, $I_i = A_i L_g$ where A_i is the representative area of the nanoparticle and L_g is the linear growth rate which, following [1], we set to $L_g = 12\,\mathrm{nm\,s^{-1}}$. A study of the influence of the parameters J_{00} and L_g on the particle growth as a function of time is given in 4.D.

4.2.2 Electrostatic and van der Waals interactions

The coagulation kernel for particles in plasma in the low-pressure regime can be expressed as the product $K_{jmpq} = \eta_{jmpq}\beta^0_{jm}$ where η_{jmpq} is the enhancement factor (see (4.1)) which takes into account the

interactions between the nanoparticles, and β_{jm}^0 is the coagulation rate coefficient for neutral particles in the free molecular regime [9],

$$\beta_{jm}^0 = \left(\frac{3}{4\pi}\right)^{1/6} \left[\frac{6k_\mathrm{B}T}{\rho_p}\left(\frac{1}{v_j}+\frac{1}{v_m}\right)\right]^{1/2} \left(v_j^{1/3}+v_m^{1/3}\right)^2, \tag{4.8}$$

Here, $\rho_p = 2330\,\mathrm{kg/m^3}$ is the mass density of silicon and T is the heavy plasma particle temperature. The enhancement factor, η_{jpmq}, depends on the electrostatic and van der Waals interactions. Within the framework of the Orbital Motion Limited (OML) theory [2] it reads [35],

$$\eta_{jpmq} = \exp\left(-\frac{\Phi_{jpmq}^{\max}}{k_\mathrm{B}T}\right)\left[1+\frac{\Phi_{jpmq}^{\max}-\Phi_{jpmq}(r_{\min})}{k_\mathrm{B}T}\right]. \tag{4.9}$$

In this expression, $r_{\min} = r_j + r_m$ is the distance between the centers of the spherical particles (j,p) and (m,q), of radius (charge number) r_j (z_p) and r_m (z_q), respectively, when they are in contact, and $\Phi_{jpmq}^{\max}$ is the maximum value of the interparticle potential. As in a previous work [35], here we calculate the enhancement factor for three electrostatic potentials, namely Coulomb, the MCP [5], and IPA [35]. The Coulomb potential describes the interaction between charged spheres without taking into account induced polarization due to their finite size and dielectric nature. The MCP includes Coulomb and a rigorous description of induced polarization, while the IPA is an approximate and simpler form of the MCP, which is more convenient for numerical calculations. The expressions of the MCP and IPA are given in Appendix B.

In addition to the electrostatic interaction, we consider the vdW interaction in the Hamaker form [12],

$$\Phi_{\mathrm{vdW}}(\tilde{r}, r_{mj}) = -\frac{A_H}{6}\left\{\frac{2r_{mj}}{\tilde{r}^2-(1+r_{mj})^2}+\frac{2r_{mj}}{\tilde{r}^2-(1-r_{mj})^2}+\ln\left[\frac{\tilde{r}^2-(1+r_{mj})^2}{\tilde{r}^2-(1-r_{mj})^2}\right]\right\}, \tag{4.10}$$

where A_H is the Hamaker constant, which is $A_H \approx 20\times10^{-20}\,\mathrm{J}$ for silicon [17], $r_{mj} = {}^{r_m}\!/_{r_j}$ and $\tilde{r} = {}^{1+r_{mj}+r}\!/_{r_j}$, with r the distance between the surfaces of the interacting particles. As can be shown easily, (4.10) has a singularity of the form $\sim r^{-1}$ near the theoretical contact distance $r = 0$. As mentioned above, a more accurate calculation taking into consideration nonlocal effects was shown to give a finite value at contact [25]. The unphysical singularity of (4.10) translates in an infinite enhancement factor through $\Phi_{jpmq}(r_{\min})$ in (4.9). To circumvent this problem, we instead use a vdW potential regularized at short separation distance as,

$$\tilde{\Phi}_{\mathrm{vdW}}(\tilde{r}, r_{mj}) = \begin{cases} \Phi_{\mathrm{vdW}}(\tilde{r}, r_{mj}), & r > r_c \\ \Phi_{\mathrm{vdW}}(\tilde{r}_c, r_{mj}), & r \le r_c, \end{cases} \tag{4.11}$$

where $\tilde{r}_c = {}^{1+r_{mj}+r_c}\!/_{r_j}$ and r_c is a free parameter whose influence has to be investigated. As a lower bound for r_c, we use twice the minimum surface roughness of a spherical silicon nanoparticle, which we estimate as the empirical radius of the silicon atom $R_{\mathrm{Si}} \approx 1.1$Å. Therefore we will consider $r_c \geq 2R_{\mathrm{Si}} = 2.1$Å.

Table 4.1: Set of reactions and rate coefficient for the plasma model. The BOLSIG+ rate constants were obtained from the referred cross-sections and fitted to the Arrhenius form $k(\varepsilon) = A\varepsilon^{\beta}\exp(-\epsilon/\varepsilon)$ for reactions 2-4 and 6-11 and, for reactions 1 and 5, to $k(\varepsilon) = A(1-\exp(-\varepsilon/\beta))$, where ε is the mean electron energy.

Name / Cross section reference	Reaction	Coefficients $A(\mathrm{m^3s^{-1}})$	β	ϵ(eV)
1. Elastic [39]	$Ar + e \longrightarrow Ar + e$	1.856×10^{-13}	1/0.1633	–
2. Ionization [39]	$Ar + e \longrightarrow Ar^+ + 2e$	7.415×10^{-14}	0.005	15.8
3. Excitation [39]	$Ar + e \longrightarrow Ar^* + e$	3.365×10^{-14}	3.76×10^{-9}	11.5
4. Metastable ioniz. [39]	$Ar^* + e \longrightarrow Ar^+ + 2e$	1.912×10^{-13}	2.619×10^{-3}	4.2
5. Elastic [39]	$SiH_4 + e \longrightarrow SiH_4 + e$	2.663×10^{-13}	1/0.2773	–
6. Diss. ionization [20]	$SiH_4 + e \longrightarrow SiH_3^+ + H + 2e$	3.687×10^{-14}	7.585×10^{-9}	12.3
7. Dissociation [39]	$SiH_4 + e \longrightarrow SiH_3 + H + e$	1.061×10^{-13}	0.077 97	8.4
8. Dissociation [39]	$SiH_4 + e \longrightarrow SiH_2 + 2H + e$	8.999×10^{-14}	9.92×10^{-10}	7.7
9. Ionization [41]	$SiH_3 + e \longrightarrow SiH_3^+ + 2e$	4.700×10^{-14}	0.163	8.0
10. Vibrational [39]	$SiH_4 + e \longrightarrow SiH_4^{v13} + e$	5.257×10^{-15}	7.676×10^{-9}	0.27
11. Vibrational [39]	$SiH_4 + e \longrightarrow SiH_4^{v24} + e$	9.647×10^{-15}	1.557×10^{-8}	0.113
12. Metastable [22]	$SiH_4 + Ar^* \longrightarrow SiH_3 + H + Ar$	1.4×10^{-16}	–	–
13. Metastable [22]	$SiH_4 + Ar^* \longrightarrow SiH_2 + 2H + Ar$	2.6×10^{-16}	–	–
14. Metastable [22]	$SiH_3 + Ar^* \longrightarrow SiH_2 + H + Ar$	1.0×10^{-16}	–	–
15. Metastable [22]	$SiH_2 + Ar^* \longrightarrow SiH + H + Ar$	1.0×10^{-16}	–	–

4.2.3 Argon-silane plasma

To compute the plasma evolution coupled to the nanoparticles charging, we used a reduced isotropic plasma model [24, 32] which retains some essential features of argon-silane plasmas such as Ar and SiH_4 excitation and ionization, and silane dissociation into SiH_3 and SiH_2. The model is composed of the 11 species e, Ar^+, Ar*, $SiH_3{}^+$, SiH_2, SiH_3, SiH_4, SiH_4^{v13}, SiH_4^{v24}, H and Ar, where Ar* stands for the close $^1S_5$ (11.55 eV) and $^1S_3$ (11.72 eV) metastable states of Ar, and of 15 reactions whose rate coefficients were obtained from cross-section data and the electron energy distribution function calculated by the software BOLSIG+ [11] and from the literature for the Ar* deexcitation. These are detailed in table 4.1.

The densities of Ar and SiH_4 are assumed to be constant due to their large abundance while the densities of the remaining species, except $SiH_3{}^+$, were computed by solving the system of differential equations,

$$\frac{\mathrm{d}n_\alpha}{\mathrm{d}t} = \sum_i k_i a_i n_\gamma n_{\gamma'} + G_\alpha - S_\alpha, \tag{4.12}$$

where α identifies the species, k_i is the rate of the reaction i between the species γ and γ' which produce a_i number of α species, and G_α and S_α are the gain and loss rates per unit volume of the species α, respectively. To ensure the exact plasma neutrality, we computed the $SiH_3{}^+$ density after each time step from the global charge balance equation, including ions, electrons, and nanoparticles.

The term G_α describes electrons gain by tunneling. For electrons and ions, the term S_α includes losses to nanoparticles due to charging [43]. For all species, S_α also includes particle losses to the boundaries of the plasma reactor. For such losses, $S_\alpha \approx \Gamma_\alpha A_r/V_r$ where Γ_α is the particle flux to the boundaries, $A_r = 2\pi RL$ is the area of the cylindrical reactor of radius R, L is the spacing between the electrodes of the capacitive discharge, and $V_r = \pi R^2 L$ is the volume of the reactor. For charged particles, $\Gamma_\alpha = h_i n_i u_B$, where $h_i = (\sqrt{3 + L/2\lambda_i})^{-1}$ is a geometric factor, λ_i is the mean free path, and u_B is the Bohm velocity. For neutral species, $\Gamma_\alpha = h_\alpha n_\alpha v_T/4$, where v_T is the thermal velocity, the geometric factor is $h_\alpha = (1 + (L/2)v_T/(4D_\alpha))^{-1}$, and D_α is the diffusion coefficient.

The plasma is sustained by injecting the power density P_ε through the following rate equation for the mean electron energy density $n_\varepsilon = \varepsilon n_e$, where ε is the average electron energy,

$$\frac{\mathrm{d}n_\varepsilon}{\mathrm{d}t} = \frac{P_\varepsilon}{V_r} - n_e \sum_i \varepsilon_i k_i a_i n_\gamma - S_\varepsilon. \tag{4.13}$$

In this expression, ε_i is the energy lost by an electron after the reaction i with the species γ. For elastic collisions $\varepsilon_\mathrm{i} = 3\varepsilon m_e/m_\gamma$. The loss term S_ε includes the power density transferred to the nanoparticles by collecting electrons and that associated to the loss of electrons to the electrodes $\Gamma_\varepsilon A_r/V_r$ where,

$$\Gamma_\varepsilon = u_B \left(\frac{5}{3} n_\varepsilon + eV_s n_e\right). \tag{4.14}$$

In this expression, $V_s = V_\mathrm{peak}/4$ where V_peak is the peak voltage of the RF source.

This reduced plasma model allowed obtaining the electron, ion, and tunnel frequencies required to compute nanoparticle charging as indicated by (4.5).

4.3 Results and discussion

In this section, we investigate successively the influence of the electrostatic interaction alone on the particle growth and the influence of the combined electrostatic and vdW interactions. The following results have been obtained using the smallest particle diameter (first volume section) of $d_0 = 0.75\,\mathrm{nm}$, and the geometric progression $v_{i+1} = 1.1599 v_i$ for the volume sections. The GDE (4.2), is discretized using finite differences with $M = 100$ volume sections and $q_\mathrm{min} = -60e$ and $q_\mathrm{max} = +5e$ charges. The reactor dimensions are $L = 4\,\mathrm{cm}$, $R = 6\,\mathrm{cm}$, with volume $V_r = \pi R^2 L$. The pressure is $p = 0.1\,\mathrm{Torr}$ and the temperature is $T = 300\,\mathrm{K}$. The argon-silane gas is mixed with the ratio $\mathrm{Ar{:}SiH_4} = 30{:}1$. The peak voltage is $V_\mathrm{peak} = 100\,\mathrm{V}$, while the power injected is held to $2210\,\mathrm{W}$. Details about the numerical calculations are provided in 4.A.

4.3.1 Electrostatic interaction

We consider two cases: 1) only coagulation and charging, and 2) the full growth model, which includes nucleation, coagulation, charging, and surface growth. The same argon-silane plasma model is used

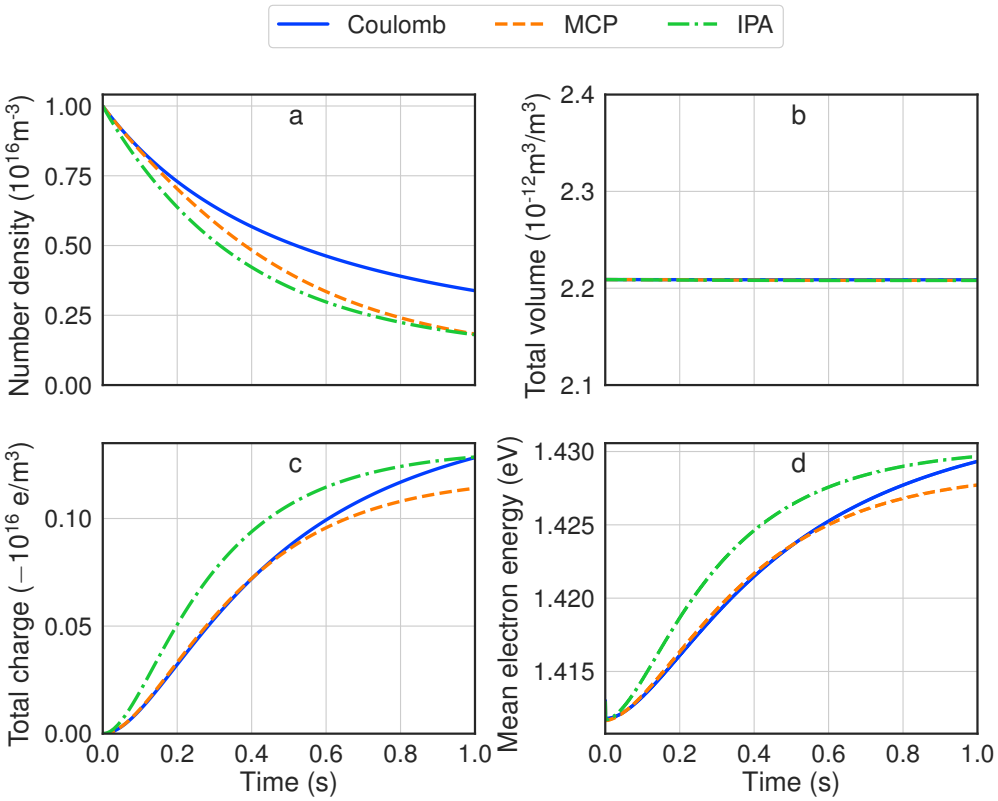

Figure 4.1: Effect of the MCP, IPA, and Coulomb potentials on the nanoparticle (a) number density, (b) total volume fraction, (c) total charge density, and (d) electron mean energy as a function of time. Only coagulation and charging are included in the particle growth model. The number density decreases as a consequence of coagulation. The constant volume validates the methods implemented as coagulation conserves volume.

in both cases. The first case aims to validate the calculation method and to focus on the effects of coagulation and charging.

In figure 4.1, we compare the effects of the three electrostatic potential models: Coulomb, MCP, and IPA for the initial neutral nanoparticle density 10^{16} m^{-3} placed in the lowest volume section. For coagulation to take place on a time scale on the order of 1 s, it is necessary to start with a sufficiently high density of nucleated particles. As expected, coagulation decreases the number of particles, while their total volume fraction remains constant. One can see that the number density decreases faster for the MCP and IPA than for the Coulomb potential. This is due to the polarization-induced attraction involved by MCP and IPA, which enhances coagulation. Defining the characteristic coagulation time τ_{coag} as the time needed to reduce the nanoparticle density by half, one finds that τ_{coag} takes the values 0.38 s, 0.31 s and 0.52 s for MCP, IPA, and Coulomb, respectively, in agreement with the trends observed in figure 4.1. In all cases, the total negative charge density is very low because particles did not grow much during the time interval considered. As is well known, at equilibrium nanoparticles

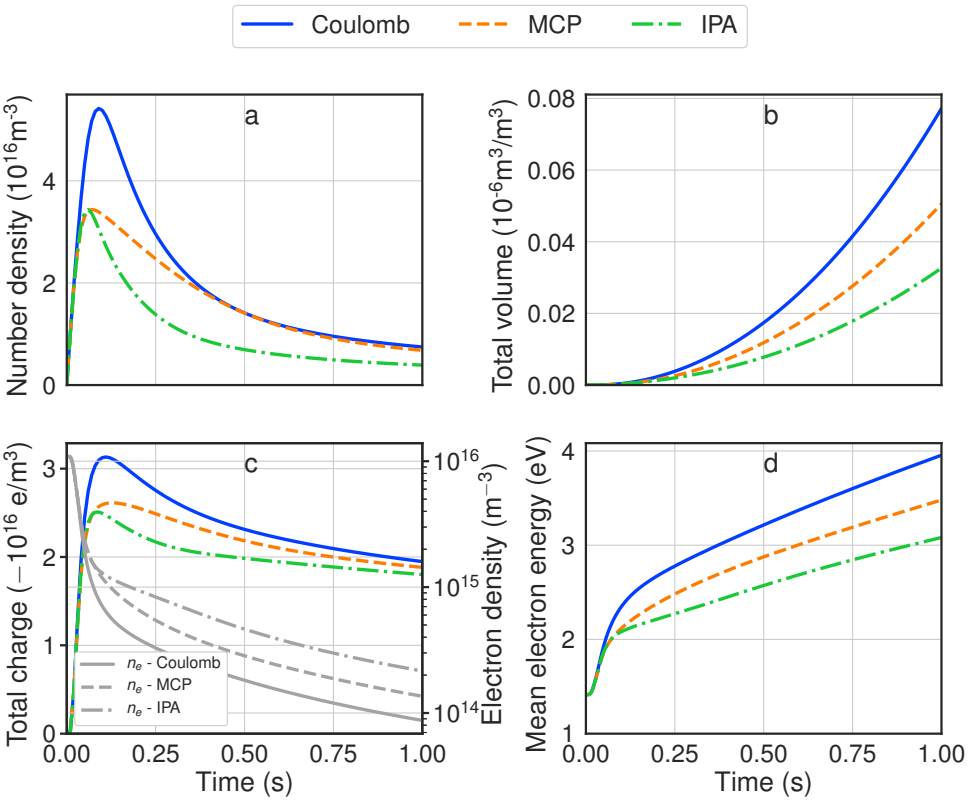

Figure 4.2: Effect of the the MCP, IPA, and Coulomb potentials on the nanoparticle (a) number density, (b) total volume fraction, (c) total charge density and electron densities, and (d) electron mean energy as a function of time. Calculations were made using the full growth model.

carry a charge proportional to their diameter [24]. In the present case, the small nanoparticles of ~ 1 nm diameter can carry only a few negative or positive charges (or no charge), positive charges arising due to the ion current, whereas the tunnel current lowers the negative charges in nanoparticles. The electron mean energy increases only slightly because the low charge density of the nanoparticles has little influence on the plasma electron density.

The second case is illustrated in figure 4.2, where we compare the effects of the three electrostatic potential models on the nanoparticle growth using an initial neutral particle density of 10^{10} m^{-3} placed in the lowest volume section. As can be seen in figure 4.2, the total volume fraction of the particles now increases in time due to continuous nucleation and surface growth. The particle density increases initially and reaches a maximum before stabilizing to a lower value. This behavior is explained by the fact that the initial particle density is insufficient to trigger significant coagulation. As the small particle density increases due to nucleation, the coagulation rate increases and eventually becomes greater than the nucleation rate, leading to a decrease in the particle density. This acceleration of the coagulation rate is partly due to the greater coagulation efficiency between bigger particles and particles of different sizes, as reflected by β^0_{jm} in (4.8) (see also figure 1 in [35]). Later, as particles become bigger, they

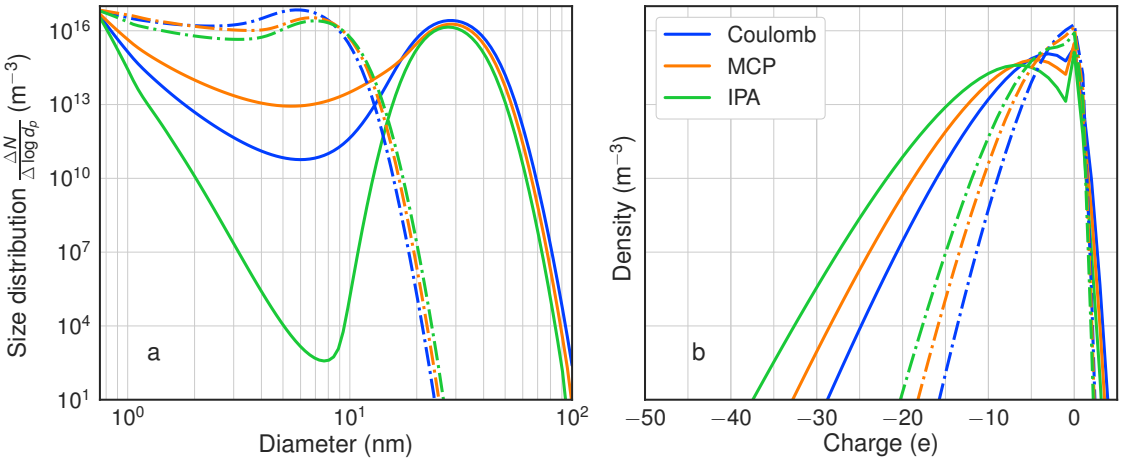

Figure 4.3: Nanoparticle distributions at 0.2 s (dash-dotted lines) and 1.0 s (solid lines), considering the full growth model for the MCP, IPA, and Coulomb potentials without the vdW interaction. a) Particle size distribution $\frac{\Delta N}{\Delta \log d_p}$ vs diameter d_p. b) Particle density integrated over diameters.

can carry more negative charges, and Coulomb repulsion slows down coagulation. Coagulation and nucleation eventually reach a quasi-equilibrium and the particle density decreases slowly.

The total negative charge density decreases in time after a speedy initial charging at a rate which is practically the same for the three potentials. This decrease in time is due to plasma electron depletion resulting from the nanoparticles charging. It is also partly due to the fact that the charge carried by a particle that results from the coagulation of two primary particles of radius R_1 and R_2 is smaller than the sum of the charges that these two primary particles can carry, as can be seen from the inequality $R_1 + R_2 > (R_1^3 + R_2^3)^{1/3}$ where it is assumed that the charge is proportional to the radius. This effect will contribute to lower the total negative charge density for the MCP and IPA as compared to the Coulomb potential since coagulation is less efficient for the latter, as was also observed in figure 4.1.

The total nanoparticle volume fraction is larger in the Coulomb case again because of the slower coagulation rate. This can be seen by considering that surface growth operates on a larger number of particles in the Coulomb case and that the surface volume growth rate of two primary particles of radius R_1 and R_2 is larger than that of the coalesced particle, as can be seen from the inequality $R_1^2 + R_2^2 > (R_1^3 + R_2^3)^{2/3}$.

The electron mean energy increases since there is a decreasing electron density available to absorb the fixed injected power density P_ε. The increase of the electron mean energy is faster for the Coulomb interaction as compared to the MCP and IPA since the nanoparticles are more charged.

Figures 4.3a and 4.3b represent the particle size and charge distribution, respectively, at 0.2 s and 1.0 s for the second case. One can see in Fig. 4.3a that our model gives a bimodal size distribution at 1.0 s. Similar size distributions have been observed in experimental [44] and in other numerical studies [18, 1]. The first peak coincides with the smallest diameter of the nucleated particles (0.75 nm).

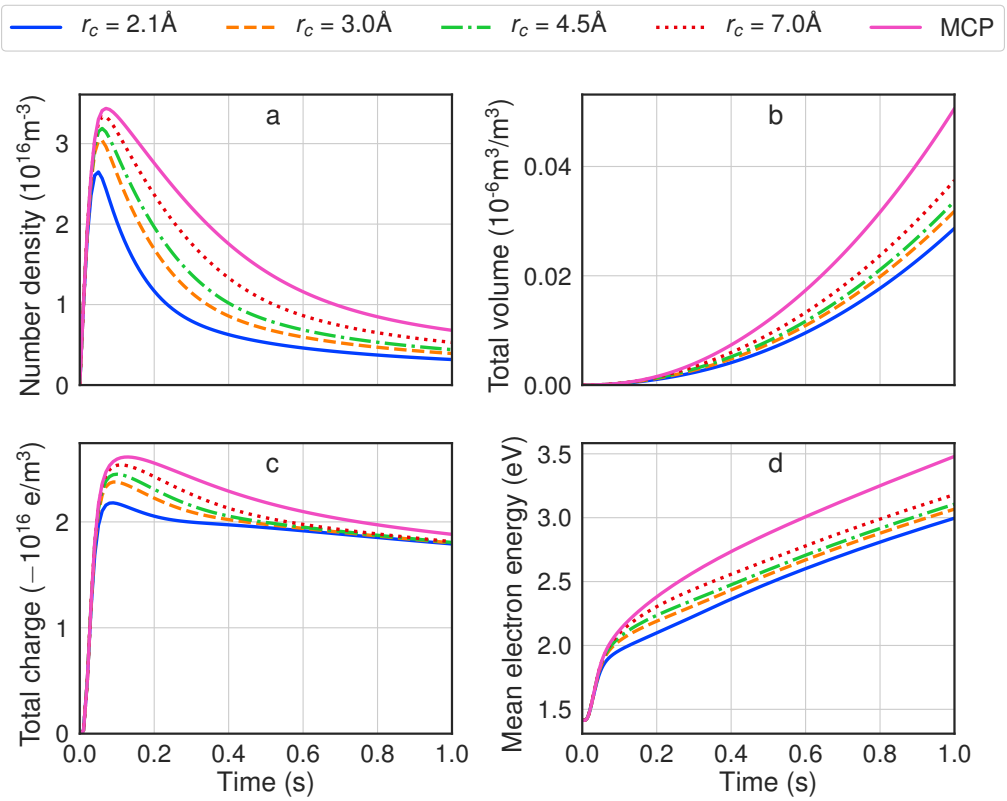

Figure 4.4: Effect of the cut-off distance r_c on the (a) nanoparticle number density, (b) total volume fraction, (c) total charge density, and (d) electron mean energy as a function of time. Calculations were made using the full growth model for the MCP+vdW and MCP interactions.

It is due to the continuous generation of small particles, while the second peak, around 25 nm, is due to both coagulation and surface growth. One observes that the Coulomb potential produces fewer large particles at 0.2 s as compared to the MCP and IPA. This explains the larger particle density at early times observed in figure 4.2. However, at 1.0 s the Coulomb potential has produced more large particles around the second peak than the MCP and IPA. This effect is related to the decrease of the electron density, as shown in figure 4.2c, which lessens the particles charge and promotes coagulation among the more numerous particles of the Coulomb case.

Fig. 4.3b shows that the Coulomb potential produces a taller but narrower distribution than the two other potentials. However, the number of particles carrying a lower charge is more significant than for the MCP and IPA. This explains the larger total charge density seen in figure 4.2. One notes that all models predict positively charged particles and a peak for neutral particles. This peak results from the fast coagulation of particles of opposite charges. It is, however, more pronounced for the MCP and IPA as compared to the Coulomb potential due to the polarization-induced effect.

4.3.2 Electrostatic and van der Waals interactions

We now add to the electrostatic potentials the vdW interaction including a cut-off distance r_c as specified in eq. 4.11. Fig. 4.4 shows the influence of r_c for the combined MCP and vdW (MCP+vdW) interactions for the full growth model, using an initial neutral density 10^{10} m^{-3} placed in the smallest volume section. The cut-off parameter r_c varies from the estimated lower limit value of 2.1 Å to $r_c \to \infty$, which is represented by the MCP. The trends are qualitatively similar to those of figure 4.2. One can see that a smaller r_c favors coagulation. This is due to the additional particle attraction induced by the vdW potential. Following the above discussion on the electrostatic potentials, faster coagulation implies slower growth of the total volume fraction, total charge density, and electron mean energy, as also observed in figure 4.2.

Fig. 4.5 shows a comparison between the particle growth processes for the three combined vdW and electrostatic potentials with $r_c = 2.1$ Å. The results for the MCP alone are also shown for comparison. For such a small value of r_c, the results for the three electrostatic potentials combined with the vdW potential are quite similar. This is attributable to the dominance of the vdW interaction over the electrostatic interaction at a short interparticle distance, which is translated into the enhancement factor eq. 4.9 through the term $\Phi_{jpmq}(r_{\min})$. However, the electrostatic potential dominates the vdW potential at a larger interparticle distance since the former goes as $\sim r^{-1}$ (induced polarization is negligible at large distance) while the (non-retarded) vdW potential goes as $\sim r^{-6}$, as can be shown from the Hamaker expression (4.10) for $r \gg r_c$. Therefore the term $\Phi^{\max}_{jpmq}$ in eq. 4.9 weakly depends on the vdW interaction. This term, which expresses Coulomb repulsion through the exponential factor, slows down coagulation efficiently in the late stage of the growth between highly charged particles. Fig. 4.5 reflects the fact that the nature of the electrostatic model used is not relevant for such a small cut-off parameter r_c.

Fig. 4.6 shows the nanoparticle size and charge distribution for the MCP+vdW interaction with $r_c = 2.1$ Å for the full growth model at 1 s. As in the purely electrostatic interaction cases (figure 4.3) the distribution is bimodal. The staggered shape of the smaller lobe on the negative charge side is due to the tunnel current. Electrons leave the nanoparticle surface at a faster rate than those arriving from the plasma. The sharp edge on the positive side sets up as a result of the balance between the lower frequency impacting positive ions and the higher electron collection frequency. We have checked that the contours of the smaller lobe become smooth when the tunnel current is deactivated. The shape of the larger lobe is smoother as the tunnel current is negligible for bigger particles. More details are provided in 4.C.

Fig. 4.7a and figure 4.7b show the particle size and charge distribution, respectively, at 1.0 s for the three electrostatic potentials combined with the vdW potential with $r_c = 2.1$ Å. The case of the pure MCP potential is also represented for comparison. The differences between MCP and MCP+vdW are very similar to those observed between the Coulomb potential and the MCP in figure 4.3 except that coagulation is slower for MCP than for MCP+vdW in the present case.

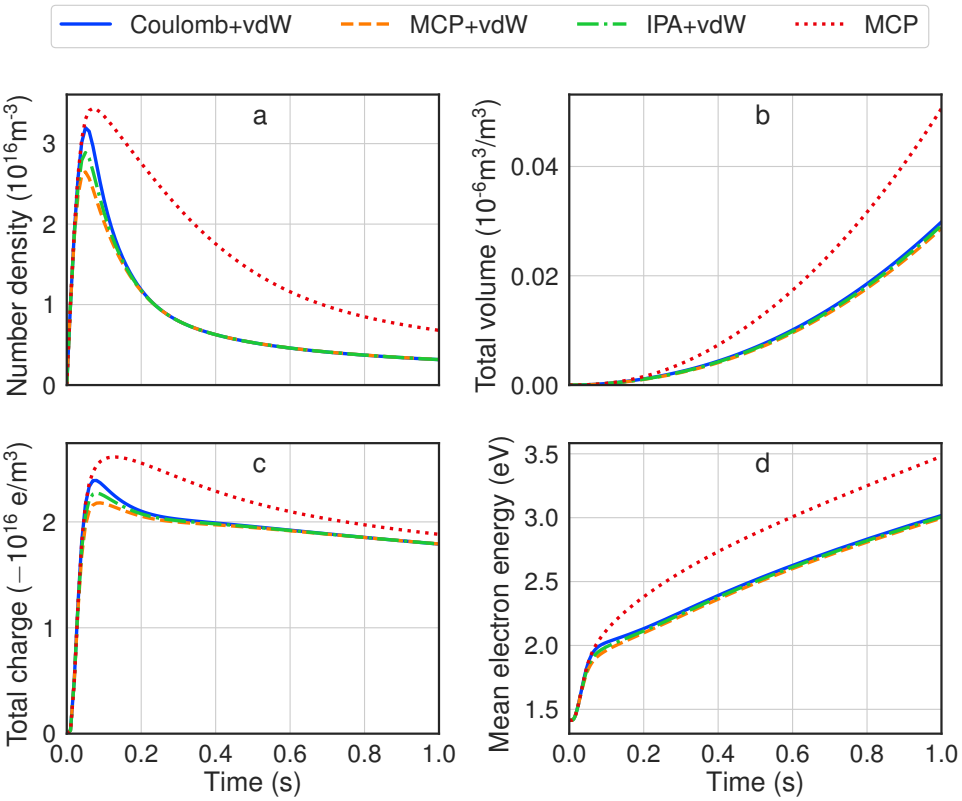

Figure 4.5: Effect of Coulomb+vdW, MCP+vdW, IPA+vdW with $r_c = 2.1$ Å, and MCP interactions on the nanoparticle (a) number density, (b) total volume fraction, (c) total charge density, and (d) electron mean energy as a function of time. Calculations were made using the full growth model.

4.4 Conclusion

We investigated the effects of the electrostatic and vdW interactions on the growth of nanoparticles in a low-temperature argon-silane plasma. The growth of nanoparticles was modeled by solving the general dynamics equation, which includes nucleation, coagulation, charging, and surface growth. Coagulation was modeled by solving the Smoluchowski equation for particle sizes, the particle charges being treated as multiple of the elementary charge, while nucleation, surface growth, and plasma dynamics were modeled using simplified approaches. The vdW interaction was modeled by using the Hamaker expression in which the unphysical singularity at the contact point was regularized by imposing a constant value for a separation distance $r \leq r_c$ where the cut-off distance r_c was left as a parameter to investigate.

In all the cases considered using the complete growth model, the density of the particles initially increases over time due to continuous nucleation, to reach a maximum and then an almost stationary value lower than the maximum. In the late stage, nucleation and coagulation reach near equilibrium, although the total volume fraction, the total charge density and the electronic average energy continue

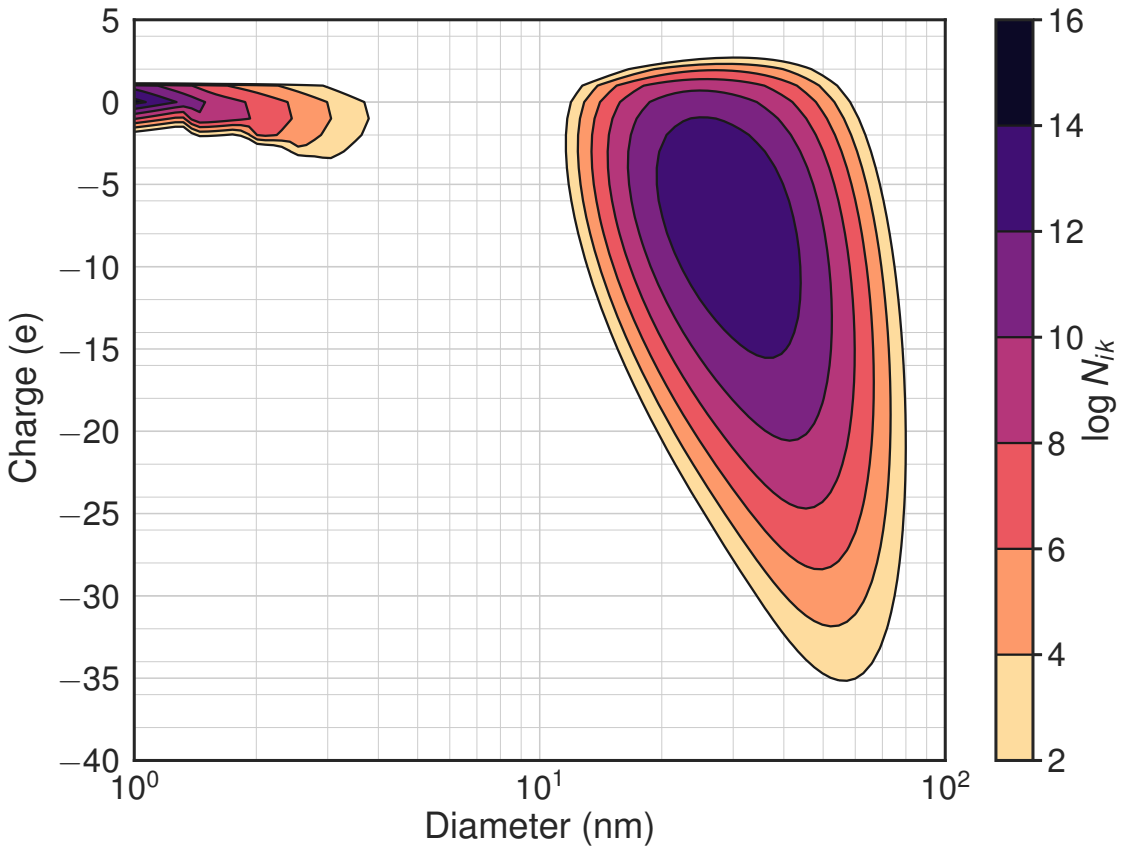

Figure 4.6: Nanoparticle size and charge distribution considering the full growth model for MCP+vdW with $r_c = 2.1\,\text{Å}$ at 1 s. The color levels represent the logarithm of the number density N_{ik}. In the first lobe, the charge limits are sharp due to tunnel current. The second lobe has a smooth shape, the charges resulting from the balance of the classical OML currents.

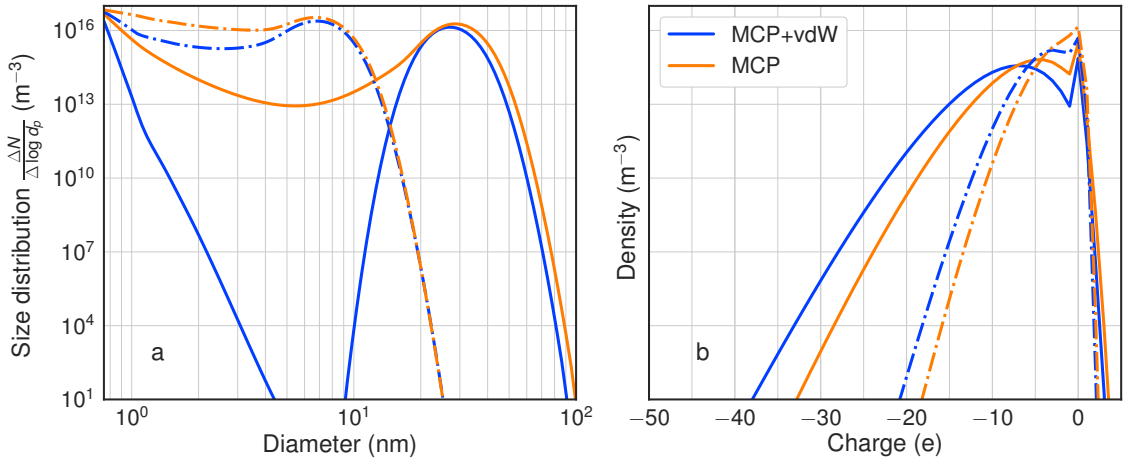

Figure 4.7: Nanoparticle distributions at 0.2 s (dash-dotted lines) and 1.0 s (solid lines), considering the full growth model for the MCP potential without and with the vdW interaction ($r_c = 2.1\,\text{Å}$). a) Particle size distribution $\frac{\Delta N}{\Delta \log d_p}$. b) Particle density integrated over diameters.

to increase. When retaining only the electrostatic interaction, coagulation is enhanced for the MCP and IPA models as compared to the Coulomb potential due to induced polarization, which favors attraction between particles. As a consequence, the particle density is lower for the MCP and IPA. Faster coagulation implies a decrease in the total charge density, the total volume fraction of the particles and the average electron energy.

When including the vdW interaction in the model, coagulation is enhanced as r_c decreases. For the lower limit value of r_c, which we estimated as the diameter of a silicon atom $\sim 2.1\,\text{Å}$, we found that the three electrostatic potentials combined with the vdW potential give very similar results since the vdW interaction dominates the short-range interaction. In all cases, the size-charge particle distribution at the largest time considered shows two distinct populations separated by a gap, in agreement with experimental observations. The smaller size population is highest at the protoparticle size (with a diameter of 0.75 nm in our model) carrying only few positive or negative elementary charges (or no charge) and a larger size and charge population, in our case centered approximately at a diameter $d \approx 25\,\text{nm}$ and a charge $q \approx -10e$.

Our results point out that the electrostatic model and the vdW interaction may both play a non-negligible role in the nanoparticle growth process. The value of the cut-off r_c used to regularize the short-range vdW potential was shown to have a critical influence. The electrostatic models investigated provided similar qualitative results, and quantitative results of the same order of magnitude for all the values of r_c investigated. We have seen that a simple Coulomb potential provides a good approximation for small values of r_c (strong vdW interaction), but that polarization-induced effects should be taken into account for large values of r_c (weak vdW interaction). Obviously, a better understanding of the vdW interaction between particles with surface roughness involving nonlocal and possibly retardation effects would be necessary for more accurate modeling of the nanoparticle growth process. The results of such an investigation could be used to regularize properly the Hamaker potential near the contact point and thus more precisely assess the importance of the van der Waals interaction in dusty plasmas. This quantitative analysis must, however, be left to future research.

4.A Numerical calculations details

We used a time-splitting approach to compute the plasma and nanoparticle evolution separately. Details of the calculation of the enhancement factor can be found in [35].

The steps of the calculation are the following:

1. Compute the enhancement factor for the given interactions.

2. Solve the plasma species densities without nanoparticles over 10 ms which defines the initial time $t^{(0)}$.

3. Solve the plasma species densities n_j, $j = \{\mathrm{e}, \mathrm{Ar}^+, \mathrm{Ar}^*, \mathrm{SiH_3}^+, \mathrm{SiH_3}, \mathrm{SiH_2}, \varepsilon\}$, at time $t^{l+1/2} = t^l + \Delta t/2$, using nanoparticle density N_{ik}^l and n_j^l to obtain $n_j \to n_j'$.

4. Solve the nanoparticle charging at time $t^{l+1/2} = t^l + \Delta t/2$, using n_j' to obtain $N \to N'$.

5. Solve the nanoparticle growth (GDE) at time $t^{l+1} = t^l + \Delta t$, using N' to obtain $N' \to N''$. As the total charge density in the system changed, one needs to recompute the plasma densities.

6. Solve the plasma species densities at time $t^{l+1} = t^{l+1/2} + \Delta t/2$, using N'' to obtain $n_j' \to n_j''$.

7. Solve the nanoparticle charging at time $t^{l+1} = t^{l+1/2} + \Delta t/2$, using n'' and N'' to obtain $N'' \to N^{l+1}$ and $n_j'' \to n_j^{l+1}$.

8. Continue to step (3) or stop the computation at the final time $t = 1\,\mathrm{s}$.

The calculations were performed using C++ and python codes along with the libraries and tools LSODA, Boost, HDF5, jupyter, matplotlib, cython, and scipy [14]. All datasets and methods needed to evaluate the conclusions in the article are present in the paper and the supplementary materials available at Zenodo `https://doi.org/10.5281/zenodo.3568131`.

4.B Interparticle electrostatic potentials

The multipolar coefficient potential (MCP) for two dielectric spherical particles is [5, 40],

$$\Phi_{\mathrm{MCP}}(r, r_i, q_i, r_j, q_j) \equiv \Phi_{\mathrm{MCP,ij}}(r) \tag{4.15}$$

$$\begin{aligned} &= K\frac{q_i q_j}{r} \\ &- \frac{q_i}{2}\sum_{m=1}^{\infty}\sum_{l=0}^{\infty} A_l \frac{(\varepsilon-1)\,m}{(\varepsilon+1)\,m+1}\frac{(l+m)!}{l!m!}\frac{r_j^{2m+1}}{r^{2m+l+2}} \\ &- \frac{1}{2K}\sum_{l=1}^{\infty} A_l^2 \frac{(\varepsilon+1)\,l+1}{(\varepsilon-1)\,l r_i^{2l+1}}, \end{aligned} \tag{4.16}$$

where r is the distance between the centers of the particles, q_i and q_j are the charges of particles i and j, respectively, and $K = (4\pi\varepsilon_0)^{-1}$. The multipolar coefficients A_l, are the solutions of the following linear system of equations,

$$\begin{aligned} A_{j_1} &= Kq_1\delta_{j_1,0} - \frac{(\varepsilon-1)\,j_1}{(\varepsilon+1)\,j_1+1}\frac{r_1^{2j_1+1}}{r^{j_1+1}}Kq_j \\ &+ \frac{(\varepsilon-1)\,j_1}{(\varepsilon+1)\,j_1+1}\sum_{j_2=0}^{\infty}\sum_{j_3=0}^{\infty}\frac{(\varepsilon-1)\,j_2}{(\varepsilon+1)\,j_2+1}\frac{(j_1+j_2)!}{j_1!j_2!}\frac{(j_2+j_3)!}{j_2!j_3!}\frac{r_i^{2j_1+1}r_j^{2j_2+1}}{r^{j_1+2j_2+j_3+2}}A_{j_3}. \end{aligned} \tag{4.17}$$

The Image Potential Approximation (IPA) reads,

$$\Phi_{\mathrm{IPA}}(r, r_i, r_j, q_i, q_j) \equiv \Phi_{\mathrm{IPA,ij}} = K\frac{q_i q_j}{r} - \frac{K\kappa q_i^2 r_j^3}{2r^2\left(r^2 - r_j^2\right)} - \frac{K\kappa q_j^2 r_i^3}{2r^2\left(r^2 - r_i^2\right)}. \tag{4.18}$$

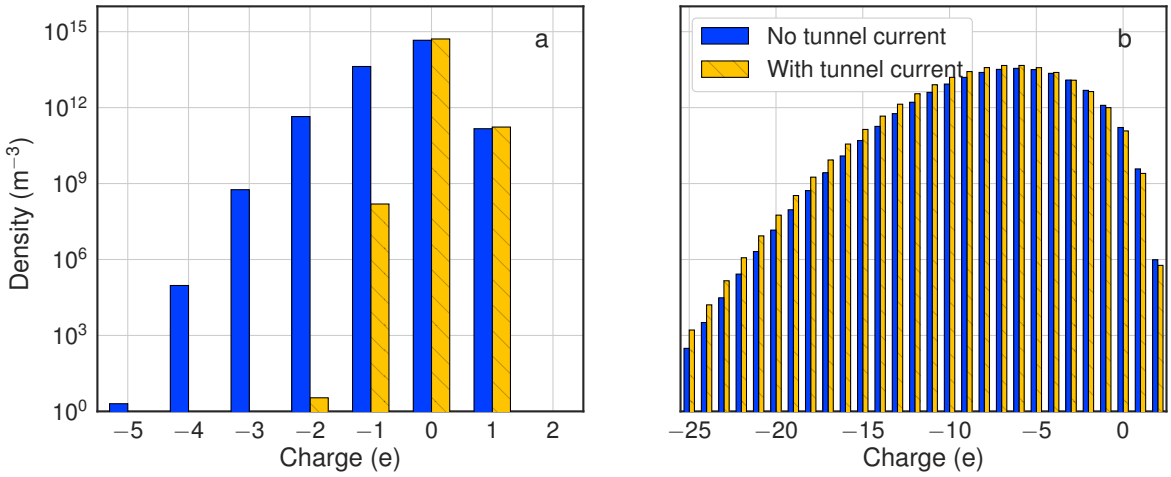

Figure 4.8: Charge distributions for diameters a) $d_p = 0.75\,\text{nm}$, and b) $d_p = 25\,\text{nm}$ for the full growth model MCP+vdW with $r_c = 2.1\text{Å}$ at 1.0 s with and without tunnel current.

where $\kappa = {}^{(\varepsilon-1)}/_{(\varepsilon+2)}$.

4.C Effects of the tunnel current on the charge distribution

To illustrate the influence of the tunnel current on the charge of particles of different sizes, we show in figure 4.8 the charge distributions at the diameters $d_p = 0.75$ nm and 25 nm which correspond to the two peaks of the size distribution of figure 4.7a for MCP+vdW with $r_c = 2.1\text{Å}$ at 1.0 s with and without the tunnel current. As Mamunuru *et al.* [26] pointed out, the tunnel current limits the negative charges, and this charge limiting effect proves to be more significant for small particles (under 10 nm) for our simulation settings, as can be seen by comparing figure 4.8a and figure 4.8b. A consequence of this charge limiting effect is to cut abruptly the small lobe in figure 4.6 for negative charges. The charge limiting effect of the tunnel current is also illustrated in figure 4.9a which shows the distribution of the three charge states, neutral, positive and negative, with and without the tunnel current in the same conditions as in figure 4.8. One can see that when the tunnel current is on, there is a depletion of negative particles for small diameters. Without the tunnel current, the density of negative particles in this group is considerably larger. However, no such significant effect of the tunnel current is observed in the larger particle group. This depletion of negatively charged particles in the small particle group can also be seen in figure 4.9b where the density of the total charge distribution shows a minimum at the charge $-e$ when the tunnel current is on. The same minimum can be seen in figure 4.7b. Without the tunnel current, a slight minimum would rather occur at $-2e$. As can be seen in figure 4.8, larger nanoparticles have a broad charge distribution, and small particles have a narrower charge distribution. Because there are two distinct populations in size at $t = 1\,\text{s}$, the overlap of broad and narrow charge

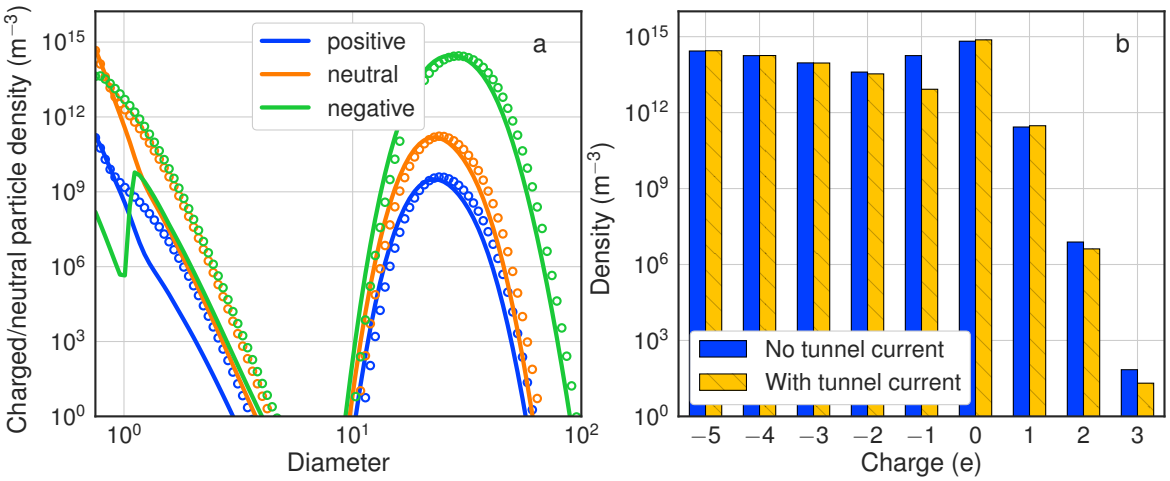

Figure 4.9: a) Positive, neutral, and negative particle distribution with tunnel current (continuous lines) and without tunnel current (circles). b) Total charge density in the conditions of figure 4.8 with and without tunnel current.

distributions produces a minimum in the total charge distribution as can be seen in figures 4.3b, 4.7b and 4.9b.

4.D Influence of nucleation and surface growth rates in the nanoparticle growth dynamics

In the results presented above, we used specific values for the nucleation rate J_{00} and the linear growth rate L_g. These values were taken from [1] who selected them using the results of a silicon hydride clustering model with detailed chemistry [4] and of a quasi-one-dimensional model for gas-phase chemistry and nanoparticle growth [3]. This Appendix aims to study the influence of these parameters on the particle growth.

4.D.1 Nucleation rate

The effects of the nucleation rate J_{00} can be understood by considering a simplified model for nucleated particles only. For these particles, the Smoluchowski equation (4.3) reads,

$$\frac{\mathrm{d}N_0}{\mathrm{d}t} = J_{00} - K_{00}N_0^2, \tag{4.19}$$

where N_0 is the nanoparticle density in the smallest section and $K_{00} = \eta_{00}\beta_{00}^0$ is the kernel of coagulation, with η_{00} the enhancement factor and the coagulation rate β_{00}^0 given by eq. 4.8. Equation (4.19) follows from the fact that nucleated particles are not generated from smaller particles, and from the assumption that these particles coagulate only between them. We neglect surface growth (considered in the next section of this Appendix).

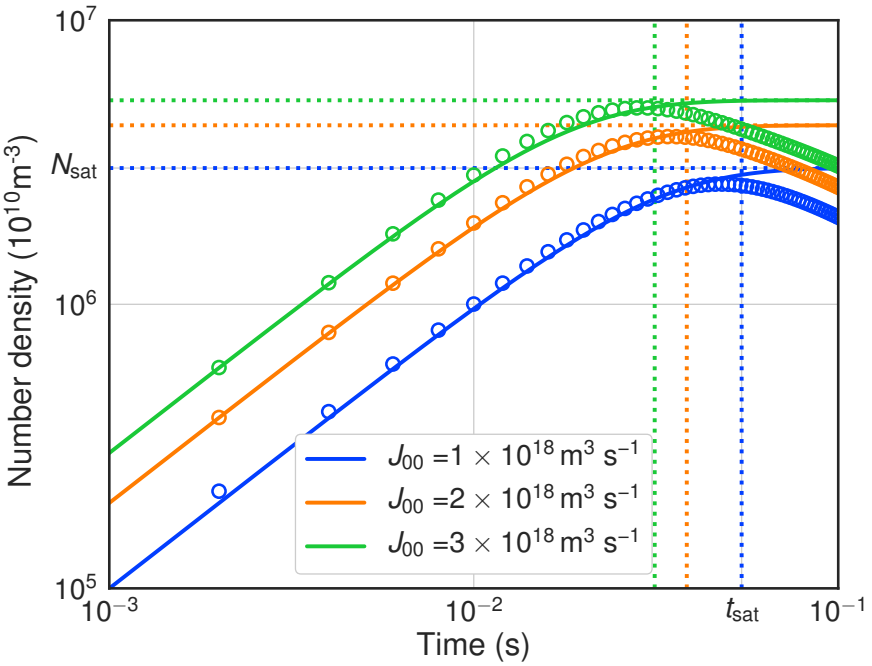

Figure 4.10: Number density as a function of time for the complete growth model with MCP+vdW (circles) for $r_c = 2.1$Å, and solution eq. 4.20 (lines), for different values of the nucleation rates J_{00}. The vertical and horizontal dotted lines represent t_{sat} and N_{sat}, respectively.

Assuming that K_{00} is independent of time, the solution of eq. 4.19 for the initial condition $N(0) = 0$ is

$$N_0(t) = \left(\frac{J_{00}}{K_{00}}\right)^{1/2} \tanh\left[(J_{00}K_{00})^{1/2}t\right] \tag{4.20}$$

It follows from this simplified model that $N_0(t) \approx J_{00}t$ when $t \ll (J_{00}K_{00})^{-1/2}$ and that $N(t)$ reaches a plateau with the value $N_0 = N_{sat} = \sqrt{J_{00}/K_{00}}$ when $t \gtrsim t_{sat} = 9/(5\sqrt{J_{00}K_{00}})$. One can see that N_{sat} rises and t_{sat} decreases when the nucleation rate increases. Moreover, N_{sat} and t_{sat} decrease for fixed nucleation rate and increasing K_{00}. In figure 4.10 we compare eq. 4.20 with the numerical solution of the complete model in the MCP+vdW case with $r_c = 2.1$Å for three values of J_{00}. In the simplified model we used the fitted value $\eta_{00} = 2.17$ for easier comparison between the two models. The results of the simplified and complete models appear to be close up to the maximum of the solution of the complete model and of the saturation value of the simplified model. Note that there is no maximum in the simplified model because the nucleated particles coagulate only between them while in the complete model coagulation takes place between particles of different sizes.

Fig. 4.10 shows that the maximum density N_{max} and the corresponding time t_{max} of the complete model behave the same way as N_{sat} and t_{sat} as J_{00} varies. Also, figure 4.4 shows that when increasing K_{00} by decreasing r_c, both N_{max} and t_{max} decrease, as indicated by N_{sat} and t_{sat}.

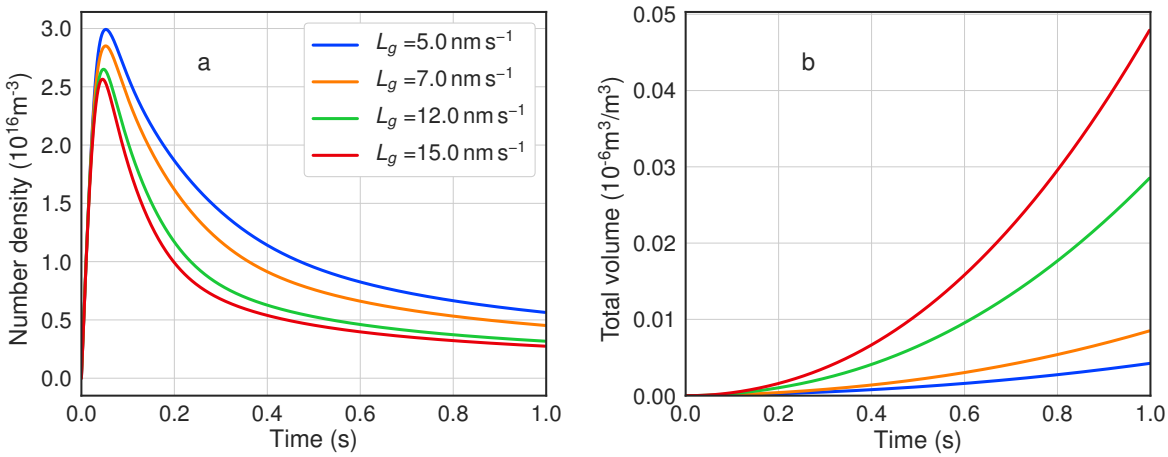

Figure 4.11: Effect of linear growth rate on the nanoparticle (a) number density, and (b) total volume fraction, as a function of time. Calculations were made using the complete growth model for MCP+vdW with $r_c = 2.1$Å.

One notes that the solution of the simplified model provides a means to obtain an effective enhancement factor defined as $\eta_{\text{eff}} = N_{\text{max}}^2/(\beta_{00}^0 J_{00})$. For $J_{00} = 1\times10^{18}$ and $3\times10^{18}\,\text{m}^3\text{s}^{-1}$ one obtains the values $\eta_{\text{eff}} = 2.81$ and 2.46, respectively, which are similar to the fitted value $\eta_{00} = 2.17$ used in figure 4.10.

4.D.2 Surface growth rate

In principle, the effects of surface growth could be understood by using the simplified model considered in the previous section of this Appendix with the difference that the particle diameter would grow in time, and thus the kernel K_{00} in (4.19) would also grow in time. Unfortunately, there is no general analytical solution of the differential equation (4.19) for a time-dependent kernel. However, according to the discussion of the previous section, a larger value of K_{00} entails a decrease of N_{sat} and t_{sat}. In addition, since β_{00}^0 is proportional to $d_p^{1/2}$, then N_{sat} and t_{sat} are proportional to $d_p^{-1/4}$. Hence, one expects a weak dependence of N_{sat} and t_{sat} (and thus of N_{max} and t_{max}) on the linear growth rate.

To verify this conclusion, we have calculated the solutions of the complete model for different values of the linear growth rate L_g. The results are shown in figure 4.11 for the four values $L_g = 5$, 7, 12, and 15 nm s^{-1}. As expected, figure 4.11a shows that N_{max} and t_{max} decrease as L_g increases and they do so with a weak dependence on L_g. On the contrary, as can be seen in figure 4.11b, the total volume fraction increases because it is proportional to d_p^3.

4.5 References

[1] P. Agarwal and S. L. Girshick. Sectional modeling of nanoparticle size and charge distributions in dusty plasmas. *Plasma Sources Sci. Technol.*, 21(5):055023, October 2012.

[2] J. E. Allen. Probe theory - the orbital motion approach. *Phys. Scr.*, 45(5):497, May 1992.

[3] U. Bhandarkar, U. Kortshagen, and S. L. Girshick. Numerical study of the effect of gas temperature on the time for onset of particle nucleation in argon–silane low-pressure plasmas. *J. Phys. D: Appl. Phys.*, 36(12):1399, 2003.

[4] U. V. Bhandarkar, M. T. Swihart, S. L. Girshick, and U. R. Kortshagen. Modelling of silicon hydride clustering in a low-pressure silane plasma. *J. Phys. D: Appl. Phys.*, 33(21):2731, November 2000.

[5] E. Bichoutskaia, A. L. Boatwright, A. Khachatourian, and A. J. Stace. Electrostatic analysis of the interactions between charged particles of dielectric materials. *The Journal of Chemical Physics*, 133(2):024105, July 2010.

[6] L. Boufendi and A. Bouchoule. Particle nucleation and growth in a low–pressure argon–silane discharge. *Plasma Sources Sci. Technol.*, 3(3):262, August 1994.

[7] L. Boufendi, M. Ch Jouanny, E. Kovacevic, J. Berndt, and M. Mikikian. Dusty plasma for nanotechnology. *J. Phys. D: Appl. Phys.*, 44(17):174035, May 2011.

[8] K. De Bleecker, A. Bogaerts, and W. Goedheer. Modelling of nanoparticle coagulation and transport dynamics in dusty silane discharges. *New J. Phys.*, 8(9):178–178, September 2006.

[9] S. K. Friedlander. *Smoke, Dust, and Haze: Fundamentals of Aerosol Dynamics*. Oxford University Press, 2000.

[10] F. Galli and U. R. Kortshagen. Charging, Coagulation, and Heating Model of Nanoparticles in a Low-Pressure Plasma Accounting for Ion #x2013;Neutral Collisions. *IEEE Transactions on Plasma Science*, 38(4), April 2010.

[11] G. J. M. Hagelaar and L. C. Pitchford. Solving the Boltzmann equation to obtain electron transport coefficients and rate coefficients for fluid models. *Plasma Sources Sci. Technol.*, 14(4):722, November 2005.

[12] H.C. Hamaker. The London-van der Waals attraction between spherical particles. *Physica IV*, 10:1058, November 1937.

[13] L. C. J. Heijmans, F. M. J. H. van de Wetering, and S. Nijdam. Comment on 'The effect of single-particle charge limits on charge distributions in dusty plasmas'. *Journal of Physics D: Applied Physics*, 49(38):388001, 2016.

[14] A. C. Hindmarsh. *ODEPACK, a systematized collection of ODE solvers*, volume (Vol. 1 of IMACS Transactions on Scientific Computation) . North-Holland, 1983; S. Frost. liblsoda. `https://github.com/sdwfrost/liblsoda.git`, 2018; Maddock J., Bristow P., Holin H., Zhang X., Lalande B., Rade J., Sewani G., and Van Den Berg T. *Boost C++ Math Toolkit*. hetp, 2009; The HDF Group. Hierarchical Data Format, version 5. `http://www.hdfgroup.org/HDF5/`, 1997-; T. Kluyver, B. Ragan-Kelley, F. Pérez, B. Granger, M. Bussonnier, J. Frederic, K. Kelley, J. Hamrick, J. Grout, S. Corlay, et al. Jupyter notebooks—a publishing format for reproducible

computational workflows. In *Positioning and Power in Academic Publishing: Players, Agents and Agendas: Proceedings of the 20th International Conference on Electronic Publishing*, page 87. IOS Press, 2016; J. D. Hunter. Matplotlib: A 2d graphics environment. *Computing In Science & Engineering*, 9(3):90–95, 2007; S. Behnel, R. Bradshaw, C. Citro, L. Dalcin, D.S. Seljebotn, and K. Smith. Cython: The best of both worlds. *Computing in Science Engineering*, 13(2):31 –39, march-april 2011.

[15] Ch. Hollenstein. The physics and chemistry of dusty plasmas. *Plasma Phys. Control. Fusion*, 42(10):R93, October 2000.

[16] D. D. Huang, J. H. Seinfeld, and K. Okuyama. Image potential between a charged particle and an uncharged particle in aerosol coagulation—enhancement in all size regimes and interplay with van der waals forces. *Journal of colloid and interface science*, 141(1):191–198, 1991.

[17] J. N. Israelachvili. Intermolecular and Surface Forces. In *Intermolecular and Surface Forces (Third Edition)*. Academic Press, San Diego, January 2011; E. Jones, T. Oliphant, and P. Peterson. SciPy: Open source scientific tools for Python, 2001–.

[18] D. J. Kim and K. S. Kim. Analysis on nanoparticle growth by coagulation in silane plasma reactor. *AIChE J.*, 48(11):2499–2509, November 2002.

[19] U. Kortshagen and U. Bhandarkar. Modeling of particulate coagulation in low pressure plasmas. *Phys. Rev. E*, 60(1):887–898, July 1999.

[20] E. Krishnakumar and S. K. Srivastava. Ionization Cross Sections of Silane and Disilane by Electron Impact. *Contributions to Plasma Physics*, 35(4-5):395–404, 1995.

[21] S. Kumar and D. Ramkrishna. On the solution of population balance equations by discretization—I. A fixed pivot technique. *Chemical Engineering Science*, 51(8):1311–1332, April 1996.

[22] M. J. Kushner. A model for the discharge kinetics and plasma chemistry during plasma enhanced chemical vapor deposition of amorphous silicon. *Journal of Applied Physics*, 63(8):2532–2551, April 1988.

[23] R. Le Picard, A. H. Markosyan, D. H. Porter, S. L. Girshick, and M. J. Kushner. Synthesis of Silicon Nanoparticles in Nonthermal Capacitively-Coupled Flowing Plasmas: Processes and Transport. *Plasma Chem Plasma Process*, 36(4):941–972, May 2016.

[24] M. A. Lieberman and A. J. Lichtenberg. *Principles of Plasma Discharges and Materials Processing*. John Wiley & Sons, April 2005.

[25] Y. Luo, R Zhao, and Pendry J. B. van der waals interactions at the nanoscale: The effects of nonlocality. *PNAS*, 111(52):18422–18427, April 2014.

[26] M. Mamunuru, R. Le Picard, Y. Sakiyama, and S. L. Girshick. The Existence of Non-negatively Charged Dust Particles in Nonthermal Plasmas. *Plasma Chem Plasma Process*, 37(3):701–715, May 2017.

[27] T. Matsoukas and M. Russell. Fokker-Planck description of particle charging in ionized gases. *Phys. Rev. E*, 55(1):991–994, January 1997.

[28] L. S. Matthews and T. W. Hyde. Effect of dipole–dipole charge interactions on dust coagulation. *New J. Phys.*, 11(6):063030, June 2009.

[29] L. S. Matthews, V. Land, and T. W. Hyde. CHARGING AND COAGULATION OF DUST IN PROTOPLANETARY PLASMA ENVIRONMENTS. *ApJ*, 744(1):8, December 2011.

[30] L.S. Matthews and T.W. Hyde. Effects of the charge-dipole interaction on the coagulation of fractal aggregates. *IEEE Transactions on Plasma Science*, 32(2):586–593, April 2004.

[31] T. Miyao and H. Spohn. The retarded van der waals potential: Revisited. *J. Math. Phys.*, 50(7):072103, August 2009.

[32] D. D. Monahan and M. M. Turner. On the global model approximation. *Plasma Sources Sci. Technol.*, 18(4):045024, September 2009.

[33] A. Priye and W. H. Marlow. Computations of Lifshitz–van der Waals interaction energies between irregular particles and surfaces at all separations for resuspension modelling. *J. Phys. D: Appl. Phys.*, 46:425306, 2013.

[34] L. Ravi and S. L. Girshick. Coagulation of nanoparticles in a plasma. *Phys. Rev. E*, 79(2):026408, February 2009.

[35] B. Santos, L. Cacot, C. Boucher, and F. Vidal. Electrostatic enhancement factor for the coagulation of silicon nanoparticles in low-temperature plasmas. *Plasma Sources Sci. Technol.*, 28(4):045002, April 2019.

[36] V. A. Schweigert and I. V. Schweigert. Coagulation in a low-temperature plasma. *J. Phys. D: Appl. Phys.*, 29(3):655, 1996.

[37] G. S. Selwyn, J. Singh, and R. S. Bennett. Insitu laser diagnostic studies of plasma-generated particulate contamination. *Journal of Vacuum Science & Technology A*, 7(4):2758–2765, July 1989.

[38] B. Shotorban. Stochastic fluctuations of dust particle charge in RF discharges. *Physics of Plasmas*, 19(5):053702, May 2012.

[39] SIGLO database. `www.lxcat.net`, retrieved on May 15, 2019.

[40] A. J. Stace and E. Bichoutskaia. Reply to the 'Comment on "Treating highly charged carbon and fullerene clusters as dielectric particles"' by H. Zettergren and H. Cederquist, Phys. Chem. Chem. Phys., 2012, 14, DOI: 10.1039/c2cp42883k. *Physical Chemistry Chemical Physics*, 14(48):16771–16772, November 2012.

[41] V. Tarnovsky, H. Deutsch, and K. Becker. Electron impact ionization of the SiDx (x=1–3) free radicals. *J. Chem. Phys.*, 105(15):6315–6321, October 1996.

[42] H. M. Vale and T. F. McKenna. Solution of the Population Balance Equation for Two-Component Aggregation by an Extended Fixed Pivot Technique. *Ind. Eng. Chem. Res.*, 44(20):7885–7891, September 2005.

[43] S. J. Warthesen and S. L. Girshick. Numerical simulation of the spatiotemporal evolution of a nanoparticle–plasma system. *Plasma Chem Plasma Process*, 27(3):292–310, June 2007.

[44] Y. Watanabe, M. Shiratani, and K. Koga. Nucleation and subsequent growth of clusters in reactive plasmas. *Plasma Sources Sci. Technol.*, 11(3A):A229, August 2002.

5 Discussion and conclusion

In Chapter 2, we studied for the first time a different approach to calculate the enhancement factor for the coagulation of nanoparticles. These results open the way to more exploration for a better description of the electrostatic interaction between nanoparticles. We showed, as in the previous works, that the image potential must be taken into account in self-consistent nanodustusty plasmas simulations.

In the second article, we developed the multipolar coefficient potential (MCP) of Bichoutskaia *et al.* [1], and developed an alternative method to calculate the enhancement factor. Induced polarization, as calculated by the MCP, produces an attractive force component when one of the two interacting particles is charged. We found differences when compared with the pure Coulomb case. We introduced an approximation, the image potential approximation (IPA), which is useful at large interparticle distance and when the particle sizes are very different.

Finally, we presented results on nanodusty plasma simulations. By analyzing these results, we conclude that the electrostatic and van der Waals interactions play an important role in the growth process of nanoparticles. It has been shown that the value of the threshold r_c used to regularize the van der Waals potential at short range has a critical influence.

The difficulties of this kind of simulations are: (i) at least two characteristics are needed to characterize a dust particle, charge and size, (ii) the nanoparticles evolution must be solved self-consistently with the plasma, (iii) plasma chemistry can involve several reactions, (iv) cross-section data for these reactions are hard to find or they have to be estimated, (v) adding a spatial degree of freedom scales the problem and extensive computational resources are needed to obtain results. Nevertheless, as in plasma global models that simplify the fluid approach, we think that this work can be extended to a formal description of a volume averaged nanoparticle growth model accounting for an approximated description of the nanoparticle flux, which was neglected in this work.

We can summarize our findings as follows. First, we determined that the enhancement factor, along with the interparticle potential, must be revisited. Then a rigorous approach for computing the interparticle potential was used to compute the enhancement factor. In that research, we obtained a new useful way to compute the enhancement factor and an approximate form for the potential between

dielectric particles. Finally, we added the van der Waals interaction and proved the previous results in self-consistent plasma-nanoparticle calculations.

A comparison of growth models of 1D/2D nanoparticles with 0D models and experiments could be useful to determine the accuracy of the simplifications and assumptions made in this work. We provide some perspectives on the development of a 1D model in the appendix.

5.1 References

[1] Bichoutskaia E, Boatwright AL, Khachatourian A & Stace AJ (2010). Electrostatic analysis of the interactions between charged particles of dielectric materials. *The Journal of Chemical Physics*, 133(2):024105. DOI:10.1063/1.3457157.

6 SOMMAIRE RÉCAPITULATIF

6.1 Introduction et motivation

Les plasmas poussiéreux sont constitués de particules neutres, de particules ionisées et de particules de matière condensée. Ces plasmas sont fréquemment présents dans la nature: anneaux planétaires, comètes, nuages interstellaires, ainsi que dans les réacteurs à plasma de laboratoire[12].

Dans le cas particulier des plasmas de laboratoire, dès 1989 Selwyn *et al.* [45] ont observé la formation de poussières dans les réacteurs à basse pression utilisés pour la gravure par plasma, ces poussières étant alors perçues comme une source de contamination. Bouchoule et Boufendi[8, 9], Hollenstein *et al.* [21] et Watanabe *et al.* [52, 50] ont étudié les plasmas poussiéreux à base de silane (SiH_4) dans des réacteurs capacitifs excités par des sources radiofréquences (RF), lesquels sont très utilisés pour la micro- et nano-fabrication de dispositifs électroniques. D'après ces études, on peut identifier trois mécanismes principaux de croissance des poussières,

- **Nucléation:** c'est le processus suivant lequel les molécules s'agglomèrent pour former de petits agrégats. Il est supposé que ces particules primaires se développent principalement à partir des ions négatifs derivés de la dissociation du silane [35]. On parle alors de la phase de chimie du plasma (voir fig. 6.1). La taille de ces particules précurseurs est de l'ordre de 1 nm.

- **Coagulation:** c'est le processus physique suivant lequel deux particules se rencontrent et coalescent pour former une nouvelle particule. Ce processus commence quand il y a suffisamment de particules primaires produites par la nucléation. Cette phase est caractérisée par une croissance rapide de la taille des particules accompagnée par une diminution de la densité des poussières comme illustré à la figure 6.1. Les poussières atteignent des rayons de quelques dizaines de nanomètres.

- **Collage ou déposition ou croissance sur la surface:** c'est la phase suivant laquelle des molécules se déposent à la surface des nanoparticules. Dans cette phase, la taille des particules peut atteindre des micromètres.

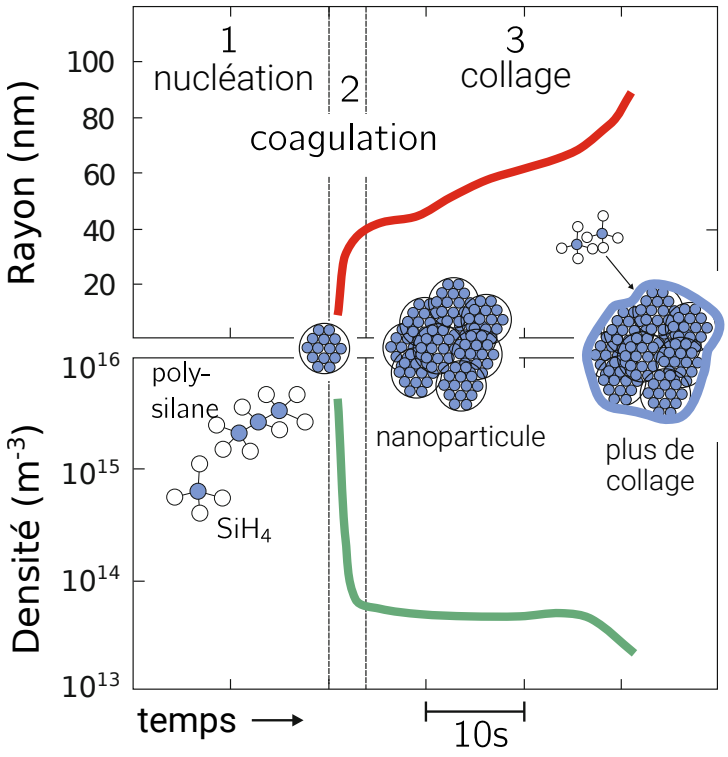

Figure 6.1: Évolution de la taille et du nombre des nanoparticules dans un plasma RF d'argon-silane (adapté [35].). La figure montre les trois phases de croissance: nucléation, coagulation et collage.

Pour décrire la croissance des nanoparticules dans un plasma, il faut prendre en compte de nombreux facteurs. D'une part, il faut considérer les particules neutres et chargées (ions et électrons) du plasma qui interagissent avec les nanoparticules. Les particules du plasma vont charger électriquement les nanoparticules. Étant donné que dans les plasmas froids les électrons sont beaucoup plus rapides que les ions, la probabilité de collision entre les électrons et les nanoparticules est beaucoup plus élevée que celle entre les ions et les nanoparticules. Par conséquent il y a plus de poussières négatives que positives ou neutres. D'autre part, il faut considérer les forces qui agissent entre les nanoparticules ainsi que que les forces qui agissent sur les nanoparticules comme la gravité, la thermophorèse, l'entraînement par les ions, etc[12, 46].

Les plasmas poussiéreux trouvent plusieurs applications [24], comme le revêtement des surfaces, la fabrication de couches minces et la synthèse de nanoparticules entre autres. C'est donc d'un grand intérêt de bien comprendre les processus physiques qui se déroulent dans les plasmas poussiéreux et de trouver les jeux de paramètres et conditions qui permettront de contrôler la taille des nanoparticules ou l'épaisseur d'un dépôt par exemple.

Dans ce travail de thèse nous employons des outils numériques pour étudier la dynamique de croissance des poussières dans les plasmas. L'emploi d'outils numériques s'avère particulièrement pertinent car la mise en oeuvre des expériences est difficile à réaliser en raison de la taille nanométrique des particules.

Récemment, Killer *et al.* [27] ont réalisé une étude spatio-temporelle de la croissance des nanoparticules, mais pour des poussières de dimension micrométrique. La modélisation des plasmas poussiéreux représente un défi en raison de leur complexité. Le fort couplage plasma-poussières fait en sorte que la charge et le transport des poussières dépendent des propriétés du plasma et, en contrepartie, les nanoparticules, par leur densité de charge électrique, qui peut devenir importante, modifient les propriétés du plasma ainsi que la distribution du champ électrique dans le plasma.

Plusieurs modèles et approches sont décrits dans la littérature. Ces derniers se répartissent en deux catégories: les distributions monodispersées, où une taille unique des poussières est considérée, et les distributions polydispersés où la distribution en tailles des poussières est prise en compte. Ces dernièr modèles, plus réalistes, ont été étudiés par le groupe de S. L. Girshick [49, 2, 42] et constituent à notre avis l'état de l'art de la modélisation spatio-temporelle des plasmas poussiéreux capacitifs d'argon-silane.

Dans le chapitre 1 nous présentons une introduction générale aux plasmas de décharge et à la croissance des nanoparticules.

Dans le chapitre 2, qui présente le premier article, nous présentons une approche différente de celles utilisées précédemment pour calculer l'interaction électrostatique entre les nanoparticules. Elle consiste à utiliser le potentiel de coefficient multipolaire (MCP) de Bichoutskaia *et al.* Cette étude a ouvert la voie à une exploration plus approfondie de l'interaction électrostatique entre nanoparticules. Nous montrons, comme dans les travaux précédents, que le potentiel d'image, qui décrit la polarisation induite dans une particule soumise à un champ électrique, doit être pris en compte dans les simulations de plasmas poussiéreux auto-cohérents. Cependant, nous employons une approche plus précise que celles employées précédemment, et qui présente l'avantage d'éviter certains inconvénients des méthodes simplifiées comme une singularité au point de contact.

Dans le chapitre 3, qui traite du second article, nous avons également employé le MCP pour calculer les forces électrostatiques entre les nanoparticules et nous avons employé une méthode alternative (OML) pour calculer le taux de coagulation (par l'intermédiaure du facteur d'augmentation). La polarisation induite telle que calculée par le MCP produit une composante de force attractive lorsque l'une des deux particules est chargée. Nous avons trouvé des différences importantes lors de la comparaison avec le cas simple de Coulomb. Aussi nous avons introduit une approximation, IPA, permettant des calculs plus rapides que MCP, qui s'avère utile à grande distance entre particules et quand les particules qui coagulent ont des tailles très différentes.

Enfin, dans le chapitre 4, qui présente le troisième article, nous discutons de l'évolution dans le temps de la croissance des nanoparticules dans un plasma d'argon-silane en prenant en compte le couplage avec le plasma dans le cadre d'un modèle global ou zéro-dimensionnel (0D). Les résultats obtenus nous permettent de conclure que les interactions électrostatique et de van der Waals jouent un rôle important dans le processus de croissance des nanoparticules. La valeur du rayon de coupure r_c

utilisé pour régulariser le potentiel de van der Waals dans la formulation de Hamaker à courte portée (qui comporte une singularité) s'est avérée avoir une influence critique sur la dyanamique de croissance des nanoparticules.

Dans les sections suivantes, nous présentons une synthèse des articles de recherche présentés dans la thèse.

6.2 Analyse de l'effet de l'interaction électrostatique sur la coagulation de nanoparticules de silicium dans des simulations de plasmas d'argon-silane

Il est connu que les nanoparticules dans les plasmas froids sont principalement chargées négativement. Récemment, Mamunuru *et al.* [34] ont constaté l'existence de nanoparticules chargées positivement. Ces dernières favorisent la coagulation à cause de l'interaction coulombienne entre les particules de charges opposées. Par ailleurs, Ravi & Girshick [42] ont étudié le facteur d'augmentation entre particules neutres et chargées en termes du potentiel d'image qui décrit la polarisation induite dans une particule par le champ électrique de l'autre particule. Le potentiel d'image utilisé dans leur travail [41] est une approximation du potentiel de Huang *et al.* [22], qui est déjà une approximation au problème des charges images. Nous avons effectué une étude numérique sur les effets de l'interaction électrostatique sur la croissance des particules de taille nanométrique de silicium dans un plasma d'argon-silane. Nos simulations sont basées sur le modèle auto-cohérent poussière-plasma proposé par le groupe de S. L. Girshick [41, 49, 2].

6.2.1 Méthodes

Pour simuler la croissance des particules, nous avons utilisé la technique du pivot fixe [30] pour résoudre l'équation de la dynamique générale (GDE) qui tient compte les processus de nucléation, coagulation, collage et chargement [41, 49, 2]. Pour le plasma, nous avons considéré les paramètres fixes qui sont indiqués dans le tableau 6.1.

Tableau 6.1: Paramètre de plasma

Pression	1 Torr
Densité des ions	$1 \times 10^{15}\,\mathrm{m}^{-3}$
Densité des électrons	$1 \times 10^{14}\,\mathrm{m}^{-3}$
Énergie moyenne des électrons	2 eV
Temperature des ions	300 K

Dans le régime moléculaire libre (marche aléatoire des nanoparticules), le taux de coagulation pour deux particules de volume v_i and v_j s'exprime de la façon suivante [42],

$$\beta(v_i, v_j) = \left(\frac{3}{4\pi}\right)^{1/6} \left[\frac{6k_B T}{\rho_p}\left(\frac{1}{v_i} + \frac{1}{v_j}\right)\right]\left(v_i^{1/3} + v_j^{1/3}\right)^2, \tag{6.1}$$

où k_B est la constante de Boltzmann, T est la température des particules, et ρ_p est la densité du silicium. La fréquence totale de collision est donnée par $\eta\beta$, avec η le facteur d'augmentation. Ouyang [38] donne la formule suivante pour le facteur d'augmentation éq. 6.2,

$$\eta_I = 1.2534\sqrt{\psi_I} \tag{6.2}$$

où le potentiel sans dimension est,

$$\psi_I = \left(\frac{\varepsilon_p - 1}{\varepsilon_p - 2}\right)\frac{ze^2}{4\pi\varepsilon_0 k T a_i}, \tag{6.3}$$

Dans cette expression ε_p est la constante diélectrique du silicium, ε_0 est la permittivité du vide, e est la charge élémentaire, et z est le nombre des charges de la particule de rayon a_i. Dans l'approche des Sceats pour calculer le facteur d'aaugmentation, nous devons résoudre la distance d'approche, où le potentiel d'interaction dépasse l'énergie thermique. Cette distance Λ est la racine de [38],

$$\frac{\Lambda}{2}\left.\frac{\mathrm{d}\phi(r^*)}{\mathrm{d}r^*}\right|_{r^*=\Lambda} = k_B T_g, \tag{6.4}$$

et le facteur d'augmentation est défini par,

$$\eta^S = \Lambda^2 \exp\left[-\frac{\phi(\Lambda)}{k_B T_g}\right]. \tag{6.5}$$

6.2.2 Résultats et discussion

En utilisant les mêmes paramètres que Ravi & Girshick [42], nous montrons dans la figure 6.2 le taux de coagulation de Ravi, calculés avec l'approche de Sceats [44] et reproduit les résultats de Ravi, et avec le potentiel éq. 6.3. Cela montre que les résultats de Ravi *et al.* surestiment l'augmentation d'un facteur 10.

Finalement, nous utilisons l'équation (6.2) pour calculer le facteur d'augmentation pour la combinaison des particules chargées et neutres. Dans la figure 6.3, nous montrons la densité de particules avec et sans le potentiel d'image. Nous pouvons voir que le potentiel d'image a un effet considérable dans la coagulation et doit être pris en compte dans les calculs de plasma auto-cohérents, car il affecte le nombre total des particules.

6.3 Facteur d'augmentation électrostatique pour la coagulation de nanoparticules de silicium dans des simulations de plasmas d'argon-silane

Dans la section précédente, nous avons montré que le potentiel choisi pour décrire l'interaction électrostatique modifie la coagulation en raison de l'attraction coulombienne entre des particules portant

Figure 6.2: Coefficients de coagulation entre la particule 1 de 1 nm et la particule 2 du diamètre indiqué sur l'axe des x. La courbe rouge représente le cas de la coagulation entre particules neutres éq. 6.1. Les courbes bleues et vertes concernent la coagulation entre la particule neutre 1 et une particule 2 portant une charge négative. En vert, en utilisant le potentiel éq. 6.3, en bleu le cas du potentiel de Ravi, et en ligne noire la coagulation de la particule 1 avec une charge élémentaire positive et la particule 2. La charge de la particule 2 est la charge la plus probable.

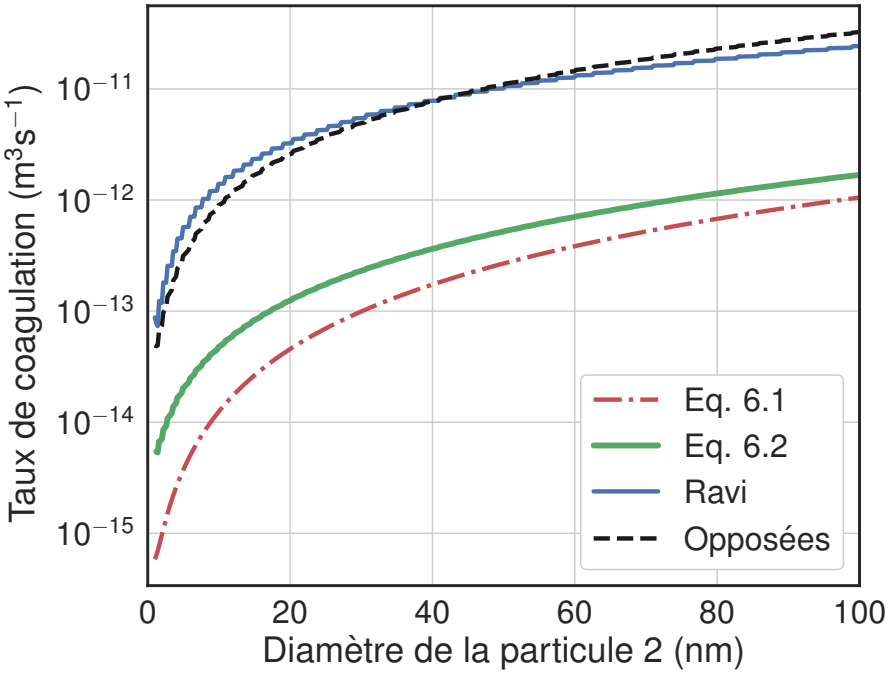

des charges de signes opposés et de l'attraction induite par la polarisation ayant lieu entre toutes les particules, mais principalement entre une particule neutre et une particule chargée.

Cette force d'attraction induite résulte de la polarisation des charges en surface par le champ électrique d'une particule, créant une charge nette dans l'autre particule. Plusieurs approches mathématiques ont été utilisées pour calculer cette force entre deux particules sphériques diélectriques (voir par exemple [32] et les références incluses). Le rapport entre le taux de coagulation dû aux forces électrostatiques et le taux de coagulation de deux particules neutres est appelé ici le facteur d'augmentation électrostatique.

Ravi & Girshick [42] ont étudié théoriquement la coagulation entre des nanoparticules de silicium neutres et chargées en utilisant le potentiel d'image approximatif proposé par Huang *et al.* [22] et l'expression d'Amadon & Marlow [4] pour calculer le facteur d'augmentation. Ils ont conclu que l'augmentation de la coagulation due à la polarisation induite pourrait être très importante. À l'aide de ce modèle, ils ont effectué de vastes simulations de plasma poussiéreux auto-cohérents en 1D pour étudier la croissance des nanoparticules et leur répartition dans le réacteur.

Figure 6.3: Densité de particules en fonction du temps. En noir, avec le potentiel d'image et en rouge, sans potentiel d'image. Des taux de coagulation plus élevés réduisent le nombre de particules.

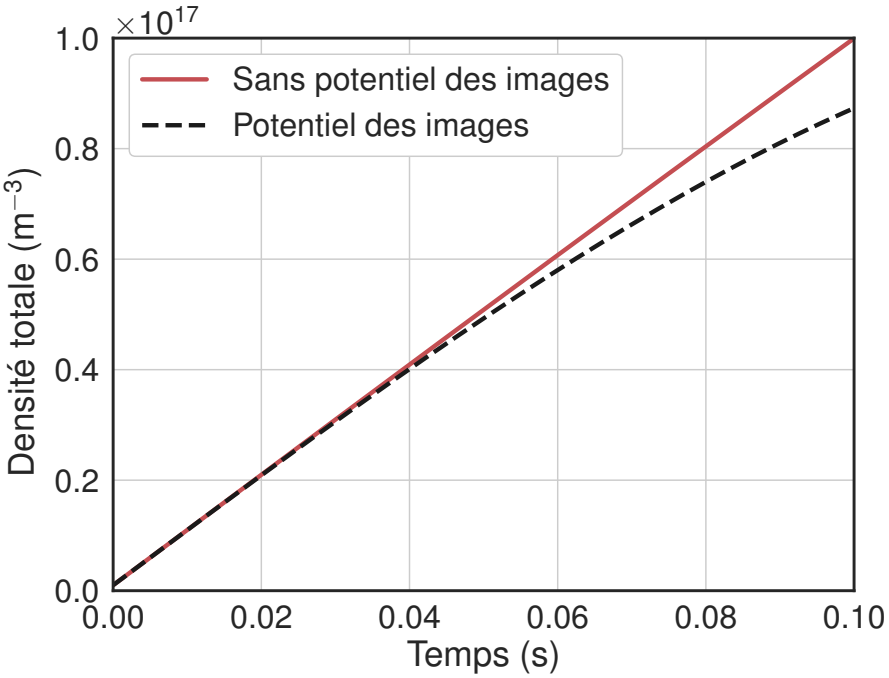

Les résultats obtenus dans la section précédente ont motivé une révision du calcul du facteur d'augmentation dû à l'interaction électrostatique entre les particules diélectriques. Dans ce travail, nous calculons ce facteur d'augmentation entre deux sphères diélectriques en utilisant le potentiel de coefficient multipolaire MCP de Bichoutskaia *et al.* [7], que nous considérons plus rigoureux et approprié pour résoudre ce problème que le potentiel de Huang *et al.* En plus, le MCP de Bichoutskaia *et al.* n'est pas singulier au point de contact, ce qui fait que la théorie OML [3] peut être utilisée pour calculer le facteur d'augmentation.

6.3.1 Méthodes

Les paramètres typiques des réacteurs RF-CCP opérant à basse pression et basse température sont présentés dans le tableau 6.2. Les choix pour p, ε, n_i et T sont motivés par des expériences et des études numériques rapportées dans [13, 34]. Nous supposons une faible densité de nanoparticules afin de pouvoir considérer que les densités ioniques et électroniques sont presque égales. Pour des densités de nanoparticules élevées, les densités éléctronique et ionique peuvent différer fortement. D'après le tableau 6.2, il est possible de déduire les propriétés suivantes du plasma,

- **Le régime moléculaire libre prévaut.** À basse pression et faible densité de gaz, les nanoparticules neutres se déplacent balistiquement et se comportent comme des sphères dures ($\lambda_p \gg d_\mathrm{p}, K_\mathrm{n} \gg 1$). En conséquence, seules les collisions binaires sont pertinentes.

Table 6.2: Paramètres de plasma poussiéreux

Paramètre	valeur
Pression (p)	100 mTorr
Énergie moyenne des électrons (ε)	3 eV
Temperature Gaz/ion/nanoparticules (T)	300 K
Densité des ions (n_i)	$10^{15}\,\mathrm{m}^{-3}$
Densité des électrons (n_e)	$10^{15}\,\mathrm{m}^{-3}$
Densité des nanoparticules (N_p)	$10^{13}\,\mathrm{m}^{-3}$
Charge des nanoparticules (q)	-238-5 e
Diamètre des nanoparticules (d_p)	1-100 nm
Libre parcours moyenne des nanoparticules (λ_p)	$\gg$1 mm
Libre parcours moyenne des neutres (λ)	0.44 mm
Libre parcours moyenne des ions (l_i)	0.30 mm
Longueur de Debye pour plasma poussiéreux (λ_D)	0.04 mm
Longueur de Debye des ions (λ_i)	0.04 mm
Distance entre particules $\left(d = (3/4\pi N_p)^{1/3}\right)$	0.03 mm
Paramètre de structure ($\kappa_\mathrm{d} = d/\lambda_\mathrm{D}$)	0.77
Nombre de Knudsen ($\mathrm{K_n} = \lambda/d_p$)	$\gg 1$
Paramètre de couplage (Γ_d)	0-48

- **L'écrantage par les ions est négligeable.** La longueur de Debye des poussières est de l'ordre de la longueur de Debye des ions, $\lambda_\mathrm{D} \sim \lambda_i$ [46]. Pour les paramètres sélectionnés, λ_D est beaucoup plus grand que la taille des nanoparticules et que la distance entre particules d. Ceci est une condition préalable à l'utilisation de la théorie OML classique pour le chargement et l'interaction des nanoparticules.

- **Les effets collectifs des nanoparticules sont négligeables.** Ces effets sont caractérisés par le paramètre de couplage $\Gamma_\mathrm{d} = \frac{1}{4\pi\varepsilon_0}\frac{q^2}{k_\mathrm{B}Td}\exp(-\kappa_\mathrm{d})$, qui est défini comme le rapport entre l'énergie d'interaction de Coulomb et l'énergie thermique des nanoparticules [46]. Ce couplage est relativement faible pour ce système. En conséquence, nous supposons que les nanoparticules n'interagissent pas fortement pour former un cristal et que la théorie électrostatique classique peut être utilisée pour décrire l'interaction entre deux particules à l'intérieur de la sphère de Debye [12].

Pour simplifier le modèle, nous faisons les hypothèses suivantes,

- **En l'absence d'un modèle de chimie du plasma, nous supposons que la charge moyenne des nanoparticules est donnée simplement par les courants des ions d'argon et des electrons.**

- **Les nanoparticules sont sphériques avec les propriétés du silicium massif**. Nous supposons qu'ils ont une permittivité relative $\varepsilon = 11.68$, une affinité électronique $A_\infty = 4.05\,\mathrm{eV}$ [39], et une densité de masse $\rho_p = 2330\,\mathrm{kg\,m}^{-3}$[19] comme dans le silicium massif à 300 K. Ce sont les seuls paramètres considérés en lien avec la composition des nanoparticules.

- **La charge est uniformément distribuée à la surface des nanoparticules**. Les nanoparticules diélectriques sont bombardées par les électrons et les ions du plasma à un rythme rapide venant de toutes les directions. Donc nous supposons, conformément à la théorie OML pour la charge, que les charges sont uniformément réparties à la surface des nanoparticules.

Dans le cadre de la théorie OML [3], le facteur d'augmentation peut s'écrire (voir 3.A),

$$\eta_{ij} = \exp\left(-\frac{\Phi_{ij,\max}}{k_B T}\right)\left[1 + \frac{\Phi_{ij,\max} - \Phi_{ij}(r_{\min})}{k_B T}\right]. \tag{6.6}$$

Dans cette expression, $r_{\min} = r_i + r_j$ est la distance entre les centres des particules sphériques i et j, de rayon r_i et r_j, respectivement, lorsqu'elles sont en contact, et $\Phi_{ij,\max}$ est la valeur maximale du potentiel d'interaction entre les particules (voir section 3.2.4). Évidemment, $\eta_{ij} = \eta_{ji}$ étant donné que $\Phi_{ij} = \Phi_{ji}$.

On peut distinguer deux cas particuliers importants,

- potentiel monotone croissant (attractif) ($\Phi_{ij}(r_{\min}) < 0, \Phi_{ij,\max} = 0$):

$$\eta_{ij} = 1 - \frac{\Phi_{ij}(r_{\min})}{k_B T}, \qquad \Phi_{ij}(r) \leq 0 \,\forall\, r \geq r_{\min}, \tag{6.7}$$

- potentiel monotone décroissant (répulsif) ($\Phi_{ij,\max} = \Phi_{ij}(r_{\min}) > 0$):

$$\eta_{ij} = \exp\left(-\frac{\Phi_{ij}(r_{\min})}{k_B T}\right), \qquad \Phi_{ij}(r) \geq 0 \,\forall\, r \geq r_{\min}. \tag{6.8}$$

Naturellement, ces deux derniers cas apparaissent quand Φ_{ij} est le potentiel de Coulomb pour des charges ponctuelles [46, 3]. Dans la situation où la polarisation induite exerce une force d'attraction entre les particules, le cas de l'équation (6.7) s'applique à l'interaction entre les particules neutres et chargées ainsi qu'entre des particules portant des charges de signes opposés, tandis que le cas de l'équation (6.8) ou le cas $\Phi_{ij,\max} > 0$ et $\Phi_{ij}(r_{\min}) < \Phi_{ij,\max}$ peuvent s'appliquer pour les particules portant des charges de mêmes signes.

Deux régimes de chargement des nanoparticules peuvent être identifiés. Dans le premier, la charge négative est limitée par l'effet tunnel, ce qui rend possible l'apparition de petites particules chargées positivement [20, 34]. Dans le second régime, la charge moyenne et la largeur de la distribution en charge sont données par l'équilibre entre les courants électroniques et ioniques, comme indiqué par la théorie OML [3]. Les fréquences de collision OML pour les espèces de plasma $j = e$, Ar^+ sur la nanoparticule de rayon r_i et charge q_i, sont [3],

$$\nu_{ji} = 4\pi r_i^2 n_j \left(\frac{E_j}{2\pi m_j}\right)^{1/2} \alpha_{ji}, \tag{6.9}$$

où n_j et m_j sont, respectivement, la densité et la masse de la particule j. E_j est l'énergie cinétique, en particulier, E_e est l'énergie moyenne des électrons et $E_{Ar^+} = 3k_BT/2$. Le coefficient α_{ji} et le potentiel ϕ_i des nanoparticules au sein du plasma sont donnés par,

$$\alpha_{ji} = \begin{cases} \exp\left(-\frac{q_j\phi_i}{k_B T_j}\right) & \text{pour } q_j q_i \geq 0, \\ 1 - \frac{q_j\phi_i}{k_B T_j} & \text{pour } q_j q_i < 0, \end{cases} \tag{6.10}$$

$$\phi_i \equiv \phi(r_i, q_i) = \frac{q_i}{4\pi\varepsilon_0 r_i}. \tag{6.11}$$

Le courant de chargement associé à l'espèce j est simplement le produit de la fréquence de collision OML nu_{ji} et de la charge q_j, $I_{j,\mathrm{OML}} = q_j\nu_{ji}$.

Le courant tunnel,s'exprime [20, 34, 16],

$$I_{e,\mathrm{tunnel}} = \frac{2|q_i|}{\hbar}\left[k_B T e\phi(r_a, q_i)\right]^{\frac{1}{2}}\left[\beta\cos^{-1}\left(\beta^{-\frac{1}{2}}\right) - (\beta-1)^{\frac{1}{2}}\right], \tag{6.12}$$

où il est supposé que $q_i \leq 0$. Dans cette expression, $\hbar$ est la constante de Planck réduite et β est donné par,

$$\beta = \frac{r_a}{r_i} = \frac{q_i}{q_i + 5e/8 - 4\pi\varepsilon_0 r_i A_\infty/e}, \tag{6.13}$$

où $A_\infty = 4.05\,\mathrm{eV}$ est l'affinité électronique du silicium, et $r_a \geq r_i$ est la distance que les électrons doivent franchir par effet tunnel pour se libérer de la nanoparticule [34]. Ce résultat utilise les faits que, sur une particule chargée négativement, les électrons se trouvent dans un puits de potentiel, caractérisé par l'affinité électronique A_∞, tandis qu'en dehors du puits, les électrons subissent la force répulsive de Coulomb. Le courant éq. 6.12 exprime la probabilité que ces électrons traversent la barrière.

Si on fait le bilan des courants, $I_{e,\mathrm{OML}} + I_{e,\mathrm{tunnel}} + I_{Ar^+,\mathrm{OML}} = 0$, la charge peut être estimée en fonction de la taille des particules. En comparant les courants positifs, il est possible de distinguer deux régimes : le régime tunnel, où $I_{e,\mathrm{tunnel}} \gg I_{Ar^+,\mathrm{OML}}$, pour $d < 4$ nm, et le régime OML, où $I_{e,\mathrm{tunnel}} \ll I_{Ar^+,\mathrm{OML}}$, pour $d > 4$ nm. Ceci est montré dans la figure figure 6.4 pour les conditions de plasma données dans le tableau 6.2. Comme le courant tunnel agit très rapidement, la charge tunnel d'équilibre peut être approximée comme la charge négative maximale que la particule peut retenir [39, 34, 20]. De plus, nous montrons dans la figure 3.2 la charge d'équilibre résultant de la théorie OML améliorée de Gatti et Kortshagen [15], qui inclut les effets collisionnels dans le courant ionique. Deux types de corrections sont considérés dans ce modèle OML amélioré: le courant amélioré par collisions (CE), qui est dû à la collecte d'ions qui restent au voisinage d'une nanoparticule ou qui sont ralentis par des collisions avec des neutres [26], et le courant hydrodynamique (HY) qui apparaît dans le régime hautement collisionnel lorsque le libre parcours moyen des ions est comparable ou inférieur à la longueur de Debye des poussières.

La figure 6.4 montre que les effets des collision ionique tendent à réduire d'un facteur compris entre 1 et 2, la charge négative des particules de taille >3 nm par rapport à la théorie OML classique.

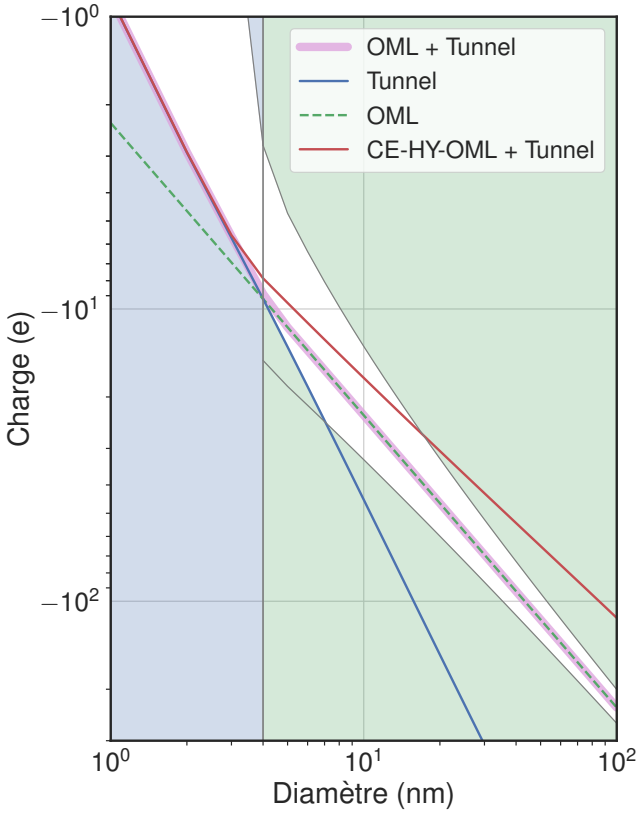

Figure 6.4: Charge à l'équilibre et largeur de la distribution des charges en fonction du diamètre des particules en utilisant les paramètres du tableau 6.2. La charge à l'équilibre dans le régime tunnel est représentée par la ligne continue bleue et est considérée comme la charge négative maximale qu'une particule peut retenir lorsqu'elle est supérieure à la charge dans le régime OML. La charge à l'équilibre dans le régime OML est donnée par la ligne pointillée verte entourée de deux lignes qui délimitent la largeur de la distribution des charges. Les zones bleues et vertes en dehors de la zone blanche indiquent des combinaisons moins probables de taille et de charge pour des nanoparticules proches à l'équilibre avec le plasma. La charge d'équilibre résultant des trois courants, $I_{e,\mathrm{OML}} + I_{e,\mathrm{tunnel}} + I_{\mathrm{Ar}^+,\mathrm{OML}} = 0$, est représenté par la courbe couleur magenta. La courbe rouge représente la charge moyenne du modèle de Gatti & Kortshagen [15], ici notée CE-HY-OML.

Il convient de souligner que, sans la prise en compte des effets des collisions dans le modèle CE-HY, une électronégativité du plasma plus faible n_e/n_i aura également tendance à diminuer la charge des nanoparticules. En revanche, une diminution de la pression ou une augmentation de la température des électrons aura l'effet inverse. Par conséquent, dans ce qui suit, nous considérons la charge d'équilibre donnée par la théorie OML classique comme référence.

Le potentiel de coefficients multipolaires (MCP), développé par Bichoutskaia *et al.* [7, 47], semble bien adapté au problème d'intérêt puisque le MCP traite l'interaction électrostatique de deux particules diélectriques avec des charges réparties à leur surface, hypothèse présente dans la théorie OML pour la charge, et l'effet tunnel. Le MCP s'est avéré fournir une solution rigoureuse qui est en accord

avec la solution plus générale, mais plus complexe de Khachatourian *et al.* [25] exprimée en termes de coordonnées bisphériques. De plus, la solution MCP converge rapidement en utilisant moins de termes dans le développement en série que la solution bisphérique [32]. Le potentiel MCP s'exprime comme [7, 47],

$$\begin{aligned}\Phi_{\mathrm{MCP}}(r, r_i, q_i, r_j, q_j) &\equiv \Phi_{\mathrm{MCP,ij}}(r) \qquad (6.14)\\ &= K\frac{q_i q_j}{r}\\ &- \frac{q_i}{2}\sum_{m=1}^{\infty}\sum_{l=0}^{\infty} A_l \frac{(\varepsilon-1)\,m}{(\varepsilon+1)\,m+1}\frac{(l+m)!}{l!m!}\frac{r_j^{2m+1}}{r^{2m+l+2}}\\ &- \frac{1}{2K}\sum_{l=1}^{\infty} A_l^2 \frac{(\varepsilon+1)\,l+1}{(\varepsilon-1)\,l r_i^{2l+1}}, \qquad (6.15)\end{aligned}$$

où r est la distance entre les centres des particules, q_i et q_j sont les charges des particules i et j, respectivement, et $K = 1/4\pi\varepsilon_0$. Les coefficients multipolaires A_l, qui tiennent compte de la polarisation mutuelle entre les particules, sont les solutions du système d'équations linéaire suivant,

$$\begin{aligned}A_{j_1} &= Kq_1\delta_{j_1,0} - \frac{(\varepsilon-1)\,j_1}{(\varepsilon+1)\,j_1+1}\frac{r_1^{2j_1+1}}{r^{j_1+1}}Kq_j\\ &+ \frac{(\varepsilon-1)\,j_1}{(\varepsilon+1)\,j_1+1}\sum_{j_2=0}^{\infty}\sum_{j_3=0}^{\infty}\frac{(\varepsilon-1)\,j_2}{(\varepsilon+1)\,j_2+1}\frac{(j_1+j_2)!}{j_1!j_2!}\frac{(j_2+j_3)!}{j_2!j_3!}\frac{r_i^{2j_1+1}r_j^{2j_2+1}}{r^{j_1+2j_2+j_3+2}}A_{j_3}. \qquad (6.16)\end{aligned}$$

Le calcul du MCP est exigeant en termes de ressoureces computationnelle. De plus, il est difficile de tirer des conclusions générales de cette formulation. Ainsi, il était souhaitable de trouver une description alternative de l'interaction électrostatique qui conserve la plupart des caractéristiques du MCP. Draine & Sutin [11] ont dérivé une expression simple pour le potentiel d'image d'une charge ponctuelle q_j et d'une sphère de rayon r_i et de la charge q_i,

$$\Phi_{\mathrm{DS}}(r, r_i, q_i, q_j) = K\frac{q_i q_j}{r} - \frac{K\kappa q_j^2 r_i^3}{2r^2\left(r^2 - r_i^2\right)}. \qquad (6.17)$$

où $\kappa = (\varepsilon-1)/(\varepsilon+2)$. Ce potentiel correspond à l'énergie potentielle d'interaction de Coulomb classique plus une correction correspondant au potentiel d'image en raison de la nature diélectrique de la particule sphérique. Pour le problème qui nous intéresse ici, il n'est pas possible de supposer une particule de charge ponctuelle. Par conséquent, une expression plus appropriée devrait inclure l'énergie potentielle d'image de la nanoparticule i dans la nanoparticule j. Un potentiel possible qui satisfait cette condition est,

$$\Phi_{\mathrm{IPA}}(r, r_i, r_j, q_i, q_j) \equiv \Phi_{\mathrm{IPA,ij}} = K\frac{q_i q_j}{r} - \frac{K\kappa q_i^2 r_j^3}{2r^2\left(r^2 - r_j^2\right)} - \frac{K\kappa q_j^2 r_i^3}{2r^2\left(r^2 - r_i^2\right)}. \qquad (6.18)$$

Nous appelons cette formulation l'approximation du potentiel d'image (IPA). A partir de l'équation (6.18), il est facile de trouver une expression analytique pour la force pouvant être utilisée pour trouver $\Phi_{ij,\max}$ (où la dérivée de la force est nulle), comme requis pour calculer le facteur d'augmentation. En plus, IPA reproduit bien le comportement à longue portée du MCP. Ceci est avantageux pour éviter la résolution du système linéaire d'équations MCP pour toutes les distances inter-particules.

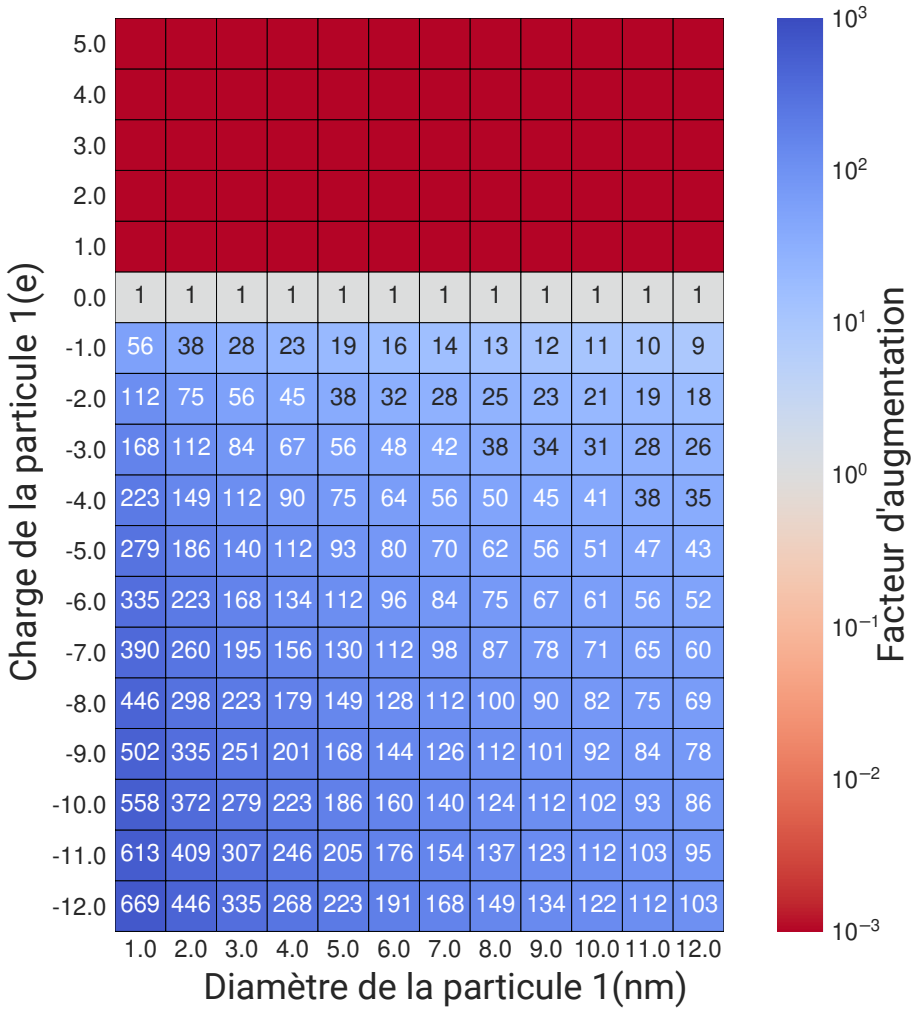

Figure 6.5: Carte du facteur d'augmentation de Coulomb pour de petites particules. La particule 2 a $d_2 = 1\,\text{nm}$ et $q_2 = +e$. Une forte suppression se produit lorsque les charges ont le même signe et le facteur d'augmentation est exactement 1 lorsque la particule 1 est neutre.

6.3.2 Résultats et discussion

D'abord, pour le potentiel de Coulomb, nous montrons dans la figure 6.5 une carte du facteur d'augmentation en fonction de la taille et de la charge de la particule 1, qui coalesce avec une particule 2 de taille 1 nm et de charge $+e$. Comme prévu, le facteur d'augmentation $\eta_{12} > 1$ (zones bleues) se produit pour les particules portant des charges de signes opposés et la suppression $\eta_{12} < 1$ (zones rouges) se produit pour les particules portant des charges de mêmes signes. Pour l'interaction entre une particule chargée et une particule neutre, le facteur d'augmentation est identique à 1.

Le facteur d'augmentation MCP est montré dans la figure 6.6. Contrairement à l'interaction de Coulomb, le facteur d'augmentation ne diminue pas toujours lorsque d_1 augmente pour l'interaction de particles portant des charges opposées, comme on peut le voir dans certains panneaux pour $q_2 = -24e$ et $-238e$. Cet effet est dû à une polarisation induite plus forte dans les particules plus grosses. On

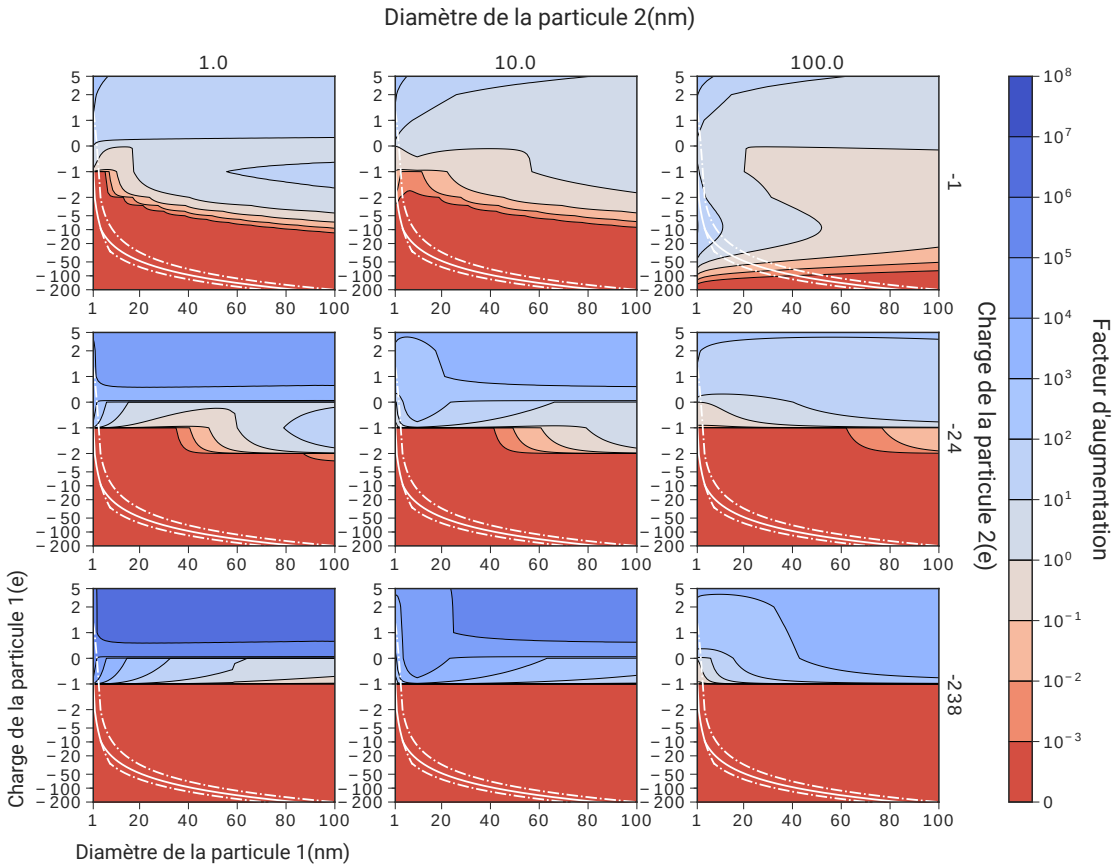

Figure 6.6: Niveaux de contour du facteur d'augmentation MCP.

observe que dans les cas limites $d_2/d_1 \ll 1$ et $d_1/d_2 \ll 1$, le facteur d'augmentation grimpe à mesure que d_1 augmente à condition que le rapport des charges $-q_1/q_2$ soit suffisamment petit. Sinon, l'attraction coulombienne domine la tendance. Pour les particules portant des charges de mêmes signes, on observe que le facteur d'augmentation peut être plus grand que 1 à mesure que d_1 augmente pourvu que la particule 2 soit suffisamment grande. Cependant, ceci a lieu en dehors de la courbe diamètre-charge d'équilibre indiquée sur la figure 6.4.

La figure 6.7 montre une carte du facteur d'augmentation pour les mêmes paires de taille et de charge que celles dans la figure 6.5. Il apparaît que la plupart des valeurs sont augmentées par rapport à la figure 3.4. En particulier, η_{12} pour les particules portant des charges de mêmes signes est plus élevé pour les plus grosses particules. Aussi, l'interaction entre une particule chargée et une particule neutre pour les plus petites particules est considérablement augmentée.

La figure 6.8 montre le facteur d'augmentation pour l'interaction entre des particules neutres 2 de différents diamètres et des particules chargées 1. On peut voir que $\eta_{12} \geq 1$ pour toutes les combinaisons de (d_1, q_1) et d_2. Certaines caractéristiques de la figure 6.8 peuvent être comprises en

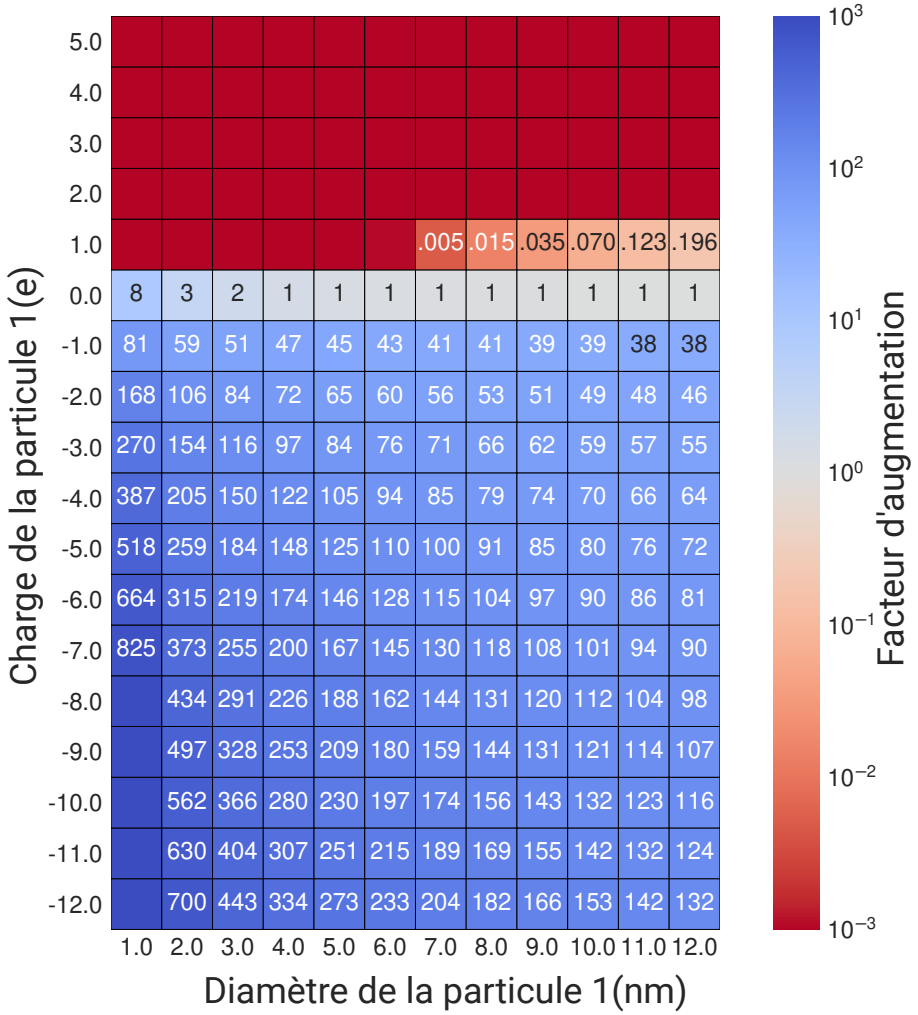

Figure 6.7: Carte du facteur d'augmentation MCP pour les petites particules. La particule 2 a $d_2 = 1$ nm et $q_2 = +e$. La plage de paramètres pour la particule 1 est la même que dans la figure 6.5 pour le cas Coulomb.

considérant la formulation IPA pour $d_2/d_1 \ll 1$,

$$\Phi_{\text{IPA},12}(r_{min}) \approx -K\kappa q_1^2 \frac{d_2^3}{d_1^4}\left(1 - 4\frac{d_2}{d_1}\right). \tag{6.19}$$

En particulier, on peut voir que $\eta_{12} - 1 \propto q_1^2 d_2^3/d_1^4$. La figure 6.9 montre le comportement de η_{12} lorsque $d_1/d_2 \sim 1$. On peut voir que le facteur d'augmentation est plus important lorsque les particules ont des tailles comparables. Il est intéressant de noter que cette tendance est opposée au comportement de la fonction β_{ij}^0 montrée dans la figure 3.1 qui indique que la de coagulation entre particules dissemblables est plus probable.

Il est intéressant de noter que la charge d'équilibre de la particule 1 (courbe blanche continue) se situe dans la région où se produit une coagulation renforcée par l'effet de polarisation, comme le montre la figure 6.8. Ainsi, du point de vue de la coagulation, la conséquence la plus importante de

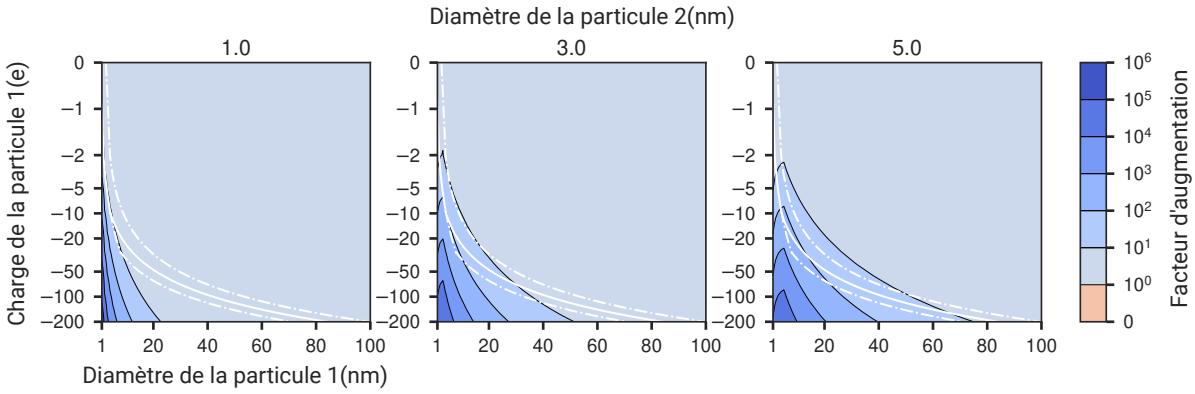

Figure 6.8: Courbes de niveau du facteur d'augmentation MCP pour l'interaction entre des particules neutres 2 de différrents diamètres et des particule chargées 1.

la polarisation induite apparaît être l'augmentation du taux de coagulation des petites particules (qui ont plus de chance d'être neutres que les plus grosses) et des particules chargées.

En comparant les figures 6.7 et 6.9, il apparaît que le facteur d'augmentation pour l'interaction entre une particule chargée et une particule neutre est toujours inférieur à celui pour l'interaction entre des particules de signes opposés pour les mêmes d_1 et q_1. Les facteurs d'augmentation pour des charges élevées de $d_1 = 1$ nm peuvent cependant être plus importants que dans le cas Coulomb de figure 3.4. De tels états de charge élevée sont cependant peu probables pour des particules ayant $d_1 = 1$ nm.

6.4 Influence de la force multipolaire electrostatique et de la force de van der Waals dans la coagulation de nanoparticules de silicium en plasmas froids d'argon silane

La nucléation, la coagulation, la charge et la croissance en surface sont les processus qui déterminent l'évolution de la taille des nanoparticules dans un plasma. Ces processus peuvent être simulés ensemble en résolvant l'équation dynamique générale (GDE). Cette approche a été utilisée dans plusieurs travaux théoriques liés à la croissance des nanoparticules dans les plasmas. Par exemple, Kortshagen *et al.* ont développé un modèle isotrope (0D) comprenant un modèle détaillé de chimie du plasma d'argon-silane couplé à la GDE [29, 6, 5]. De Bleecker *et al.* ont élaboré un modèle de plasma d'acétylène 1D avec transport [10]. Girshick *et al.* ont développé des modèles 1D et 2D en couplant le plasma d'argon-silane aux processus de croissance des nanoparticules [49, 42, 2, 40].

Le taux de coagulation, R_{jpmq}, entre une particule de taille j et charge p, et une particule de taille m et charge q peut être exprimé comme le taux de coagulation pour des sphères neutres en marche aléatoire qui adhèrent au contact, R^0_{jpmq}, multiplié par le facteur d'augmentation, η_{jpmq}, qui dépend

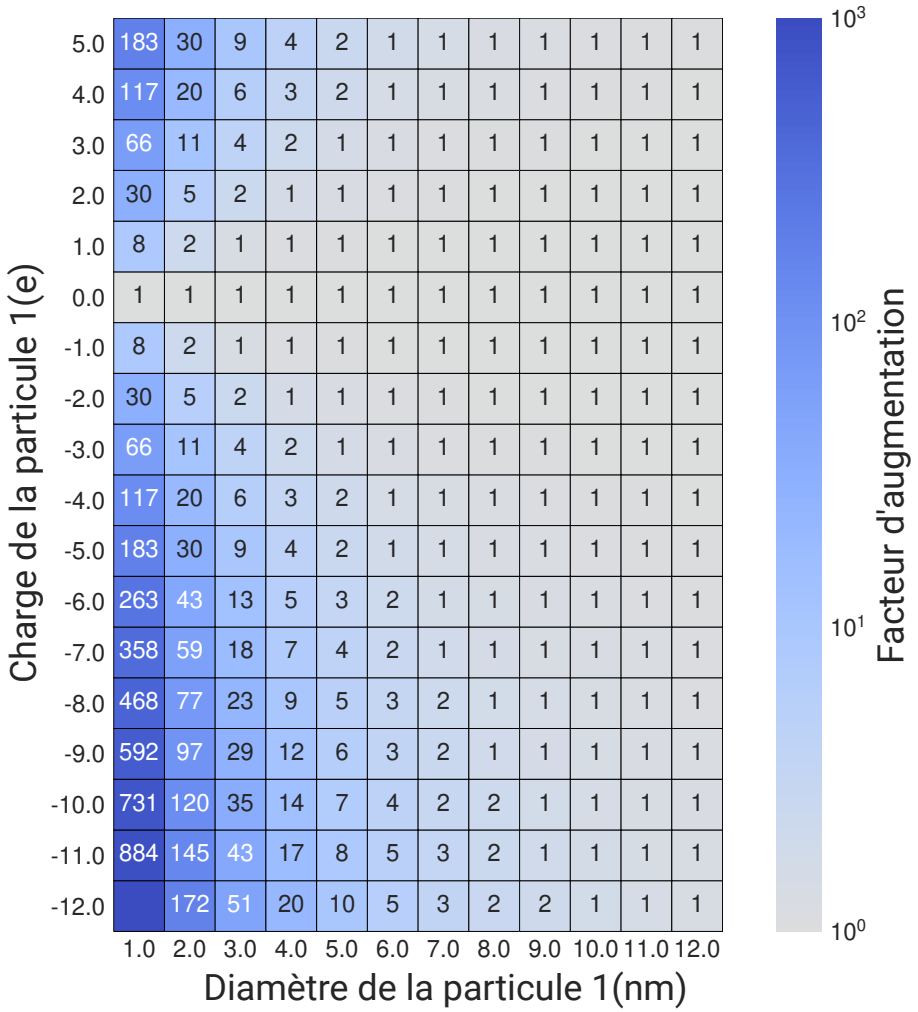

Figure 6.9: Carte du facteur d'augmentation MCP pour de petites particules 1 et une particule 2 neutre de diamètre $d_2 = 1$.

des forces agissant entre les particules [2],

$$R_{jpmq} = \eta_{jpmq} R^0_{jpmq}. \tag{6.20}$$

Ces forces sont essentiellement les forces de van der Waals (vdW) et les forces électrostatiques. Ces dernières résultent des charges acquises par les collisions électroniques et ioniques sur les nanoparticules. Leur charge globale est négative en raison de la plus grande mobilité des électrons par rapport aux ions. Pour les petites particules, les électrons peuvent s'échapper de la surface grâce à l'effet tunnel [20], ce qui réduit le taux de collecte des électrons et augmente la probabilité de formation de particules neutres et chargées positivement. Les nanoparticules étant des objets de taille finie, des effets induits par la polarisation peuvent se produire en plus de l'interaction de Coulomb. Dans la section précédente, nous avons dérivé le facteur d'augmentation pour le potentiel MCP [7] qui fournit une description plus rigoureuse de l'interaction électrostatique entre les particules diélectriques que celle de Huang *et al.* [43]. En particulier, contrairement à cette dernière approche, le MCP ne souffre pas d'une singularité

non-physique au point de contact. Cette propriété nous a permis d'utiliser la théorie OML [3] pour calculer le facteur d'augmentation.

Dans cette section, nous avons résolu la GDE pour un plasma poussiéreux isotrope afin d'étudier l'évolution dans le temps de la taille et de la charge des nanoparticules en utilisant les potentiels électrostatiques MCP, IPA et Coulomb ainsi que l'interaction vdW donnée par le potentiel Hamaker [18]. Cette dernière provient des moments dipolaires fluctuants des molécules dans les particules sphériques. Cependant, l'interaction dipôle-dipôle locale sous-jacente au résultat de Hamaker produit une singularité de la forme $\sim r^{-1}$ au point de contact, où r est la distance la plus courte entre les surfaces des particules sphériques. Cependant, il a été démontré qu'une dérivation appropriée de l'interaction de vdW qui inclut des effets non-locaux conduit à une valeur finie du potentiel de vdW au point de contact [33]. Malgré les efforts déployés pour aller au-delà du résultat de Hamaker, dans ce travail, nous adoptons une approche plus simple qui consiste à régularisation le potentiel de Hamaker en supposant que celui-ci est constant pour $r \leq r_c$, avec r_c un paramètre à étudier. En plus de la complexité d'inclure des effets non-locaux (et des effets de retard [36]) dans l'interaction de vdW, nous justifions cette approche par le fait que les nanoparticules réelles ont une rugosité de surface indéterminée [45] qui adoucit potentiel de vdW près du point de contact [1]. À notre connaissance, une recherche centrée sur l'influence des forces fondamentales sur la croissance des particules dans les plasmas n'a jamais été réalisée à ce jour.

6.4.1 Méthodes

La modélisation de la croissance des particules est traitée par l'équation de dynamique générale (GDE) pour un plasma poussiéreux, qui exprime le taux de variation de la densité des particules de poussière de taille i et charge k [2],

$$\frac{\partial N_{i,k}}{\partial t} + \nabla \Gamma_{i,k} = \left[\frac{\mathrm{d}N_{i,k}}{\mathrm{d}t}\right]_{\text{coag}} + \left[\frac{\mathrm{d}N_{i,k}}{\mathrm{d}t}\right]_{\text{charge}} + \left[\frac{\mathrm{d}N_{i,k}}{\mathrm{d}t}\right]_{\text{nuc}} + \left[\frac{\mathrm{d}N_{i,k}}{\mathrm{d}t}\right]_{\text{collage}}. \tag{6.21}$$

Dans cette expression, $N_{i,k}$ est la densité des nanoparticules, exprimée en nombre par unité de volume (m^{-3}) et $\Gamma_{i,k}$ est le flux spatial local. Les quatre termes sur le côté droit représentent respectivement la coagulation, le chargement, la nucléation et le collage. Dans ce travail, nous négligeons les pertes de nanoparticules vers les parois du réacteur afin de mieux suivre le bilan des nanoparticules. Comme nous considérons un plasma poussiéreux isotrope, nous posons $\nabla \Gamma_{i,k} = 0$.

La coagulation se produit lorsque deux nanoparticules entrent en collision et adhèrent pour former une nouvelle particule avec un volume égal à la somme des volumens des deux particules primaires. L'équation de Smoluchowski décrit le taux de coagulation. Pour résoudre cette équation numériquement, nous avons utilisé la technique du pivot fixe [30] pour le volume et efectué un calcul exact pour la somme des charges. Cette approche hybride est plus précise qu'un pivot fixe à deux composants [48] car elle évite de sectionner la charge, qui est une valeur entière en unités de la charge élémentaire. Partitionnant le volume v dans les sections M et considérant les limites supérieures pour les charges

négatives et positives, $q_{\min}$ et $q_{\max}$, respectivement, la forme discrétisée de l'équation de Smoluchowski s'écrit comme suit,

$$\left[\frac{\mathrm{d}N_{i,k}}{\mathrm{d}t}\right]_{\text{coag}} = \frac{1}{2}\sum_{\substack{\tilde{v}_{i-1}\leq v<\tilde{v}_{i+1}\\ p+q=k}} \xi_i K_{jpmq} N_{jp} N_{mq} - N_{ik}\sum_{p=-q_{\min}}^{q_{\max}}\sum_{m=1}^{M} K_{ikmp} N_{mp}. \tag{6.22}$$

où les indices j, m, p et q parcourent toute leur range de valeurs dans la somme. Dans ces équations, K est le noyau de coagulation en $\mathrm{m^3 s^{-1}}$, $v = \tilde{v}_j + \tilde{v}_m$ est le volume après la coagulation, $\tilde{v}_i$ est le volume représentatif inclus dans la section i, qui est définie par l'intervalle $\left[\frac{1}{2}(\tilde{v}_{i-1}+\tilde{v}_i), \frac{1}{2}(\tilde{v}_i+\tilde{v}_{i+1})\right]$, et le facteur de pondération est donné par,

$$\xi_i = \begin{cases} \frac{\tilde{v}_{i+1}-v}{\tilde{v}_{i+1}-\tilde{v}_i}, & \tilde{v}_i \leq v \leq \tilde{v}_{i+1} \\ \frac{v-\tilde{v}_{i-1}}{\tilde{v}_i-\tilde{v}_{i-1}}, & \tilde{v}_{i-1} \leq v \leq \tilde{v}_i \end{cases}. \tag{6.23}$$

La charge des nanoparticules est liée au plasma via les fréquences de collision des électrons, ν_e, et des ions positifs, ν_+, avec des nanoparticules comme indiqué par la théorie OML [43]. De plus, la fréquence tunnel ν_T est nécessaire pour décrire les électrons qui s'échappent du puits du potentiel d'affinité [20, 43]. Le taux de chargement peut s'exprimer comme suit,

$$\begin{aligned}\left[\frac{\mathrm{d}N_{i,k}}{\mathrm{d}t}\right]_{\text{charge}} &= \left(\nu_{+(i,k-1)} + \nu_{T(i,k-1)}\right) N_{i,k-1} + \nu_{e(i,k+1)} N_{i,k+1} \\ &\quad - \left(\nu_{+(i,k)} + \nu_{T(i,k)} + \nu_{e(i,k)}\right) N_{ik},\end{aligned} \tag{6.24}$$

où les fréquences OML ν_e, ν_+ et ν_T sont données dans la section 3.2.3. Il est important de remarquer que cette approche est purement déterministe car elle néglige le comportement stochastique du processus de chargement électrique [14].

La nucléation est la formation des plus petites nanoparticules par les processus de chimie du plasma. Elle n'intervient que dans la première section de volume. Dans cette étude, qui se concentre sur le processus de coagulation, nous suivons [2] et supposons que le taux de nucléation prend la valeur constante $J_{00} = 10^{18}\ \mathrm{m^{-3}\ s^{-1}}$. Ainsi, le taux de nucléation s'exprime comme suit,

$$\left[\frac{\mathrm{d}N_{i,k}}{\mathrm{d}t}\right]_{\text{nuc}} = \delta_{i,0}\delta_{k,0} J_{00}, \tag{6.25}$$

où δ est la fonction delta de Kronecker.

Le processus de croissance en surface est calculé de manière cohérente avec le modèle sectionnel par la formule à deux points,

$$\left[\frac{\mathrm{d}N_i}{\mathrm{d}t}\right]_{\text{collage}} = \frac{I_{i-1}N_{i-1}}{v_i - v_{i-1}} - \frac{I_i N_i}{v_{i+1} - v_i}. \tag{6.26}$$

En plus de l'interaction électrostatique, expliqué dans la section précédente, nous considérons l'interaction de vdW dans la formulation de Hamaker [18],

$$\Phi_{\mathrm{vdW}}(\tilde{r}, r_{mj}) = -\frac{A_H}{6}\left\{\frac{2r_{mj}}{\tilde{r}^2-(1+r_{mj})^2}+\frac{2r_{mj}}{\tilde{r}^2-(1-r_{mj})^2}+\ln\left[\frac{\tilde{r}^2-(1+r_{mj})^2}{\tilde{r}^2-(1-r_{mj})^2}\right]\right\}, \tag{6.27}$$

où A_H est la constante de Hamaker, qui est $A_H \approx 20\times10^{-20}$ J pour le silicium [23], $r_{mj} = r_m/r_j$ et $\tilde{r} = 1 + r_{mj} + r/r_j$, avec r la distance entre les surfaces des particules en interaction. Évidemment, l'équation 6.27 a une singularité de la forme $\sim r^{-1}$ près de la distance de contact théorique $r = 0$. La singularité non-physique de (6.27) se traduit par un facteur d'augmentation infini. Pour contourner ce problème, nous utilisons un potentiel de vdW régularisé à courte distance de séparation comme,

$$\tilde{\Phi}_{\mathrm{vdW}}(\tilde{r}, r_{mj}) = \begin{cases} \Phi_{\mathrm{vdW}}(\tilde{r}, r_{mj}), & r > r_c \\ \Phi_{\mathrm{vdW}}(\tilde{r}_c, r_{mj}), & r \le r_c, \end{cases} \tag{6.28}$$

où $\tilde{r}_c = 1 + r_{mj} + r_c/r_j$ et r_c est un paramètre libre dont l'influence sera étudiée. Comme limite inférieure pour r_c, nous utilisons deux fois la rugosité de surface minimale d'une nanoparticule de silicium sphérique, quantité que nous estimons comme le rayon d'un atome de silicium $R_{\mathrm{Si}} \approx 1.1$Å. Par conséquent, nous considérerons $r_c \ge 2R_{\mathrm{Si}} = 2.1$Å.

Pour calculer l'évolution du plasma couplée à la charge des nanoparticules, nous avons utilisé un modèle de plasma isotrope simplifié [31, 37] qui conserve certaines caractéristiques essentielles des plasmas d'argon-silane telles que l'excitation de l'Ar et du SiH_4, l'ionisation du silane et sa dissociation en SiH_3 etSiH_2. Le modèle est composé des 11 espèces e, Ar^+, Ar*, $SiH_3{}^+$, SiH_2, SiH_3, SiH_4, SiH_4^{v13}, SiH_4^{v24}, H et Ar, pour lesquelles les taux de réactions ont été obtenus des sections efficaces et de la fonction de distribution en énergie des électrons calculée par le logiciel `BOLSIG+` [17]. Les taux de réaction obtenus ainsi que ceux tirés de la littérature sont donnés dans le tableau 4.1.

Les densités de Ar et de SiH_4 sont supposées constantes en raison de leur grande abondance tandis que les densités des espèces restantes, à l'exception de $SiH_3{}^+$, ont été calculées en résolvant le système d'équations différentielles,

$$\frac{\mathrm{d}n_\alpha}{\mathrm{d}t} = \sum_i k_i \nu_i n_\gamma n_{\gamma'} + G_\alpha - S_\alpha, \tag{6.29}$$

où α identifie l'espèce du plasma, ν_i est le taux de la réaction i entre les espèces γ et γ', et G_α et S_α sont respectivement les taux de gain et de perte par unité de volume de l'espèce α. Pour garantir la neutralité du plasma, nous avons calculé la densité $n_{SiH_3{}^+}$ après chaque pas de temps à partir de l'équation de bilan de la charge, qui comprend les ions, les électrons et les nanoparticules.

Le terme G_α décrit le gain d'électrons par effet tunnel. Pour les électrons et les ions, le terme S_α inclut les pertes de nanoparticules dues au chargement [49]. Pour toutes les espèces, S_α inclut également les pertes de particules vers les parois du réacteur. Pour ces pertes, $S_\alpha \approx \Gamma_\alpha A_r/V_r$ où Γ_α est le flux de particules, $A_r = 2\pi RL$ est l'aire du réacteur cylindrique de rayon R, où L est l'espacement entre les électrodes de la décharge capacitive, et $V_r = \pi R^2 L$ est le volume du réacteur.

Pour les particules chargées, $\Gamma_\alpha = h_i u_B$, où $h_i = (\sqrt{3 + L/2\lambda_i})^{-1}$ est un facteur géométrique, λ_i est le parcours libre moyen, et u_B est la vitesse de Bohm. Pour les espèces neutres, $\Gamma_\alpha = h_n v_T/4$, où v_T est la vitesse thermique. Pour les neutres, le facteur géométrique est $h_n = (1 + (L/2)v_T/(4D_n))^{-1}$ et D_n est le coefficient de diffusion.

Le plasma est maintenu par la densité de puissance absorbée P_ε. L'équation pour la densité d'énergie des électrons $n_\varepsilon = \varepsilon n_e$ s'écrit comme,

$$\frac{\mathrm{d}n_\varepsilon}{\mathrm{d}t} = \frac{P_\varepsilon}{V_r} - n_e \sum_i \varepsilon_i k_i \nu_i n_\gamma - S_\varepsilon. \tag{6.30}$$

Dans cette expression, ε_i est l'énergie perdue par un électron après la réaction i avec l'espèce du plasma γ. Pour les collisions élastiques, $\varepsilon_\mathrm{i} = 3\varepsilon m_e/m_\gamma$. Le terme de perte S_ε comprend la densité de puissance transférée aux nanoparticules par capture des électrons et celle associée à la perte d'électrons sur les électrodes $\Gamma_\varepsilon A_r/V_r$, où,

$$\Gamma_\varepsilon = u_B \left(\frac{5}{3} n_\varepsilon + e V_s n_e \right). \tag{6.31}$$

Dans cette expression, $V_s = V_\mathrm{pic}/4$ où V_pic est la tension de voltage pic de la source RF.

Ce modèle de plasma réduit a permis d'obtenir les fréquences OML et tunnel nécessaires pour calculer la charge des nanoparticules.

6.4.2 Résultats et discussion

Nous avons étudié l'influence de l'interaction électrostatique sur la croissance des particules et l'influence des interactions électrostatiques et vdW combinées. Les résultats suivants ont été obtenus en utilisant un diamètre minimum des nanoparticules (première section de volume) de $d_0 = 0.75\,\mathrm{nm}$. Les sections de volume suivent la progression géométrique $v_{i+1} = 1.1599 v_i$. La GDE éq. 6.21, est discrétisée en utilisant des différences finies sur $M = 100$ sections de volume et les charges sont réparties entre $q_\mathrm{min} = -60e$ et $q_\mathrm{max} = +5e$. Les dimensions du réacteur sont $L = 4\,\mathrm{cm}$, $R = 6\,\mathrm{cm}$, avec un volume $V_r = \pi R^2 L$. La pression est $p = 0.1\,\mathrm{Torr}$, et la température est $T = 300\,\mathrm{K}$. Le gaz d'argon-silane est mélangé avec le rapport Ar: SiH_4 = 30 : 1. La tension de voltage pic est $V_\mathrm{pic} = 100\,\mathrm{V}$, tandis que la puissance injectée est maintenue à $eV_r P_\varepsilon = 1\,\mathrm{eVm^3 s^{-1}}$. Les détails sur les calculs numériques sont fournis dans l'annexe.

Dans la figure 6.10, nous comparons les effets des trois modèles de potentiel électrostatique sur la croissance des nanoparticules en utilisant une densité initiale de particules neutres de $10^{10}\ \mathrm{m^{-3}}$ placée dans la première section de volume. Comme on peut le voir dans la figure 6.10, le volume total des particules augmente dans le temps à cause de la nucléation continue et de la croissance en surface. La densité des particules augmente initialement et atteint un maximum avant de se stabiliser à une valeur inférieure. Ce comportement s'explique par le fait que la densité initiale des particules est insuffisante pour déclencher la coagulation. À mesure que la densité des petites particules augmente à cause de la nucléation, le taux de coagulation augmente et devient finalement supérieur au taux de nucléation,

entraînant une diminution de la densité des particules. Cette accélération du taux de coagulation est en partie due à une plus grande efficacité de la coagulation entre des particules plus grosses et entre des particules de tailles différentes. Plus tard, à mesure que les particules grossissent, elles peuvent porter plus de charges négatives et la répulsion de Coulomb ralentit la coagulation. La coagulation et la nucléation atteignent finalement un équilibre et la densité des particules reste constante.

La charge négative totale diminue dans le temps après un chargement initial rapide à un taux qui est pratiquement le même pour les trois potentiels. Cette diminution dans le temps est principalement due à la diminution de la densité électronique. Elle est due aussi en partie au fait que la charge que peut transporter une particule résultant de la coagulation de deux particules primaires de rayon R_1 et R_2 est inférieure à la somme des charges que ces deux particules primaires peuvent porter, comme le montre l'inégalité $R_1 + R_2 > (R_1^3 + R_2^3)^{1/3}$ où l'on suppose que la charge est proportionnelle au rayon. Cet effet contribuera à abaisser davantage la charge négative totale pour le MCP et l'IPA par rapport au potentiel de Coulomb car la coagulation est moins efficace pour ce dernier (comme cela est aussi observé dans la figure 4.1).

Le volume total de nanoparticules est plus grand dans le cas de Coulomb en raison du taux de coagulation plus lent. Cela peut se comprendre en considérant que la croissance de surface opère sur un plus grand nombre de particules dans le cas de Coulomb et que le taux de croissance du volume de deux particules primaires de rayon R_1 et R_2 est plus grand que celui de la particule coalescée, comme on peut s'en convaincre en utilisant l'inégalité $R_1^2 + R_2^2 > (R_1^3 + R_2^3)^{2/3}$.

L'énergie moyenne des électrons augmente car il y a de moins en moins d'électrons disponibles pour absorber la densité de puissance injectée fixe P_ϵ. L'augmentation de l'énergie moyenne des électrons est plus rapide pour l'interaction coulombienne par rapport au MCP et IPA car les nanoparticules sont plus chargées.

Les figures 6.11a et 6.11b représentent la densité de particules intégrée sur les charges et sur les diamètres, respectivement, à 0.2 s et 1.0 s pour les mêmes cas. On peut voir dans figure 6.11a que notre modèle donne une distribution bimodale en taille à 1.0 s. Des distributions en taille qualitativement similaires ont été observées dans des experiences [51] et dans d'autres études numériques [28, 2]. Le premier pic coïncide avec le plus petit diamètre des particules nucléées (0.75 nm). Il est dû à la génération continue de petites particules, tandis que le deuxième pic, autour de 25 nm, est dû à la fois à la coagulation et à la croissance en surface. On observe que le potentiel de Coulomb produit moins de grosses particules à 0.2 s par rapport au MCP et à l'IPA. Ceci explique la plus grande densité de particules dans les premiers temps observée dans figure 6.10. Cependant, à 1.0 s, le potentiel de Coulomb a produit plus de grosses particules autour du deuxième pic que le MCP et l'IPA. Cet effet est lié à la diminution de la densité électronique, comme le montre figure 6.10c, qui diminue la charge des particules et favorise la coagulation parmi les particules plus nombreuses du cas Coulomb.

La figure 6.11b montre que le potentiel de Coulomb produit une distribution plus haute mais plus étroite que les deux autres potentiels. Cependant, le nombre de particules portant une charge plus

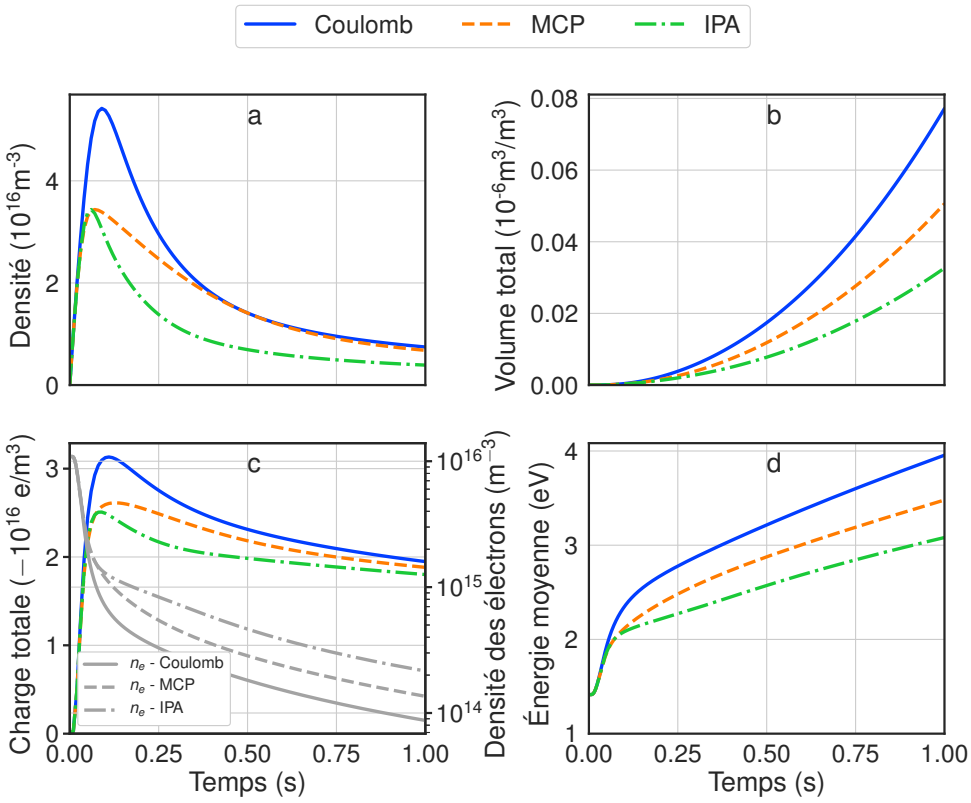

Figure 6.10: Effet des potentiels MCP, IPA et Coulomb sur (a) la densité, (b) le volume total, (c) la charge totale, la densité d'électrons, et (d) l'énergie moyenne en fonction du temps. Les calculs ont été effectués en utilisant le modèle de croissance complet sans l'interaction de vdW.

faible est plus important que pour le MCP et l'IPA. Cela explique la charge totale plus importante observée dans la figure 6.10. On note que tous les modèles prédisent des particules chargées positivement et un pic pour les particules neutres. Ce pic résulte de la coagulation rapide de particules de charges opposées. Il est cependant plus prononcé pour le MCP et l'IPA que pour le potentiel de Coulomb en raison de l'attraction induite par la polarisation dans les cas MCP et IPA. La figure 6.12 montre une comparaison entre les processus de croissance des particules pour les trois potentiels électrostatiques combinés avec le potentiel vdW vdW avec $r_c = 2.1\,\text{Å}$. Les résultats pour le MCP sont également présentés à titre de comparaison. Pour une si petite valeur de r_c, les résultats pour les trois potentiels électrostatiques combinés avec le potentiel vdW sont assez similaires. Cela est attribuable à la dominance de l'interaction de vdW sur l'interaction électrostatique à une courte distance interparticulaire, qui affecte le facteur d'augmentation éq. 6.6 par le terme $\Phi_{jpmq}(r_{\text{min}})$. Cependant, le potentiel électrostatique domine le potentiel de vdW à une plus grande distance interparticulaire puisque le premier va comme $\sim r^{-1}$ (la polarisation induite est négligeable à grande distance) tandis que le potentiel vdW (non retardé) va comme $\sim r^{-6}$, comme le montre l'expression de Hamaker (6.27) pour $r \gg r_c$. Par conséquent, le terme Φ^{max}_{jpmq} de l'éq. 6.6 dépend faiblement de l'interaction de vdW. Ce terme, qui

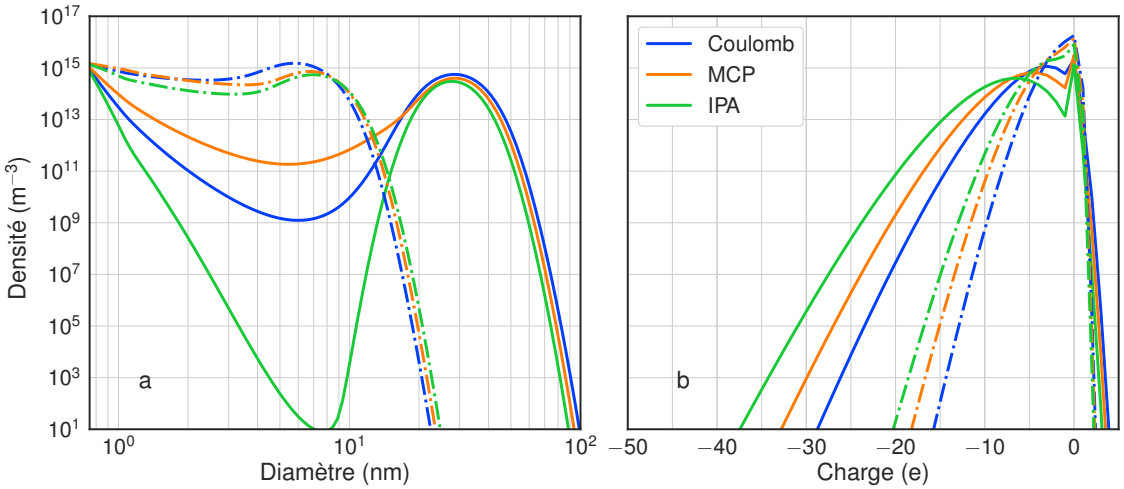

Figure 6.11: Distributions de nanoparticules à 0.2 s (traits discontinus) et 1.0 s, en considérant le modèle de croissance complet pour les potentiels MCP, IPA et Coulomb sans interaction vdW. a) Densité des particules intégrée sur les charges. b) Densité des particules intégrée sur les diamètres.

exprime la répulsion coulombienne à travers le facteur exponentiel, ralentit efficacement la coagulation au stade avancé de la croissance entre les particules fortement chargées.

La figure 6.13 montre la taille des nanoparticules et la distribution des charge pour l'interaction MCP+vdW avec $r_c = 2.1\,\text{Å}$ pour le modèle de croissance complet à 1 s. Comme dans le cas des interactions purement électrostatiques (figure 6.11) la distribution est bimodale. La forme décalée du plus petit lobe du côté des charges négatives est due au courant tunnel. Les électrons quittent la surface des nanoparticules à un rythme plus rapide que ceux arrivant du plasma. La forme du plus grand lobe est plus lisse car le courant tunnel est négligeable pour les particules plus grosses. On observe que le pic du deuxième lobe se produit pour une taille et une plage similaires à celles des cas purement électrostatiques.

6.5 Conclusions et travaux futurs

Nous avons montré l'importance de l'interaction électrostatique dans la coagulation des nanoparticules dans les plasmas poussiéreux. La polarisation induite apparaît être particulièrement importante dans la coagulation entre une particule neutre et une particule chargée. Aussi, nous avons reproduit la distribution bimodale des tailles observée dans des expériences.

Dans ce travail, nous avons introduit l'interaction de van der Waals pour calculer le facteur d'augmentation dans la coagulation. Nous avons réalisé une étude numérique qui montre que l'interaction de van der Waals est importante à prendre en compte dans la modélisation des plasmas poussiéreux. Cependant, les résultats dépendent fortement de la façon dont le potentiel de van der Waals est régularisé près du point de contact des particules.

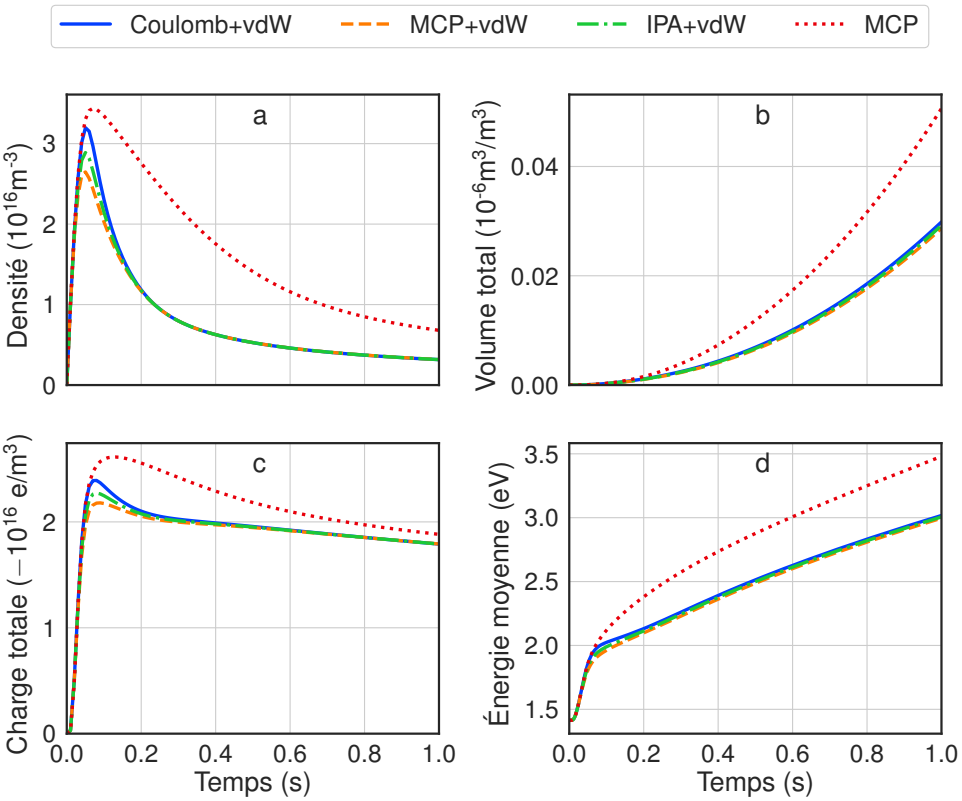

Figure 6.12: Effet des interactions Coulomb+vdW, MCP+vdW, IPA+vdW et MCP sur (a) la densité de particules, (b) le volume total, (c) la charge totale, et (d) l'énergie moyenne des électrons en fonction du temps. Les calculs ont été effectués en utilisant le modèle de croissance complet.

Les difficultés de ce type de simulations sont les suivantes: (i) au moins deux paramètres sont nécessaires pour décrire une particule de poussière, la charge et la taille, (ii) l'évolution des nanoparticules doitt être résolue d'une manière auto-cohérente avec le plasma, (iii) la chimie du plasma peut impliquer de très nombreuses réactions, (iv) les section efficaces pour ces réactions ne sont pas toujours connues et elles doivent parfois faire l'objet d'approximations, (v) en ajoutant un degré de liberté spatial le problème devient très exigeant en temps de calcul.

Une comparaison des modèles de croissance des nanoparticules 1D / 2D avec les modèles 0D et les expériences pourrait être utile pour déterminer la précision des simplifications et des hypothèses de ce travail. Nous présentons quelques perspectives concernant le développement d'un modèle 1D dans l'annexe.

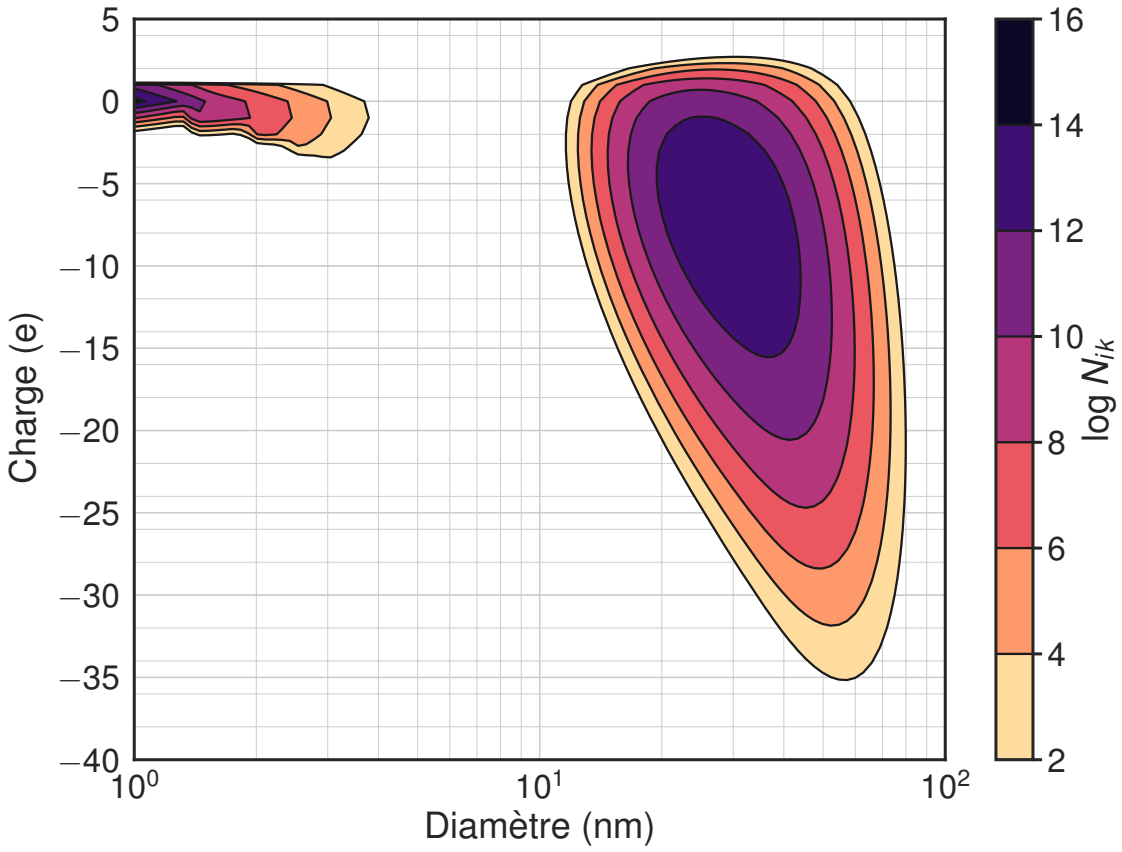

Figure 6.13: Taille des nanoparticules et distribution des charges d'après le modèle de croissance complet pour MCP+vdW à 1 s. Les niveaux de couleur représentent le logarithme de la densité N_{ik}. Dans le premier lobe, le courant tunnel limite la charge de façon abrupte. Le second lobe a une forme lisse. Ici les charges résultent de l'équilibre des courants OML classiques.

6.6 Bibliographie

[1] P. Aashish and William H. M. Computations of Lifshitz–van der Waals interaction energies between irregular particles and surfaces at all separations for resuspension modelling. *J. Phys. D: Appl. Phys.*, 46:425306, 2013.

[2] P. Agarwal and S. L. Girshick. Sectional modeling of nanoparticle size and charge distributions in dusty plasmas. *Plasma Sources Sci. Technol.*, 21(5):055023, October 2012.

[3] J. E. Allen. Probe theory - the orbital motion approach. *Phys. Scr.*, 45(5):497, May 1992.

[4] A. S. Amadon and W. H. Marlow. Cluster-collision frequency. II. Estimation of the collision rate. *Physical Review A*, 43(10):5493–5499, May 1991.

[5] U. Bhandarkar, U. Kortshagen, and S. L. Girshick. Numerical study of the effect of gas temperature on the time for onset of particle nucleation in argon–silane low-pressure plasmas. *J. Phys. D: Appl. Phys.*, 36(12):1399, 2003.

[6] U. Bhandarkar, M. T. Swihart, S. L. Girshick, and U. R. Kortshagen. Modelling of silicon hydride clustering in a low-pressure silane plasma. *J. Phys. D: Appl. Phys.*, 33(21):2731, November 2000.

[7] E. Bichoutskaia, A. L. Boatwright, A. Khachatourian, and A. J. Stace. Electrostatic analysis of the interactions between charged particles of dielectric materials. *The Journal of Chemical Physics*, 133(2):024105, July 2010.

[8] A. Bouchoule, A. Plain, L. Boufendi, J. Ph Blondeau, and C. Laure. Particle generation and behavior in a silane-argon low-pressure discharge under continuous or pulsed radio-frequency excitation. *Journal of Applied Physics*, 70(4):1991–2000, August 1991.

[9] L. Boufendi and A. Bouchoule. Particle nucleation and growth in a low–pressure argon–silane discharge. *Plasma Sources Sci. Technol.*, 3(3):262, August 1994.

[10] K. De Bleecker, A. Bogaerts, and W. Goedheer. Modelling of nanoparticle coagulation and transport dynamics in dusty silane discharges. *New J. Phys.*, 8(9):178–178, September 2006.

[11] B. T. Draine and Brian Sutin. Collisional charging of interstellar grains. *The Astrophysical Journal*, 320:803, September 1987.

[12] V. E. Fortov, A. G. Khrapak, S. A. Khrapak, V. I. Molotkov, and Petrov Petrov. Dusty plasmas. *Physics - Uspekhi*, 47:447–492, 2004.

[13] A. A. Fridman, L. Boufendi, T. Hbid, B. V. Potapkin, and A. Bouchoule. Dusty plasma formation: Physics and critical phenomena. Theoretical approach. *Journal of Applied Physics*, 79(3), February 1996.

[14] F. Galli and U. Kortshagen. Charging, Coagulation, and Heating Model of Nanoparticles in a Low-Pressure Plasma Accounting for Ion #x2013;Neutral Collisions. *IEEE Transactions on Plasma Science*, 38(4), April 2010.

[15] M. Gatti and U. Kortshagen. Analytical model of particle charging in plasmas over a wide range of collisionality. *Physical Review E*, 78(4):046402, October 2008.

[16] D. J. Griffiths. *Introduction to Quantum Mechanics*, chapter The WKB Approximation, pages 315–339. Pearson Prentice Hall, Upper Saddle River, NJ, 2nd edition, 2005.

[17] G. J. M. Hagelaar and L. C. Pitchford. Solving the Boltzmann equation to obtain electron transport coefficients and rate coefficients for fluid models. *Plasma Sources Sci. Technol.*, 14(4):722, November 2005.

[18] H. C. Hamaker. The London-van der Waals attraction between spherical particles. *Physica IV*, 10:1058, November 1937.

[19] W.M. Haynes. *CRC Handbook of Chemistry and Physics, 97th Edition*. CRC Press, 2016.

[20] L. C. J. Heijmans, F. M. J. H. van de Wetering, and S. Nijdam. Comment on 'The effect of single-particle charge limits on charge distributions in dusty plasmas'. *Journal of Physics D: Applied Physics*, 49(38):388001, 2016.

[21] C. Hollenstein, J.-L. Dorier, J. Dutta, L. Sansonnens, and A. A. Howling. Diagnostics of particle genesis and growth in RF silane plasmas by ion mass spectrometry and light scattering. *Plasma Sources Sci. Technol.*, 3(3):278, August 1994.

[22] D. D. Huang, J. H. Seinfeld, and K. Okuyama. Image potential between a charged particle and an uncharged particle in aerosol coagulation—enhancement in all size regimes and interplay with van der waals forces. *Journal of colloid and interface science*, 141(1):191–198, 1991.

[23] J. N. Israelachvili. Intermolecular and Surface Forces. In *Intermolecular and Surface Forces (Third Edition)*. Academic Press, San Diego, January 2011.

[24] H. Kersten and M. Wolter. Complex (dusty) plasmas: Application in material processing and tools for plasma diagnostics. In Michael Bonitz, Norman Horing, and Patrick Ludwig, editors, *Introduction to Complex Plasmas*, number 59 in Springer Series on Atomic, Optical, and Plasma Physics, pages 395–442. Springer Berlin Heidelberg, January 2010.

[25] A. Khachatourian, H.-K. Chan, A. J. Stace, and E. Bichoutskaia. Electrostatic force between a charged sphere and a planar surface: A general solution for dielectric materials. *The Journal of Chemical Physics*, 140(7):074107, February 2014.

[26] S. A. Khrapak, S. V. Ratynskaia, A. V. Zobnin, A. D. Usachev, V. V. Yaroshenko, M. H. Thoma, M. Kretschmer, H. Höfner, G. E. Morfill, O. F. Petrov, and V. E. Fortov. Particle charge in the bulk of gas discharges. *Physical Review E*, 72(1):016406, July 2005.

[27] C. Killer, M. Mulsow, and A. Melzer. Spatio-temporal evolution of the dust particle size distribution in dusty argon rf plasmas. *Plasma Sources Sci. Technol.*, 24(2):025029, April 2015.

[28] D.-J. Kim and K.-S. Kim. Analysis on nanoparticle growth by coagulation in silane plasma reactor. *AIChE J.*, 48(11):2499–2509, November 2002.

[29] U. Kortshagen and U. Bhandarkar. Modeling of particulate coagulation in low pressure plasmas. *Phys. Rev. E*, 60(1):887–898, July 1999.

[30] Sanjeev Kumar and D. Ramkrishna. On the solution of population balance equations by discretization—I. A fixed pivot technique. *Chemical Engineering Science*, 51(8):1311–1332, April 1996.

[31] M. A. Lieberman and A. J. Lichtenberg. *Principles of Plasma Discharges and Materials Processing*. John Wiley & Sons, April 2005.

[32] E. B. Lindgren, H.-K. Chan, A. J. Stace, and E. Besley. Progress in the theory of electrostatic interactions between charged particles. *Physical Chemistry Chemical Physics*, 18(8):5883–5895, February 2016.

[33] Y. Luo, R. Zhao, and J. B. Pendry. van der Waals interactions at the nanoscale: The effects of nonlocality. *Proceedings of the National Academy of Sciences*, 111(52):18422–18427, 2014.

[34] M. Mamunuru, R. Le Picard, Y. Sakiyama, and S. L. Girshick. The Existence of Non-negatively Charged Dust Particles in Nonthermal Plasmas. *Plasma Chem Plasma Process*, 37(3):701–715, May 2017.

[35] André Melzer. *Physics of Dusty Plasmas: An Introduction*. Number 962 in Lecture Notes in Physics. Springer International Publishing, 1st edition, 2019.

[36] T. Miyao and H. Spohn. The retarded van der waals potential: Revisited. *J. Math. Phys.*, 50(7):072103, August 2009.

[37] D. D. Monahan and M. M. Turner. On the global model approximation. *Plasma Sources Sci. Technol.*, 18(4):045024, September 2009.

[38] H. Ouyang, R. Gopalakrishnan, and Jr. C. J. Hogan. Nanoparticle collisions in the gas phase in the presence of singular contact potentials. *The Journal of Chemical Physics*, 137(6):064316, August 2012.

[39] R. Le Picard and S. L. Girshick. The effect of single-particle charge limits on charge distributions in dusty plasmas. *Journal of Physics D: Applied Physics*, 49(9):095201, 2016.

[40] R. Le Picard, A. H. Markosyan, D. H. Porter, S. L. Girshick, and M. J. Kushner. Synthesis of Silicon Nanoparticles in Nonthermal Capacitively-Coupled Flowing Plasmas: Processes and Transport. *Plasma Chem Plasma Process*, 36(4):941–972, May 2016.

[41] L. Ravi. *Numerical Study of Nanodusty Plasmas*. PhD thesis, 2008.

[42] L. Ravi and S. L. Girshick. Coagulation of nanoparticles in a plasma. *Phys. Rev. E*, 79(2):026408, February 2009.

[43] B. Santos, L. Cacot, C. Boucher, and F. Vidal. Electrostatic enhancement factor for the coagulation of silicon nanoparticles in low-temperature plasmas. *Plasma Sources Sci. Technol.*, 28(4):045002, April 2019.

[44] M. G. Sceats. Brownian coagulation in aerosols—the role of long range forces. *Journal of Colloid and Interface Science*, 129(1):105–112, April 1989.

[45] G. S. Selwyn, J. Singh, and R. S. Bennett. Insitu laser diagnostic studies of plasma-generated particulate contamination. *Journal of Vacuum Science & Technology A*, 7(4):2758–2765, July 1989.

[46] P. Shukla. Colloquium: Fundamentals of dust-plasma interactions. *Rev. Mod. Phys.*, 81(1):25–44, 2009.

[47] A. J. Stace and BichoutskaiaE. Reply to the 'Comment on "Treating highly charged carbon and fullerene clusters as dielectric particles"' by H. Zettergren and H. Cederquist, Phys. Chem. Chem. Phys., 2012, 14, DOI: 10.1039/c2cp42883k. *Physical Chemistry Chemical Physics*, 14(48):16771–16772, November 2012.

[48] H. M. Vale and T. F. McKenna. Solution of the Population Balance Equation for Two-Component Aggregation by an Extended Fixed Pivot Technique. *Ind. Eng. Chem. Res.*, 44(20):7885–7891, September 2005.

[49] S. J. Warthesen and S. L. Girshick. Numerical simulation of the spatiotemporal evolution of a nanoparticle–plasma system. *Plasma Chem Plasma Process*, 27(3):292–310, June 2007.

[50] Y. Watanabe, M. Shiratani, H. Kawasaki, S. Singh, T. Fukuzawa, Y. Ueda, and H. Ohkura. Growth processes of particles in high frequency silane plasmas. *Journal of Vacuum Science & Technology A*, 14(2):540–545, March 1996.

[51] Y. Watanabe, M. Shiratani, and K. Koga. Nucleation and subsequent growth of clusters in reactive plasmas. *Plasma Sources Sci. Technol.*, 11(3A):A229, August 2002.

[52] Y. Watanabe, M. Shiratani, and M. Yamashita. Study of growth kinetics and behaviour of particles in a helium-silane RF plasma using laser diagnostic methods. *Plasma Sources Sci. Technol.*, 2(1):35, February 1993.

7 APPENDIX I Numerical methods

7.1 Plasma fluid model

Scharfetter-Gummel Method. This method is numerically convenient to discretise the particle (and electron energy) flux, where we have steep spatial variations of the density n_α. The flux is rewritten as follows [12, 2],

$$\Gamma_{\alpha,i} = -D_{\alpha,i}\frac{\mathrm{d}n_\alpha}{\mathrm{d}x} - q_\alpha \mu_{\alpha,i} n_\alpha \frac{\mathrm{d}\phi}{\mathrm{d}x},$$

where q_α, μ_α, and D_α, represent the charge, mobility and diffusion coefficient for the α species at position i. The one-dimensional spatial discretization, shown in figure 7.1, is given by,

$$\Gamma_{\alpha,i} = -\frac{D^k_{\alpha,i}}{\Delta x}\left[f_1(z_i)n^{k+1}_{\alpha,i+\frac{1}{2}} - f_2(z_i)n^{k+1}_{\alpha,i-\frac{1}{2}}\right],$$

along with the Bernoulli function,

$$f_1(z) \equiv \frac{z}{e^z - 1}, \qquad f_2(z) = \frac{ze^z}{e^z - 1} = f_1(-z),$$

and,

$$z_i \equiv -\frac{q_\alpha \mu^k_{\alpha,i}}{D^k_{\alpha,i}}\left(\phi^{k+1}_{i+\frac{1}{2}} - \phi^{k+1}_{i-\frac{1}{2}}\right).$$

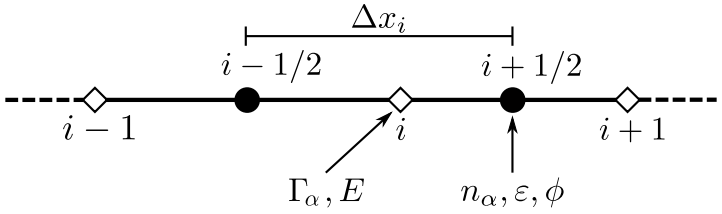

Figure 7.1: Flux spatial discretization

Drift-diffusion equations. The drift-diffusion equation for particle (α) is,

$$\frac{\mathrm{d}n_\alpha}{\mathrm{d}t} + \frac{\mathrm{d}\Gamma_\alpha}{\mathrm{d}x} = S_\alpha \tag{7.1}$$

where n_α, Γ_α, and S_α are the density, flux, and source terme for particle α. It can be discretized in the following way,

$$\frac{n^{k+1}_{\alpha,i+\frac{1}{2}} - n^{k}_{\alpha,i+\frac{1}{2}}}{\Delta t^k} + \frac{\Gamma_{\alpha,i+1} - \Gamma_{\alpha,i}}{\Delta x} = S^k_{\alpha,i+\frac{1}{2}},$$

here k is an index related to the time discretization.

Poisson equation. The Poisson equation is written as,

$$\frac{\mathrm{d}}{\mathrm{d}x}\left(\varepsilon_0 \frac{\mathrm{d}}{\mathrm{d}x}\phi(t+\Delta t)\right) = -\rho(t+\Delta t),$$

and the charge density is,

$$\rho(t) = \sum_\alpha e q_\alpha n_\alpha(t),$$

which we can expand up to first order $\rho(t+\Delta t)$,

$$\begin{aligned} \rho(t+\Delta t) &= \rho(t) + \Delta t \frac{\partial \rho(t)}{\partial t}, \\ \frac{\partial \rho(t)}{\partial t} &= \sum_{\alpha'} e q_{\alpha'} \frac{\partial n_{\alpha'}(t)}{\partial t}. \end{aligned} \tag{7.2}$$

In this equation (7.2), the subindex α' indicates only the plasma charged species, because we are looking for equilibrium when the nanoparticle density is fixed. In other words, for a plasma time step, the charge of nanoparticles is assumed to be stationary. From the drift-diffusion equation 7.1, we obtain for the charge density the following result,

$$\rho(t+\Delta t) = \sum_\alpha e q_\alpha n_\alpha(t) + \Delta t \sum_{\alpha'} e q_{\alpha'} \left(S_{\alpha'} - \frac{\mathrm{d}\Gamma_{\alpha'}}{\mathrm{d}x}\right).$$

with this formulation for the Poisson equation, we can decouple this calculation from the drift-diffusion equations[5].

Source term The gain and sink S_α is,

$$S_\alpha = \sum_r R_r - L_\alpha,$$

where R_r represents the reaction rate due to process r (for instance ionization or excitation). L_α is the loss term of species (α) towards the nanoparticle,

$$L_\alpha = \sum_l \sum_m N_{l,m} \nu_{\alpha(l,m)},$$

and $N_{l,m}$ is the nanoparticle density for size l and charge m. $\nu_{\alpha(l,m)}$ is the collision frequency of particles α with the dust particle, from the OML theory [15]. For instance, the ionization rate is R_{ion} [15], may be written as,

$$R_{\text{ion}} = n_e n_g A_{\text{ion}} \exp\left(-\frac{\varepsilon_{\text{ion}}}{k_{\text{B}} T_e}\right).$$

where n_g, A_{ion}, ε_{ion}, and T_e are respectively the gas density, a constant, ionization threshold energy and electronic temperature.

Electron energy density The continuity equation for the electron energy density is,

$$\frac{\mathrm{d}n_\varepsilon}{\mathrm{d}t} + \frac{\mathrm{d}\Gamma_\varepsilon}{\mathrm{d}x} = S_\varepsilon,$$

where the energy density is defined by $n_\varepsilon = n_e\bar{\varepsilon}$, and the density energy flux is written as,

$$\Gamma_\varepsilon = -\frac{5}{3}\mu_e e E n_\varepsilon - \frac{5}{3}D_e\frac{\mathrm{d}n_\varepsilon}{\mathrm{d}x}.$$

This formulation is convenient because we can reuse the solvers applied to the continuity density equations [5]. The discretization is given by,

$$\Gamma_{\varepsilon,i} = -\frac{5}{3}\frac{D^k_{e,i}}{\Delta x}\left[f_1(z_{e,i})n^{k+1}_{\varepsilon,i+\frac{1}{2}} - f_2(z_{e,i})n^{k+1}_{\varepsilon,i-\frac{1}{2}}\right],$$

along with,

$$z_{e,i} = \frac{\mu^k_{e,i}}{D^k_{e,i}}\left(\phi^{k+1}_{i+\frac{1}{2}} - \phi^{k+1}_{i-\frac{1}{2}}\right),$$

and the source term,

$$\begin{aligned} S_\varepsilon &= -e\Gamma_e E - \sum_r^{\mathrm{Re}} \varepsilon_r n_e n_r k_\mathrm{r} - \sum_l\sum_m \left(N_{l,m}\nu_{e(l,m)}\phi_{l,m}\right) \\ &= S_E + S_\mathrm{Re} + S_\mathrm{NPC}, \end{aligned}$$

where ε_r is the energy lost or gained in electron collision. S_E, S_Re and S_NPC, represent the heating, the energy involved in reactions, and the energy lost in electron-nanoparticle collisions.

7.2 Argon-Silane global plasma model

We solve for the electron energy density n_ε, and for the densities of the following species,

$$\mathrm{e}, \mathrm{Ar}^+, \mathrm{Ar}^*, {\mathrm{SiH_3}}^+, \mathrm{SiH_3}, \mathrm{SiH_2}. \tag{7.3}$$

along with set of equations,

$$\begin{aligned} \frac{\mathrm{d}n_\mathrm{e}}{\mathrm{d}t} &= k_\mathrm{i} n_\mathrm{e} n_\mathrm{Ar} + k_{\mathrm{i},\mathrm{Ar}^+} n_\mathrm{e} n_{\mathrm{Ar}^*} + k_{\mathrm{di},\mathrm{SiH_4}} n_\mathrm{e} n_{\mathrm{SiH_4}} + k_{\mathrm{i},\mathrm{SiH_3}} n_\mathrm{e} n_{\mathrm{SiH_3}} \\ &\quad - \frac{A}{V}\Gamma_{\mathrm{Ar}^+} n_{\mathrm{Ar}^+} - \frac{A}{V}\Gamma_{{\mathrm{SiH_3}}^+} n_{{\mathrm{SiH_3}}^+} - \sum_{ik} L^e_{ik} n_\mathrm{e}, \end{aligned} \tag{7.4}$$

$$\begin{aligned} \frac{\mathrm{d}n_{\mathrm{Ar}^*}}{\mathrm{d}t} &= k_\mathrm{ex} n_\mathrm{Ar} n_\mathrm{e} - k_{\mathrm{i},\mathrm{Ar}^+} n_\mathrm{e} n_{\mathrm{Ar}^*} - k_{12} n_{\mathrm{Ar}^*} n_{\mathrm{SiH_4}} - k_{13} n_{\mathrm{Ar}^*} n_{\mathrm{SiH_4}} - k_{14} n_{\mathrm{Ar}^*} n_{\mathrm{SiH_3}} \\ &\quad - k_{15} n_{\mathrm{Ar}^*} n_{\mathrm{SiH_2}} - \frac{A}{V}\Gamma_{\mathrm{Ar}^*} n_{\mathrm{Ar}^*}, \end{aligned} \tag{7.5}$$

$$\frac{\mathrm{d}{\mathrm{SiH_3}}^+}{\mathrm{d}t} = k_{\mathrm{di},\mathrm{SiH_4}} n_\mathrm{e} n_{\mathrm{SiH_4}} - k_{\mathrm{i},\mathrm{SiH_3}} n_\mathrm{e} n_{\mathrm{SiH_3}} - \frac{A}{V}\Gamma_{{\mathrm{SiH_3}}^+} n_{{\mathrm{SiH_3}}^+}, \tag{7.6}$$

$$\frac{\mathrm{d}\mathrm{SiH_3}}{\mathrm{d}t} = k_{\mathrm{d},\mathrm{SiH_3}} n_\mathrm{e} n_{\mathrm{SiH_4}} - k_{\mathrm{i},\mathrm{SiH_3}} n_\mathrm{e} n_{\mathrm{SiH_4}} + k_{12} n_{\mathrm{Ar}^*} n_{\mathrm{SiH_4}} - k_{14} n_{\mathrm{Ar}^*} n_{\mathrm{SiH_4}} - \frac{A}{V}\Gamma_{\mathrm{SiH_3}} n_{\mathrm{SiH_3}}, \tag{7.7}$$

$$\frac{\mathrm{d}\mathrm{SiH_2}}{\mathrm{d}t} = k_{\mathrm{d},\mathrm{SiH_2}} n_\mathrm{e} n_{\mathrm{SiH_4}} + k_{13} n_{\mathrm{Ar}^*} n_{\mathrm{SiH_4}} + k_{14} n_{\mathrm{Ar}^*} n_{\mathrm{SiH_3}} - k_{15} n_{\mathrm{Ar}^*} n_{\mathrm{SiH_2}} - \frac{A}{V}\Gamma_{\mathrm{SiH_2}} n_{\mathrm{SiH_2}}, \tag{7.8}$$

$$\tag{7.9}$$

along with the equation for the energy density,

$$\begin{aligned}\frac{\mathrm{d}n_\varepsilon}{\mathrm{d}t} = &\frac{P}{V} - \varepsilon_{\mathrm{i}} k_{\mathrm{i}} n_{\mathrm{Ar}} n_{\mathrm{e}} - \varepsilon_{\mathrm{ex}} k_{\mathrm{ex}} n_{\mathrm{Ar}} n_{\mathrm{e}} - \varepsilon_{\mathrm{i,Ar^+}} k_{\mathrm{i,Ar^+}} n_{\mathrm{Ar^*}} n_{\mathrm{e}} - \frac{5}{3}\frac{A}{V} v_{\mathrm{Bohm,Ar^+}} n_\varepsilon - eV_{\mathrm{sheath}} \frac{A}{V} v_{\mathrm{Bohm,Ar^+}} n_{\mathrm{e}} \\ &- 3\frac{m_e}{m_{\mathrm{Ar}}} k_{\mathrm{el}} n_\varepsilon n_{\mathrm{Ar}} - 3\frac{m_e}{m_{\mathrm{SiH_4}}} k_{\mathrm{el,SiH_4}} n_\varepsilon n_{\mathrm{SiH_4}} - \varepsilon_{\mathrm{i,SiH_3}} k_{\mathrm{i,SiH_3}} n_{\mathrm{e}} n_{\mathrm{SiH_3}} \\ &- \varepsilon_{\mathrm{di,SiH_4}} k_{\mathrm{di,SiH_4}} n_{\mathrm{e}} n_{\mathrm{SiH_4}} - \varepsilon_{\mathrm{d,SiH_3}} k_{\mathrm{d,SiH_3}} n_{\mathrm{e}} n_{\mathrm{SiH_4}} - \varepsilon_{\mathrm{d,SiH_2}} k_{\mathrm{d,SiH_2}} n_{\mathrm{e}} n_{\mathrm{SiH_4}} \\ &- \varepsilon_{\mathrm{v13}} k_{\mathrm{v13}} n_{\mathrm{e}} n_{\mathrm{SiH_4}} - \varepsilon_{\mathrm{v24}} k_{\mathrm{v24}} n_{\mathrm{e}} n_{\mathrm{SiH_4}} - \sum_{ik} \Phi_{ik} L^e_{ik} n_{\mathrm{e}}, \end{aligned} \tag{7.10}$$

and the quasi-neutrality condition,

$$n_{\mathrm{Ar^+}} = n_{\mathrm{e}} - n_{\mathrm{SiH_3^+}} + N^Q_{\mathrm{NP}}. \tag{7.11}$$

Here A and V are the area and volume of the reactor, Γ is the flux, L^e_{ik} is the loss of electrons to nanoparticles (in s^{-1} see below) P is the power density, Φ_{ik} the surface potential of nanoparticle i with charge k in eV, and N^Q_{NP} is the net charge on nanoparticles.

From OML theory the loss term is expressed as,

$$L^e_{ik} = 4\pi N_{ik} r_i^2 \left(\frac{K_B T_e}{2\pi m_e}\right)^{1/2} \alpha_e, \tag{7.12}$$

where α_e is,

$$\alpha_e = \begin{cases} \exp\left(\frac{e\Phi_{ik}}{K_B T_e}\right), & k < 0, \\ \left(1 + \frac{e\Phi_{ik}}{K_B T_e}\right), & k > 0. \end{cases} \tag{7.13}$$

We can summarize the assumptions embedded in the model as follows,

- The electron flux has been matched to the total ion flux.
- The power is held constant.
- For a plasma iteration the nanoparticle charge is assumed to remain constant. In fact, the real frequency for the loss of electrons has n_e instead of N_{ik} (eq. 7.12) but has been switched to express the explicit dependency of this term to n_e, i.e,

$$\nu^e_{ik} = 4\pi n_e r_i^2 \left(\frac{K_B T_e}{2\pi m_e}\right)^{1/2} \alpha_e, \tag{7.14}$$

$$\bar{L}^e_{ik} = N_{ik} \nu^e_{ik} = n_e L^e_{ik}. \tag{7.15}$$

- The density of $n_{\mathrm{Ar^+}}$ is computed from the quasi-neutrality condition.

7.3 Nanoparticle growth model

Recalling the GDE eq. 1.69,

$$\frac{\mathrm{d}N_{i,k}}{\mathrm{d}t} + \nabla\Gamma_{i,k} = \left[\frac{\mathrm{d}N_{i,k}}{\mathrm{d}t}\right]_{\text{nuc}} + \left[\frac{\mathrm{d}N_{i,k}}{\mathrm{d}t}\right]_{\text{coag}} + \left[\frac{\mathrm{d}N_{i,k}}{\mathrm{d}t}\right]_{\text{growth}} + \left[\frac{\mathrm{d}N_{i,k}}{\mathrm{d}t}\right]_{\text{charging}}, \tag{7.16}$$

where $N_{i,k}$ is the particle density, expressed in number of particles per unit volume (m^{-3}) and $\Gamma_{i,k}$ is the local spatial flux.

7.3.1 Nucleation

This term only applies to the first size $i = 1$ of dust particles [1],

$$\left[\frac{\mathrm{d}N_{i,k}}{\mathrm{d}t}\right]_{\text{nuc}} = \delta_{i,1} J_i, \tag{7.17}$$

Agarwal used $J_i = 10^{12}\,\mathrm{cm}^{-3}\,\mathrm{s}^{-1}$.

7.3.2 Coagulation

This process occurs when two dust particles collide and adhere to form a new particle with volume equal to the sum of that of the two original particles. Thus, coagulation is a volume conserving process.

7.3.2.1 Coagulation between uncharged particles

7.3.2.2 Continuous formulation

Here we follow Friedlander[4]: let $\mathrm{d}N$ to be the number of particles per unit volume of gas at a given position in space represented by r, and at given time t in the particle volume range v to $v + \mathrm{d}v$,

$$\mathrm{d}N = n(v, \mathbf{r}, t)\,\mathrm{d}v\,, \tag{7.18}$$

this expression defines the particle size distribution $n(v, \mathbf{r}, t)$ in terms of particle volume with dimensions,

$$[n] = L^{-3} I^{-3}, \tag{7.19}$$

the symbols L and I refer to a length dimension for the gas and for the particle size, respectively. These dimensions are not interchangeable, then both characteristic lengths must be treated independently when using dimensional analysis.

Now, allow us to consider the collision rate between particles in the volume ranges v to $v + \mathrm{d}v$ and u to $u + \mathrm{d}u$ given by,

$$\text{collision rate} = \beta(u, v) n(u) n(v)\,\mathrm{d}u\,\mathrm{d}v\,, \tag{7.20}$$

which has the same dimensions as (1.36),

$$[\text{collision rate}] = \frac{\cancel{L^3}}{T}\frac{1}{\cancel{I^3}\cancel{L^3}}\frac{1}{\cancel{I^3}L^3}\cancel{I^3}\cancel{I^3} = \frac{1}{L^3 T} \tag{7.21}$$

Then, the rate of formation of particles with volume v by collision of smaller particles with volumes $v-u$ and u is,

$$\text{formation in range } \mathrm{d}v = \frac{1}{2}\int_0^v \beta(u, v-u)n(u)n(v-u)\,\mathrm{d}u\,\mathrm{d}v\,, \tag{7.22}$$

and the rate of loss is,

$$\text{loss in range } \mathrm{d}v = \int_0^\infty \beta(u, v)n(u)n(v)\,\mathrm{d}u\,\mathrm{d}v\,, \tag{7.23}$$

the net rate of formation of particles with volume v is,

$$\frac{\partial(n\,\mathrm{d}v)}{\partial t} = \frac{1}{2}\int_0^v \beta(u, v-u)n(u)n(v-u)\,\mathrm{d}u\,\mathrm{d}v - \int_0^\infty \beta(u, v)n(u)n(v)\,\mathrm{d}u\,\mathrm{d}v\,, \tag{7.24}$$

dividing by $\mathrm{d}v$, we obtain

$$\frac{\partial n}{\partial t} = \frac{1}{2}\int_0^v \beta(u, v-u)n(u)n(v-u)\,\mathrm{d}u - \int_0^\infty \beta(u, v)n(u)n(v)\,\mathrm{d}u\,, \tag{7.25}$$

which is known as the Smoluchowski coagulation equation. The correct dimensions for this equation are guaranteed by the definition of the particle size density function (7.18) with dimensions (7.19), the collision rate (7.20) with dimensions (7.21), where the collision frequency function is given in m^3/s.

7.3.2.3 Collision frequency function for Brownian coagulation

In the continuum regime the diameter of particles are much greater that the mean free path. The collision frequency function or collision kernel is given by[4],

$$\beta(v_i, v_j) = \frac{2k_\mathrm{B}T}{3\mu}\left(\frac{1}{v_i^{1/3}} + \frac{1}{v_j^{1/3}}\right)\left(v_i^{1/3} + v_j^{1/3}\right). \tag{7.26}$$

In the free molecular regime the diameter of the particles is much smaller than the mean free path. In this case, the collision frequency function is,

$$\beta(v_i, v_j) = \left(\frac{3}{4\pi}\right)^{1/6}\left(\frac{6k_\mathrm{B}T}{\rho_p}\right)^{1/2}\left(\frac{1}{v_i} + \frac{1}{v_j}\right)^{\frac{1}{2}}\left(v_i^{1/3} + v_j^{1/3}\right)^2. \tag{7.27}$$

7.3.2.4 Coagulation between charged particles

Working with tens of elementary charges Allow us to define the particle size-charge density $n_k(v, t)$ in a given position $\mathbf{r}$ and time t as

$$\mathrm{d}N_k = n_k(v, \mathbf{r}, t)\,\mathrm{d}v\,, \tag{7.28}$$

where k is the charge index (could be negative) and $\mathrm{d}N_k$ is the number of particles per unit volume with charge k electrons in the particle volume range v to $v + \mathrm{d}v$. Then we have again the same dimensions for the density $[n_q] = L^{-3}I^{-3}$.

The collision rate is expressed as follows,

$$F_{pq}(u,v) = K_{pq}(u,v)n_p(u)n_q(v)\,\mathrm{d}u\,\mathrm{d}v\,, \tag{7.29}$$

which implies the collision between a particle with volume in the range u to $u+\mathrm{d}u$ and charge number q with a particle of volume in the range v to $v+\mathrm{d}v$ with p electrons. And K is the collision kernel for charged particles, that in the case of dusty plasma can be expressed as[1],

$$\begin{gathered} K = \text{enhancement factor } \times \text{collision kernel in the free molecular regime,} \\ K_{pq}(u,v) = f_{pq}(u,v)\beta(u,v), \end{gathered} \tag{7.30}$$

here the enhancement factor takes into account the effects of the charge on the collisions and it is a dimensionless quantity, therefore K has the dimensions of β.

Now we can write the rate of formation of a particle of volume v and charge k by collision of a smaller particle of volume $v-u$ and charge number q with a particle of volume u and charge p,

$$\text{formation in range } \mathrm{d}v = \frac{1}{2}\sum_{p+q=k}\int_0^v K_{pq}(u,v-u)n_p(u)n_q(v-u)\,\mathrm{d}u\,\mathrm{d}v\,, \tag{7.31}$$

and the rate of loss is,

$$\text{loss in range } \mathrm{d}v = \sum_{p=-\infty}^{\infty}\int_0^{\infty} K_{kp}(u,v)n_p(u)n_k(v)\,\mathrm{d}u\,\mathrm{d}v\,, \tag{7.32}$$

the net rate of formation of particles of volume v is,

$$\frac{\partial(n_k(v,t)\,\mathrm{d}v)}{\partial t} = \frac{1}{2}\sum_{p+q=k}\int_0^v K_{pq}(u,v-u)n_p(u)n_q(v-u)\,\mathrm{d}u\,\mathrm{d}v \tag{7.33}$$

$$- \sum_{p=-\infty}^{\infty}\int_0^{\infty} K_{kp}(u,v)n_p(u)n_k(v)\,\mathrm{d}u\,\mathrm{d}v\,, \tag{7.34}$$

dividing by $\mathrm{d}v$, we obtain

$$\boxed{\frac{\partial n_k}{\partial t} = \frac{1}{2}\sum_{p+q=k}\int_0^v K_{pq}(u,v-u)n_p(u)n_q(v-u)\,\mathrm{d}u - n_k(v)\sum_{p=-\infty}^{\infty}\int_0^{\infty} K_{kp}(u,v)n_p(u)\,\mathrm{d}u} \tag{7.35}$$

Now we can use the fixed pivot technique[8] to obtain a discretized form for the coagulation equation (7.35).

Fixed pivot technique. With this technique we achieve two goals: one is to solve the equation (7.35) by a discretization of the particle volume domain and the second is to preserve (at least) two quantities of interest during the coagulation of particles.

We choose a representative volume $\tilde{v}_i$ to lay in the cell or section $C_i \equiv [v_i, v_{i+1}]$. In figure 7.2, we represent the representative volumes or grid points and the cells. Usually the interface is expressed as an arithmetic mean: $v_i = \frac{\tilde{v}_{i-1}+\tilde{v}_i}{2}$ or conversely $\tilde{v}_i = \frac{v_{i+1}+v_i}{2}$.

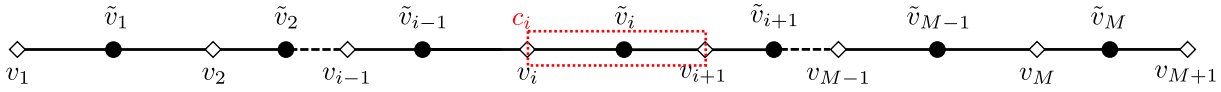

Figure 7.2: Grid for the particle volume.

In our case we want to describe accurately the volume and the number of particles. Therefore, when a new particle is created we need to assign the proper fractions between two grid points by imposing the conservation of the particle volume and number. This is expressed mathematically as follows,

$$a_1(v, \tilde{v}_i) + a_2(v, \tilde{v}_{i+1}) = 1 \quad \text{number conservation and} \tag{7.36}$$

$$a_1(v, \tilde{v}_i)\tilde{v}_i + a_2(v, \tilde{v}_{i+1})\tilde{v}_{i+1} = v \quad \text{volume conservation,} \tag{7.37}$$

where a_1, a_2 is the fraction assigned to pivot $\tilde{v}_i$ and $\tilde{v}_{i+1}$, respectively. Because we are interested in particle volumes that lies in the range C_i we solve for a_1,

$$a_1(v, \tilde{v}_i) = \frac{\tilde{v}_{i+1} - v}{\tilde{v}_{i+1} - \tilde{v}_i}. \tag{7.38}$$

Similarly, for the conservation of volume and number in the cell C_{i-1} we have,

$$a_1(v, \tilde{v}_{i-1}) + a_2(v, \tilde{v}_i) = 1 \quad \text{number conservation and} \tag{7.39}$$

$$a_1(v, \tilde{v}_{i-1})\tilde{v}_{i-1} + a_2(v, \tilde{v}_i)\tilde{v}_i = v \quad \text{volume conservation,} \tag{7.40}$$

in this case a_2 is the fraction added to C_i,

$$a_2(v, \tilde{v}_i) = \frac{v - \tilde{v}_{i-1}}{\tilde{v}_i - \tilde{v}_{i-1}}. \tag{7.41}$$

Then, the total fraction of particles added to cell C_i which preserves particle number and volume is,

$$\eta = \begin{cases} \frac{\tilde{v}_{i+1} - v}{\tilde{v}_{i+1} - \tilde{v}_i}, & \tilde{v}_i \le v \le \tilde{v}_{i+1} \\ \frac{v - \tilde{v}_{i-1}}{\tilde{v}_i - \tilde{v}_{i-1}}, & \tilde{v}_{i-1} \le v \le \tilde{v}_i \end{cases}.$$

Now, note that the integral (7.28) in a cell C_i, give us the density of particles (m^{-3}) with charge number k in this section C_i,

$$N_{ik} = \int_{v_i}^{v_{i+1}} n_k(v, \mathbf{r}, t)\, \mathrm{d}v\,. \tag{7.42}$$

Also, we can assume that the particles belong to a representative volume in this cell or section C_i,

$$n_k(v, t) = \sum_{i=1}^{M} N_{ik}\delta(v - \tilde{v}_i). \tag{7.43}$$

Now we can integrate (7.35), taking into account the fraction of particles formed in $R_i \equiv \{v : \tilde{v}_{i-1} \le v \le \tilde{v}_{i+1}\}$ that enters into the cell C_i,

$$\int_{C_i} \frac{\partial n_k}{\partial t}\, \mathrm{d}v = \frac{\partial}{\partial t}\int_{C_i} n_k\, \mathrm{d}v = \frac{1}{2}\int_{R_i} \mathrm{d}v \sum_{p+q=k} \int_0^v \eta_i K_{pq}(u, v-u) n_p(u) n_q(v-u)\, \mathrm{d}u$$

$$- \int_{C_i} n_k(v)\, \mathrm{d}v \sum_{p=-\infty}^{\infty} \int_0^{\infty} K_{kp}(u, v) n_p(u)\, \mathrm{d}u \tag{7.44}$$

rearranging and using (7.43), we get,

$$\frac{\mathrm{d}N_{ik}}{\mathrm{d}t} = \frac{1}{2}\sum_{p+q=k}\sum_{j,m=1}^{M,M}\int_{R_i}\int_0^v \eta_i K_{pq}(u, v-u)N_{jp}\delta(u-\tilde{u}_j)N_{mq}\delta(v-\tilde{v}_m-u)\,\mathrm{d}u\,\mathrm{d}v$$
$$- N_{ik}\sum_{p=-\infty}^{\infty}\sum_{m=1}^{M}\int_0^{\infty} K_{kp}(u, v_i)N_{mp}\delta(u-\tilde{u}_m)\,\mathrm{d}u\,, \tag{7.45}$$

applying the sifting property of the Dirac Delta function, we have,

$$\frac{\mathrm{d}N_{ik}}{\mathrm{d}t} = \frac{1}{2}\sum_{p+q=k}\sum_{j=1}^{i}\sum_{m=1}^{M}\int_{R_i} \eta_i K_{pq}(\tilde{u}_j, v-\tilde{u}_j)N_{jp}N_{mq}\delta(v-\tilde{v}_m-\tilde{u}_j)\,\mathrm{d}v$$
$$- N_{ik}\sum_{p=-\infty}^{\infty}\sum_{m=1}^{M} K_{imkp}N_{mp}, \tag{7.46}$$

where the integral is nonzero for $\tilde{v}_m + \tilde{v}_j = v \in R_i$ ($\tilde{u}_j$ is a dummy variable, we can replace it for $\tilde{v}_j$), therefore, we must have,

$$\frac{\mathrm{d}N_{ik}}{\mathrm{d}t} = \frac{1}{2}\sum_{p+q=k}\sum_{\Omega_i}\eta_i K_{jmpq}N_{jp}N_{mq} - N_{ik}\sum_{p=-\infty}^{\infty}\sum_{m=1}^{M} K_{imkp}N_{mp}. \tag{7.47}$$

where Ω_i is defined as follows,

$$\Omega_i \equiv \left\{\{j, m\} : 1 \le j \le i, 1 \le m \le i; v = \tilde{v}_j + \tilde{v}_m \in R_i\right\}, \tag{7.48}$$

or,

$$\frac{\mathrm{d}N_{ik}}{\mathrm{d}t} = \frac{1}{2}\sum_{\Omega_{ik}}\eta_i K_{jmpq}N_{jp}N_{mq} - N_{ik}\sum_{p=-Q}^{Q}\sum_{m=1}^{M} K_{imkp}N_{mp}, \tag{7.49}$$

$$\Omega_{ik} = \{\{j, p, m, q\} : 1 \le j \le i, -Q \le p \le Q, 1 \le m \le i, -Q \le q \le Q; v \in R_i, p+q=k\}, \tag{7.50}$$

where Q is the maximum number of charges and,

$$R_i \equiv \{v, : \tilde{v}_{i-1} < v < \tilde{v}_{i+1}, \} \tag{7.51}$$

Let us consider the summations in the birth term,

- the volume constraint is $\tilde{v}_j + \tilde{v}_m = v$, and $\tilde{v}_{i-1} < v < \tilde{v}_{i+1}$,
- we have repetitions $\tilde{v}_j + \tilde{v}_m = \tilde{v}_m + \tilde{v}_j$,
- the charge constraint is $p + q = k$, and $|k| \le Q$ for a fixed grid.

Considering these constraints and the repeated terms we can rewrite (7.49) as follows,

$$\frac{\mathrm{d}N_{ik}}{\mathrm{d}t} = \sum_{\Omega_{ik}} \eta_i K_{jmpq} N_{jp} N_{mq} - N_{ik} \sum_{m=1}^{M} \sum_{p=-Q}^{Q} K_{imkp} N_{mp}, \tag{7.52}$$

$$\Omega_{ik} = \{\{j,p,m,q\} : 1 \leq j \leq i, 1 \leq m \leq i, -Q + k\Theta(k) \leq p \leq Q + k\Theta(-k), q = k - p; v \in R_i\}, \tag{7.53}$$

where Θ is the Heaviside step function.

Volume and charge pivoting Following Vale [14], the extended pivot technique conserving properties u and v gives,

$$\frac{\mathrm{d}N_{ik}}{\mathrm{d}t} = \frac{1}{2} \sum_{\Omega_{ik}} \eta_{ik}(u,v) K_{jmpq} N_{jp} N_{mq} - N_{ik} \sum_{m=1}^{M} \sum_{p=1}^{P} K_{imkp} N_{mp}, \tag{7.54}$$

and,

$$\Omega_{ik} = \left\{\{j,p,m,q\} : 1 \leq j,m \leq i, 1 \leq p,q \leq k, (u,v) \in R_{ij}\right\}, \tag{7.55}$$

$$R_{ij} \equiv \left\{(u,v) : u_{i-1} < u < u_{i+1}, v_{j-1} < v < v_{j+1}\right\}. \tag{7.56}$$

Removing the repeated combinations in the first sum in eq. (7.54), we have

$$\frac{\mathrm{d}N_{ik}}{\mathrm{d}t} = \sum_{\Omega_{ik}} \left[1 - \frac{1}{2}\delta_{jm}\delta_{pq}\right] \eta_{ik}(u,v) K_{jmpq} N_{jp} N_{mq} - N_{ik} \sum_{m=1}^{M} \sum_{p=1}^{P} K_{imkp} N_{mp}, \tag{7.57}$$

$$\Omega_{ik} = \left\{\{j,p,m,q\} : 1 \leq j \leq i, 1 \leq p \leq k, p \leq q \leq k, 1 + \delta_{pq}(j-1) \leq m \leq i, (u,v) \in R_{ij}\right\}. \tag{7.58}$$

7.3.3 Surface Growth

In this phase particles grow in size from the nanometer to micrometer range by surface growth: molecules stick to the surface of particles creating layers. Note that surface growth does not affect particle charge and it is more important when considering the growth of particles towards the micrometer size. In terms of sections, Agarwal [1] mathematically expresses the surface growth as follows,

$$\left[\frac{\mathrm{d}N_i}{\mathrm{d}t}\right]_{\text{growth}} = \frac{\dot{B}_i V_i}{\bar{v}_{p,i}} + \frac{\dot{C}_{i-1} V_i}{\bar{v}_{p,i}} - \frac{\dot{C}_i V_i}{\bar{v}_{p,i}}. \tag{7.59}$$

where B_i and C_i are, respectively, intra- and intersectional growth coefficients (in units of s^{-1}). As usual the index i denotes the section, and $\bar{v}_{p,i}$ and V_i are, respectively, the average particle volume and the total volume of particle per unit volume of gas in section i.

The rate of volume addition to particles in section i can be written as,

$$\dot{B}_i V_i = \dot{N}_s v_m \bar{A}_{p,i} N_i, \tag{7.60}$$

where $\dot{N}_s$ is the rate of particle growth in terms of molecules added per unit particle surface area. v_m is the molecular volume added to the particle. As pointed by Agarwal[1] $\dot{N}_s v_m$ represents the linear growth rate ($\mathrm{nm\,s^{-1}}$) of particles due to surface growth. Evaluation of $\dot{N}_s$ requires a suitable sub-model, for example involving growth of particles by heterogeneous chemical reactions on their surfaces. Agarwal used $12\,\mathrm{nm\,s^{-1}}$ as the value for linear growth.

The relation between the intra- and intersectional growth coefficients is,

$$\dot{C}_i = \dot{B}_i \frac{\bar{v}_{p,i+1}}{\bar{v}_{p,i+1} - \bar{v}_{p,i}}. \tag{7.61}$$

7.3.3.1 Dimensional Analysis

For consistency, we checked the dimensions of the growth equations in terms of the quantities defined above. The sectionals coefficients as rates have the dimension of the inverse of time,

$$[\dot{B}_i] = [\dot{C}_i] = \frac{1}{T}, \tag{7.62}$$

and the fraction must have the following dimensions,

$$\left[\frac{\dot{B}_i V_i}{\bar{v}_{p,i}}\right] = \frac{1}{T}\frac{\cancel{l^3}}{L^3}\frac{1}{\cancel{l^3}} = \frac{1}{L^3 T} = \left[\frac{\mathrm{d}N_i}{\mathrm{d}t}\right]. \tag{7.63}$$

Now we want to check the dimensions of equation (7.60). First the linear growth rate has dimensions of,

$$[\dot{N}_s v_m] = \frac{1}{l^2 T} l^3 = \frac{l}{T}, \tag{7.64}$$

thus,

$$[\dot{B}_i V_i] = \frac{1}{T}\frac{l^3}{L^3} = [\dot{N}_s v_m \bar{A}_{p,i} N_i] = \frac{l}{T} l^2 \frac{1}{L^3 T} = \frac{1}{T}\frac{l^3}{L^3}. \tag{7.65}$$

7.3.3.2 Park and Rogak Surface Growth Model

This model[11] aims to reduce the numerical diffusion which exists in the surface growth formulation for fixed sectional models. The surface growth rate is expressed as,

$$\left[\frac{\mathrm{d}N_i}{\mathrm{d}t}\right]_{\text{growth}} = \frac{A_{i-1} I_{i-1} N_{i-1}}{v_{i-1}} + \frac{B_i I_i N_i}{v_i} + \frac{C_{i+1} I_{i+1} N_{i+1}}{v_{i+1}}, \tag{7.66}$$

where the coefficients A_i, B_i, and C_i are to be determined.

The jth moment of the size distribution is defined as

$$M_j = \sum_{i=1}^{M} v_i^j N_i, \tag{7.67}$$

and the changes in the moments in the moving-sectional model,

$$\frac{\mathrm{d}M_j}{\mathrm{d}t} = j \sum_{i=1}^{M} v_i^{j-1} I_i N_i, \tag{7.68}$$

along with,

$$I_i = \frac{\mathrm{d}v_i}{\mathrm{d}t}. \tag{7.69}$$

For the fixed-sectional model we have,

$$\frac{\mathrm{d}M_j}{\mathrm{d}t} = \sum_{i=1}^{M} \left(A_i f_s^j + B_i + C_i f_s^{-j}\right) v_i^{j-1} I_i N_i - A_M f_s^j v_M^{j-1} I_M N_M - C_1 f_s^{-j} v_1^{j-1} N_1, \tag{7.70}$$

and $f_s = \frac{v_{i+1}}{v_i}$ the section spacing factor, which is constant in the case of a geometric grid. Comparison between equations (7.68) and (7.70) shows that,

$$j = A_i f_s^j + B_i + C_i f_s^{-j}, \tag{7.71}$$

with $C_i = A_M = 0$. For number and mass conservation $j = 0, 1$ and $i = 1$ we have,

$$A_1 = \frac{1}{f_s - 1}, \tag{7.72}$$

$$B_1 = -\frac{1}{f_s - 1}, \tag{7.73}$$

$$B_M = \frac{f_s}{f_s - 1}, \tag{7.74}$$

$$C_M = -\frac{f_s}{f_s - 1}. \tag{7.75}$$

For $2 \leq i \leq M$,

$$A_i = \frac{k f_s^{k-1}(f_s - 1) - (f_s^k - 1)}{(f_s - 1)(f_s^{k-1} - 1)(f_s^k - 1)}, \tag{7.76}$$

$$B_i = \frac{(f_s^k + 1)(f_s^k - 1) - k f_s^{k-1}(f_s - 1)(f_s + 1)}{(f_s - 1)(f_s^{k-1} - 1)(f_s^k - 1)}, \tag{7.77}$$

$$C_i = \frac{f_s^k[k(f_s - 1) - (f_s^k - 1)]}{(f_s - 1)(f_s^{k-1} - 1)(f_s^k - 1)}. \tag{7.78}$$

Now, using $k = 2$ the three-point method is obtained,

$$\left[\frac{\mathrm{d}N_i}{\mathrm{d}t}\right]_{\text{growth}} = \frac{A_{i-1} I_{i-1} N_{i-1} - C_i I_i N_i / f_s}{v_{i-1}} - \frac{A_i I_i N_i - C_{i+1} I_{i+1} N_{i+1} / f_s}{v_i}. \tag{7.79}$$

To mitigate instabilities in the three point method, Park and Rogak propose the following coefficients,

$$B_i = \begin{cases} -\frac{f_s}{f_s - 1} \operatorname{erf}\left(\frac{1}{4} \frac{\mathrm{d}\ln N_i}{\mathrm{d}\ln v_i}\right), \frac{\mathrm{d}\ln N_i}{\mathrm{d}\ln v_i} \leq 0, \\ -\frac{1}{f_s - 1} \operatorname{erf}\left(\frac{1}{4} \frac{\mathrm{d}\ln N_i}{\mathrm{d}\ln v_i}\right), \frac{\mathrm{d}\ln N_i}{\mathrm{d}\ln v_i} > 0. \end{cases} \tag{7.80}$$

$$A_i = \frac{f_s - B_i(f_s - 1)}{f_s^2 - 1} \tag{7.81}$$

$$C_i = -(A_i + B_i). \tag{7.82}$$

7.3.3.3 Two point method

This is the easiest way to describe surface growth, is equivalent to the fixed point coagulation model adapted to describe surface growth.

$$\left[\frac{\mathrm{d}N_i}{\mathrm{d}t}\right]_{\text{growth}} = \frac{I_{i-1}N_{i-1}}{v_i - v_{i-1}} + \frac{I_{i+1}N_{i+1}}{v_{i+1} - v_i}. \tag{7.83}$$

or, alternatively,

$$\left[\frac{\mathrm{d}N_i}{\mathrm{d}t}\right]_{\text{growth}} = \frac{I_{i-1}N_{i-1}}{v_i - v_{i-1}} - \frac{I_i N_i}{v_{i+1} - v_i}. \tag{7.84}$$

7.3.4 Charging

7.3.4.1 Semi-implicit charging

Agarwal [1] assumes that all particle charging events change the particle charge by ± 1 electrons, then he expressed the particle charging term as,

$$\left[\frac{\mathrm{d}N_{ik}}{\mathrm{d}t}\right]_{\text{charging}} = \nu_{+(i,k-1)}N_{i,k-1} + \nu_{e(i,k+1)}N_{i,k+1} - \left(\nu_{+(i,k)} + \nu_{e(i,k)}\right)N_{ik}, \tag{7.85}$$

where $\nu_{+/e}$ is the collision frequency between ions/electrons and nanoparticles. The last equation can be discretized in semi-implicit form as follows,

$$N_{ik}^{s+1} = N_{ik}^{s} + \frac{\Delta t\left[\nu_{+(i,k-1)}N_{i,k-1}^{s} + \nu_{e(i,k+1)}N_{i,k+1}^{s}\right]}{1 + \Delta t\left(\nu_{+(i,k)} + \nu_{e(i,k)}\right)}. \tag{7.86}$$

7.3.4.2 Implicit charging

$$\frac{N_{ik}^{s+1} - N_{ik}^{s}}{\Delta t} = \nu_{+(i,k-1)}N_{i,k-1}^{s+1} + \nu_{e(i,k+1)}N_{i,k+1}^{s+1} - \left(\nu_{+(i,k)} + \nu_{e(i,k)}\right)N_{ik}^{s+1} + S_{ik}^{s}, \tag{7.87}$$

where the source term S_{ik}^{s} is given by:

$$S_{ik}^{s} = \left[\frac{\mathrm{d}N_{i,k}}{\mathrm{d}t}\right]_{\text{nuc}}^{s} + \left[\frac{\mathrm{d}N_{i,k}}{\mathrm{d}t}\right]_{\text{coag}}^{s} + \left[\frac{\mathrm{d}N_{i,k}}{\mathrm{d}t}\right]_{\text{growth}}^{s} \tag{7.88}$$

the tridiagonal system is,

$$F_{i,k-1}^{+}N_{i,k-1}^{s+1} + F_{i,k}N_{ik}^{s+1} + F_{i,k+1}^{e}N_{i,k+1}^{s+1} = G_{ik}^{s}, \tag{7.89}$$

along with the following definitions,

$$F_{i,k-1}^{+} = -\Delta t\nu_{+(i,k-1)} \tag{7.90}$$

$$F_{i,k} = 1 + \Delta t\left(\nu_{+(i,k)} + \nu_{e(i,k)}\right) \tag{7.91}$$

$$F_{i,k+1}^{e} = -\Delta t\nu_{e(i,k+1)} \tag{7.92}$$

$$G_{ik}^{s} = N_{i,k}^{s} + \Delta t S_{ik}^{s}, \tag{7.93}$$

and the boundary conditions,

$$F^{+}_{i,Q_-} = 0 \qquad F^{+}_{i,Q_+} = -\Delta t \nu_{+(i,Q_+-1)} \tag{7.94}$$

$$F^{e}_{i,Q_-} = -\Delta t \nu_{e(i,Q_-+1)} \qquad F^{e}_{i,Q_+} = 0 \tag{7.95}$$

$$\tag{7.96}$$

7.4 Interparticle interaction

7.4.1 Marlow enhancement factor

In this section we developed Marlow's derivation for the enhancement factor [9]. Let us consider the collision between two spherical particles of radius and mass r_i, m_i and r_j, m_j embedded in a gas of temperature T_g. Also, let us define the following quantities: the reduced mass $\mu = m_i m_j/(m_i + m_j)$, $r_{ij} = r_i + r_j$, the dimensionless velocity of the sphere of radius r_{ij}: $\bar{v} = \sqrt{\mu/2k_B T_g}v$, with k_B the Boltzmann constant. In spherical coordinates the velocity is expressed as,

$$\mathbf{v} = v_r\hat{\mathbf{r}} + v_\theta\hat{\boldsymbol{\theta}} + v_\varphi\hat{\boldsymbol{\varphi}} = \dot{r}\hat{\mathbf{r}} + r\dot{\theta}\hat{\boldsymbol{\theta}} + r\dot{\varphi}\sin\theta\hat{\boldsymbol{\varphi}}.$$

Then the angular moment $\boldsymbol{J} = \boldsymbol{r} \times \boldsymbol{p} = \mu\boldsymbol{r} \times \boldsymbol{v}$ is,

$$\boldsymbol{J} = -\mu r^2\dot{\varphi}\sin\theta\hat{\boldsymbol{\theta}} + \mu r^2\dot{\theta}\hat{\boldsymbol{\varphi}},$$

where,

$$J^2 = \mu^2 r^2(r^2\dot{\varphi}^2\sin^2\theta + r^2\dot{\theta}^2) = \mu^2 r^2(v_\theta^2 + v_\varphi^2),$$

The Hamiltonian is,

$$H = \frac{p^2}{2\mu} + V = \frac{\mu v^2}{2} + V = \frac{\mu(v_r^2 + v_\theta^2 + v_\varphi^2)}{2} + V,$$

and the dimensionless Hamiltonian is,

$$\hat{H} = \frac{H}{k_B T_g} = (\bar{v}_r^2 + \bar{v}_\theta^2 + \bar{v}_\varphi^2) + \frac{V}{k_B T_g},$$

or in terms of angular momentum, and setting $V \equiv V(r)$,

$$\hat{H} = \bar{v}_r^2 + \frac{\bar{J}^2}{r^2} + \frac{V(r)}{k_B T_g},$$

with $\bar{J}^2 = \frac{\mu}{2k_B T_g}J^2$. A dimensionless effective potential can be defined as follows,

$$V_{\text{eff}}(r) = \frac{\bar{J}^2}{r^2} + \frac{V(r)}{k_B T_g}.$$

The maximum (minimum) of this effective potential occurs at σ when,

$$\left.\frac{\mathrm{d}V_{\mathrm{eff}}}{\mathrm{d}r}\right|_{\sigma} = 0.$$

which implies that,

$$\frac{2\bar{J}^2}{\sigma^3} = \left[\frac{\mathrm{d}}{\mathrm{d}r}\left(\frac{V(r)}{k_{\mathrm{B}}T_g}\right)\right]_{\sigma}.$$

Now we write σ to be explicitly dependent on $\bar{J}$,

$$\bar{J}^2 = \frac{1}{k_{\mathrm{B}}T_g}\frac{\sigma^3(\bar{J})}{2}\frac{\mathrm{d}V(\sigma)}{\mathrm{d}\sigma}.$$

The particle in the center of mass system has the Maxwellian distribution in terms of H,

$$f = \left(\frac{\mu}{2\pi k_{\mathrm{B}}T_g}\right)^{3/2}\exp\bigl(-\hat{H}\bigr),$$

In the free molecular regime a particle with $\bar{v}_r < 0$ and a distance $\sigma(\bar{J})$ from the center of mass it will be collected to the surface r_{ij} due to the attracting potential, then the flux of particles to the surface of radius $\sigma(\bar{J})$ is,

$$F(\sigma(\bar{J})) = 4\pi\sigma^2(\bar{J})\int_{\bar{v}_r<0}\mathrm{d}\bar{v}_r\,\bar{v}_r f(\bar{J}, v_r).$$

Integrating the flux over all angular velocities will give the total flux,

$$F(\sigma(\bar{J})) = 4\pi\int\int \mathrm{d}v_\theta \mathrm{d}v_\varphi \sigma^2(\bar{J})\int_{\bar{v}_r<0}\mathrm{d}\bar{v}_r\,\bar{v}_r f(\bar{J}, v_r)$$

For

$$H_0 = \frac{\bar{J}^2}{\sigma^2(\bar{J})} + \frac{V(r)}{k_{\mathrm{B}}T_g},$$

and integrating over $\bar{v}_r$ gives,

$$F = v_{\mathrm{av}}\int\int \mathrm{d}\bar{v}_\theta \mathrm{d}\bar{v}_\varphi \sigma^2(\bar{J})\exp\left[-H_0(\bar{J})\right],$$

with,

$$v_{\mathrm{av}} = \sqrt{\frac{8k_{\mathrm{B}}T_g}{\pi\mu}}.$$

Now, $w^2 = \bar{v}_\theta^2 + \bar{v}_\varphi^2$, and integrating over the $w^2 =$ constant sphere in velocity space, finally the flux is,

$$F = \pi v_{\mathrm{av}}\int_0^\infty \mathrm{d}^2 w\sigma^2(w)\exp\left[-H_0(w)\right],$$

since $J^2 = \sigma^2 w^2$,

$$w^2 = \frac{\sigma}{k_B T_g} \frac{dV(\sigma)}{d\sigma}.$$

In the free molecular regime $w^2 = 0 \Rightarrow \sigma = \infty$, then the flux is,

$$F^{FM} = -\pi v_{av} \int_{r_{ij}}^{\infty} d\sigma \frac{1}{k_B T_g} \left[\frac{dV(\sigma)}{d\sigma} + \sigma \frac{d^2V(\sigma)}{d\sigma^2} \right] \sigma^2 \exp\left\{ -\left(\frac{1}{k_B T_g} \right) \left[\frac{\sigma}{2} \frac{dV(\sigma)}{d\sigma} + V(\sigma) \right] \right\}.$$

Finally, the Marlow enhancement factor is,

$$\eta^{FM} = \pi v_{av} r_{ij}^2 \exp\left\{ -\left[\frac{V(r_{ij})}{k_B T_g} + \frac{r_{ij}}{2 k_B T_g} \left. \frac{dV(\sigma)}{d\sigma} \right|_{r_{ij}} \right] \right\}$$
$$- \frac{\pi v_{av}}{2 k_B T_g} \int_{r_{ij}}^{\infty} d\sigma \frac{1}{k_B T_g} \left[\frac{dV(\sigma)}{d\sigma} + \sigma \frac{d^2V(\sigma)}{d\sigma^2} \right] \sigma^2 \exp\left\{ -\left(\frac{1}{k_B T_g} \right) \left[\frac{\sigma}{2} \frac{dV(\sigma)}{d\sigma} + V(\sigma) \right] \right\}. \quad (7.97)$$

7.4.2 Huang's approximation

The effect of image charges in the coagulation of aerosol particles was introduced by Huang[6], hereafter we follow his theory.

Let q_1, R_1, q_2 and R_2 be the initial charge and radius of particle 1 and 2, respectively; also denote ϵ as the particle dielectric constant and r as the distance between the two particle centers, as shown in figure 7.3

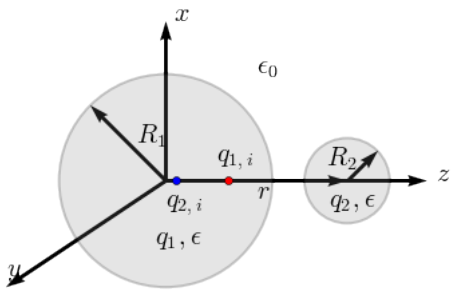

Figure 7.3: Set of image charges proposed to solve the potential

Huang proposes to set an image charge of $q_2(q_1)$ in particle 1(2) at a distance R_1^2/r $\left(R_2^2/r\right)$ from the center of particle 2(1). The values and positions of image charges are suggested by a textbook problem of image charges, solved by Lord Kelvin, that can be found in [7],

$$q_{1,i} = -\left(\frac{\epsilon-\epsilon_0}{\epsilon+\epsilon_0}\right)\frac{q_2 R_1}{r} = -\left(\frac{\epsilon_r-1}{\epsilon_r+1}\right)\frac{q_2 R_1}{r}, \tag{7.98}$$

$$q_{2,i} = -\left(\frac{\epsilon-\epsilon_0}{\epsilon+\epsilon_0}\right)\frac{q_1 R_2}{r} = -\left(\frac{\epsilon_r-1}{\epsilon_r+1}\right)\frac{q_1 R_2}{r}, \tag{7.99}$$

with $\epsilon_r = \epsilon/\epsilon_0$. Note that Huang does not consider higher order images, infinite images are needed to solve correctly this problem. The total charge for each sphere will be the sum of its initial charge plus the image charge,

$$z_1 e = q_1 + q_{1,i} = q_1 - \left(\frac{\epsilon_r-1}{\epsilon_r+1}\right)\frac{q_2 R_1}{r}, \tag{7.100}$$

$$z_2 e = q_2 + q_{2,i} = q_2 - \left(\frac{\epsilon_r-1}{\epsilon_r+1}\right)\frac{q_1 R_2}{r}. \tag{7.101}$$

Solving these equations for q_1 and q_2, respectively,

$$q_1(r) = \frac{z_1 e + z_2 e\left(\frac{\epsilon_r-1}{\epsilon_r+1}\right)\frac{R_1}{r}}{1-\left(\frac{\epsilon_r-1}{\epsilon_r+1}\right)^2\frac{R_1 R_2}{r^2}}, \tag{7.102}$$

$$q_2(r) = \frac{z_2 e + z_1 e\left(\frac{\epsilon_r-1}{\epsilon_r+1}\right)\frac{R_2}{r}}{1-\left(\frac{\epsilon_r-1}{\epsilon_r+1}\right)^2\frac{R_1 R_2}{r^2}}. \tag{7.103}$$

The electric forces between charge pairs are,

$$F_1(q_1, q_2, r) = \frac{1}{4\pi\epsilon_0}\frac{q_1 q_2}{r^2}, \tag{7.104}$$

$$F_2(q_1, q_{2,i}, r) = \frac{1}{4\pi\epsilon_0}\frac{q_1\left(-\frac{\epsilon_r-1}{\epsilon_r+1}\right)\frac{q_1 R_2}{r}}{(r^2-R_2^2)^2/r^2}, \tag{7.105}$$

$$F_3(q_2, q_{1,i}, r) = \frac{1}{4\pi\epsilon_0}\frac{q_2\left(-\frac{\epsilon_r-1}{\epsilon_r+1}\right)\frac{q_2 R_1}{r}}{(r^2-R_1^2)^2/r^2}, \tag{7.106}$$

$$F_4(q_{1,i}, q_{2,i}, r) = \frac{1}{4\pi\epsilon_0}\frac{\left(\frac{\epsilon_r-1}{\epsilon_r+1}\right)^2\frac{q_1 q_2 R_1 R_2}{r^2}}{(r^2-R_1^2-R_2^2)^2/r^2}. \tag{7.107}$$

We can nondimensionalize the force according to,

$$\frac{R_1+R_2}{k_bT_g}\sum_{i=1}^{4}F_i = M\sum_{i=1}^{4}\mathcal{F}_i, \tag{7.108}$$

$$M \equiv \frac{e^2}{4\pi\epsilon_0 k_b T_g\,(R_1+R_2)}. \tag{7.109}$$

and $\mathcal{F}_i$ can be written as,

$$\mathcal{F}_1 = k_1 k_2 x^2, \tag{7.110}$$

$$\mathcal{F}_2 = \frac{-pk_1^2(1-s)x^3}{\left[1-(1-s)^2x^2\right]^2}, \tag{7.111}$$

$$\mathcal{F}_3 = \frac{-pk_2^2 s x^3}{\left[1-s^2x^2\right]^2}, \tag{7.112}$$

$$\mathcal{F}_4 = \frac{-p^2k_1k_2(1-s)x^4}{\left[1-s^2x^2-(1-s)^2x^2\right]^2}, \tag{7.113}$$

with the following definitions,

$$k_1 \equiv \frac{q_1}{e}; \qquad k_2 \equiv \frac{q_2}{e}; \qquad x \equiv \frac{R_1+R_2}{r}; \qquad s \equiv \frac{R_1}{R_1+R_2}; \qquad p \equiv \frac{\epsilon_r-1}{\epsilon_r+1}. \tag{7.114}$$

Or in terms of the final charges z_1 and z_2,

$$k_1 = \frac{z_1 + z_2\left(\frac{\epsilon_r-1}{\epsilon_r+1}\right)\frac{R_1}{r}}{1-\left(\frac{\epsilon_r-1}{\epsilon_r+1}\right)^2\frac{R_1R_2}{r^2}} = \frac{z_1+pz_2sx}{1-p^2s(1-s)x^2}, \tag{7.115}$$

$$k_2 = \frac{z_2 + z_1\left(\frac{\epsilon_r-1}{\epsilon_r+1}\right)\frac{R_2}{r}}{1-\left(\frac{\epsilon_r-1}{\epsilon_r+1}\right)^2\frac{R_1R_2}{r^2}} = \frac{z_2+pz_1(1-s)x}{1-p^2s(1-s)x^2}. \tag{7.116}$$

The dimensionless image potential $\hat{\Phi}$ is obtained by integrating the forces over the radial distance,

$$\hat{\Phi}(x) = -M\int_{x=0}^{x}\sum_{i=1}^{4}\mathcal{F}_i \mathrm{d}\left(\frac{1}{x}\right) = M\sum_{i=1}^{4}\int_{x=0}^{x}\frac{\mathcal{F}_i}{x^2}\mathrm{d}x. \tag{7.117}$$

In the situation that one of the particles is uncharged $z_2 = 0$, and integrating the force we finally have,

Table 7.1: Estimation of forces in nanoparticles [10].

Force	10 nm	50 nm
Electrostatic	$\sim 2 \times 10^{-14}$ N	$\sim 10^{-13}$ N
Neutral drag	$\sim 10^{-17}$ N	$\sim 10^{-16}$ N
Ion drag	$\sim 5 \times 10^{-16}$ N	$\sim 5 \times 10^{-15}$ N
Thermophoresis	$\sim 10^{-17}$ N	$\sim 10^{-16}$ N
Gravity	$\sim 10^{-19}$ N	$\sim 5 \times 10^{-18}$ N

$$\hat{\Phi}_1(x) = \frac{aMx^2}{2(1-bx^2)}, \tag{7.118}$$

$$\hat{\Phi}_2(x) = \begin{cases} -\frac{aM}{2(b-c)^2}\left[\frac{b^2x^2}{1-bx^2} + \frac{c^2x^2}{1-cx^2}\right] + \frac{abcM}{(b-c)^3}\ln\left(\frac{1-cx^2}{1-bx^2}\right), & \text{if } b \neq c, \\ \frac{aM}{6b}\left[1 - \frac{1}{(1-bx^2)^3}\right], & \text{if } b = c, \end{cases} \tag{7.119}$$

$$\hat{\Phi}_3(x) = \begin{cases} -\frac{aM}{2(b-\alpha_3)^2}\left[\frac{b^2x^2}{1-bx^2} + \frac{bx^2\alpha_3}{1-\alpha_3x^2}\right] + M\left(\frac{ab^2+ab\alpha_3}{2(b-\alpha_3)^3}\right)\ln\left(\frac{1-\alpha_3x^2}{1-bx^2}\right), & \text{if } b \neq \alpha_3, \\ \frac{aM}{12b}\left[\frac{3bx^2-1}{(bx^2-1)^3} - 1\right], & \text{if } b = \alpha_3, \end{cases} \tag{7.120}$$

$$\hat{\Phi}_4(x) = \begin{cases} \frac{aM}{2(b-\alpha_4)^2}\left[\frac{b^2x^2}{1-bx^2} + \frac{bx^2\alpha_4}{1-\alpha_4x^2}\right] - M\left(\frac{ab^2+ab\alpha_4}{2(b-\alpha_4)^3}\right)\ln\left(\frac{1-\alpha_4x^2}{1-bx^2}\right), & \text{if } b \neq \alpha_4, \\ \frac{aM}{12b}\left[1 - \frac{3bx^2-1}{(bx^2-1)^3}\right], & \text{if } b = \alpha_4, \end{cases} \tag{7.121}$$

along with the following definitions,

$$\begin{aligned} a &\equiv pz_1^2(1-s) \quad ; \qquad \alpha_3 \equiv s^2, \\ b &\equiv p^2s(1-s) \quad ; \qquad \alpha_4 \equiv s^2 + (1-s)^2 = \alpha_3 + c, \\ c &\equiv (1-s)^2. \end{aligned} \tag{7.122}$$

7.4.3 Forces

In table 7.1 we give an estimate of the forces between nanoparticles for two sizes.

The linear Debye length is defined as follows,

$$\lambda_{\mathrm{L}} = \frac{\lambda_e\lambda_i}{\sqrt{\lambda_e^2 + \lambda_i^2}}. \tag{7.123}$$

With this definition we can write the electrostatic force [3],

$$\boldsymbol{F}_{\mathrm{E}} = Q_d\boldsymbol{E}\left(1 + \frac{(r_d/\lambda_{\mathrm{L}})^2}{3\,(1 + r_d/\lambda_{\mathrm{L}})}\right). \tag{7.124}$$

The neutral drag force is proportional to the relative velocity of the nanoparticle with respect to the gas [13],

$$\boldsymbol{F}_{\mathrm{ND}} = -\frac{4}{3}\pi r_d^2 m_g n_g v_g\left(\boldsymbol{u}_D - \boldsymbol{u}_g\right), \times \left(1 + \alpha\frac{\pi}{8}\right) \tag{7.125}$$

where m_g, n_g, v_g are the mass, density, and thermal velocity of molecules of the neutral gas, respectively. Here $\alpha = 0.9$, is the accommodation coefficient.

The ion drag force is [13],

$$\boldsymbol{F}_{\mathrm{ID}} = \pi n_i u_s m_i \boldsymbol{u}_i \left(h_j^2 + 4h_{\pi/2}^2 \gamma \right) \tag{7.126}$$

where n_i, m_i, u_s, and $\boldsymbol{u}_i$ are respectively the density, mass, mean velocity, and velocity of ions. In this expression,

$$h_j = r_d \left(1 - \frac{2q_j \phi_d}{m_j v_j^2} \right)^{1/2}, \tag{7.127}$$

is the impact parameter, and $h_{\pi/2}$ is the impact parameter for 90° deflections,

$$h_{\pi/2} = r_d \left(-\frac{q_j \phi_d}{m_j v_j^2} \right), \tag{7.128}$$

and γ is,

$$\gamma = \frac{1}{2} \ln \left(\frac{\lambda_{\mathrm{L}}^2 + h_{\pi/2}^2}{h_j^2 + h_{\pi/2}^2} \right). \tag{7.129}$$

The thermophoretic force arises from the temperature gradient [13],

$$\boldsymbol{F}_{\mathrm{T}} = -\frac{32}{15} \frac{r_d^2}{v_g} \kappa_{\mathrm{T}} \nabla T \left(1 + \frac{5\pi}{32} (1 - \alpha) \right), \tag{7.130}$$

$$\kappa_{\mathrm{T}} = \frac{15 k_{\mathrm{B}} \mu}{4 m_g} \tag{7.131}$$

where μ is the dynamic viscosity.

The gravitational force is proportional to the density and volume of the particle [13],

$$\boldsymbol{F}_{\mathrm{G}} = \frac{4}{3} \pi r_d^3 \rho \boldsymbol{g}, \tag{7.132}$$

where ρ, and $\boldsymbol{g}$ are the particle density and the gravitational acceleration. Finally, nanoparticles diffuse to the walls from the bulk which has a higher concentration. The diffusion coefficient is given by [13],

$$D_p = \frac{1}{r_d^2 n_g} \sqrt{\frac{k_{\mathrm{B}} T_g}{2\pi m_g}} \left(\frac{3}{8} \right) \left(1 + \alpha \frac{\pi}{8} \right)^{-1}. \tag{7.133}$$

7.5 References

[1] P. Agarwal and S.L. Girshick. Sectional modeling of nanoparticle size and charge distributions in dusty plasmas. *Plasma Sources Sci. Technol.*, 21(5):055023, October 2012.

[2] J.-P. Boeuf. Numerical model of rf glow discharges. *Phys. Rev. A*, 36(6):2782–2792, September 1987.

[3] J. E. Daugherty, R. K. Porteous, and D. B. Graves. Electrostatic forces on small particles in low-pressure discharges. *Journal of Applied Physics*, 73(4):1617–1620, February 1993.

[4] S. K. Friedlander. *Smoke, Dust, and Haze: Fundamentals of Aerosol Dynamics*. Oxford University Press, 2000.

[5] G. J. M. Hagelaar and G. M. W. Kroesen. Speeding up fluid models for gas discharges by implicit treatment of the electron energy source term. *Journal of Computational Physics*, 159(1):1–12, March 2000.

[6] D. D. Huang, J. H. Seinfeld, and K. Okuyama. Image potential between a charged particle and an uncharged particle in aerosol coagulation—enhancement in all size regimes and interplay with van der waals forces. *Journal of colloid and interface science*, 141(1):191–198, 1991.

[7] J. D. Jackson. *Classical electrodynamics*. Wiley, New York, NY, 3rd ed. edition, 1999.

[8] S. Kumar and D. Ramkrishna. On the solution of population balance equations by discretization—I. A fixed pivot technique. *Chemical Engineering Science*, 51(8):1311–1332, April 1996.

[9] Marlow, H.W. Derivation of aerosol collision rates for singular attractive contact potentials. *The Journal of Chemical Physics*, 73(12):6284–6287, December 1980.

[10] A. Michau. *Modélisation numérique d'une décharge DC poussiéreuse : couplage entre équilibre de la décharge, croissance moléculaire et dynamique d'aérosol*. PhD thesis, 2012.

[11] S. H. Park and S. N. Rogak. A novel fixed-sectional model for the formation and growth of aerosol agglomerates. *Journal of Aerosol Science*, 35(11):1385–1404, November 2004.

[12] D. L. Scharfetter and H. K. Gummel. Large-signal analysis of a silicon read diode oscillator. *IEEE Transactions on Electron Devices*, 16(1):64–77, 1969.

[13] P. K. Shukla and A. A. Mamun. *Introduction to Dusty Plasma Physics*. CRC Press, December 2010.

[14] H. M. Vale and T. F. McKenna. Solution of the Population Balance Equation for Two-Component Aggregation by an Extended Fixed Pivot Technique. *Ind. Eng. Chem. Res.*, 44(20):7885–7891, September 2005.

[15] S. J. Warthesen and S. L. Girshick. Numerical simulation of the spatiotemporal evolution of a nanoparticle–plasma system. *Plasma Chem Plasma Process*, 27(3):292–310, June 2007.